



Etude optique de nanofils GaN et de microcavités GaN/AlN

Diane Sam-Giao Sam-Giao

► To cite this version:

Diane Sam-Giao Sam-Giao. Etude optique de nanofils GaN et de microcavités GaN/AlN. Autre [cond-mat.other]. Université de Grenoble, 2012. Français. NNT : 2012GRENY075 . tel-00870498

HAL Id: tel-00870498

<https://theses.hal.science/tel-00870498>

Submitted on 7 Oct 2013

HAL is a multi-disciplinary open access archive for the deposit and dissemination of scientific research documents, whether they are published or not. The documents may come from teaching and research institutions in France or abroad, or from public or private research centers.

L'archive ouverte pluridisciplinaire **HAL**, est destinée au dépôt et à la diffusion de documents scientifiques de niveau recherche, publiés ou non, émanant des établissements d'enseignement et de recherche français ou étrangers, des laboratoires publics ou privés.

THÈSE

Pour obtenir le grade de

DOCTEUR DE L'UNIVERSITÉ DE GRENOBLE

Spécialité : **Physique de la matière condensée et du rayonnement**

Arrêté ministériel : 7 août 2006

Présentée par

Diane Sam-Giao

Thèse dirigée par **Bruno Gayral**

préparée au sein de l'Equipe mixte CEA-CNRS "Nanophysique et
semiconducteurs"
et de l'Ecole doctorale de Physique

Optical study of GaN nanowires and GaN/AlN microcavities

Thèse soutenue publiquement le **15 novembre 2012**,
devant le jury composé de :

M. Pierre Lefebvre

CNRS - Laboratoire Charles Coulomb, Président et Rapporteur

M. Joël Leymarie

CNRS - Laboratoire des sciences et matériaux pour l'électronique et
l'automatique, Rapporteur

M. Raphaël Butté

Ecole polytechnique fédérale de Lausanne, Examineur

Mme Sophie Bouchoule

CNRS - Laboratoire de photonique et nanostructures, Examinatrice

M. David Ferrand

Université Joseph Fourier, Examineur

M. Bruno Gayral

CEA - Institut nanosciences et cryogénie, Directeur de thèse



Contents

1	From bulk GaN to nitride nanowires and UV nanoresonators	9
1.1	Structural and electronic properties of bulk nitride semiconductors	10
1.1.1	Crystal phase	10
1.1.2	Growth	12
1.1.3	Spontaneous polarization and piezoelectricity	13
1.1.4	Band structures	15
1.2	Optical properties of bulk nitride materials	17
1.2.1	Excitons	17
1.2.2	Bandgap-related effects	20
1.3	Peculiarities of GaN nanostructures	22
1.3.1	Band offsets and excitonic confinement	22
1.3.2	Quantum-confined Stark effect	23
1.4	On the interest of nitride nanowires	26
1.4.1	Electronic properties: excitonic confinement	26
1.4.2	Consequences of large surface to volume ratio	28
1.4.3	Photonic properties	31
1.4.4	New substrates for growing novel heterostructures?	33
1.4.5	Nitride nanowire-based light-emitting diodes	34
1.5	Nitride microcavities for UV nanoresonators	35
1.5.1	Theory of cavity quantum electrodynamics in the weak coupling regime	36
1.5.2	Different types of semiconductor microcavities	37
1.5.3	Historical background and applications of cavity quantum electrodynamics	39
1.5.4	State of the art with nitride cavities	41
2	Optical properties of GaN nanowires	43
2.1	Spontaneous growth of GaN nano- and micro-wires	44

2.1.1	Plasma-assisted molecular beam epitaxy	44
2.1.2	Metal organic chemical vapor deposition	46
2.2	Optical properties of an ensemble of wurtzite GaN nanowires grown by MBE	48
2.2.1	Non-intentionally doped samples	48
2.2.2	p-doped nanowires	50
2.3	Optical spectroscopy of a single nanowire	52
2.3.1	Dispersion method	52
2.3.2	Discrepancies between the emission properties of an ensemble of nanowires and of a single nanowire, grown by MBE	53
2.3.3	Non-intentionally doped microwires grown by MOCVD	55
2.3.4	Non-intentionally doped nanowires grown by MOCVD in low-flux growth conditions	56
2.4	Varying the diameter to observe quantum confinement	58
2.4.1	Looking for one-dimensional confinement in as-grown nanowires	58
2.4.2	Fabricating quantum wires	62
2.5	Optical properties of cubic GaN nanowires	63
2.5.1	Cubic GaN growth and structural characterizations	64
2.5.2	Identification of bound, free and split-off exciton	65
2.5.3	Luminescence enhancement with laser exposure	67
3	The mysterious emission at 3.45 eV	69
3.1	State of the art: the controversy	70
3.2	Polarization of this line	72
3.3	Magnetophotoluminescence experiments	73
3.3.1	Magneto-optical measurement of the line at 3.45 eV	76
3.3.2	Magneto-optical properties of bound excitons	77
3.4	Mechanisms responsible for a quenching of the 3.45 eV transition	80
3.4.1	Variable emission from wire to wire	80
3.4.2	Consequences of p-doping	81
3.4.3	Orientation of the silicon substrate	82
3.4.4	Influence of the growth techniques	82
3.5	Influence of the nanocolumn density on the intensity of the emission at 3.45 eV	83
3.5.1	Growth conditions and optical results	84
3.5.2	Discussion	88
3.6	Influence of the nanocolumn density on the decay dynamics of the near band edge	92
3.6.1	Preamble on decay time measurements	93
3.6.2	Decay dynamics of dense GaN nanowires	93
3.6.3	Variation of the spontaneous emission rate	95
3.6.4	Results	96

3.6.5	Discussion and perspectives	97
4	Spectroscopy of GaN / AlN microdisk resonators	99
4.1	Whispering gallery modes	100
4.1.1	The slab waveguide	101
4.1.2	Whispering gallery mode approximation	104
4.1.3	Intensity profile of a given mode (ℓ, m, n)	105
4.2	Fabrication	106
4.2.1	The active layer	106
4.2.2	Design of the microdisk geometry	108
4.2.3	Studied samples	109
4.3	Free spectral range and diameter	110
4.3.1	Comparison with calculations in the whispering gallery mode approximation	110
4.3.2	Comparison with FDTD simulations	112
4.4	Measurements of record quality factors	113
4.4.1	Measurements of the quality factor	113
4.4.2	Origins of losses in the microdisk resonator	114
4.5	Directionality and polarization of the emission	120
4.5.1	Directionality of the emission	120
4.5.2	Polarization of the emission	122
4.6	Whispering gallery modes — towards a Purcell-enhanced microdisk laser	123
5	Optical study of GaN/AlN nanocavities in photonic crystal waveguides	125
5.1	Introduction	127
5.1.1	Opening of a photonic bandgap around 3.2 eV	127
5.1.2	Fabrication process	127
5.1.3	Design	128
5.2	First experimental results and simulations	130
5.2.1	Mode spectral positions	130
5.2.2	FDTD simulations	131
5.3	Identification of the modes	133
5.3.1	By their spectral positions	133
5.3.2	By comparison with calculated mode splittings	134
5.3.3	By micro-photoluminescence scan along the waveguide axis	136
5.4	Quality factors	140
5.4.1	Origin of extrinsic losses	141
5.4.2	Record value of the quality factor	142
5.5	Highest energy series: towards UV nanoresonators	144
5.5.1	Mode spectral positions and splittings	144
5.5.2	Quality factor at 3.46 eV	145

5.6	Chapter conclusion : towards the Purcell effect	146
6	Towards the Purcell effect and lasing with GaN/AlN cavities	147
6.1	Towards the Purcell effect with nitrides	148
6.1.1	Experimental demonstrations of the Purcell effect in arsenide compounds	148
6.1.2	The expected Purcell effect in GaN/AlN cavities — dependence on the homogeneous linewidth of the emitters	150
6.1.3	Measurements on GaN/AlN microdisks	154
6.1.4	Measurements on GaN/AlN nanocavities embedded in photonic crystal waveguide	155
6.2	Modal instability with exposure time	157
6.2.1	Instability of a whispering gallery mode under pulsed excitation .	158
6.2.2	Whispering gallery mode shifting under continuous-wave excitation	160
6.2.3	Photonic crystal cavity mode: stable or instable?	163
6.2.4	Possible explanations for cavity mode shift	166
6.3	Instability of quantum dot emission under long exposure	170
6.3.1	Checking the stability of non-etched quantum dots	170
6.3.2	Instability of etched quantum dots	171
6.3.3	Possible processes resulting in the blueshift and a quenching of the emission of etched samples	173
6.4	Towards UV microlasers	175
6.4.1	Theory	175
6.4.2	Lasing experiments	179
6.4.3	Comparison between our system and experimental demonstrations of lasing microcavities	179
6.4.4	Prospects to achieve lasing with GaN/AlN microcavities	182
7	Conclusion and prospects	187
7.1	Main results	187
7.2	Prospects	189
7.2.1	GaN nanowires	189
7.2.2	GaN/AlN microcavities	191
A	Résumé en français	195
B	Experimental techniques	199
C	Publications	205
	Index	207
	Bibliography	209

Remerciements

Les travaux présentés dans ce manuscrit ont été réalisés au sein de l'équipe mixte CEA/CNRS/UJF Nanophysique et Semiconducteurs : merci à Jean-Michel Gérard et Henri Mariette pour leur accueil chaleureux d'abord pour mon stage de master, puis pour ma thèse.

Un grand merci également à l'ensemble de mon jury de thèse. J'ai beaucoup apprécié leur lecture détaillée du manuscrit et leur attention sans faille pendant la présentation, qui a largement contribué à me mettre à l'aise. Je remercie chaleureusement Pierre Lefebvre pour avoir accepté d'être rapporteur et de jouer également le rôle de président du jury, pour les discussions animées - scientifiques ou non - que nous avons eues avant, pendant et après la soutenance. Je suis reconnaissante envers Joël Leymarie pour son travail de rapporteur. Merci aussi à Raphaël Butté pour les commentaires sur le manuscrit, ainsi qu'à Sophie Bouchoule et David Ferrand.

Avant tout, je tiens à souligner que ce projet n'aurait pas pu se concrétiser sans bourse, et je suis très reconnaissante envers Bruno Gayral, Bruno Daudin, et l'ANR pour m'avoir permis de l'obtenir.

Merci à Henri Mariette, directeur de ma thèse pendant la première année.

Bruno Gayral, qui a toujours suivi mes travaux, a ensuite pris le relais officiellement : je tiens à le remercier pour sa compréhension, sa patience et sa pédagogie pour partager la grande culture scientifique qu'il possède. Je lui dois la majorité de ce que j'ai appris pendant ces trois ans et demi. Je salue particulièrement son soutien et sa disponibilité pendant la préparation de la soutenance, et l'attention qu'il continue à me porter dans cette période de recherche d'emploi.

Une grande partie de ces études n'aurait jamais vu le jour sans l'aide précieuse de Joël Bleuse, qui a réussi à trouver des créneaux libres sur la manip' résolue en temps, mais aussi pour avoir solutionné un certain nombre de problèmes complexes. La précision de ses conseils m'a été très utile.

La spectroscopie optique n'étant rien sans bons échantillons, je suis reconnaissante envers toutes les équipes qui m'ont fourni des structures de qualité.

Merci à Bruno Daudin et son équipe, Karine Hestroffer, Aurélie Pierret, Gabriel

Tourbot, Vincent Fellmann, sans oublier Rafael Mata, et plus récemment Robert Estivill et Thomas Auzelle à qui je souhaite bonne chance pour mener de front la croissance, les calibrations et assimilés, et les caractérisations optiques. Les échanges avec les épitaxieurs ont été très fréquents et agréables et m’ont permis de connaître des rudiments de MBE sans avoir jamais touché à la machine.

Je remercie aussi chaleureusement les membres de l’ANR Sinphoni. Tout d’abord, un grand merci à Fabrice Semond et Sylvain Sargent puis Mohammad-Junaebur Rashid pour la fabrication de couches de boîtes quantiques à la fois très fines et très luminescentes et des premiers microdisques ! Le design et la réalisation des cavités reviennent à Philippe Boucaud et Delphine Néel, la modélisation de ces structures complexes, à Xavier Chécoury et l’exploration de la face arrière par FIB, à Sylvain David. Je n’oublie pas non plus Thierry Guillet, Christelle Brimont et Meletis Mexis pour leurs propres caractérisations optiques, et leur accueil lors de ma visite en 2010.

Enfin, j’ai eu beaucoup de plaisir à travailler avec les épitaxieurs de la MOCVD du NPSC et suivre les avancées de leurs travaux. Merci à Joël Eymery, Christophe Durand, Damien Salomon, Chen Xiaojun et Robert Köster pour les discussions intéressantes.

Merci également à Marek Potemski et Andrzej Wyszomolek de m’avoir permis de travailler au LCMI, et de l’aide apportée à la fois pendant les manips et le dépouillement des données.

Je n’oublierai pas l’accueil “VIP” qui m’a été réservé à Magdebourg par l’équipe de Jürgen Christen. Je leur suis sincèrement reconnaissante de m’avoir permis d’étudier mes nanofils avec un tel outil - la STEM-CL à 4 K : un grand merci à Frank Bertram, Peter Veit, Gordon Schmidt et Marcus Müller.

Je suis infiniment reconnaissante envers les personnes qui ont pris sur leur temps libre pour la relecture constructive du manuscrit : Joël Bleuse, Jan-Peter Richters, et Gabriel Tourbot. Un grand merci à toutes les personnes qui m’ont aidée à préparer la soutenance : Bruno Daudin, Henri Mariette, Julien Claudon, Catherine Bougerol, Joël Bleuse, mais aussi Andrzej Wyszomolek depuis la Pologne, Le Si Dang depuis le Vietnam et, surtout Ronald Cox pour sa maîtrise des problématiques liées aux règles de sélection et sa grande connaissance de la spectroscopie fine des semiconducteurs en général.

Et enfin, merci à Hervé, Julien, Lionel, Emmanuel, Jan-Peter, Fernando, Jean, Yann, Vincent, Joël et Joël pour votre bonne humeur, aux auteurs respectifs de marietteries et régisseries, ainsi qu’à Adrien et Damien pour vos propositions de sortie. Merci à Karine d’avoir partagé le bureau avec moi pendant ces trois années. Merci à Aurélie pour les soirées à la colloc’, Pamela pour les leçons d’espagnol, Miryam pour les soirées Halloween qui resteront célèbres, à Sirona pour l’aide à apprivoiser LaTeX, à Martien, pour les membranes TEM, à Yoann, pour Linux, et Olivier, pour le kéké et autres bêtises, sans oublier les conseils en tout genre... J’ai vraiment beaucoup apprécié la bonne ambiance qui règne au labo, et les discussions aux pauses café ou à midi. J’espère sincèrement rencontrer dans ma future vie professionnelle des collègues de travail aussi agréables et enrichissants.

Je tiens à remercier tous ceux qui m’ont aidé de près ou de loin dans ma recherche d’emploi : Régis pour les suggestions concernant le CV, Henri pour ses pistes et la diffusion des annonces, Bruno pour les recommandations, sans oublier l’association Valoridoc, et en particulier, Philippe et Gérard.

Je n'oublie pas Pauline et Solveig, qui m'ont toujours écoutée quand j'avais besoin de parler et avec qui j'ai passé de très bons moments depuis la 1A de PG... et les réunions et sorties avec AITAP (les lasagnes et les tiramisus vont me manquer).

Enfin, un énorme merci à ma famille, qui m'a toujours soutenue et a toujours su me redonner confiance en moi : à ma maman, à Christophe (merci pour le prêt forcé de l'ordi pendant un an et désolée pour ta créativité musicale), à Flo et JM pour leurs conseils, leur écoute et leur soutien dans tous les moments critiques, sans oublier tous les contacts pour chercher du boulot ! Merci à Mamie, Papy, Nounouche, Dédé, France, et Didier d'être venus à Grenoble ce fameux 15 novembre 2012.

Enfin, comme l'a dit le physicien Samuel C. C. Ting, prix Nobel de physique en 1976 : *“Si vous savez ce que vous cherchez, et que vous le trouvez, vous n'avez rien appris. L'important, c'est de trouver ce que vous n'attendiez pas”*. Merci à TOI, pour ta patience (de me supporter au quotidien), ta confiance, ton aide dans toutes les épreuves auxquelles j'ai été confronté durant ces trois ans ; et pour toutes les belles découvertes et toutes les petites attentions du quotidien.

Introduction

Context

Nitride semiconductors, *i.e.* III-V materials with nitrogen as the V-element, are usually put aside from other III-V materials due to their rather peculiar properties. Their band gaps span from ultraviolet — 6.25 eV (198 nm) for AlN, 3.51 eV (353 nm) for GaN, to infrared — 0.7 eV (1770 nm) for InN. Figure 1 illustrates the band gap of most semiconductors. The extended range of achievable wavelengths makes them very attractive for light emitting diode and laser applications. Both actual and potential markets are wide and include optical data storage, public and housing lighting, sterilization by DNA destruction, and optical lithography.

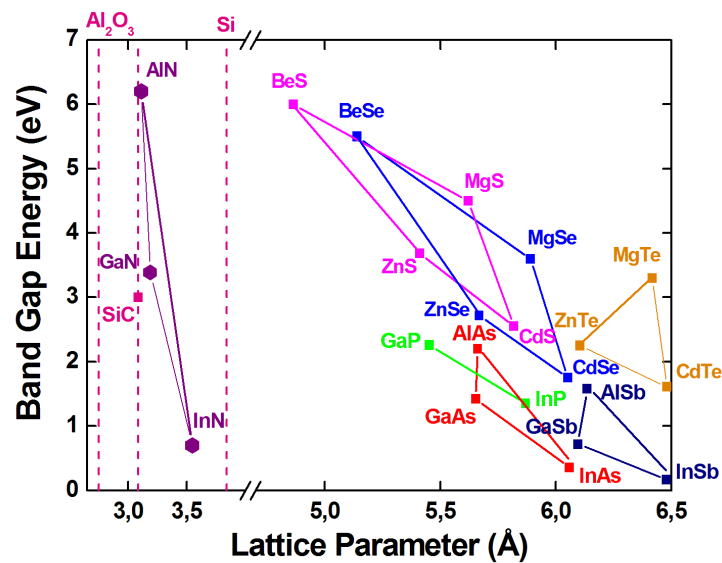


Figure 1 – Energy gap of III-V, II-VI and IV semiconductors versus their lattice parameters [Ser09a]

Yet, extensive studies related to nitride materials began two decades ago only, with the first light-emitting diode containing nitride materials in 1991 [Nak91]. It is indeed difficult to obtain high-quality nitride semiconductors. The lack of low-cost nitride substrates — drastic conditions are needed to grow bulk GaN [Dwi08][Por98], as well as the absence of adapted heterosubstrates for epitaxial growth, lead to highly-defective materials. Moreover, nitride heterostructures exhibit strong electric fields due to the difference of spontaneous and piezoelectric polarizations between the various compounds composing the heterostructure. By spatially separating electrons from holes, the spontaneous emission rate is lowered [Bre03].

Achieving 60% of external quantum efficiency in low-In content InGaN / GaN quantum well light-emitting diodes [Kha08] was therefore unexpected good news. Yet, these exceptional performances are limited to the blue-violet wavelength range: when going towards either green [Kha09] or UV wavelengths [Kha08], the efficiency strongly drops.

In parallel, during the past thirty years, the field of cavity quantum electrodynamics has developed in both the arsenide and the silicon communities. Both strong and weak coupling regimes were explored, in various three-dimensional photonic boxes such as micropillars [G98], microdisks [Gay01] and photonic crystal cavities [Aka03], making use of an assembly of quantum dots, or a single resonant emitter [Pet05b]. In nitride microcavities, only strong coupling was demonstrated in one-dimensional structures [Mal02][Chr07][Chr08]. The lack of efficient small lasers emitting in the near UV range makes three-dimensional cavities embedding GaN/AlN quantum dots appealing.

Furthermore, during the past ten years, nanowires have been attracting the interest of the whole semiconductor community [Aga06]. In nitride compounds, the one-dimensional geometry offers the advantage of lateral strain relaxation compared to strongly-strained two-dimensional layers [Gla06][Ray06]. It allows to foresee the realization of quasi defect-free heterostructures with high lattice mismatch, such as high-In or Al content in (In)GaN / (Al)GaN heterostructures. It is thus necessary to study the optical properties of these novel objects, in order to determine their potential compared to that of bulk material.

In this context, this work aims at performing optical spectroscopy on both GaN nanowires and AlN microcavities embedding GaN quantum dots.

Overview of the thesis

The first chapter will be an introduction to nitrides materials, to the specificities of the nanocolumnar geometry, as well as to the field of cavity quantum electrodynamics.

In the second chapter, we will study the optical properties of as-grown GaN nanowires obtained by plasma-assisted MBE, as well as nanorods grown either by MBE or MOCVD

and dispersed on a host substrate to perform spectroscopy of a single object. The first studies on diameter tuning will be then presented. Finally, we will see that it is possible to tune the crystal phase from wurtzite to zinc-blende. The resulting cubic GaN is of excellent optical quality and allows a precise study of its photoluminescence.

The third chapter will discuss the nature of the line at 3.45 eV in the photoluminescence of GaN nanowires obtained by plasma-assisted MBE. On bulk GaN, optical studies allowed to attribute this emission to a two-electron satellite of the donor bound exciton [Fio97]. In nanowires, this line has been ascribed to the same origin as in bulk, but originating from the surface of the nanorods [Cor09]. According to this interpretation, its greater intensity in nanocolumns would be explained by a greater surface to volume ratio [Lef11]. We will show that many basic properties of this line differ from that of the bulk two-electron satellite.

Then, chapter 4 will present the optical properties of GaN / AlN quantum dot microdisks, for which state-of-the art quality factors are obtained. In microdisks of 2- μm diameter exhibiting a low enough number of modes, the latter will be indexed. The origin of photon losses will be analyzed, from intrinsic ones to absorption, scattering losses and light coupling to the underneath silicon post. Finally, the directionality of the emission from whispering gallery modes will be investigated.

In chapter 5, we will study the optical spectroscopy of GaN / AlN photonic crystal nanocavities embedded into photonic waveguides. Experimental results will be compared to simulations in order to index the modes. Additional measurements will confirm the attribution of each mode as originating either from the cavity or from the waveguide. Then, by studying the quality factors of these structures, we will compare their robustness to more standard photonic crystal cavities.

In chapter 6, we will present the experiments we performed in order to evidence the Purcell effect in both the microdisks and the photonic crystal cavities depicted in chapters 4 and 5, respectively. We will see that unexpected phenomena occur when performing long acquisitions. Furthermore, we will discuss the potentialities of our photonic structures in terms of lasing performances.

Finally, the perspectives raised by the results of this work will be developed in a last chapter.

From bulk GaN to nitride nanowires and UV nanoresonators

IN THIS FIRST CHAPTER, the most important intrinsic properties of nitride semiconductors will be reviewed. Then, we will see how we can make use of nitride nanowires to fabricate novel devices or to explore the physics of one-dimensional objects. The potentialities of nitride microcavities for UV nanoresonators will be addressed.

Contents

1.1	Structural and electronic properties of bulk nitride semiconductors	10
1.1.1	Crystal phase	10
1.1.2	Growth	12
1.1.3	Spontaneous polarization and piezoelectricity	13
1.1.4	Band structures	15
1.2	Optical properties of bulk nitride materials	17
1.2.1	Excitons	17
1.2.2	Bandgap-related effects	20
1.3	Peculiarities of GaN nanostructures	22
1.3.1	Band offsets and excitonic confinement	22
1.3.2	Quantum-confined Stark effect	23
1.4	On the interest of nitride nanowires	26
1.4.1	Electronic properties: excitonic confinement	26
1.4.2	Consequences of large surface to volume ratio	28
1.4.3	Photonic properties	31
1.4.4	New substrates for growing novel heterostructures?	33
1.4.5	Nitride nanowire-based light-emitting diodes	34

by $\vec{u} = \frac{3}{8}\vec{c}$. Each of these lattices is composed by cations or anions only and shows the typical stacking of hexagonal structures, *i.e.* ABABAB. Under certain conditions, nitrides can also exhibit a *zinc-blende* structure (see figure 1.1 (a)). Two face-centered cubic lattices, one with anions and the other with cations, are shifted by $\frac{1}{4}[1,1,1]$, *i.e.* in the direction of the main diagonal of the cube. The stacking is here ABCABC. c and a are the lattice parameters along the vertical axis and in-plane, respectively. We use the notation $\vec{c} = [0001]$ and $-\vec{c} = [000\bar{1}]$. In the hexagonal system, the four-index notations is used. A typical example is $[hkil]$ where $h + k + i = 0$. Note that the indexes h and k are not equivalent to that used to label an $[hkl]$ direction in a cubic lattice.

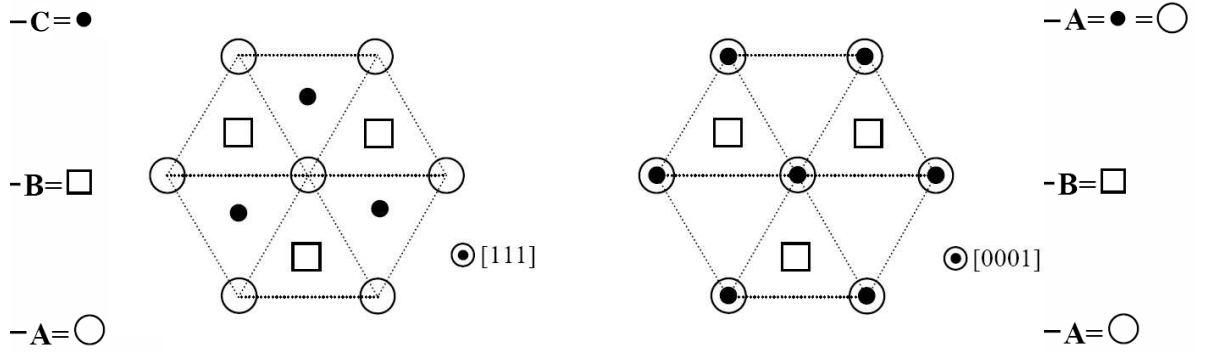


Figure 1.2 – Layer stacking in the zinc-blende phase along the $[111]$ direction (left) and the wurtzite phase along the $[0001]$ direction (right). The layers A, B and C refer to the labeling of figure 1.1 - extracted from [Yeh92]

In both cases, each cation (respectively anion) is surrounded by four anions (respectively cations), forming a perfectly symmetrical tetrahedron. In the ideal wurtzite structure, one can notice that $\frac{c}{a} = \sqrt{\frac{8}{3}} \approx 1.633$. We will see that in the real structure, $\frac{c}{a}$ deviates from this value.

From figure 1.2, one can notice that both phases are very similar: the difference between a cubic stacking in the $[111]$ direction and an hexagonal stacking in the $[0001]$ direction differs only by the third layer of deposited atoms. Quantitatively, their formation energy differs by only 10 meV/atom [Sta99]. Experimentally, the growth of nitride materials in standard conditions leads to wurtzite crystals. Cubic substrates are usually used when one wants to grow zinc blende layers. Yet due to this small energy difference, cubic GaN crystals often exhibit hexagonal phase inclusions and stacking faults.

Note that the wurtzite crystal is the highest-symmetry lattice allowing to be *non-centrosymmetrical*. Besides, in the realistic wurtzite structure grown along $[0001]$, the polarity of the Ga-N bond either compresses or extends the tetrahedron. Thus both lattices are not shifted exactly by $\frac{3}{8}\vec{c}$ in the hexagonal case and by $\frac{1}{4}(\vec{a} + \vec{b} + \vec{c})$ in the cubic. This distortion gives a second contribution to the non-centrosymmetrical feature of the ideal wurtzite stacking. Table 1.1 displays the lattice parameters of both phases, and the resulting $\frac{c}{a}$ ratio, to be compared to the ideal value of $\sqrt{\frac{8}{3}} \approx 1.633$. The non-

structure	parameter	AlN	GaN	InN
wurtzite	a (Å)	3.112	3.189	3.545
wurtzite	c (Å)	4.982	5.185	5.703
wurtzite	c/a	1.601	1.626	1.609
zinc blende	a (Å)	4.38	4.50	4.98

Table 1.1 – AlN, GaN, InN lattice parameters at 300 K [Vur03]

centrosymmetry of the \vec{c} axis leads to the non-equivalence between layers grown along the \vec{c} and $-\vec{c}$ directions. We define the *polarity* of the layer as Ga-polar if it is grown along \vec{c} and as N-polar if it is grown along the $-\vec{c}$ direction. Both cases are illustrated on figure 1.3.

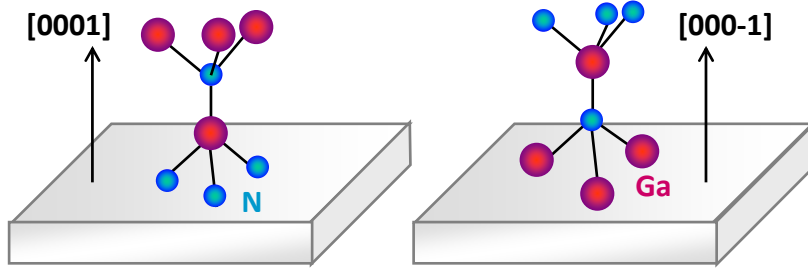


Figure 1.3 – Illustration of Ga-polarity (left) and N-polarity (right)

1.1.2 Growth

Nitride wafers are very scarce because their fabrication requires drastic conditions [Dwi08][Por98]. For now, only small wafers can be fabricated. This is the reason why nitride semiconductors are mainly grown by *heteroepitaxy* techniques. Epitaxy refers to the deposition of a crystal on a substrate where both crystalline lattices are aligned. *Heteroepitaxy*, contrary to *homoepitaxy*, is defined as the growth of a layer over a material of different nature. The lack of substrates adapted to nitrides — both in terms of lattice mismatches and thermal expansion coefficients (see table 1.2) — has proven to be very detrimental to the quality of the materials. Indeed, the strain accumulated inside the layer increases after each deposited monolayer. Eventually, the crystal relaxes plastically, and one obtains a very high *dislocation density*, in the range of 10^8 to 10^{10} cm $^{-2}$, to be compared to 10^2 – 10^4 cm $^{-2}$ in homoepitaxial GaAs.

Nitride semiconductors are usually grown by three main different epitaxy techniques: molecular beam epitaxy, metal-organic chemical vapour deposition and hydride vapor phase epitaxy. *Molecular beam epitaxy* consists in sending atoms or molecules on a heated substrate. The chamber being in ultra-high vacuum, their trajectory is ballistic from the effusion cells towards the sample surface. Nitrogen can be provided either by a

Crystal	a(Å)	$\frac{a_{\text{GaN}} - a_{\text{substrate}}}{a_{\text{GaN}}} (\%)$	$\frac{a_{\text{AlN}} - a_{\text{substrate}}}{a_{\text{AlN}}} (\%)$
GaN (0001)	3.189	0	2.4
AlN (0001)	3.112	-2.4	0
Sapphire (0001)	4.758	14 (30°rotation)	13
Silicon (111)	3.845	-21	-19
Silicon carbide 6H	3.082	3	1

Crystal	$\alpha (10^{-6} \text{ K}^{-1})$	$\frac{\alpha_{\text{GaN}} - \alpha_{\text{substrate}}}{\alpha_{\text{GaN}}} (\%)$	$\frac{\alpha_{\text{AlN}} - \alpha_{\text{substrate}}}{\alpha_{\text{AlN}}} (\%)$
GaN (0001)	4.3	0	-30
AlN (0001)	3.0	30	0
Sapphire (0001)	7.5	-441	79
Silicon (111)	2.59	40	-38
Silicon carbide 6H	4.7	-32	12

Table 1.2 – Differences in lattice parameters and thermal expansion coefficients between GaN, AlN and the substrates which are most commonly used for heteroepitaxy of nitride materials

flux of N_2 cracked in a radio-frequency plasma (plasma-assisted MBE) or by a NH_3 flux: ammonia will decompose at the surface of the heated sample (ammonia-MBE). *Metal-organic chemical vapor deposition* is the most widely used technique. Metal-containing organic molecules and ammonia are provided in the gas phase at nearly atmospheric pressure and cracked in the vicinity of the substrate heated around 1000°C . *Hydride vapor phase epitaxy* was the first nitride deposition method to be developed. It is based on the reaction between halogenides and gas containing nitrogen.

1.1.3 Spontaneous polarization and piezoelectricity

Figure 1.4 illustrates the atomic arrangement of one entire lattice cell (left) and the first neighbors around a nitrogen atom (right). The polarization in a nitride layer has two origins: the spontaneous and the piezoelectric polarizations. The spontaneous polarization can be described as follows. We have seen in 1.1.1 that nitride crystals are non-centrosymmetrical because of their wurtzite crystalline structure and the polarity of the Ga-N bond induced by a strong electronegativity difference between both atoms. As a consequence, electrons are more strongly attracted to nitrogen than gallium. At the atomic scale, it leads to a shorter Ga-N bond in the \vec{c} direction (lower bound of the tetrahedron on figure 1.4(b) (right panel)) compared to other directions (three upper bounds) [Yeh92]. Each tetrahedron is thus distorted along the \vec{c} axis, resulting in a macroscopic polarization for layers grown along this axis. Indeed, the crystal keeps its macroscopic neutrality, but the first charge layer on each surface side remains uncompensated. This is called the *spontaneous polarization* and exists even if the crystal is strain-free. The values of the spontaneous polarization are given in table 1.3. Note

that the polarization cannot be directly measured: only a polarization difference is measurable. On the contrary, if the same structure is grown along a non-polar axis, as the spontaneous polarization still lies along the \vec{c} axis, one will not be able to measure it. Indeed, what we measure is the projection along the growth axis of the polarization difference between two surfaces.

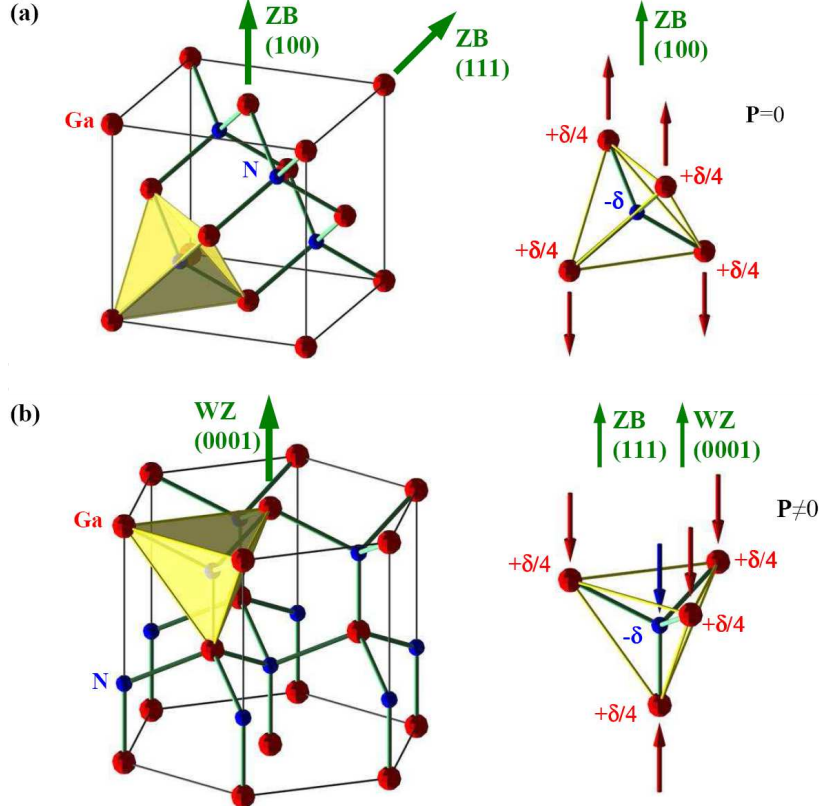


Figure 1.4 – Lattice and associated deformation of the tetrahedron in case of an applied stress: (a) in the [100] cubic direction, no dipole appear. (b) either in the [0001] hexagonal direction or in the [111] cubic direction, the tetrahedron becomes non-symmetrical, creating a macroscopic piezoelectric polarization - extracted from [Rol07a]

We have seen that growing nitride materials leads to strained layers because of lattice and thermal mismatches both with the substrate and between the various nitride compounds forming an heterostructure. If a compressive strain is applied along a polar direction, the [0001] growth direction, the tetrahedron will be distorted along this axis and will create a macroscopic polarization called *piezoelectric polarization*. This is the case of GaN pseudomorphically grown on an AlN layer.

To evaluate the total polarization \vec{P} , we need to know the values of both spontaneous \vec{P}_{sp} and piezoelectric \vec{P}_{pz} polarizations:

$$\vec{P} = \vec{P}_{sp} + \vec{P}_{pz} = \vec{P}_{sp} + (e) \cdot \vec{\epsilon} \quad (1.1)$$

where (e) is the matrix containing all the piezoelectric coefficients and $\vec{\epsilon}$ is the six component-stress vector after transformation from the 3×3 matrix. Therefore,

spontaneous and piezoelectric polarizations add up to form a measurable polarization difference.

Parameter (C.m^{-2})	AlN	GaN	InN
Spontaneous polarization	-0.081	-0.029	-0.032
Piezoelectric coefficient e_{31}	-0.60	-0.49	-0.55

Table 1.3 – Spontaneous and piezoelectric polarizations in AlN, GaN and InN - extracted from [Ber97]

When the growth is performed along the \vec{c} axis, which is the direction chosen for the samples we have studied in this work, (e) reduces to a scalar e_{31} . Its value is given in table 1.3. Most cubic semiconductors are piezoelectric if the strain is applied in the $[111]$ direction. The calculated value of their piezoelectric coefficient, however, is a factor of 5 to 10 lower than that of nitrides grown in the hexagonal phase [Ber97].

1.1.4 Band structures

In this part, we present the electronic dispersion relation in nitride semiconductors. The band structure is partly determined by the symmetry of the lattice. As all nitride materials exhibit a direct band gap (except cubic AlN which will not be studied in this work), we focus our analysis around the center of the Brillouin zone only.

The values of AlN, GaN, and InN bandgaps, for both crystal phases, are given in table 1.4.

	wurtzite			zinc blende		
Parameter	AlN	GaN	InN	AlN	GaN	InN
Gap (eV)	6.25	3.51	0.78	5.4 (Γ) - 4.9 (X)	3.299	0.78
Δ_{CR} (meV)	-169	10	40	—	—	—
Δ_{SO} (meV)	19	17	5	19	17	5
m_e^* (m_0)	0.31	0.2	0.07	0.25	0.15	0.07

Table 1.4 – GaN and AlN band parameters: band gap at 0 K, crystal field and spin orbit splittings, conduction band effective masses at the center of the Brillouin zone [Vur03]

In the zinc-blende phase, the conduction band is two-fold spin degenerated. As this band originates directly from the s-symmetry of both electronic states of anions and cations, the kinetic momentum is equal to zero. The valence band is built from p-symmetry bands and each of the p_x , p_y , and p_z are two-fold spin-degenerated. Figure 1.5a illustrates the construction of the cubic GaN band diagram. The spin-orbit coupling lifts the degeneracy of these bands, both energy levels being split in a degeneracy 4 and

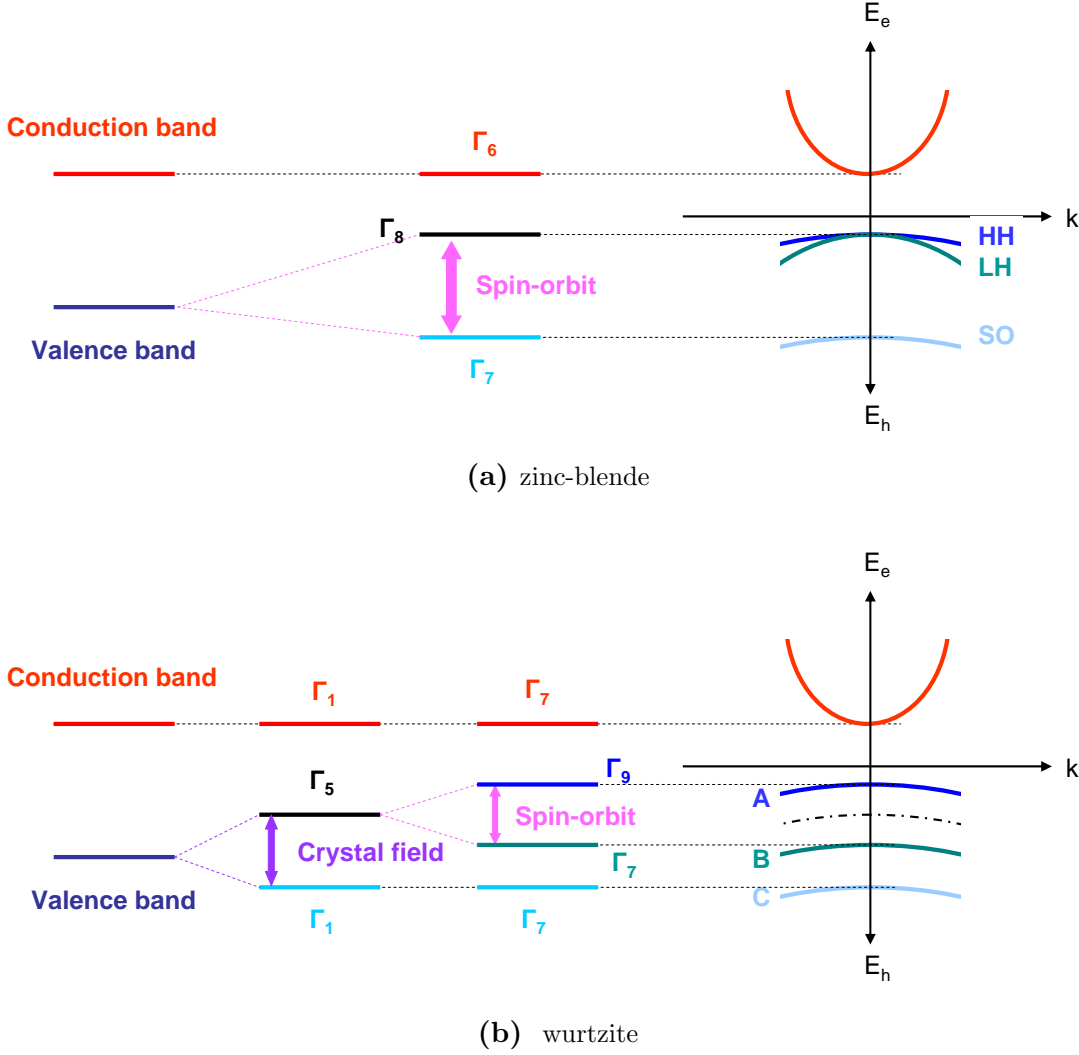


Figure 1.5 – Construction of the GaN band diagram in the Γ point

2 by the spin-orbit coupling constant Δ_{SO} given in table 1.4. The highest band ¹ is therefore called the *spin-orbit band*. The four low-energy bands are further split in two when leaving the $\vec{k} = \vec{0}$ region because their effective masses are different. The band exhibiting the lowest (respectively highest) curvature is called *heavy* (respectively *light*) *hole band*. The calculated band structure is given in figure 1.6 (left plot).

In the wurtzite configuration, as illustrated on figure 1.5b, its lower symmetry leads to the apparition of a non-zero crystal field Δ_{CR} , whose values are given in table 1.4. The valence band is thus split into a group of degeneracy 4 and another of degeneracy 2. Spin-orbit interaction further splits the four-time degenerated group into a heavy-hole and a light-hole band. This way, the band structure has been calculated: the results are plotted in figure 1.6 (right plot). These three bands are commonly referred to as *A*, *B* and *C bands*, by increasing energy¹. Depending on the either repulsive or attractive

¹ with the convention that the energy axis for holes is orientated in the opposite direction than that of electrons

nature of the crystal field, the order of the bands will be modified and will not refer to the same symmetry.

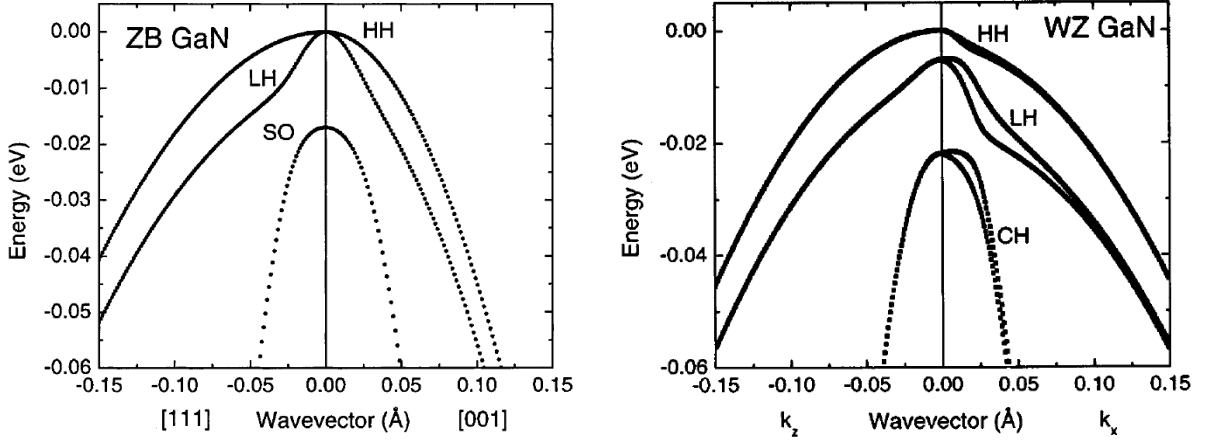


Figure 1.6 – Calculated valence band structure - extracted from [Vur03]

To describe the electronic dispersion relation around $\vec{k} = \vec{0}$, one commonly uses the effective mass approximation:

$$E(\vec{k}) = \frac{\hbar^2 \vec{k}^2}{2m^*} \quad (1.2)$$

where $E(\vec{k})$ is the energy of an electron of wavevector \vec{k} , m^* its effective mass and \hbar the reduced Planck's constant. This model fits well to the conduction band. However, a strong deviation from the pure parabolicity for the valence band of both cubic and hexagonal phases (see figure 1.6), as well as experimental issues, make the evaluation of the hole effective mass very difficult. Therefore the values given in the literature exhibit a large dispersion. It also appears to be very anisotropic for each valence band: for the A band, the longitudinal mass is 1.8, while the transverse one is around 0.4 [Rod01][Rin08].

1.2 Optical properties of bulk nitride materials

Now that electronic properties have been studied, the optical characterizations of bulk GaN can be addressed. They will help us understand the properties of GaN nanostructures such as nanowires and quantum dots. In a first part, we will focus on exciton-related features. Then, more general properties of nitride bulk material will be reminded.

1.2.1 Excitons

One of the most interesting properties of wide-band gap semiconductors lies in their strong excitonic emission from helium temperature to room temperature. After defining

an exciton and the parameters one uses to describe it, we will analyze the spectroscopy of homoepitaxial GaN layers.

When exciting a semiconductor above its bandgap, *e.g.* by photoexcitation, we promote electrons from the valence band to the conduction band. An exciton can be seen as a system similar to the hydrogen atom. One electron, together with one hole that was formed during the excitation process, can bind by Coulomb interactions to create a quasi-particle called an *exciton*. Consequently, this attractive interaction decreases the total energy of the electron-hole pair by the *excitonic binding energy*:

$$E_B^X = -\frac{\mu R_y}{m_0 \epsilon_r^2} \quad (1.3)$$

One can also define its *Bohr radius* as:

$$a_B^X = \frac{m_0 \epsilon_r a_0}{\mu} \quad (1.4)$$

$R_y = -13.6$ eV being the hydrogen Rydberg energy, $a_0=0.529$ Å the hydrogen Bohr radius, μ the excitonic reduced mass: $1/\mu = 1/m_e + 1/m_h$, m_e the electron and m_h the hole masses, respectively, and ϵ_r the dielectric permittivity of the semiconductor. The values of the binding energy in nitrides are given by table 1.5, as well as that of other semiconductors for comparison.

Parameter	AlN	GaN	GaAs	ZnSe	ZnO
E_B^X (meV)	44	28	5.1	17	60
a_B^X (nm)	1.9	2.8	11.3	4	0.9
Reference	[Onu02]	[Ram00]	[Fu99]	[Pel92]	[Fon04]

Table 1.5 – Exciton binding energy and exciton Bohr radius of AlN, GaN and other materials

We see that both ZnO and AlN exhibit stronger excitons than other semiconductors. GaN has a binding energy high enough to keep the exciton until room temperature ($kT=25$ meV at 300 K), which is not the case of GaAs and ZnSe.

In the following, the spectroscopy of highest-quality GaN (in terms of defect density and spectral linewidths) is presented. Figure 1.7 depicts both the low-temperature photoluminescence (top curve) and reflectivity (bottom curve) of a 1.5- μm homoepitaxial layer of GaN. Note that GaN is a non-intentionally n-type doped semiconductor; the donors are mainly silicon and oxygen. This is confirmed by the optical measurements described in the following paragraph:

The photoluminescence spectrum (top spectrum) is dominated by both the donor-bound exciton (D^0 , $X_A^{n=1}$) and acceptor-bound exciton (A^0 , $X_A^{n=1}$) lines in which the hole originates from the A valence band. The feature at 3.474 eV (not indexed) is

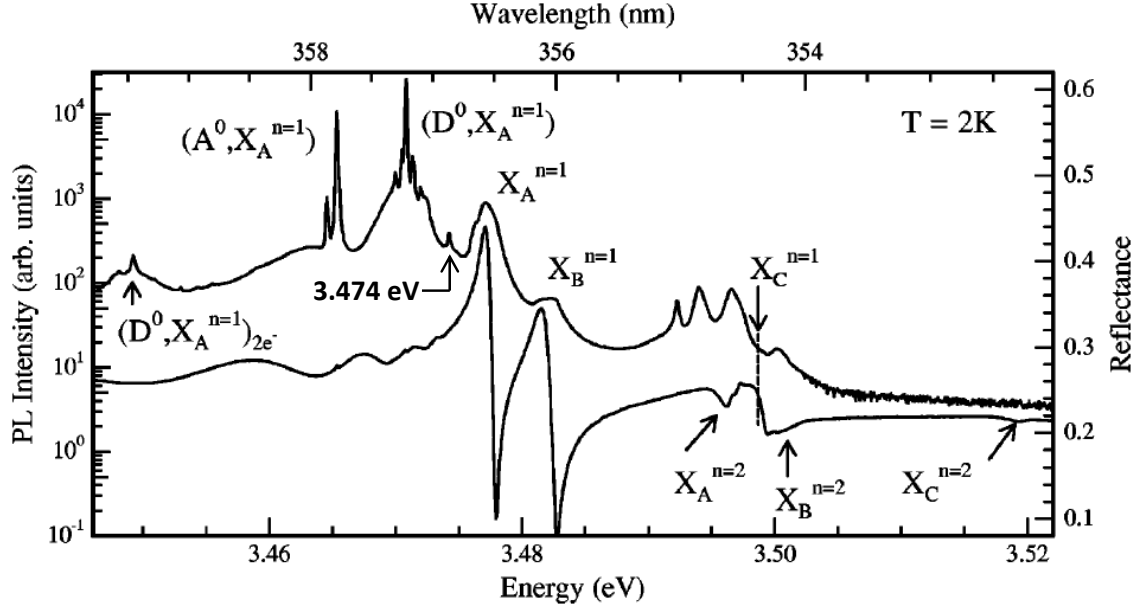


Figure 1.7 – Photoluminescence (top curve) and reflectivity (bottom curve) measurements of homoepitaxial GaN at low temperature [Kor99]

attributed to the donor-bound exciton with the hole in the B valence band [Mon08]. Note also the presence of both free-excitons with holes from band A and B — $X_A^{n=1}$ and $X_B^{n=1}$ — as well as their excited states, while the C-exciton is undetectable. At 4 K, no emission is detected from this higher energy level because of the thermalization of the holes located in the C band towards the A and B bands and because of its polarization selection rule (see next paragraph). The intensity of both A and B free-excitons is less than 10% of their corresponding bound excitons: this observation confirms the preeminence of defect bound excitons in the low-temperature photoluminescence spectra [Din71] due to efficient thermalization processes. For the donor (respectively acceptor), the authors reported impurity binding energies $E_B^D=6.2$ meV and $E_B^A=11.6$ meV for the acceptors [Kor99]. On the contrary, the reflectance spectrum (bottom spectrum) is dominated by both the A and B free-excitons, respectively at 3.477 and 3.482 eV, and the C exciton is well resolved at 3.498 eV. Donor-bound excitons are hardly detectable because their density of states is much smaller than that of free excitons. A reflectance experiment indeed probes the actual density of states, contrary to photoluminescence which allows to measure thermalized states.

To further understand the relative intensities between excitons from different valence bands, one must study their *polarization selection rules*. We have seen that A, B, and C holes were built from different valence bands, displaying different symmetries. Table 1.6 summarizes the symmetry allowed for an exciton built from each of the A, B and C valence band. The A exciton is completely polarized with its dipole perpendicular to the \vec{c} axis and will only be detected during an experiment which measures the electric field \vec{E} perpendicular to \vec{c} , whereas the B exciton is allowed whatever the direction of the electric field, and the C exciton is *quasi*-completely polarized parallel to \vec{c} . As a

consequence, if we detect the photoluminescence with the optical axis parallel to the growth axis, the A exciton will dominate the spectrum. On the contrary, detecting the electric field parallel to \vec{c} will promote the C exciton at the expense of both the A and B excitons.

Exciton	$\vec{E} \perp \vec{c}$	$\vec{E} \parallel \vec{c}$
A	0.5	0
B	0.44	0.12
C	0.06	0.77

Table 1.6 – Interband transition matrix elements for GaN A, B and C excitons in GaN, normalized to the sum of the A, B and C matrix elements for TE polarization — extracted from figure 7 of [Chu96]

Please note that the oscillator strengths of both B and C excitons strongly depend on the stress state of the layer as discussed in [Gil97].

1.2.2 Bandgap-related effects

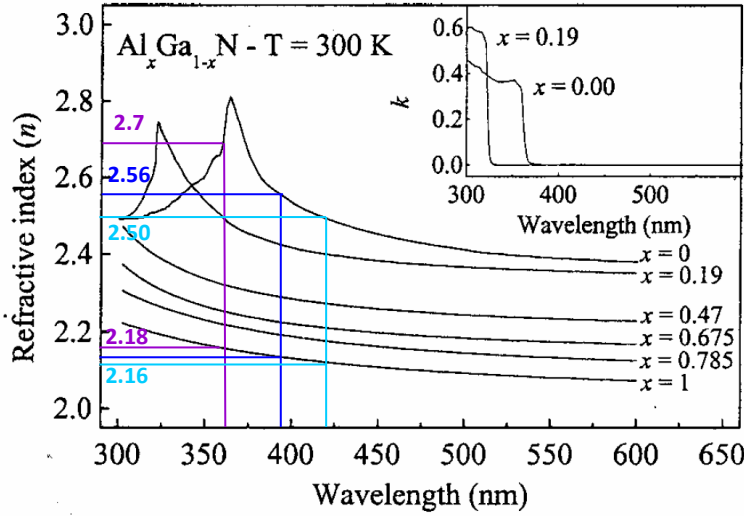


Figure 1.8 – Dispersion of the refractive index of $\text{Al}_x\text{Ga}_{1-x}\text{N}$ layers [AV03]

The value of the *refractive index* is of huge importance when one wants to confine light inside a semiconductor, and it strongly varies with the wavelength and with the bandgap of a semiconductor. On figure 1.8, we have reported the values of the refractive index of GaN, AlN and their alloys in the spectral regions of interest for our studies: at the GaN bandgap (360 nm), at the maximal emission of the GaN / AlN quantum dots considered in this work (390 nm), and at both higher and lower limit of the spectral range covered by these quantum dots (from 360 to 420 nm). Note that the "bumps" in the plots — *i.e.* Van Hove singularities — originate from the bandgap (from Kramers-Krönig's dispersion relation).

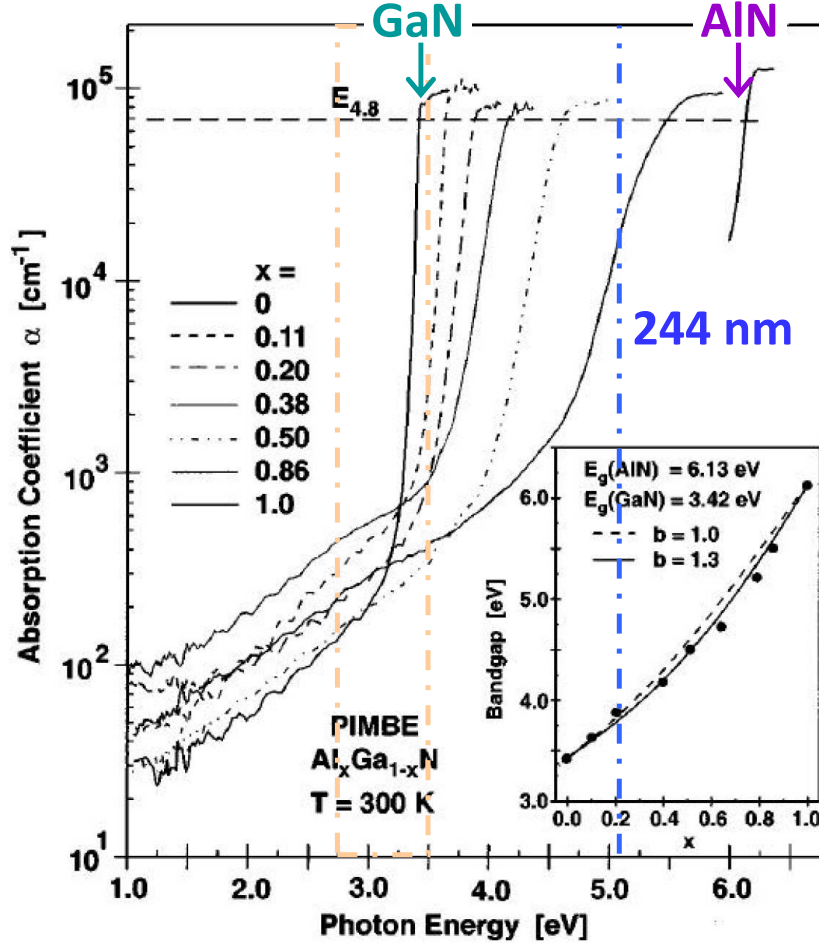


Figure 1.9 – Dispersion of the absorption coefficient of $\text{Al}_x\text{Ga}_{1-x}\text{N}$ layers [Bru97]

Furthermore, in order to efficiently trap light inside a microcavity, one must keep in mind that *absorption* can be a dominant source of photon losses. Besides, one has to know the absorption coefficient of a given layer in order to evaluate the typical amount of material which is actually probed by a photoluminescence experiment before the whole excitation power is absorbed. From figure 1.9, we see that typical absorption coefficients are around 10^2 cm^{-1} for an incident light well below the band gap of a material: in this case, a layer as thick as a few $100 \mu\text{m}$ is needed to absorb the light. Absorption coefficients reach 10^5 cm^{-1} above the bandgap: a thickness of a few 100 nm absorbs the totality of the incident light. The spectral position of the frequency-doubled Ar laser is also shown on figure 1.9, as well as that of the quantum dots we studied in this work.

Both refractive index and absorption coefficients are related to the bandgap of the material. Yet the *temperature-dependence of the bandgap* should not be forgotten. The evolution of the bandgap of a semiconductor with temperature can be described by the phenomenological Varshni's law [Var67]:

$$E_g(T) = E_g(T = 0 \text{ K}) - \frac{\alpha T^2}{\beta + T} \quad (1.5)$$

where α can be seen as the slope at high enough temperature and β is a temperature of the same order of magnitude as the Debye temperature. Table 1.7 gives an example of reported values of α and β for nitride materials. Yet very dispersed values of α and β are reported in the literature. This originates from imprecisions during the fitting process because β , which is of the order of magnitude of the Debye temperature (870 K), is usually much larger than the explored range of temperature. Thus Varshi's law cannot fit our results in an appropriate way in the usual range of temperature (4 – 300 K). Other fitting functions prove to be more appropriate [Päs01].

	AlN	GaN	InN
Gap (eV)	6.25	3.51	0.78
α (meV / K)	1.799	0.909	0.245
β (K)	1452	830	624

Table 1.7 – GaN and AlN band gaps at 0 K and Varshni parameters [Vur01]

1.3 Peculiarities of GaN nanostructures

Now that the optical properties of bulk GaN have been examined, we will discuss how quantum confinement can modify the emission. After a few figures showing why GaN / AlN nanostructures are attractive and the definition of the possible confinement regimes, we will move on to the quantum-confined Stark effect, its description and its consequences.

1.3.1 Band offsets and excitonic confinement

GaN/AlN nanostructures are attractive for their large *band offsets* (see table 1.8) and the high robustness of the exciton in GaN.

Parameter	Value (eV)
Difference between gaps	2.71
Valence band offset	0.70
Conduction band offset	2.04

Table 1.8 – GaN/AlN heterostructure band offsets - extracted from [Wu09]

In order to evidence *excitonic confinement*, one can perform continuous-wave photoluminescence experiment: in usual semiconductor heterostructures, an emission above the bandgap of the bulk material is a direct proof of quantum confinement. The dynamics of the excitonic transition can give further information. We remind that the

oscillator strength measures the efficiency of the coupling between an emitter and the electric field. It thus depends on the overlap between electron and hole, and therefore on the geometry of the confinement. Two regimes can be distinguished. First, if the typical dimension of the nanostructure is larger than the Bohr radius, the confinement is considered to be *weak*. In this case, the preeminent term in the excitonic Hamiltonian is the attractive interaction between the electron and the hole, while the confinement will concern only the excitonic center of mass. On the contrary, if the nanostructure has a dimension smaller than the Bohr radius, we enter the regime of *strong* confinement. The dominant contribution in the excitonic Hamiltonian will be the confinement energy, determined separately for the electron and the hole. Then, the coulombian term is considered as a perturbative term.

1.3.2 Quantum-confined Stark effect

One of the most striking properties exhibited by nitride heterostructures is the quantum-confined Stark effect. We have seen in 1.1.3 that the spontaneous polarization was an intrinsic consequence of the wurtzite lattice. It induces a charged layer on each side of the surface perpendicular to the \vec{c} axis. We have also evidenced a piezoelectric polarization in the case of stressed layers. Let us consider a GaN quantum well grown in-between two AlN barriers. In this case, the lattice parameter of the well is compressed and that of the barrier is extended. Therefore, we must consider both polarizations in any nitride heterostructure. These two contributions lead to the apparition of an electric field which modifies the band structure of the nanostructure: this is the *quantum-confined Stark effect*.

In the following we treat the example of the GaN/AlN quantum well. Let us note \vec{P}_B the polarization of the AlN barrier and \vec{P}_W the polarization of the GaN well. The surface density of charges in the system reads:

$$\sigma = (\vec{P}_B - \vec{P}_W) \cdot \vec{c} \quad (1.6)$$

The following approximations are made: both displacement field and potential are continuous at the interface, the dielectric constants in the barrier ϵ_B and in the well ϵ_W are equal to an average value ϵ_r : $\epsilon_B \approx \epsilon_W \approx \epsilon_r$, and the GaN / AlN layer stacking is considered as infinite. This leads to a transition at the energy:

$$E = E_g(\text{GaN}) + E_1^e + E_1^h - eL_B \frac{\vec{P}_B - \vec{P}_W}{\epsilon_0 \epsilon_r} \quad (1.7)$$

where E_1^e and E_1^h are the energy levels of the electron and the hole without taking into account the quantum-confined Stark effect, e is the elementary charge and L_B is the thickness of the quantum well. Figure 1.10 illustrates both the spontaneous and piezoelectric polarizations. Piezoelectric polarizations are in opposed direction in

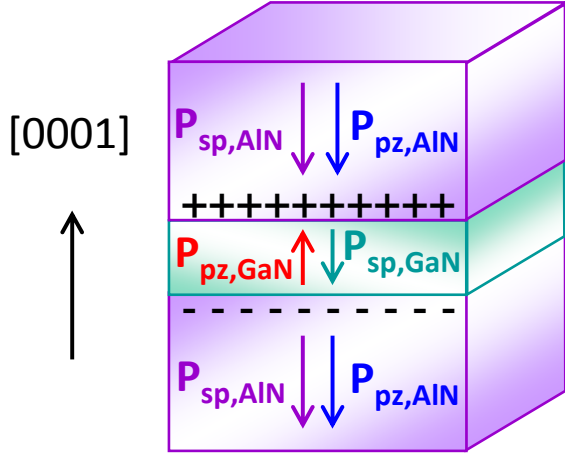


Figure 1.10 – Directions of the spontaneous and piezoelectric polarizations in a GaN / AlN quantum well

AlN and in GaN because the AlN layer is under tensile strain, while the GaN layer is compressed. They only partly compensate each other because the piezoelectric coefficients are different². However, the spontaneous electric fields are in the same direction because both layers are grown in the same Ga polarity.

An order of magnitude obtained for a 2.5% lattice mismatch and typical polarization values² gives: $P_W=0.096$ C/m² and $P_B=-0.041$ C/m² for GaN and AlN, respectively. For $\epsilon_r = 5.3$, we obtain a total field in the order of 10 MV/cm, in good qualitative agreement with experimental results on GaN / AlN quantum dots [Bre03]. Yet, experimentally it is very difficult to decorrelate both polarizations: the macroscopic value we can measure is the total electric field induced by both mechanisms. Simon *et al.* have shown that both had similar orders of magnitude [Sim00].

As a consequence, the quantum-confined Stark effect generates an electric field that bends both the conduction and the valence bands. In figure 1.11a we have plotted the band structure and the associated carrier wavefunctions when the quantum-confined Stark effect is ignored. It has to be compared to the case of a 5 MV/cm field, displayed in figure 1.11b. Before reaching equilibrium, both conduction and valence bands, as well as the Fermi level, vary linearly both in the barrier and in the well. Charge transfer allows to readjust the Fermi level to a constant value inside the whole heterostructure [Sim01]. Experimentally, the value of the Fermi level at equilibrium is unknown. It depends on the thickness of the barriers (which were taken of infinite length in the model) [CM10] and the surface states on the top free surface. As a consequence, the model displayed above aims at calculating the energy states inside the quantum well only.

At equilibrium, the bands in the quantum well still exhibit a triangular shape. Electrons and holes being spatially separated from each others, the first consequence is a redshift of the emission compared to that calculated without taking into account the electric field. *This redshift increases linearly when the well thickness is increased and the emission is eventually detected below the GaN bandgap.* Furthermore, one

²see table 1.3

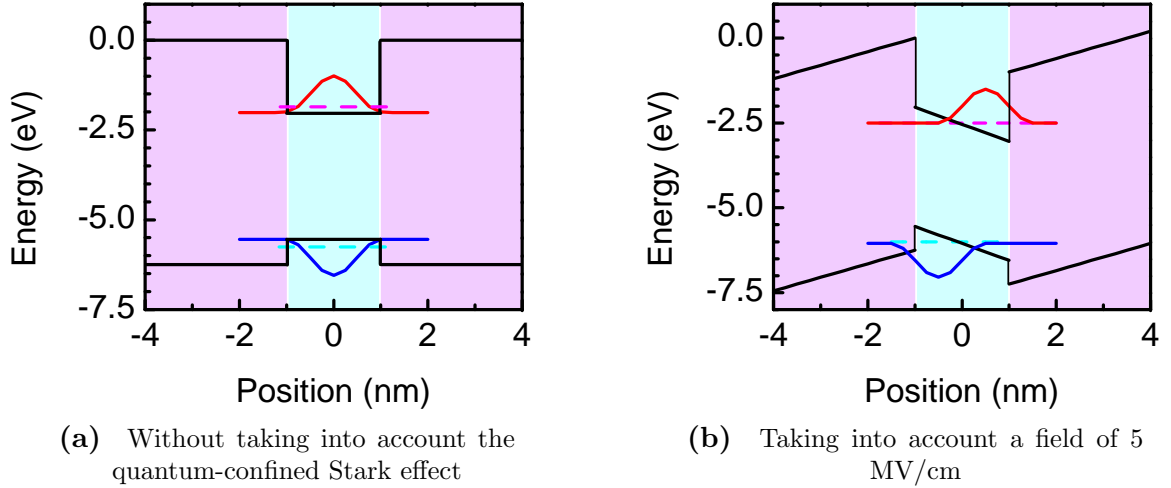


Figure 1.11 – Calculated band diagram of a GaN/AlN 2-nm quantum well and associated wavefunctions of both electron and hole

can evidence an increased decay time compared to the field-free structure, due to a decreased overlap between the electron and hole wavefunctions. *The radiative decay time is expected to increase exponentially with the well thickness.* It is measurable as long as non-radiative defects are slower mechanisms than radiative recombinations. Microsecond lifetimes have been measured on thick GaN / AlN heterostructures [Bre03].

Modeling a quantum well is quite simple. In the case of quantum dots, the analytic calculation of the electric field becomes much more complicated because it requires the knowledge of the exact strain state: Stranski-Krastanov quantum dots form thanks to a purely elastic strain relaxation, but the strain is unknown at a smaller scale. Moreover, one also needs to know the exact direction of each facet, in order to determine their projection on the \vec{c} axis

However, as explained above, a good way to evidence the consequences of quantum-confined Stark effect on their emission is to compare both the spectral positions and the recombination times of polar quantum dots, to that of cubic or non-polar quantum dots, when varying their height. In the study performed by Simon *et al.* [Sim03], the spectral position of the emission shifts by 200 meV in the case of cubic quantum dots, whereas the shift is 1.2 eV with hexagonal quantum dots, both with a height varying from 3 to 5.5 nm. This results in an estimation of the electric field around 7 MV/cm for wurtzite, and null for cubic structures. In particular, the authors observed that for a 2-nm high dot, the emission is at the spectral position of the bulk GaN bandgap, evidencing that this is the thickness where the quantum-confined Stark effect becomes dominant compared to confinement.

This is corroborated by time-resolved photoluminescence experiments: in zinc-blende quantum dots, the authors measured decay times ranging between 200 and 300 ps whatever the emission energy of the dots [Sim03]. By temperature-dependent

measurements, they checked that the strong shortening of the photoluminescence decay time compared to the typical values measured in hexagonal quantum dots was not due to the enhancement of fast non-radiative recombinations in the zinc-blende phase compared to what was observed on the wurtzite phase. Similar results were obtained on non-polar GaN/AlN quantum dots, where the decay times range from 200 to 500 ps [Rol07b]. In comparison, by studying both the spectral position and the decay time of the emission, Bretagnon *et al.* estimated an electric field of 9 MV/cm [Bre06] and measured radiative decay time from a few ns to several 100 μ s (see figure 1.12)!

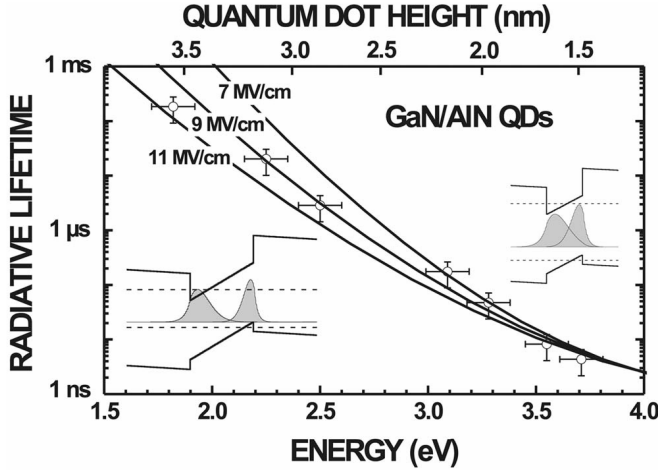


Figure 1.12 – Experimental evidences of quantum-confined Stark effect in GaN/AlN quantum dots: measured radiative lifetimes versus measured energy of photoluminescence peak. The dot height is calculated by taking a 9 MV/cm field [Bre06]

1.4 On the interest of nitride nanowires

We have seen in 1.1.2 that nitride materials lack adapted substrates. As a consequence, heteroepitaxial layers suffer from a high dislocation density (around 10^9 cm^{-2}). Compared to two-dimensional layers, the one-dimensional geometry allows for additional relaxation on the lateral free surfaces of the crystal, resulting in potentially improved structural and optical properties. In small enough nanorods, quantum confinement can be evidenced; this is the first topic we will investigate. Besides, the strong enhancement of the surface to volume ratio can also strongly modify the properties of these nanowires, as we will discuss in 1.4.2.

1.4.1 Electronic properties: excitonic confinement

We want to evaluate the excitonic confinement in a GaN nanowire of diameter d . Qualitatively, we expect to reach the strong confinement regime when the spatial extension of the exciton, given by the Bohr radius (2.8 nm in GaN [Ram00]), is of the same order of magnitude as the diameter. Yet, the weak confinement regime should be reached for wider nanocolumn diameter. Theoretically, the confinement should become noticeable when the splitting between two successive sub-bands becomes of the same order of magnitude as thermal energy ($kT=300 \text{ } \mu\text{eV}$ at 4 K).

Let us estimate the confinement energy of a weakly confined exciton (by its center of mass) in the case of an infinitely long nanocolumn of diameter d surrounded by air, considered as an infinite potential barrier at $r = d/2$. We take an excitonic effective mass $M^* = m_e^* + m_{h,t}^*$ where m_e^* is the electronic effective mass, and $m_{h,t}^*$, the transverse A hole effective mass. The Schrödinger equation reads:

$$-\frac{\hbar^2}{2M^*}\nabla^2\Psi = E\Psi \quad (1.8)$$

where Ψ is the wavefunction of the excitonic center of mass and \hbar is the reduced Planck's constant. In cylindrical coordinates, after separation of z -, r - and θ -dependences, and knowing that the cylindrical geometry implies that $\Psi(\theta)$ is proportional to $\exp im\theta$ (m is an integer number), equation 1.8 therefore becomes:

$$\frac{-\hbar^2}{2M^*}\left(\frac{\partial^2}{\partial r^2} + \frac{1}{r}\frac{\partial}{\partial r} - \frac{m^2}{r^2}\right)\Psi = E\Psi \quad (1.9)$$

The solution of 1.9 is a Bessel function of the first kind:

$$\Psi(r) \propto J_m\left(\sqrt{\frac{2M^*E}{\hbar^2}}r\right) \quad (1.10)$$

The boundary condition is:

$$\Psi(r = d/2) = 0 \Leftrightarrow J_m\left(\sqrt{\frac{M^*E}{\hbar^2}}d\right) = 0 \quad (1.11)$$

The exciton's fundamental state is thus given by the first zero $x_{1,0} \approx 2.4$ of the $m = 0$ Bessel function:

$$E_{1,0} = \frac{2x_{1,0}^2\hbar^2}{M^*d^2} \quad (1.12)$$

For the exciton effective mass, we take $M^* = m_e^* + m_{h,t}^* = 0.2 + 0.33 = 0.53m_0$ [Rod01], where m_0 is the electronic mass. The results are shown in figure 1.13.

Before analyzing the results, one can note that, experimentally, a significant blueshift of the excitonic emission will be observed in a photoluminescence spectrum only if it is at least of the same order of magnitude as the linewidth. From figure 1.13, we can draw the following conclusions. The diameter corresponding to twice the Bohr radius is marked in the plot: such a nanocolumn diameter will induce a shift of the order of 50 meV. In our samples grown by MBE, we typically measure an excitonic broadening of the donor-bound exciton of the order of 1-2 meV. The diameter of these nanowires is around 50 nm, leading to a confinement energy of 1 meV. We will discuss this aspect in chapter 2. It seems that reaching a diameter below 10 nm would allow to evidence a clear blueshift in the range of 10 meV. We will investigate in 2.4 some possibilities to obtain such small nanowires. In MOCVD-grown microwires, exhibiting diameters

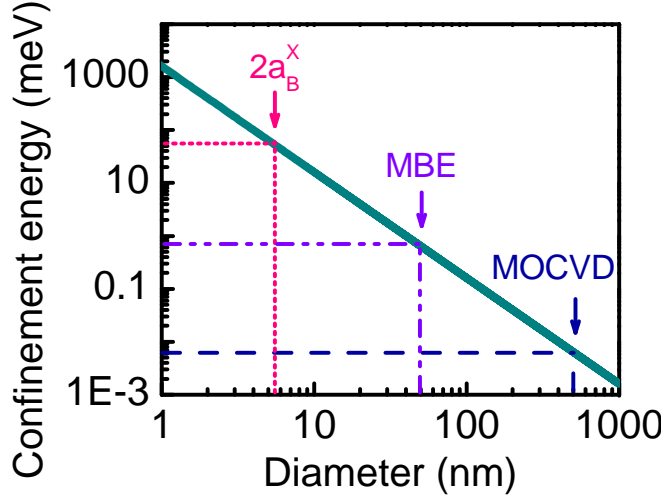


Figure 1.13 – Excitonic confinement energy for an exciton in a nanowire of varying diameter

around 500 nm, the lateral confinement is negligible.

Before concluding, a question remains: are both the donor-bound exciton and the free-exciton able to “feel” the confinement potential? Indeed, we can already qualitatively predict that even in a nanocolumn of diameter small enough to induce confinement, if the spatial localization of the donor-bound exciton is much smaller than the diameter, no confinement will be observed on this line. On the contrary, a free-exciton is supposed to probe the whole diameter if its recombination time is large enough. The spatial extension ρ of a bound exciton is given by:

$$\rho = \frac{\hbar}{\sqrt{2m_0 E_B^D}} \quad (1.13)$$

where E_B^D is the donor binding energy and m_0 is the excitonic mass. With the donor and acceptor binding energies given by Kornitzer *et al.* [Kor99], a spatial extension of 2 to 3 nm is obtained. It is therefore unlikely that a bound exciton is able to “feel” the weak confinement induced by a small enough nanocolumn, unless it is localized in a surface shell of 2-nm thickness of the nanowire. As the impurity distribution in a nanocolumn is unknown, we will conclude that *the confinement regime is reachable for diameter around 10 nm on the free-exciton line.*

1.4.2 Consequences of large surface to volume ratio

One of the main peculiarities provided by the nanocolumn geometry lies in the high surface to volume ratio. In figure 1.14, we have plotted the ratio of the volume close to the surface, *i.e.* the volume of the shell of thickness a_B^X , normalized to the total volume of the wire. Note that choosing the Bohr radius as representative of the characteristic thickness of the “shell” is a pure convention. We can see that for MBE-grown nanowires of diameter 40 nm, 25% of the volume is made by surface material. Taking into account a donor concentration of 10^{17} cm^{-3} leads to the average incorporation of 100 donors

per nanocolumn of 20-nm radius. If the donor distribution is homogeneous, 25% of the donor-bound excitons may be affected by the proximity of the surface.

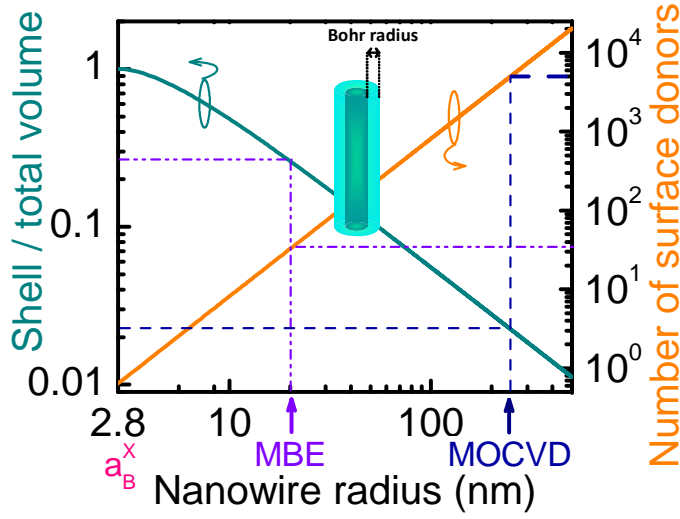


Figure 1.14 – Ratio of the volume where bulk properties are likely to be modified by the proximity to the surface, normalized to the total nanowire volume. Inset: schematics of what is considered as "surface"

The preeminence of surface states compared to bulk states can strongly modify the band structure of the semiconductor nanowire compared to that of the bulk. As surface levels are not located at the same energy than bulk levels, charges are transferred from bulk to surface and vice-versa. This transfer induces a band bending close to the surface.

Calarco *et al.* have studied the electrical transport under UV illumination of MBE-grown nanowires of various diameters [Cal05]. The authors evidenced two regimes: the photocurrent is very size-sensitive and increases with diameter when diameters are smaller than 80 nm, and then remains almost constant for wider nanowires. Let us keep in mind that in the range of non-intentional n-doping, surface states pin the Fermi level 0.5 eV above the conduction band, resulting in an *upwards bending of both conduction and valence bands*. In bulk GaN, bands are flat far enough from the surface. The spatial region corresponding to bent bands is called the space charge layer or depletion layer. In nanowires, the authors explained their results by the comparison of the nanocolumn diameter to the depletion layer extension (between 50 and 100 nm) [Cal05] (see figure 1.15):

- for diameters well above the extension of the space charge zone (figure 1.15, right), both valence and conduction bands are flat in the core of the nanorod, opening a conduction channel;
- for diameters comparable to the extension of the space charge layer (figure 1.15, middle), both conduction and valence bands are bent along the whole nanocolumn radius:
- for diameters much smaller than the extension of the space charge layer (figure 1.15, left), the band curvature is "incomplete", thus reducing the recombination barrier Φ , and enhancing recombination efficiency again.

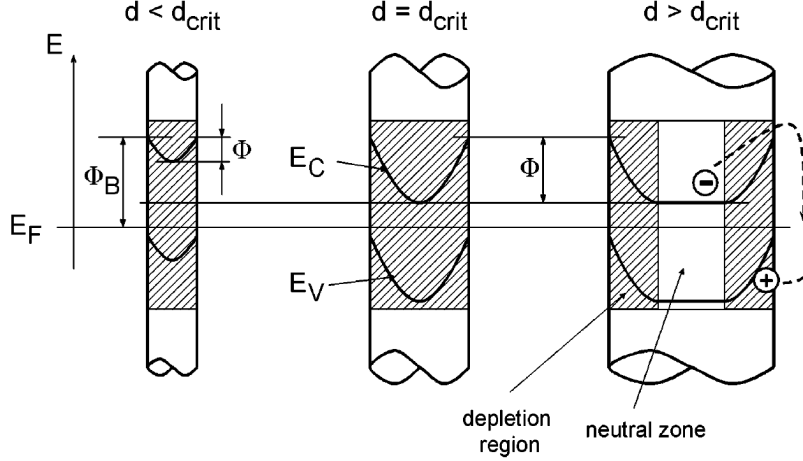


Figure 1.15 – Dependence of the depletion region, shape of the conduction and the valence bands and recombination barrier on the nanowire diameter [Cal05]

This experiment suggests that typical nanowires obtained by MBE growth are fully depleted. We should hence not be able to observe the donor-bound exciton recombination in low-temperature photoluminescence measurements on GaN nanowires.

The preeminence of surface states in nanowires can also be evidenced by photoluminescence experiments. In ZnO nanowires, for example, a surface-excitonic emission has been reported [Wis06], whose intensity increases with decreasing nanowires diameter: it dominates the spectrum together with the donor-bound exciton line for wires smaller than 200 nm and its intensity quenches to one fifth of the donor-bound exciton one for diameters greater than 500 nm. The limited density of states due to the surface nature of this line is evidenced by a clear saturation well below that of the donor-bound exciton. Further studies aiming at changing the surface states have successfully demonstrated the surface origin of this line. Polymer and alumina coatings lead to a strong enhancement of the intensity of this recombination [Vos10] and a quenching of donor-bound exciton emission. This observation is consistent with a change of the dielectric environment, enhancing charge screening around the surface and thus leading to a decreased band bending. On the contrary, metallic coatings quench this surface emission. Indeed, the metal introduces deep states in the ZnO bandgap, which can trap the carriers more efficiently than surface states [Vos10].

In GaN, a line detected at 3.45 eV in the low temperature photoluminescence spectrum of nanowires grown by MBE seems to be related to the surface [Cor09]. An intensive study of this line will be provided in chapter 3. However, the stability of GaN surfaces, especially the lateral surfaces of the nanorods (\vec{m} planes) is unknown compared to that of ZnO.

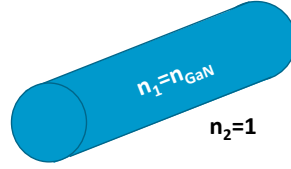


Figure 1.16 – Schematics of a photonic wire

1.4.3 Photonic properties

Semiconductor nanowires can be used as single-mode photonic cylindrical waveguides if their diameter is of the order of magnitude of the wavelength. One generally tries to enhance the emission from embedded emitters into a particular mode, and quench the coupling to other modes in order to obtain the maximum number of photons displaying common properties. These in-resonance emitters can be excitons from the “bulk”, *i.e.* from the material composing the wire, or from a quantum dot embedded into the wire. Regarding possible applications, one can cite efficient single photon sources for quantum cryptography [Cla10]. One-dimensional geometry could also provides an enhanced light extraction [Hen11], compared to the situation in two-dimensional layers where light is trapped in the high refractive index layer. For both MBE- and MOCVD-grown nano- and micro-columns studied in this work, it is therefore necessary to evaluate the guiding potentialities in GaN nanowires. Here we present the waveguiding properties of cylindrical objects as a function of their radius. The whole analytic treatment can be found in [Yar97].

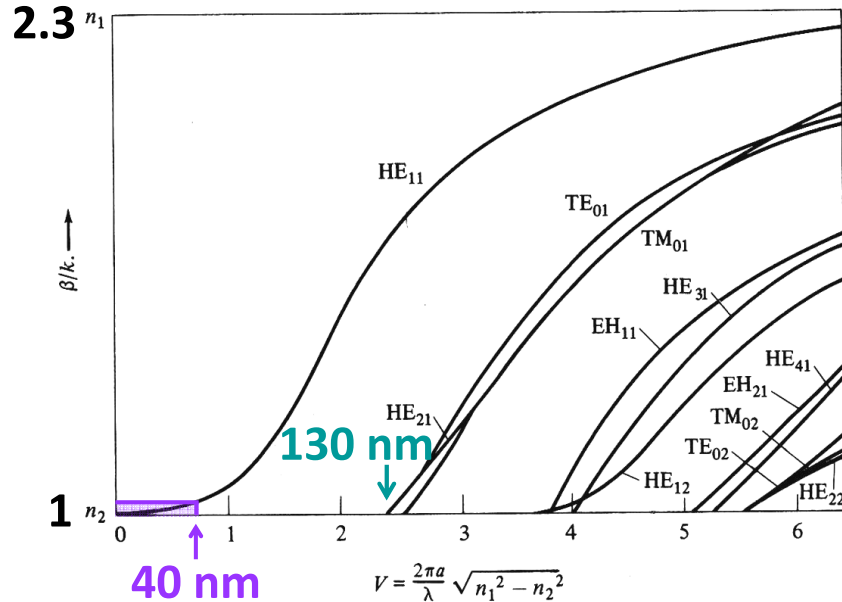


Figure 1.17 – Effective index of guided modes inside a photonic wire - extracted from [Yar97]

Figure 1.17 displays the effective refractive index of the guided mode as a function

of the reduced frequency, defined by:

$$v = \frac{2\pi a}{\lambda_0} \sqrt{n_1^2 - n_2^2} \quad (1.14)$$

where a is the radius of the nanocolumn, $\lambda_0=357$ nm the vacuum wavelength, $n_1=2.3$ and $n_2=1$ the wire and air refractive index, respectively. Values of the reduced frequency for diameters of 40 nm — the mean size of MBE-grown GaN nanowires — are given in figure 1.17. The guided modes of a cylindrical waveguide can have various symmetries, purely transverse electric (respectively magnetic) TE (respectively TM). Their symmetry can also be hybrid: HE modes are approximately TM, while EH modes are rather TE. More interestingly, figure 1.17 evidences that *the fundamental mode HE_{11} does not have any cut-off frequency: it means that whatever the diameter of the wire, this mode is always guided*. Furthermore, for diameters smaller than 130 nm, the wire is monomode. In the cases studied in this work:

- A MBE-grown GaN nanowire is around 40 nm in diameter: $v_{MBE}=0.7$. In this case, the effective index is close to 1: the fundamental mode strongly leaks into the air surrounding the column.
- A MOCVD-grown GaN microwire is about 500 nm in diameter, therefore $v_{MOCVD}=9$ and this wire can guide more than ten modes with high effective index values.

In this last part, only guided modes have been considered. Yet, in practice, an emitter can couple to various modes, *i.e.* other guided modes and *radiative*, also called *free space* or *leaky* modes. Usually one wants to efficiently couple an emitter to a single guided mode, and decrease the coupling to any other mode to its minimum. Figure 1.18 depicts the spontaneous emission rate normalized to the total emission rate of an emitter located along the axis of a GaAs nanowire. We can distinguish two contributions: P_M stands for the emission into the fundamental mode HE_{11} , while γ stands for the emission into all other modes. β is the ratio of photons feeding the fundamental mode on the total number of emitted photons. The plot displays normalized dimensions, but cannot be quantitatively scaled to GaN emission at 357 nm because of the difference in dielectric constant of both materials. Still, for a GaAs nanocolumn:

- for waveguides with diameter around 0.25λ , most of the emission feeds the fundamental mode.
- for wires much smaller than 0.2λ , the emission is inhibited in both the HE_{11} and radiative modes. This is confirmed by theoretical calculations focused on GaN nanowires [Mas06]. Experimentally, this is the case of MBE-grown nanowires where $D/\lambda=0.1$.

- for diameter much greater than 0.3λ , an increasing part of the emitted photons is lost into higher-order guided modes. For MOCVD-grown nanowires, $D/\lambda=0.7$

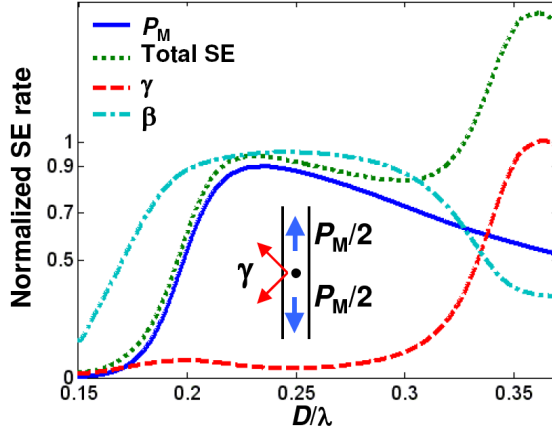


Figure 1.18 – Normalized spontaneous emission rate of a radial dipole embedded in an infinite cylindrical GaAs nanowire and located on the wire axis [Fri09]

More adapted simulations for wide-bandgap semiconductor nanowires, such as [Mas06] will be used in chapter 3. Note that in all available calculations of the coupling between a nanocolumn and an emitter, the following hypothesis were made. The nanorod is assumed to be of infinite length and isolated: neither substrate nor adjacent nanorod, nor breaking of the cylindrical symmetry on both tips are considered. This case-study is far from the experimental system we experimentally study.

1.4.4 New substrates for growing novel heterostructures?

We have seen that nanowires of diameter around 40 nm (typically obtained by self-assembled MBE growth) were not small enough to exhibit electronic confinement, and too small to serve as efficient cylindrical waveguides. Yet, one of the main interests of these structures lies in a much better flexibility to grow heterostructures: the nanowire geometry offers much more variety of both composition and size compared to two-dimensional structures. This is possible thanks to the *efficient relaxation on the lateral free surfaces*.

The left panel of figure 1.19 depicts the maximal thickness (of a layer B) on top of a nanowire (made of A material) that one can grow without plastic relaxation. Of course, this critical thickness decreases when increasing lattice mismatch. However, whatever the lattice misfit, there exists a diameter range for the underlying nanocolumn diameter (A) where no plastic relaxation can happen [Gla06]. Typically, as pointed out by the left plots of figure 1.19, on a GaN nanocolumn of radius smaller than 70 nm, no plastic relaxation should occur if one grows an AlN layer on top of this nanocolumn, whatever the thickness of the top layer, . This is a clear improvement compared to the case of two-dimensional layers.

One can perform the same kind of calculations for core-shell heterostructures. This

geometry is made possible by the cylindrical geometry and does not have any two-dimensional equivalent. The right plot of figure 1.19 displays the maximal radius a GaN nanocolumn can have, to be able to elastically relax the strain created by an $\text{Al}_x\text{Ga}_{1-x}\text{N}$ shell of various thickness and various Al concentration (equivalent to various lattice mismatch). From this plot, one can evidence that there always exists a critical core radius below which no plastic relaxation is needed, whatever shell thickness. Furthermore, at a given GaN core radius, the maximum thickness of an $\text{Al}_x\text{Ga}_{1-x}\text{N}$ shell coherently grown on a GaN nanocolumn of fixed radius gets smaller when x increases. Yet from figure 1.19, one can see that there is no real advantage to grown radial heterostructures compared to two-dimensional layers: in order to grow an $\text{Al}_{0.5}\text{Ga}_{0.5}\text{N}$ shell on a GaN core without plastic relaxation, the core radius must be smaller than 10 nm. This is half the size of MBE-grown GaN nanowires. Therefore, only either small lattice mismatches or small nanowires are compatible with elastically relaxed core-shell heterostructures.

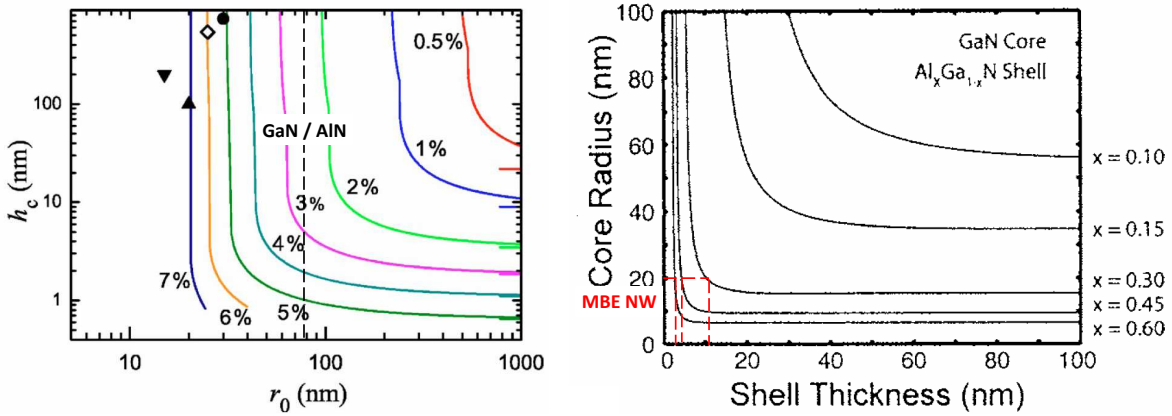


Figure 1.19 – Calculated critical dimensions: (left) critical thickness of an axial layer as a function of the nanocolumn radius and the misfit [Gla06]. (right) critical GaN core radius in a GaN / $\text{Al}_x\text{Ga}_{1-x}\text{N}$ core-shell heterostructure for varying x [Ray06]

1.4.5 Nitride nanowire-based light-emitting diodes

The possibility to grow coherent heterostructures, as mentioned in the last subsection, as well as the new geometries offered by the wire geometry, are attractive for the realization of nitride light emitting diodes. Commercially-available InGaN / GaN quantum well blue diodes exhibit a very satisfactory external quantum efficiency of the order of 60% [Kha08]. However, their performances collapse — internal efficiency of a few % only — when one wants to increase the In content to reach wider wavelength emission in the green-yellow range. This is the so-called green gap, which can be attributed to a degradation of the material quality due to the increased lattice mismatch between well and barrier materials. Other factors further decrease the efficiency: one can think of the increasing quantum-confined Stark effect, which decreases the spontaneous emission rate. The same is true for UV emission with AlGaIn / GaN quantum well diodes [Kha08] when trying to emit deeper in the UV range by increasing Al incorporation.

The main advantages of the nanowire geometry are:

- the perspective to grow elastically-relaxed nitride heterostructures made by highly-mismatched materials [Ray06] [Gla06];
- the increase of the active layer surface by at least a factor of 10 compared to planar structures when using a core-shell geometry [Waa11];
- the controlled variation of nanocolumn diameter, achieved by selective-area growth, possibly leading to a variation of the In or Al incorporation by the strain difference with varying diameter [Sek10];
- the improvement of the extraction efficiency thanks to (i) the lower refractive index mismatch between the effective nanocolumn layer and the superstrate [Hen11] compared to the two-dimensional case, (ii) a possible photonic crystal effect, favoring the coupling to leaky modes or (iii) an enhanced photon diffusion due to the porosity of the layer.

However, achieving high-performance nanowire-based diodes requires to perfectly control the growth steps, from nucleation to vertical growth. One also has to control both diameter and density. Moreover, efficient processes in order to contact the nanorod layer have to be developed. The first step is of course to master the structural and optical properties of these nanowires in order to be able to understand the devices in which they are used as active layer. This is the reason why, before processing and testing the electroluminescence of the devices, basic characterizations such as photoluminescence are of fundamental use.

1.5 Nitride microcavities for UV nanoresonators

This work was also focused on the spectroscopy of other nitride structures, *i.e.* AlN microcavities with embedded GaN quantum dots. The idea of cavity quantum electrodynamics is to change the photonic environment of the emitter, in order to modify the properties of its emission. In order to effectively concentrate all the photons into a given mode and kill the emission in other modes, one puts the emitter inside a “photonic box”, the *cavity*. If these phenomena are well-known and mastered in purely atomic systems, they remain much more difficult to control for solid-state materials. In semiconductors, photonic cavities have been first developed with arsenide materials. After a reminder of the basic concepts of cavity quantum electrodynamics, we will describe the different possible geometries of such photonic cavities. A brief outlook of the historical background of photonic cavities will be given. Then, the case of nitride cavities will be examined.

1.5.1 Theory of cavity quantum electrodynamics in the weak coupling regime

This part mostly uses the description of [Lou08]. We will consider here a two-level photon emitter. Experimentally, it would be a quantum dot. A single emitter placed in free space and coupled to an electromagnetic field emits photons rather isotropically and with a natural decay time τ_{nat} . This is called *spontaneous emission*, corresponding to the decay time in free space of an emitter prepared into its excited state. Let us consider a single emitter at ω_{em} put into a cavity and in resonance with its only mode. \vec{E} is the normalized local electric field which obeys Maxwell equations, n is the effective refractive index, \vec{d} is the dipole moment of the emitter, λ_{cav} is the wavelength of the cavity mode, and:

$$V_{eff} = \frac{\iiint_r n(r)^2 \left| \vec{E}(r) \right|^2 d^3r}{n(r)^2 \left| \vec{E}(r) \right|^2} \quad (1.15)$$

is the cavity *effective volume*. It quantifies the spatial confinement of the electric field: the smallest V_{eff} , the more effective is the cavity confinement.

This system can be seen as two coupled oscillators, periodically exchanging energy: the excited emitter creates a photon in order to return to its ground state, and the photon excites the emitter again,... This phenomenon is known as Rabi oscillations, observable in the *strong coupling regime* between the emitter and the cavity field. These oscillations would last forever in an ideal, lossless system.

In the real world, there are always losses: the fact that the photons stay only a finite time inside the cavity broadens the cavity mode linewidth (due to Heisenberg's inequality). We describe this photon loss with the cavity *quality factor* $Q = \frac{\omega_{cav}}{\Delta\omega_{cav}}$ where ω_{cav} is the angular frequency of the cavity mode and $\Delta\omega_{cav}$, its linewidth. The case where the coupling between electric field and emitter is weaker than the losses induced by the cavity imperfection is called the *weak coupling regime*. We will therefore consider that the modification created by the cavity surroundings can be treated in a perturbative framework.

Applying Fermi's golden rule in both free space and in the cavity mode leads to the following ratio of emission rate inside the cavity mode to the emission rate into free space:

$$\frac{\tau_{nat}}{\tau_{cav}} = \frac{3}{4} \frac{Q (\lambda_{cav}/n)^3}{\pi^2 V_{eff}} \cdot \frac{\left| \vec{d} \cdot \vec{E}(\vec{r}_e) \right|^2}{\left| \vec{d} \right|^2} \cdot \frac{\Delta\omega_{cav}^2}{4(\omega_{em} - \omega_{cav})^2 + \Delta\omega_{cav}^2} \quad (1.16)$$

where τ_{cav} is the decay time of the emitter in resonance with the cavity mode, $\vec{E}(\vec{r}_e)$ is the electric field in the cavity at the position of the emitter \vec{r}_e .

We see that the maximum enhancement we can obtain is given by the factor on the

left, as the second and third ones are always lower than 1 and are respectively due to (i) the dipole orientation and localization mismatches compared to that of the maximum electric field and (ii) the spectral mismatch between cavity mode and emitter.

The figure of merit is thus given by the Purcell factor:

$$F_P = \frac{3Q(\lambda_{cav}/n)^3}{4\pi^2 V_{eff}} \quad (1.17)$$

as foreseen by Purcell in his article [Pur46].

1.5.2 Different types of semiconductor microcavities

In this work, microdisks and photonic crystal cavities have been studied. This part aims at giving a quick overview of both types of microcavity. Further details will be provided in chapters 4 and 5, respectively.

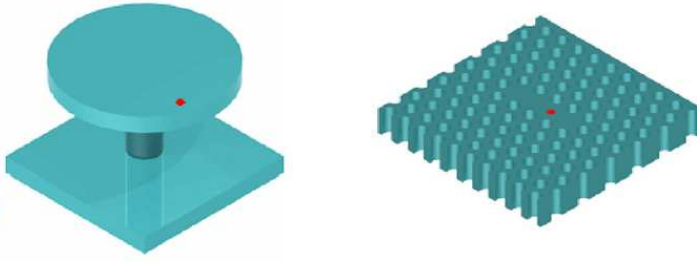


Figure 1.20 – Types of three-dimensional solid-state cavities [Rei08]: (right) two-dimensional photonic crystal cavity; (left) microdisk. The red point stands for the quantum dot position where the coupling to the cavity electric field is expected to be maximum.

In *microdisk resonators* (figure 1.20 (left)), the vertical confinement is provided by waveguiding, making use of the difference between the dielectric constants of the layer and the surrounding air. The microdisk usually seats on an underlying post. In the slab plane, light is guided by total internal reflection, responsible for the so-called *whispering gallery modes*. In a classical vision, photons turn around the microdisk axis during a time given by the value of the quality factor. Expected effective volumes are of the order of $6 (\lambda_{cav}/n)^3$ for a $2\text{-}\mu\text{m}$ disk [Gay99] and quality factors around 10 000 are typically obtained in III-V compounds [Pet05a], the record value being 10^8 [Sri07]. We can thus routinely expect Purcell factors as high as 150. The fabrication process being by far the simplest in all microcavities, these objects are good candidates for cavity quantum electrodynamics experiments.

In *photonic crystal cavities* (figure 1.20 (right)), light is confined on a photonic defect, providing discretized allowed states inside a photonic bandgap. The idea of creating materials showing a *photonic band gap*, in the same way that semiconductors exhibit an electronic band gap, stemmed from both Pr. Yablonovitch [Yab87] and Pr. Sajeev [Joh87] in 1987. In this publication, the author foresaw a total inhibition of the

spontaneous emission in a given energy-wavevector domain if the dielectric permittivity of the material $\epsilon(r)$ is periodically modulated. A photon having a wavevector and an energy inside the photonic band gap will not be able to propagate inside the structure: it will be reflected back.

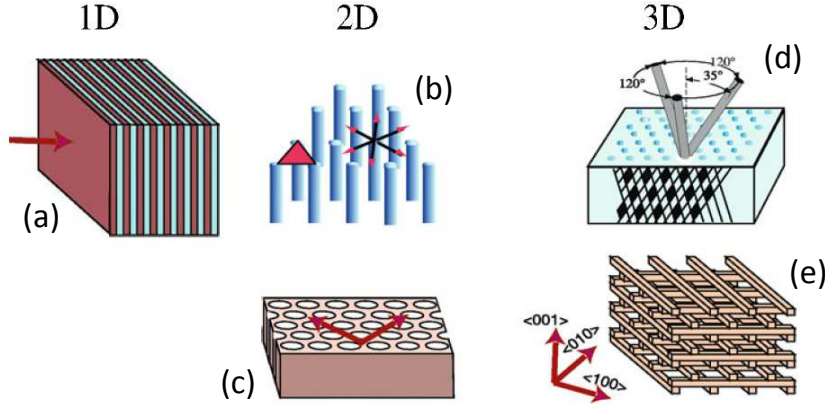


Figure 1.21 – (a) one-dimensional photonic crystal: left: a Bragg mirror; middle: two-dimensional photonic crystal: hexagonal lattices of rods (b) and holes (c); right: three-dimensional photonic crystal: "yablonovite" (d) and "woodpile" (e) structures [Lou08]

Figure 1.21 illustrates that this photonic band gap can be engineered in one to three dimension(s). (a) A stacking of layers made of various refractive indexes is a Bragg mirror. In this case, the photonic band gap is one-dimensional. (b) A periodic array of rods made of high index material and surrounded by air creates a two-dimensional photonic band gap, in the same way that (c) a layer of high index material periodically etched, forming air holes. In both cases, the thickness of the effective layer can provide light confinement in the third, transverse direction. (d) A bulk material can be etched in order to form a three-dimensional period of air holes. (e) Layers providing one-dimensional variation of the refractive index can be stacked so as to obtain a three-dimensional variation of the refractive index. Both structures can lead to a three-dimensional band gap. In practice, three-dimensional photonic crystals are very difficult to fabricate. That is the reason why the community is generally focusing on two-dimensional structures.

We define the photonic density of states as the number of photonic modes allowed per frequency unit. In free space, the density of states is continuous (see figure 1.22, left). Let us imagine that the dielectric periodicity opens a photonic band gap for a given range of wavevector and energy, and that we include a defect in order to locally break this periodicity. This defect will localize light otherwise forbidden into this crystal: it will create a singularity, due to the apparition of a photonic mode inside the gap. This phenomenon is illustrated in figure 1.22, right plot. This is a *photonic crystal cavity*. The tuning of the emission energy can be achieved by varying the cavity size (see figure 1.23).

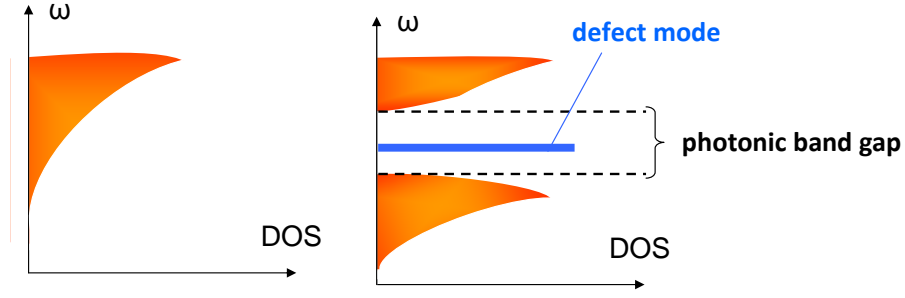


Figure 1.22 – Schematics comparison of the density of states in free space (left) and in a photonic crystal containing a point defect (right)

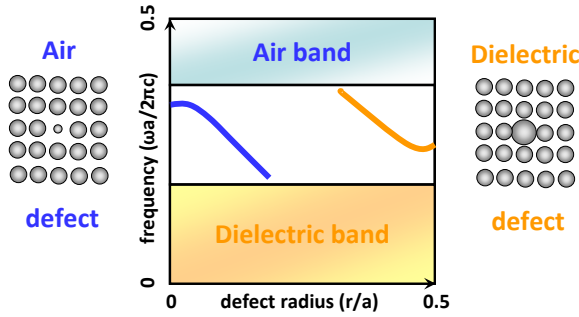


Figure 1.23 – Localized states in the gap for a defect formed by varying the radius r of a single rod in a square lattice of dielectric rods with lattice constant a

Two-dimensional photonic crystal cavities exhibit the smallest effective volumes of any semiconductor cavity — less than $(\lambda_{cav}/n)^3$ [Aka03]. Quality factors were first limited by diffusion processes outside the slab, but can now experimentally reach several 10^6 [Kur06]. The Purcell factors expected for these cavities are therefore the highest of all the microcavities.

1.5.3 Historical background and applications of cavity quantum electrodynamics

From table 1.9, we can notice that the field of cavity quantum electrodynamics has begun to develop with arsenide materials. Strong coupling in one-dimensional cavities was demonstrated, followed by weak coupling signatures and finally both weak and strong couplings with a single emitter. The breakthroughs relative to nitride microcavities are highlighted in gray.

Year	System	Achievement	T (K)	Ref.
1992	GaAs / AlGaAs quantum wells in Bragg reflector	strong coupling	5	[Wei92]
1993	InGaAs quantum wells in InP / InGaAsP microdisks	lasing	77	[Slu93]
1998	InAs / GaAs quantum dot micropillar	Purcell effect	8	[G'98]
1999	GaN microdisk	lasing	300	[Cha99]
1999	InAs / GaAs quantum dot microdisk	Q=12000	8	[Gay99]
2001	InAs / GaAs quantum dot microdisk	$F_{P,measured}=12$	8	[Gay01]
2003	Si photonic crystal	Q=45000 and $V=0.7(\lambda/n)^3$	300 ?	[Aka03]
2004	InGaN / GaN quantum well microdisk	lasing	10	[Hab04]
2004	single InAs / GaAs quantum dot in photonic crystal	strong coupling	13 – 29	[Yos04]
2004	InGaAsP / InP quantum well in photonic crystal	electrically-pumped lasing	300	[Par04]
2004	single In(Ga)As / GaAs quantum dot micropillar	strong coupling	5 – 30	[Rei04]
2005	single GaAs / AlGaAs quantum dot microdisk	strong coupling	7 – 45	[Pet05b]
2005	InAs / GaAs quantum dot microdisk	lasing	8	[Pet05a]
2006	single InAs / GaAs quantum dot in photonic crystal	lasing	4 – 80	[Str06]
2006	CdTe / CdMgTe quantum well Bragg mirror	Bose-Einstein condensation of polaritons	5	[Kas06]
2007	bulk GaN in Bragg mirror	polariton lasing	300	[Chr07]
2007	GaN/AlN quantum dot in photonic crystal	Q=2400 at 383 nm	300	[Ari07]
2008	InGaN / GaN quantum well photonic crystal	electrically-pumped lasing	300	[Mat08]

Table 1.9 – Some historical landmarks in the field of semiconductor microcavities

1.5.4 State of the art with nitride cavities

Performing cavity quantum electrodynamics with nitride cavities is appealing: the robustness of the exciton up to room temperature, as well as the large band offsets make them good candidates to explore this field in the UV range and at room temperature. The study of nitride microcavities began in the beginning of the 2000's. Strong coupling in one-dimensional cavities has been evidenced, as well as better and better quality factors. However, no evidence of either an enhancement or an inhibition of the spontaneous emission rate of an emitter in a nitride cavity has been reported up to now.

Nitride microcavities are challenging to fabricate, first because the UV wavelength range imposes smaller dimensions and better precision. Much of the current studies focus on InGaN / GaN heterostructures as emitters, which prevents from going into the UV emission range. Moreover, nitride materials are rather inert when etched with standard III-V processes. Their bad chemical selectivity, making etching processes very complex, is another drawback. Furthermore, the sensitivity of UV light to scattering defects is enhanced compared to that of visible wavelengths because the typical size of the process-induced defects is in the same range of dimension as the wavelength of the cavity mode. Another issue lies in the weak refractive index of nitride materials, which makes the removal of the underneath layer, *i.e.* either the substrate or the cladding layer, mandatory to avoid leakage. Most of the cavities fabricated up to now make use of a sacrificial layer, etched by a complex electro-chemical process enhanced by light exposure at a given wavelength [Sim07].

Optical properties of GaN nanowires

WE HAVE SEEN IN 1.4 that nanowires were currently under extensive studies. They can provide us with new growth possibilities thanks to enhanced surface relaxation or with new physical systems to study, e.g. one-dimensional confinement. Yet fundamental studies are still under way, and necessary to assess the full potentialities of these new structures.

We will begin by giving the main growth conditions leading to GaN nanowires, and depict the optical properties of as-grown samples. Then, the peculiarities of the emission of single nanowires will be analyzed. Further experiments to tune their intrinsic properties — by modifying either their dimensions or crystal phase — will then be discussed.

Contents

2.1	Spontaneous growth of GaN nano- and micro-wires	44
2.1.1	Plasma-assisted molecular beam epitaxy	44
2.1.2	Metal organic chemical vapor deposition	46
2.2	Optical properties of an ensemble of wurtzite GaN nanowires grown by MBE	48
2.2.1	Non-intentionally doped samples	48
2.2.2	p-doped nanowires	50
2.3	Optical spectroscopy of a single nanowire	52
2.3.1	Dispersion method	52
2.3.2	Discrepancies between the emission properties of an ensemble of nanowires and of a single nanowire, grown by MBE	53
2.3.3	Non-intentionally doped microwires grown by MOCVD . . .	55
2.3.4	Non-intentionally doped nanowires grown by MOCVD in low-flux growth conditions	56
2.4	Varying the diameter to observe quantum confinement . .	58

2.4.1	Looking for one-dimensional confinement in as-grown nanowires	58
2.4.2	Fabricating quantum wires	62
2.5	Optical properties of cubic GaN nanowires	63
2.5.1	Cubic GaN growth and structural characterizations	64
2.5.2	Identification of bound, free and split-off exciton	65
2.5.3	Luminescence enhancement with laser exposure	67

2.1 Spontaneous growth of GaN nano- and micro-wires

In our laboratory, we can grow GaN nanowires with different epitaxy techniques, molecular beam epitaxy¹ and metal organic chemical vapour deposition², leading to different morphologies, sizes and optical properties, as will be investigated in 2.2 and 2.3.3. In this section, we briefly present the basics of the growth of non-catalyzed GaN nanorods using these techniques. We will not develop here the growth of catalyzed nanowires [Zho03], [Che10], as we did not study them.

2.1.1 Plasma-assisted molecular beam epitaxy

MBE consists in depositing the III elements — Ga, Al, In and sometimes dopants — as atomic beams onto the heated and rotating substrate. These atoms are contained in crucibles: when heated, a liquid-vapor or solid-vapor equilibrium appears. As the chamber is kept under ultra-high vacuum (10^{-10} mbar) between successive growths and high vacuum (10^{-5} mbar) during the growth process, the trajectory of the vapor-phase atoms is ballistic. Simultaneously, in plasma-assisted growth, N_2 is provided and cracked with a radio frequency excitation, creating a plasma containing active species that are incorporated into the grown layer.

The substrate is a two-inch, n-doped silicon (111) wafer, deoxidized in fluoridric acid before being inserted into the chamber. A 3-nm thick AlN buffer layer can be deposited prior to the nanocolumn growth. This was indeed reported to improve the verticality of the wires [Son07], even if nanowires can also be grown successfully without any buffer layer. When Ga and active N adatoms are provided for the first time, nucleation takes places. The values of both the temperature and the fluxes during this first step will fix the nanorod density on the sample.

It has to be mentioned that the growth mechanism is known to be very different from the nucleation of GaN/AlN Stranski-Krastanov quantum dots [Lan09], in which

¹The growth of GaN nanowires by PA-MBE was mainly performed by either Gabriel Tourbot, Aurélie Pierret, Karine Hestroffer or Bruno Daudin.

²The growth of GaN microwires by MOCVD was mainly performed by either Robert Köster, Chen Xiaojun, Damien Salomon, Christophe Durand or Joël Eymery.

case only elastic strain relaxation occurs. Due to the larger diameter of nanowires, plastic strain relaxation is very efficient. Moreover, the nucleation process appears to be very different on bare silicon and on AlN buffer layer [Hes12]. As-grown nanowires have a typical diameter of 40 nm, while the density is around $100 \mu\text{m}^{-2}$. If this density is high enough, wires of larger diameters can be obtained by the coalescence of several columns [Con09]. The length is controlled by adjusting the growth time.

The growth of GaN nanowires was quasi-simultaneously demonstrated for the first time on sapphire [Yos97] in 1997 and on silicon (111) [SG98]. The typical conditions needed for one-dimensional growth, whatever the substrate nature, is an excess of nitrogen ($\text{N}/\text{Ga}=3$) and a substrate temperature close to 800°C , higher than that used to grow two-dimensional layers. A growth diagram has been proposed by Fernandez-Garrido [FG09] (see the left panel of figure 2.1).

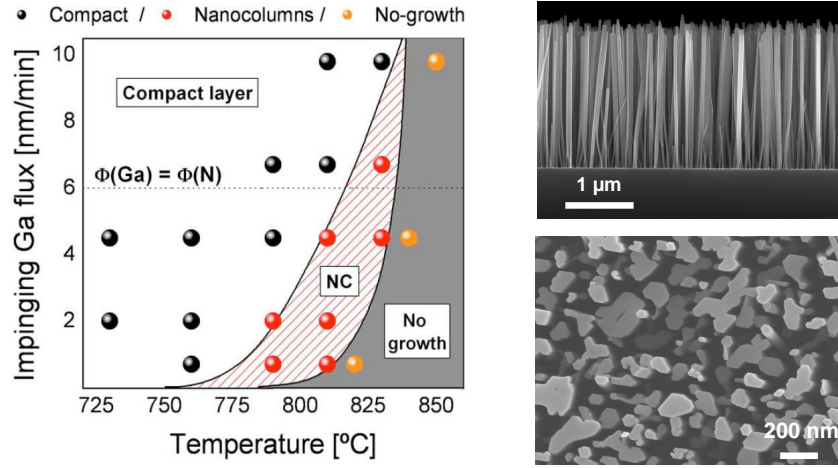


Figure 2.1 – (left) PA-MBE growth diagram for GaN nanowires [FG09]. (right) SEM images of the resulting nanowires

According to figure 2.1 (left panel), the important parameters are temperature and Ga/N flux ratio. Achieving columnar growth requires $\text{N}/\text{Ga} > 1$. Increasing the Ga/N *flux ratio* leads to higher density and smaller diameters. N-rich conditions are known to reduce the mobility of Ga atoms on GaN surfaces [Zyw98]. As the nanocolumn geometry is achieved through the diffusion of Ga atoms both on the substrate and on the sidewalls for several hundreds of nm, a high *temperature* is required in order to counterbalance the effect of the high nitrogen flux on adatom mobility. This effect will be discussed further in 2.4.1. The temperature is the crucial parameter to control the final density of the sample. Yet it is difficult to measure accurately. Therefore, experimentally, the desorption time needed to recover a bare silicon surface after a prior deposition of gallium is used as a temperature calibration. More details can be found in [Lan08]. The temperature is also very inhomogeneous — more than 30°C difference from center to edge of the wafer [Mat11].

SEM images of typical nanowires grown in our laboratory are provided in figure 2.1 (right panel). Lateral surfaces are constituted of $\vec{m}=[1\bar{1}00]$ planes [Lar08]. Contrary to

two-dimensional layers grown with the same technique and on the same substrate, the nanocolumns (either on bare Si(111) or on a 2-nm thick AlN buffer layer) were found to be N-polar [Hes11].

MBE growth leads to high quality layers, but it suffers from a very low growth rate (around 0.5 Å/s). This is the reason why one-dimensional growth is also investigated using more industrial methods, such as MOCVD.

2.1.2 Metal organic chemical vapor deposition

MOCVD processes benefit from a much faster growth rate. This deposition technique uses a carrier gas (usually H₂) containing complex organic molecules. For example, trimethylgallium is the precursor used for Ga and ammonia, for N. The atoms that will participate in the growth are released through thermal decomposition of these precursors on the heated substrate. During the whole process, the pressure is kept constant thanks to the use of an exhaust pump in order to remove the gas products of the chemical reaction. Growth is performed both on Si(111) and \bar{c} -sapphire substrates. In our group, the growth conditions to obtain microwires have been studied [Che11], giving the main parameters to control as the temperature, the precursor flows, the carrier gas flow, and the reactor pressure.

Similar to MBE processes, both the temperature and the V/III flux ratio must be kept high. Temperature is used to enhance diffusion. At higher temperature, fewer nuclei of wider diameter are created. As a consequence, the density will be lower and the wires longer. Standard growths are performed at around 1100°C. Furthermore, after the seed formation, the axial growth is promoted with respect to the lateral growth if the precursor flows are kept low and the V/III flux ratio is around 25.

More specifically to MOCVD processes, the pressure in the growth chamber is in the range of 800 mbar. A carrier gas flow is used to transport the precursors into the reactor chamber. In order to grow microwires, the reactor pressure must be kept high in order to enhance pre-reactions in the gas phase and keep a homogeneous local pressure close to the substrate.

Yet, these parameters are not sufficient conditions to achieve a one-dimensional growth. *The key parameter to obtain high one-dimensional growth is to incorporate silane.* It was indeed shown in [Koe10] PB REF that growing without adding silane leads to the formation of planar hexagonal disks (diameter of several μm). However, with a high enough silane flux, one-dimensional growth is obtained. A 3-nm SiN_x layer is formed around the nucleus. It actually behaves like a mask passivating the sidewalls and preventing lateral growth. Once axial growth is promoted compared to lateral growth, the silane flux can be turned off while keeping the columnar geometry.

When using conditions similar to those used to grow two-dimensional layers with a

simultaneous incorporation of silane, diameters of about 500 nm and lengths of hundreds of μm are typically obtained, at growth rates of about 100 $\mu\text{m}/\text{h}$ with a density of the order of 10^7 cm^{-2} . The resulting microwires are depicted in figure 2.2.

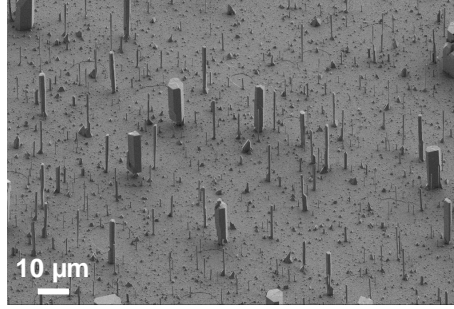


Figure 2.2 – SEM picture of GaN nanowires grown by self-assembled MOCVD

These wires are mainly N-polar, even if some Ga-polar domains can be evidenced in a N-polar microwire [Che10]. On the contrary, growing GaN on a pre-patterned mask to support one-dimensional growth leads to pyramidal-shaped objects if the growth is forced in the Ga-polarity by using Ga-polar substrates. Our group indeed reported that columnar growth is possible only in the N-polar direction [Che10].

The growth of microwires by MOCVD using standard flux values results in silicon incorporation. Silicon is a well-known n-dopant for GaN: its presence during growth is expected to affect the properties of the resulting GaN microwires, as we will see in 2.3.3. The doping level in the region where silicon was incorporated indeed reaches 10^{20} cm^{-3} , deduced from the spectral position of the near band edge measured by cathodoluminescence [Koe10]. Exploring totally different growth conditions in which silicon passivation is not necessary thus seems interesting.

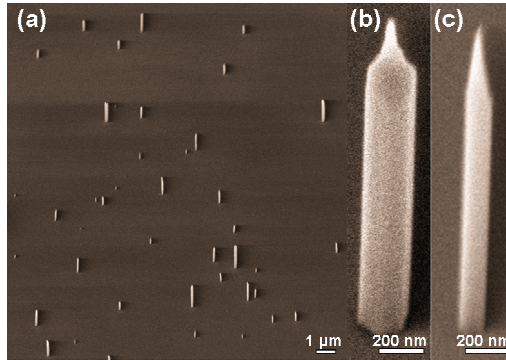


Figure 2.3 – (a) 45°-tilted SEM image of GaN nanowires grown at low precursor flows. (b) and (c) SEM images of single nanocolumn with higher magnification.

One can change the usual mass-flows in order to reach *smaller impinging fluxes*, typically 25 times smaller for trimethylgallium and 70 times smaller for NH_3 . A simultaneous decrease of the total pressure around 100 mbar while keeping the temperature at 1000°C leads to the growth of nanowires with diameters smaller than 200 nm and without needing neither SiN_x passivation nor AlN buffer layer. Figure 2.3(a) is a bird-view of the sample, while (b) and (c) focus on single nanocolumns.

A nanocolumn density of about 10^3 cm^{-2} and diameters around 200 nm were obtained when applying these growth conditions on sapphire substrates. Note that

a thick two-dimensional layer was grown non-intentionally in-between the nanowires. These nanorods proved to be Ga-polar, contrary to usual columns routinely obtained by MOCVD growth [Che10]. This suggests that the growth mechanism for both types should be very different, as discussed in [Che11]. The resulting objects are actually closer to the MBE-grown nanowires than MOCVD microwires obtained in standard growth conditions, as can be inferred by their comparable growth rate (in the order of 100 nm/h) and diameter.

2.2 Optical properties of an ensemble of wurtzite GaN nanowires grown by MBE

As mentioned in 1.4, MBE-grown nanowires are very interesting materials because of their mean diameter of 40 nm. As a consequence, the high surface to volume ratio allows an efficient surface relaxation which leads to excellent crystal quality compared to other heteroepitaxially-grown GaN layers. On the contrary, microwires grown by MOCVD exhibit a larger diameter and a high density of silicon dopants. The surface relaxation mechanism, combined with crystal disorder and band filling induced by the high doping level, are expected to result in a material of lower quality. These microwires will be studied in 2.3.3. One of the most powerful tool to study nanowires is photoluminescence: indeed, this spectroscopic method is very sensitive to defects. Our macrophotoluminescence excitation uses a frequency-doubled 244 nm argon laser for excitation, focused as a 50-100 μm spot on the sample³. The resulting density of MBE-grown nanocolumn sample is around 100 μm^{-2} . We thus simultaneously probe the luminescence of about 10^5 to 10^6 nanowires. The spectroscopy of non-intentionally doped nanowires will be analyzed first. Then, the consequences of a slight p-doping will be addressed.

2.2.1 Non-intentionally doped samples

Figure 2.4a shows the full-range low-temperature photoluminescence spectrum of an ensemble of nanowires. We can first evidence the absence of any deep defect luminescence such as the yellow band emission described in the literature at 2.27 eV [Res05]. The spectrum is dominated by the GaN near band edge emission between 3.4 and 3.5 eV [Cal00]. In figure 2.4b, we can observe the emission originating from the near band edge with more details. We can identify the emission from the well-known features: the donor-bound exciton A at 3.471 eV (D^0X_A), the donor bound exciton B at 3.474 eV (D^0X_B), the free exciton A at 3.478 eV (FX_A), and the free exciton B at 3.482 eV (FX_B). These values are consistent with the ones reported in literature on homoepitaxial, and

³Details of the macrophotoluminescence setup are provided on page 199

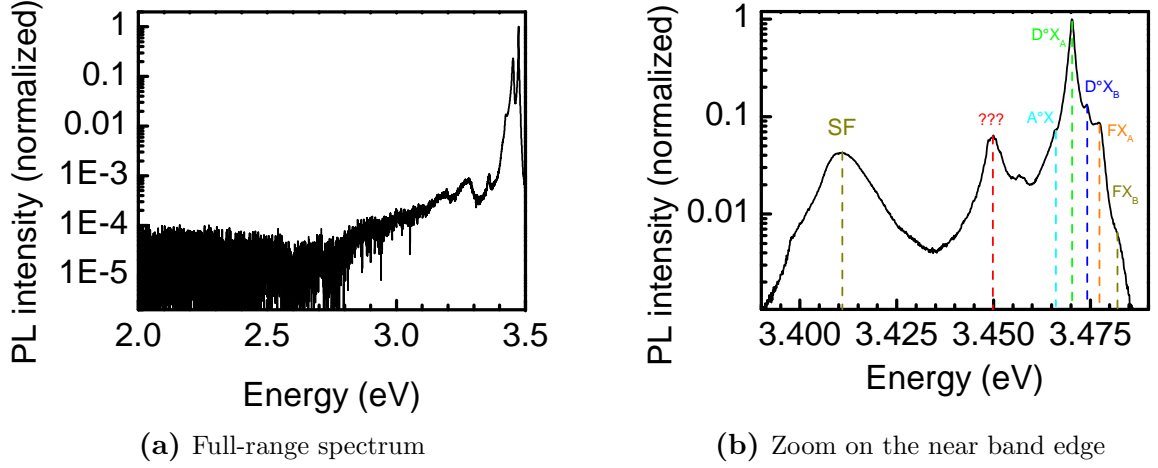


Figure 2.4 – Macrophotoluminescence of an ensemble of GaN nanowires at 4 K

therefore totally relaxed GaN [Kor99]. A weak feature observed at 3.466 eV is ascribed to the acceptor-bound exciton [Kor99]. We will see that intentional p-doping is necessary to better detect this line, as the non-intentional doping is of almost pure n-type. Let us note that the observation of neutral donor-bound excitons suggests that all dopants are not ionized unlike what has been foreseen by photocurrent measurements [Cal05]. Further studies are needed to understand the discrepancy between photocurrent and photoluminescence results.

Moreover, the full width at half maximum of the donor-bound exciton emission is of the order of 1 to 3 meV, a state-of-the art value for GaN nanowires (see [Bra10], [VN06]), meaning that the strain in the nanocolumn is homogeneous. This is still one order of magnitude greater than the linewidths reported on homoepitaxial GaN [Kor99], but a significant improvement compared to heteroepitaxial layers. It is remarkable that a very low layer thickness (*i.e.* nanorod height) of a few 100 nm only leads to such a narrow linewidth. On the contrary, several μm -thick GaN layers grown on sapphire or silicon are still inhomogeneously stressed and optical linewidths are at best in the few meV range [Cal97].

The emission from the excitons bound to stacking faults (SF) in the 3.41 - 3.42 eV region [Con09] is much weaker than that of the donor-bound exciton. This also confirms that these defects, known to appear mainly during the coalescence of neighbouring columns, are not present in the volume probed in this photoluminescence experiment. This sample is indeed composed of several μm -long nanorods.

An emission band at 3.45 eV is also measured and will be discussed in the chapter 3.

However, as photoluminescence provides information on the lower energy states, the C exciton is not observed at 4 K. On the contrary, absorption, photoluminescence excitation or reflectivity setups enable to measure the real density of states. On figure 2.5 we can see the *absorption* spectrum at low temperature of GaN

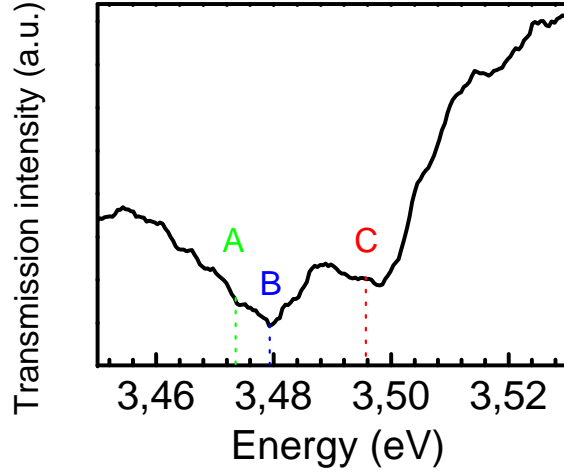


Figure 2.5 – Absorption spectrum of an ensemble of GaN nanowires at 4 K

nanowires⁴.

For this measurement, as we need a substrate transparent at the energy of the GaN bandgap, as-grown nanowires were laid on a double-face polished sapphire substrate so as to obtain a dense layer. In this case, the nanowires are randomly orientated parallel to the host substrate. We used a non-polarized excitation beam perpendicular to the sample. As seen in table 1.6 from chapter 1, the A-exciton is polarized perpendicular to the \vec{c} axis. The dipole polarization of the B-exciton displays a contribution parallel and another perpendicular to \vec{c} . However the C-exciton is polarized only parallel to \vec{c} . In the geometry of the transmission experiment, both the excitation and the detection of B and C excitons are more favorable than that of A excitons. Experimentally, in addition to the B exciton, the C exciton is clearly visible whereas the A exciton, is hardly detectable (its expected position is given on figure 2.5).

2.2.2 p-doped nanowires

Here we focus on the optical properties of Mg-doped GaN nanorods grown on top of undoped GaN nanowires. We are unable to quantify the doping level, as the magnesium cell is not calibrated, and thus one cannot use the reported cell temperature (170°C) to compare with other experiments. Yet we will see that optical characterizations provide a qualitative evaluation of the doping.

The full-range photoluminescence spectrum of this sample is depicted on figure 2.6a, while figure 2.6b focuses on the near-band edge. We observe the same features as already reported on figure 2.4b (D^0X_A , D^0X_B , FX_A and FX_B), as well as additional ones. In the following, we thus focus on the peculiarities of this spectrum compared to that of figure 2.4b. The Mg-acceptor-bound exciton emission is at 3.466 eV, its spectral position expected for a totally relaxed crystal [Kor99]. The p-doping seems to compensate the

⁴Details of absorption the setup are provided on page 202.

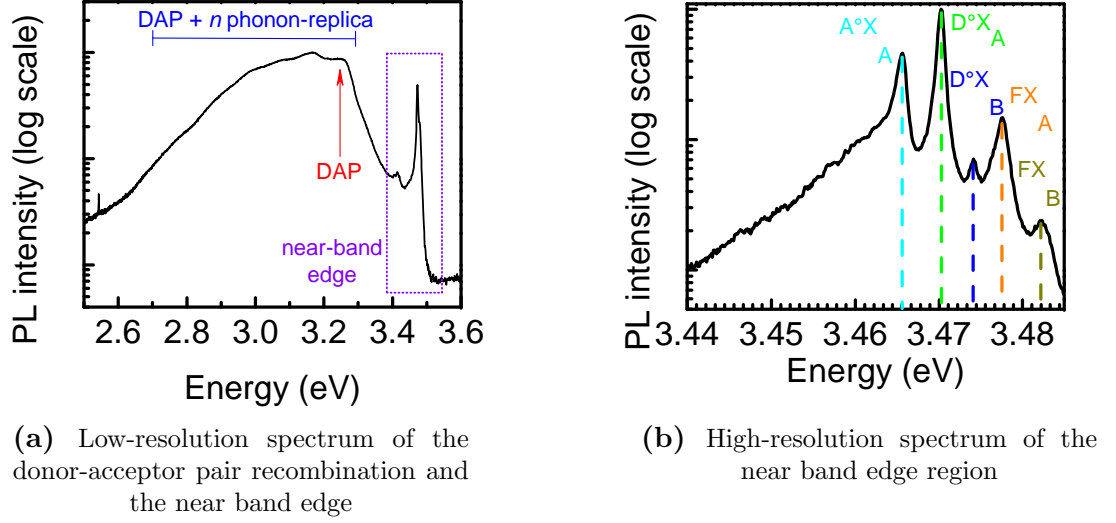


Figure 2.6 – Macrophotoluminescence of p-doped nanowires at 4 K - sample N1434

residual n-doping, as indicated by a similar order of magnitude of the intensity of the acceptor-bound exciton emission compared to that of the donor-bound exciton. The ratio of the intensity of the acceptor-bound exciton to that of the donor-bound exciton is around five times enhanced compared to the feature in undoped samples as illustrated by figure 2.4b.

In figure 2.6a, the donor-acceptor pair recombination [Res05] is observed at 3.27 eV, as well as its longitudinal-optical phonon replica separated by 92 meV [Res05]. We evaluated the integrated intensity of the donor-acceptor pair recombinations (*i.e.* 1/5 of the total integrated intensity of the broad peak labeled DAP+ n phonon-replica, if this peak contains the zero-phonon line and four phonon replica of the same intensity), the donor-bound exciton and the acceptor-bound exciton displayed on figure 2.6a. This allows us to quantify the ratio of isolated neutral donors to 10% and isolated neutral acceptors to 5%. This shows that the achieved p-doping level is indeed in the same range as the residual n-doping level. If one considers a doping of the order of 10^{17} cm^{-3} , a 20-nm nanorod contains on average 100 dopants⁵. In this sample, this calculation shows that less than ten donors or acceptors are optically active per nanocolumn, the rest of them are all involved in the donor-acceptor pair recombination.

The doping level remains low enough not to broaden the bound exciton lines. On the contrary, in this sample the full width at half maximum of all bound excitons is smaller than in the best undoped samples we have. Here we measured 850 μeV for the acceptor-bound exciton recombination and 680 μeV for the donor-bound exciton one. This result, suggesting a better crystal homogeneity, may be explained by a surfactant effect of Mg on the \bar{m} -sidewalls, which has been reported on \bar{c} surfaces, as well as non-polar $[11\bar{2}0]$ surfaces [Mon04] [Lah09]. We suggest that this could modify the distribution of

⁵as discussed in 1.4.2

optically-active isolated donors, favouring the donor-acceptor recombination compared to the donor-bound exciton transition close to the surface. Hence this could quench the luminescence from surface donor-bound excitons, which is reported to be at a higher energy than “bulk” donor-bound exciton ([Pfü10], [Bra10]), and thus sharpen the linewidths. This could also decrease the strain homogeneity in the crystal.

The emission at 3.45 eV totally disappears compared to the spectra of undoped samples such as in figure 2.4b. This point will be discussed later on 3.4.2.

Conclusion

In this section, we have studied the low-temperature optical properties of GaN nanowires grown by MBE. It appears that their emission is comparable to that of high-quality, thick epilayers, in terms of both spectral position and linewidth of the donor-bound exciton. Furthermore, a significant improvement of the excitonic linewidth is observed with a slight p-doping level.

2.3 Optical spectroscopy of a single nanowire

We have seen in the last part that as-grown optical characterizations give statistical information, as we simultaneously probe around 10^6 nanowires at the same time. To get more insight on the emission of these nano-objects, it is highly desirable to perform the spectroscopy of a single nanocolumn. To achieve this goal, however, the density has to be decreased by several orders of magnitude. We therefore need to develop a method to efficiently isolate single nanowires. *Dispersing* them on a bare substrate is the most common approach.

2.3.1 Dispersion method

Dispersing nanorods can be achieved by two means. The first method consists in scratching the as-grown sample with another substrate, like bare silicon, in order to break the nanowires at their bottom part and to transfer them to this new substrate. One can also immerse an as-grown sample into a solvent (here ethanol) and sonicate it to break them close to their base. Droplets of the resulting suspension are then deposited directly onto the host substrate. The solution can also be further diluted prior to deposition in order to lower the wire density even more.

These transferring methods seem at first sight to be the simplest, because they do not require any further growth development. However their efficiency to decrease the density is limited by the nanocolumn coalescence caused by too high a density during growth. Another reason is the sticking of several nanowires during the dispersion process, as

a result of Van der Waals attraction, if the sonication power is not strong enough to separate them in the suspension. Therefore, from sample to sample, it can be difficult or even impossible to obtain isolated nanowires. Figure 2.7 (left) depicts the ideal case of an isolated wire, while figure 2.7 (right) shows a nanorod aggregate.

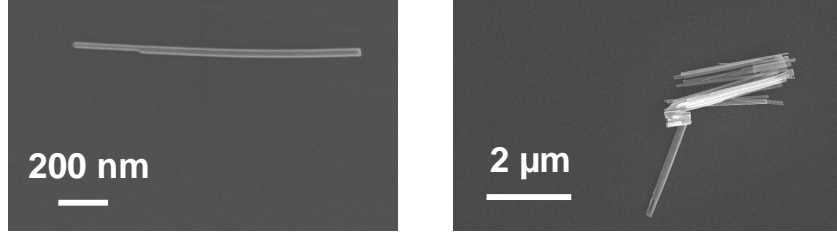


Figure 2.7 – SEM images of GaN wires scratched or dispersed by sonication

From the statistics we performed, it seems that the sonication and suspension method results in slightly less coalesced nanowires after dispersion than the scratching method. Yet, the contact of the nanocolumns with solvent might be detrimental to their optical properties. It is at this point difficult to evaluate the consequences of the organic layer embedding the nanorods after their dispersion by suspension in a solvent.

2.3.2 Discrepancies between the emission properties of an ensemble of nanowires and of a single nanowire, grown by MBE

In figure 2.8a, we plot the spectra of single wires grown by MBE and dispersed by the sonication and suspension method on several host substrates: silicon, either bare or coated with a few 100-nm of gold or aluminium (from top to bottom). The macrophotoluminescence of the ensemble is also displayed for reference (at the very bottom). It is important to keep in mind that each probed nanocolumn gave a unique spectrum, as observed in [Pfü10] and [Bra10], where the authors have studied nanowires dispersed on a silicon substrate only. The figure only intends to show a representative behaviour of the influence of the host substrate.

From the statistics we performed, we observed that on each nanocolumn dispersed on silicon, both the 3.45 eV and the donor-bound exciton contributions are shifted compared to the emission from the as-grown sample. *A significant discrepancy was found from wire to wire: both contributions can be either blueshifted or redshifted.* On the top spectrum presented on figure 2.8a, the emission at 3.45 eV is blueshifted by 3 meV, while the donor-bound exciton line is redshifted by 3 meV. In the literature, the redshifted emission of a GaN nanocolumn has been ascribed to different thermal coefficients between GaN and the host substrate⁶. Lowering the temperature thus leads to an increased strain in the GaN nanorod [Sch06][Sch08]. Besides, the blueshift of the donor-bound exciton recombination compared to its as-grown, relaxed value has been

⁶For Si and GaN, see table 1.2.

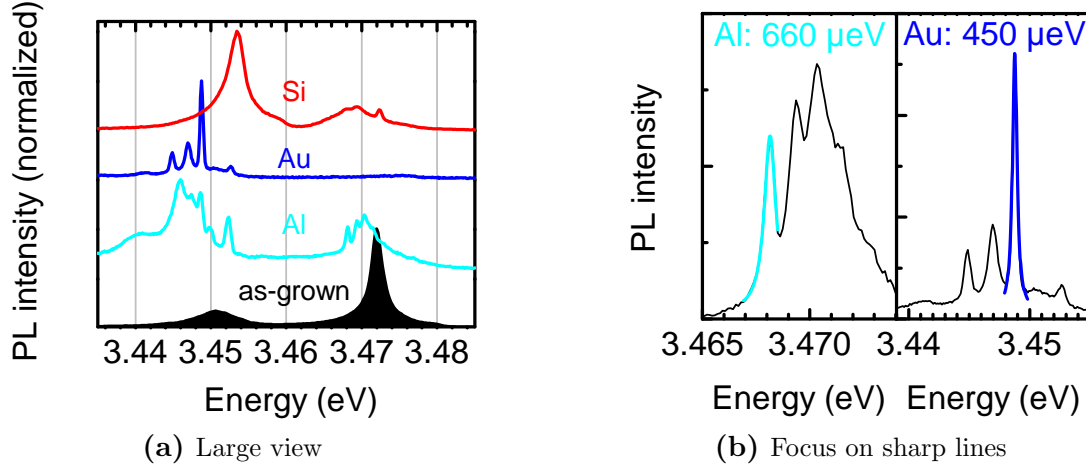


Figure 2.8 – Comparison between the low-temperature micro-photoluminescence emission of single nanowires dispersed on several host substrates and macrophotoluminescence of an ensemble of the same sample N1006

attributed to excitons bound on surface donors. The proximity of nanocolumn sidewalls is indeed expected to strongly decrease the exciton binding energy. The presence of surface donor-bound exciton is indeed well-known in other materials like ZnO [Wis06].

The common point to all the spectra of nanowires dispersed on Si we acquired is the *broadening of both lines compared to the as-grown sample*. This is corroborated by the observation by Brandt *et al.* of a 20-meV broad donor-bound exciton emission of a single nanocolumn dispersed on Si [Bra10]. According to the authors, this effect is due to strain inhomogeneities from one part of the wire to the other (due to different interaction intensity with the host substrate) [Bra10]. Another reason for the broad full width at half maximum could be insufficient heat or charge dissipation (similar to spectral diffusion), both processes inducing spectral broadening.

This assumption made us investigate the dispersion on metal substrates. The resulting spectra exhibited sharp lines that may be below the resolution of our setup⁷. On aluminium, we recorded narrow emissions in the spectral range of the donor-bound exciton. For example, a 660 μeV peak at 3.468 eV is ascribed to an exciton bound to a single donor, as displayed on figure 2.8b (left panel). The spectral dispersion from one sharp line to another is attributed to different exciton binding energy and agrees well with [Bra10]. On gold, sharp lines as narrow as 450 μeV were also observed at 3.449 eV, as depicted on figure 2.8b (right panel). They can be attributed to an exciton bound to a single, localized defect. Yet, both the 3.45 eV and the donor-bound exciton emissions are still shifted when nanowires are dispersed on metal-coated silicon. As a consequence, the shifts observed on nanorods dispersed on silicon substrates cannot be explained by a

⁷These measurements were performed with a 1800 line/cm grating allowing for a resolution of 500 μeV and a calibration thanks to the 365.015 nm line of a mercury lamp led to a spectral accuracy of a few 100 μeV .

bad heat or charge dissipation induced by the proximity of silicon. It may be intrinsic to the emission of a single dispersed nanocolumn, whatever the nature of the host substrate.

Nanowires lying on metal substrates generally exhibit an array of sharps lines. The envelope of this ensemble of lines is however larger than the emission of as-grown nanowires at 3.45 eV and of the donor-bound exciton. On dielectric substrates such as Si, nanocolumn emission lines are broader than on metals and than the as-grown emission. This difference can be tentatively attributed to a better charge and heat dissipation when metal host substrates are used compared to dielectric ones. It proves difficult to determine whether this discrepancy from nanocolumn to nanocolumn is intrinsic, *i.e.* all nanowires exhibit a different spectrum, or due to the interactions with the underneath substrate. In particular, different donor (or defect) positions along the nanocolumn radius should induce inhomogeneous broadening. In the case of as-grown samples, when simultaneously probing the luminescence of 10^5 nanowires, the broadening is expected to be enhanced compared to that of a single nanocolumn, containing only a few donors. We are still unable to explain this paradox. In the next chapter, other methods allowing to perform the spectroscopy of a single, as-grown nanorod will be investigated.

Whatever the nature of the host substrate, some nanowires exhibit emissions at 3.45 eV and from the donor-bound exciton, while others do not. It will be discussed in more details in 3.4. Let us notice that the emission at 3.45 eV is clearly enhanced in the emission of single dispersed wire compared to the ensemble reference. This is due to the polarization of this line, which is parallel to the growth axis (see 3.2). Thus, in the geometry of a wire lying on a substrate, the detection of this optical transition is more efficient than in the geometry chosen for macrophotoluminescence measurements of as-grown nanowires.

2.3.3 Non-intentionally doped microwires grown by MOCVD

During MOCVD, microwires are obtained thanks to the silicon passivation of lateral surfaces. We thus expect the silicon incorporation to have serious consequences on the optical properties of the material. Besides, the low density obtained in these growth conditions leads to a non-negligible parasitic growth of a two-dimensional layer between the microwires. Therefore, optical characterizations cannot be performed on the as-grown samples, and dispersion is needed to isolate the wires from this two-dimensional layer. In figure 2.9, we present the full-range micro-photoluminescence spectrum of a single microwire dispersed by sonication and suspension, both on the bottom- and the top-part of the wire.

As far as the near band edge is concerned, the emission energies at 3.52 eV (bottom) and 3.49 eV (top) indicate compressive strain for both zones. The more pronounced blueshift of the signal emanating from the bottom part is due to conduction band-filling

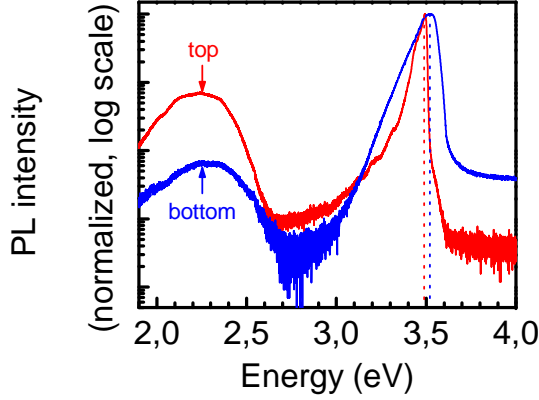


Figure 2.9 – Microphotoluminescence spectrum of a single nanowire taken at both the bottom of the wire, which is passivated by the SiN_x mask, and on the upper part of wire

generated by n-doping [Ler97] and higher compressive strain, both effects attributed to the presence of a SiN_x coating.

The linewidth of the near band edge emission is 110 meV on the SiN_x -coated region and 40 meV on the unintentionally-doped part. As MOCVD-grown microwires obtained in the usual conditions described in 2.1.2 exhibit much wider diameters than their MBE counterparts, surface relaxation is not so efficient. This leads to a strain inhomogeneity that broadens the excitonic line. The larger full width at half maximum on the lower part of the wire could be attributed to inhomogeneous strain distribution and increased population of high electronic states on the conduction band, both mechanisms being enhanced by doping.

The yellow band emission originating from deep defects is detected everywhere on the wire, with a greater intensity compared to that of the near band edge in the top (only one order of magnitude smaller), which is not silicon-passivated. As this luminescence is reported to originate from complexes formed by Ga vacancies and oxygen substituted to nitrogen atoms [Pol07][Res05], it is likely that the silicon doping may modify the incorporation of the point defects originating from the yellow band and therefore decrease the intensity from this defect band as already pointed out in [Neu94].

From these optical results, these wires can be seen as lying in-between totally-relaxed nanowires grown by PAMBE, and highly-strained epitaxially-grown two-dimensional layers. Even if strain relaxation is incomplete, we can take advantage of their columnar geometry to grow radial heterostructures. MOCVD can also be used in non-standard conditions to obtain smaller nanowires, where strain relaxation is more efficient. This is the topic of the next subsection.

2.3.4 Non-intentionally doped nanowires grown by MOCVD in low-flux growth conditions

As described in 2.1.2, nanowires with size comparable to that obtained by MBE can be grown by decreasing the growth rate. Thanks to the intrinsically low density

resulting from this growth process and the near absence of luminescence from the two-dimensional overgrowth, microphotoluminescence can be performed directly on the as-grown sample.

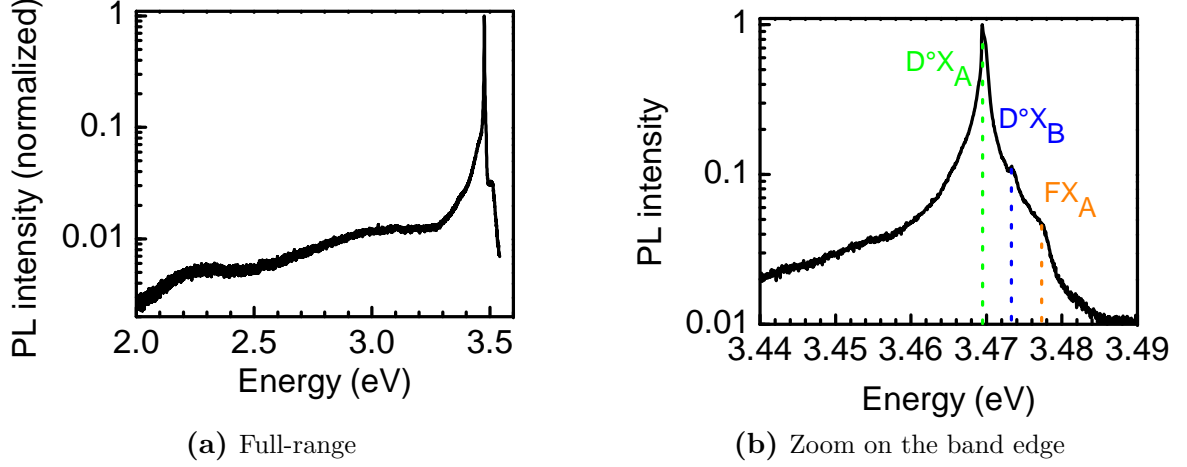


Figure 2.10 – Microphotoluminescence at 4 K spectrum of single standing GaN nanowire grown by MOCVD with low-flux conditions

Figure 2.10a shows the low-temperature full-range photoluminescence spectrum: a weak yellow luminescence is detected, 200 times weaker than the emission from the donor-bound exciton and thus strongly reduced compared to the emission of standard MOCVD-grown microcolumns, as seen previously in figure 2.9. Note that the blue band centered around 2.9 eV was detected anywhere on the sample, even on the spots where no near band edge luminescence was detected. We therefore assume that this blue band originates from the two-dimensional layer grown in-between the nanorods. More interestingly, the near band edge of these wires exhibit very narrow lines, as sharp as 1.7 meV, a state-of-the-art value for MBE-grown GaN nanowires [VN06], as can be seen in figure 2.10b. The usual exciton recombination lines (the A and B donor-bound excitons D^0X_A , D^0X_B and the A free exciton FX_A) are detected at their relaxed positions, showing the nearly strain-free character of the system.

Conclusion

In this section, we showed that whatever the nature of the host substrate, dispersed nanowires are intrinsically a different system than as-grown, free-standing nanowires. This is partly due to the fact that the nanocolumn surface is no longer strain-free. This could explain why the emission of a single dispersed nanocolumn is broader than that of 10^5 as-grown nanowires. Besides, in some cases, spatially isolating the nanorods proved to be impossible because their as-grown density was too high so that they tend to aggregate during the dispersion process. These are the reasons why other methods have been investigated to obtain low-density as-grown samples. This will be discussed in the next chapter. Furthermore,

we have observed that MOCVD microwires exhibit a broad near band edge recombination due to the silicon incorporation resulting from the silane flux used during growth. Yet, growing with low-flux conditions allows to obtain one-dimensional objects without the need of silicon passivation, and leads to state of the art nanowires in terms of optical properties.

2.4 Varying the diameter to observe quantum confinement

In nanowires, surface states appear to play a leading role in determining the optical properties. Yet very little is known about the nature and the consequences of these surface states in GaN. For example, it is already well-known that in ZnO nanowires, some photoluminescence features originate specifically on the surfaces [Wis06]. In GaN nanowires, the surface nature of the 3.45 eV line is still under debate and will be discussed in details in chapter 3. The spatial localization of donors along the nanocolumn diameter is also unknown but predicted to be inhomogeneous due to self-purification mechanisms [Bra10]. In order to answer these questions, varying the diameter, and hence the predominance of surface effects, is of paramount importance.

From a theoretical point of view, an exciton behaves like a one-dimensional object in the weak confinement regime if the movement of its center of mass is confined. This leads to a splitting of its band structure. In order to be experimentally observable, this splitting must be at least comparable to both the thermal energy (0.3 meV at 4 K) and the full width at half maximum of the photoluminescence lines (a few meV).

2.4.1 Looking for one-dimensional confinement in as-grown nanowires

A one-dimensional exciton would be evidenced by several specific signatures already described in the literature and summarized in the next parts. We will then compare our results to these references and conclude.

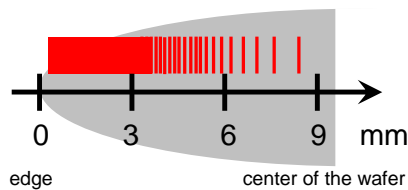


Figure 2.11 – Schematics describing how the position is noted along the radius of sample N1405: 0 mm is at the rim, and the position is measured towards the center of the wafer

The first evidence of a one-dimensional excitonic confinement lies in a *blueshift of the free-exciton* emission compared to that of the bulk material. In the samples studied in 2.2, the nanocolumn diameter was around 50 nm. This is too wide to exhibit

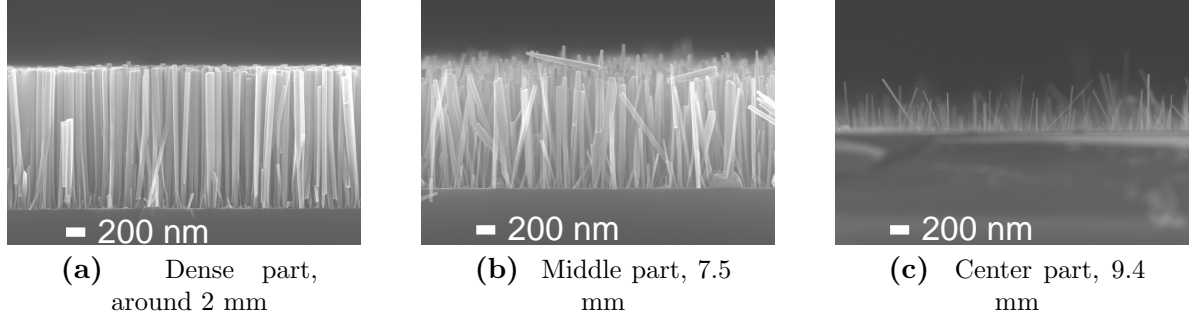


Figure 2.12 – SEM images of sample N1405 at different positions along the wafer diameter

quantum confinement⁸. A sample was grown at a peculiar high temperature: 850°C instead of 800°C in standard conditions, and without any AlN buffer layer. This favours a temperature gradient during the growth and this sample thus exhibits a nanorod density-and size-gradient along the wafer radius. When scanning along the wafer radius, the nanorod diameter decreases from coalesced wires of diameter larger than 50 nm to single wires of 15 nm diameter in average. Note that a *large dispersion in diameter* was observed. Please refer to figure 2.11 for a schematics of the sample, to figure 3.15 for SEM pictures of the sample at different positions, and to figure 2.13a for the diameter and filling factor (defined as the surface GaN amount covering a given surface of the Si substrate). We investigated these thin nanocolumns for any evidence of quantum confinement.

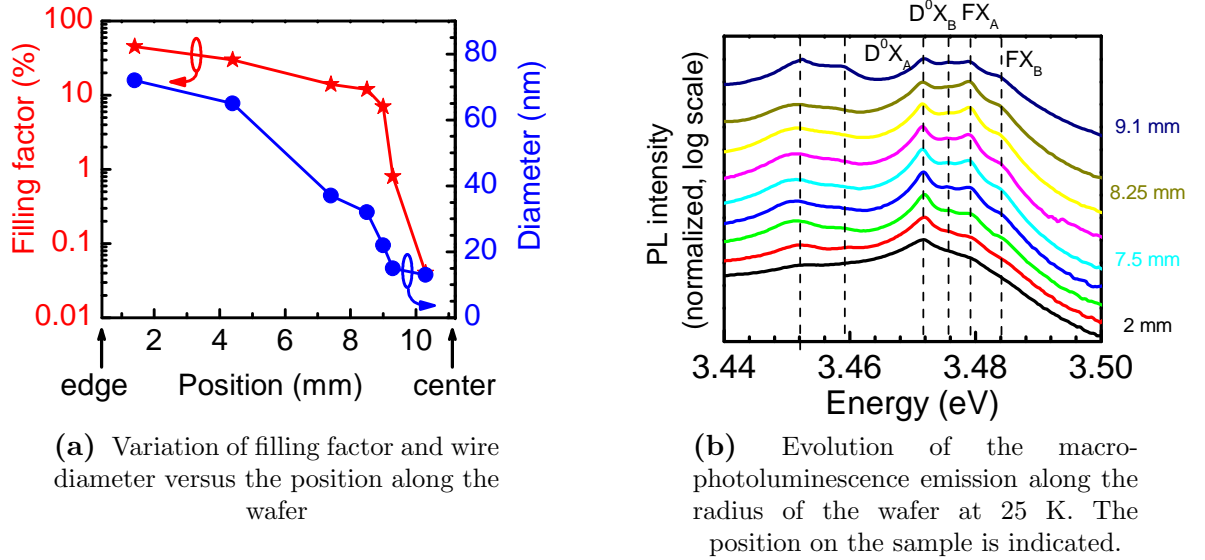


Figure 2.13 – Structural and optical characterizations on sample sample N1405

A blueshift in the order of 10 meV of the free-exciton line is expected for nanorod diameters below 15 nm⁸. We scanned the sample along the wafer radius,

⁸as discussed in 1.4.1

in order to address the different nanocolumn diameters available on this sample. The study was performed with the macrophotoluminescence setup at 25 K, which is the ideal temperature to study the free-exciton recombination, as it becomes as intense as the donor-bound exciton, while maintaining the contribution of non-radiative recombinations low. The results are plotted on figure 2.13b, which displays the spectra with decreasing the average nanocolumn diameter from bottom to top spectrum. The contributions from both the A and B donor-bound excitons and the free excitons are clearly visible. However, no free-exciton blueshift is observed on the photoluminescence spectrum even at a wafer position of 9.1 mm, corresponding to a diameter of around 15 nm.

We therefore performed microphotoluminescence experiments as a function of the position along the wafer. The results (not shown here) were identical, *i.e.* no blueshift was obtained even when we looked for any emission at a position of 13 mm. One explanation for this observation may lay in the enhancement of non-radiative recombination channels in nanowires of smaller diameters: they may not exhibit any luminescence. As this sample results from self-assembled growth, wires are not localized on the substrate and we only acquire the spectra of luminescent zones, located thanks to our visualization setup⁹. As a consequence, our statistics on the low-diameter regions of the sample only rely on luminescent spots, which could be the nanowires of greater diameter only. This possibility is illustrated on figure 2.14. It explains why no blueshift can be observed at 9 mm, in the region where the mean diameter is 20 nm, if the nanowires of diameter smaller than 20 nm do not show any luminescence. A comparison with the distribution at 6 mm where the mean diameter is 50 nm is also depicted.

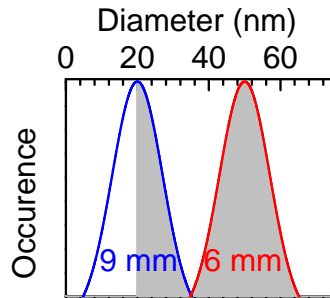


Figure 2.14 – Schematics of the nanocolumn diameter distribution at 9 mm and 6 mm (Gaussian plots) and distribution of nanowires exhibiting luminescence (shaded areas) in the hypothesis explained in the text

A second way to evidence quantum confinement is to measure the variation of the excitonic decay time with temperature. The discretization of the density of states with reduced exciton dimensionality leads to less efficient thermalisation processes than in a bulk semiconductor [Aki94]. Hence the evolution of the recombination time with increasing temperature is related to the excitonic dimensionality. More precisely, the theory predicts: $\tau_{3D} \propto T^{3/2}$, while $\tau_{2D} \propto T$, and finally $\tau_{1D} \propto T^{1/2}$. Note that this regime is observable only in the temperature range where non-radiative recombinations can be neglected.

⁹More details about our micro-photoluminescence experiment can be found in page 200.

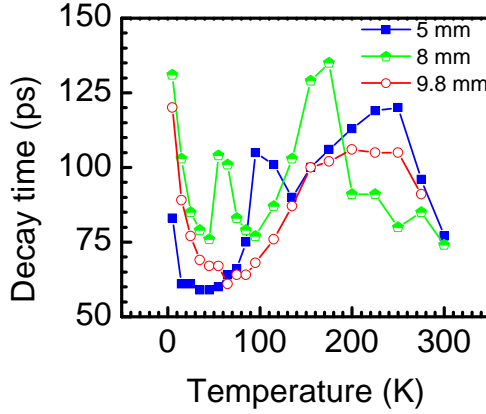


Figure 2.15 – Evolution of the decay time of the free exciton line with temperature at different spots on the sample. At 5 mm, the diameter is around 60 nm. It is 35 nm at 8 mm and 15 nm at 9.8 mm.

Figure 2.15 gives the dependence of the free exciton decay time when increasing temperature, at different spots on the sample, corresponding to various mean nanocolumn diameter. In our case, probing the decay times versus temperature at different spots on the sample leads each time to the same decrease from 4 to about 50 K. Yet this is the temperature range where a quantum effect could be observable because non-radiative recombinations are expected to be low. Then, it increases up to 150 - 200 K, due to the population of non-radiative states, enhanced by thermal energy. In this temperature range, the theory predicts that the increase of the decay time varies differently, depending on the exciton dimensionality. This is not observed experimentally. The last drop up to 300 K may be due to non-radiative recombinations.

Coming back to the behaviour at low-temperature, the reasons why no visible variation of the decay time depending on the nanocolumn diameter may be various. We may not reach the three to one-dimensional regime because the smallest nanowires studied are still too large: the splittings of the excitonic states may still be too small compared to thermal energy. Otherwise, we may not reach the one-dimensional regime because the smallest nanowires do not show any luminescence, as already suggested previously by continuous-wave experiments. Non-radiative processes may become dominant when the diameter decreases. Yet, if these recombination channels are preminent, they must be so from 4 K to 300 K. Indeed, the measured decay time do not monotonously decrease with increasing temperature, which is the trend we would expect for thermally-activated recombination channels.

Moreover, the small valence band splittings — the A and B valence bands are split by 3 meV, equivalent to a temperature of 40 K — may distort the resulting data. Indeed, if the A, B, and C excitons do not have the same oscillator strength, as the weight of each contribution changes a lot between 4 K and 300 K, we may actually measure a combination of several excitonic bands. This effect should be considered mainly in the high-temperature part of the graph.

A confusion between donor-bound exciton and free-exciton may also appear. When we aim at measuring the decay of the free-exciton, we actually measure a convolution of both at most of the useful temperature values: *at low temperature, the free-exciton decay*

time is hindered by that of the donor-bound exciton due to its too low intensity. This could induce errors in the low-temperature part of the graph and explain the initial decrease of the decay time between 4 and 50 K. This hypothesis is corroborated if one remembers that at 30 K, both free-exciton and donor-bound exciton populations are comparable: their intensity are indeed similar, as pointed out on figure 2.13b.

From the initial decrease of the free-exciton decay time at low temperature and the absence of blueshift in continuous-wave experiments, the most probable hypothesis lies in *non-radiative recombination channels that would already be active at 4 K in smaller nanowires*.

2.4.2 Fabricating quantum wires

Our first attempt to demonstrate quantum confinement with “small” as-grown nanowires on a temperature-gradient sample failed. Therefore we decided to decrease their diameter after they were grown in the standard conditions¹⁰. In the nitride community, it is known that GaN can *decompose under ultra-high-vacuum in a MBE reactor, if the sample is heated around 800°C*. Indeed, directly after the growth of a nanocolumn sample, it was possible to decrease the nanorod diameter by keeping the substrate heated at the same temperature and stopping the atomic fluxes¹¹. Figures 2.16(a) and 2.16(b) show the as-grown sample with no further post-growth treatment, while figures 2.16(c) and

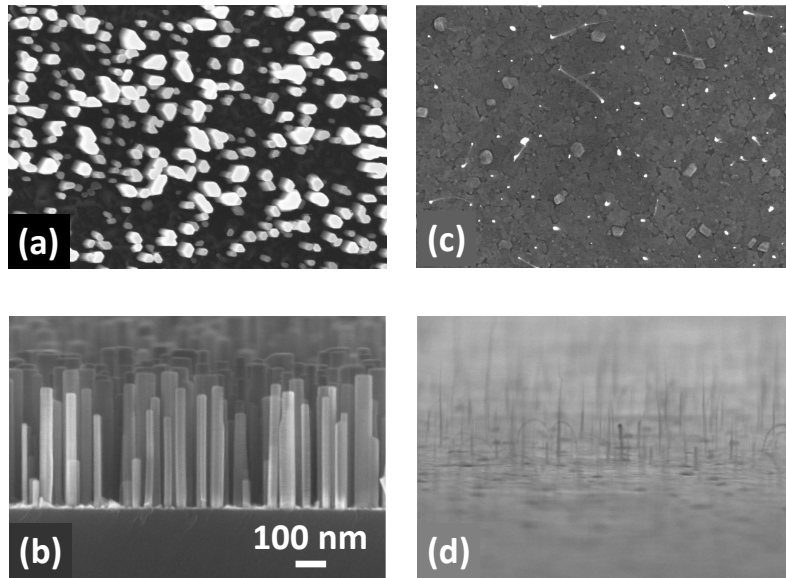


Figure 2.16 – SEM picture of top and side view of GaN nanowires: (a), (b) as-grown and (c), (d) after heated two hours in the MBE chamber - sample N1880-A and -C - courtesy R. Estivill

We performed macrophotoluminescence on this sample. The spectrum is depicted

¹⁰as those depicted in 2.1.1

¹¹This experiment was performed by Robert Estivill

on figure 2.17. The signal is very weak — around a factor 10^4 lower than that of as-grown sample (not shown here), but we observe an emission above the GaN bandgap, centered at 3.7 eV (corresponding to a diameter of 8 nm according to our calculations¹²). This emission can be attributed to the photoluminescence of quantum wires. In these nanorods, the excitonic center-of-mass should be confined. The 800-meV linewidth may due to inhomogeneous broadening: as can be seen on figures 2.16(c) and (d), the distribution in diameter is large. Note that an emission was measured at an energy as high as 4 eV, corresponding to a diameter of 5 nm¹². However, we did not find any satisfactory explanation accounting for the emission below the band gap of "bulk" GaN; these results are only preliminary. Furthermore expect the emission from a single quantum wire to be sharper: it would have to be confirmed by microphotoluminescence measurements on single nanorods.

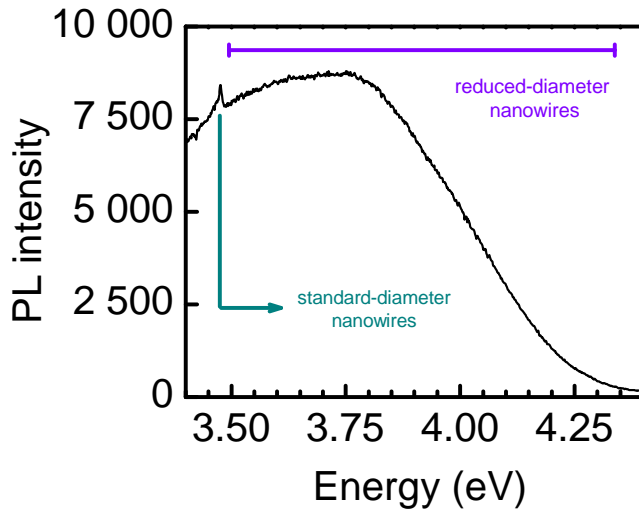


Figure 2.17 – Low-temperature macrophotoluminescence spectrum of an ensemble of GaN nanowires grown in standard conditions by PA-MBE, heated during one hour around 800°C. The near band edge of the reduced-diameter nanowires, as well as that of the standard-diameter nanorods, are clearly observable - sample N1880B - courtesy R. Estivill

Conclusion

It seems that growing nanowires small enough so that excitonic confinement is observable will be difficult. However, a post-growth method has been validated: it consists in the decomposition of GaN at high temperature and under ultra high vacuum. Preliminary experiments have shown an emission above the GaN bandgap and are thus promising results.

2.5 Optical properties of cubic GaN nanowires

When growing GaN / InGa_N / GaN axial heterostructures in nanowires, it is necessary to lower the growth temperature of the capping GaN barrier in order to prevent the decomposition of InGa_N [Tou12]. Our team thus investigated the properties of GaN

¹² see figure 1.13, chapter 1

grown at low-temperature on top of GaN nanowires grown under usual conditions. We discovered that this low-temperature GaN exhibited a cubic lattice.

We have seen in 1.1.3 and in 1.3.2 that cubic GaN presents interesting properties because of the absence of spontaneous polarization. Yet growing a high-quality zinc-blende GaN layer is a challenge. In order to grow two-dimensional zinc blende GaN, zinc blende substrates must be used, and the temperature should be lowered. As mentioned in [Zyw98], this is a metastable phase compared to its wurtzite counterpart — which is the thermodynamically stable phase — but it can be favoured kinetically. The first possibility is to lower the temperature and choose a flux ratio so as to obtain a nitrogen excess [Zyw98]. We will see that this is the case here, since the V/III flux ratio remained unchanged after the prior growth of usual wurtzite nanowires, the only changed parameter being the temperature. One can also use the growth temperature usually chosen to grow wurtzite GaN with peculiar Ga-rich conditions, ensuring a very smooth surface (low substrate roughness and low growth rate) [Dau98]. However, the crystalline quality of bulk material is limited by hexagonal phase inclusions, a large dislocation density and strain inhomogeneities. Hence, the best full width at half maximum reported until now was 5 meV [Yag98] on a heteroepitaxial layer grown by MOVPE on SiC(001). This large value does not allow to precisely probe the optical properties of this material.

The nanowire geometry gives the possibility to relax strain more efficiently and can change the relative stability of the crystalline phases. For example, bulk GaAs usually crystallizes in the cubic phase, but MBE-grown nanowires can spontaneously grow in the wurtzite phase under particular conditions [Gla07]. In nitride nanowires, Jacopin *et al.* investigated the optical properties of cubic / hexagonal crystal heterostructures in a GaN nanocolumn grown at lower temperature than the standard conditions [Jac11].

2.5.1 Cubic GaN growth and structural characterizations

After a thin AlN buffer layer, usual wurtzite GaN nanowires were grown at 850°C to form a 500-nm high base. Then the temperature was lowered to 580°C. The RHEED pattern changed significantly and exhibited additional spots typical of the GaN cubic structure. We then investigated the optical properties of this sample, confirming its zinc-blende structure.

SEM and high resolution transmission electron microscopy images are displayed on figure 2.18. We clearly see a transition phase zone containing stacking faults, but above stands a purely cubic material, being about 70-nm thick. The diameter increase results from the lower Ga atom diffusion along the facets due to the lower growth temperature. This leads to an increased lateral growth compared to axial growth. The crystalline orientations are also depicted on the TEM image.

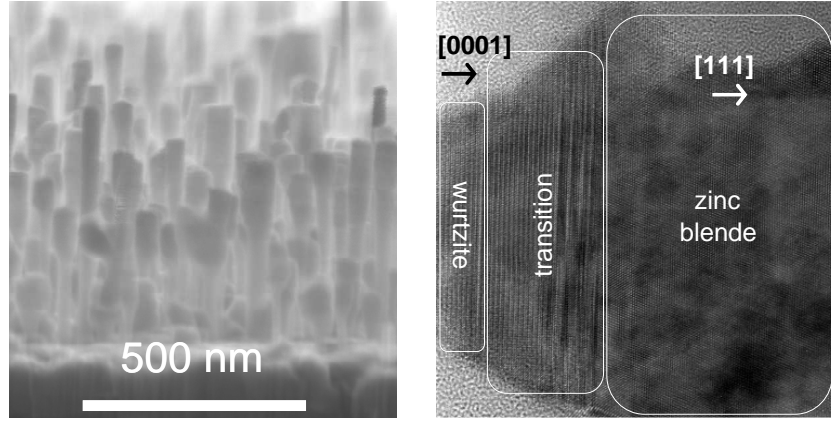


Figure 2.18 – Structural characterization of sample N1130: SEM (left) and TEM (right) images

2.5.2 Identification of bound, free and split-off exciton

The crystalline phase modification was induced by changing the growth conditions. The nanocolumn geometry allowed an efficient strain relaxation of the cubic phase. One may therefore expect better optical properties than that exhibited by two-dimensional epilayers.

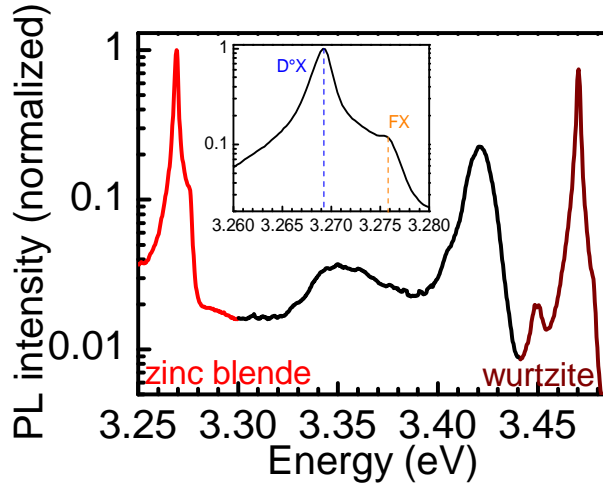


Figure 2.19 – Macrophotoluminescence spectrum at 4 K of an ensemble of cubic nanowires on top of wurtzite nanowires - sample N1130

The low-temperature photoluminescence spectrum is plotted on figure 2.19. Around 3.47 eV we can see the luminescence from the hexagonal phase near band edge (in brown) and that from the cubic GaN band edge around 3.27 eV (in red). The strong emission at 3.42 eV is associated to the recombination of excitons bound to stacking faults, originating from the intermediate part of the wires. Zooming in onto the cubic part of the spectrum (see inset of figure 2.19) allows to report the precise values of the recombination energies after careful calibrations¹³: the donor-bound exciton energy is

¹³These measurements were performed with a 1800 line/cm grating allowing for a resolution of 500 μeV and a calibration thanks to the 365.015 nm line of a mercury lamp led to a spectral accuracy of a few 100 μeV .

3.2691 eV while that of the free-exciton is 3.2757 eV. This leads to an exciton binding energy of 6.6 meV. This measurement was possible due to a low enough full width at half maximum, down to 1.6 meV on the best spots on the sample.

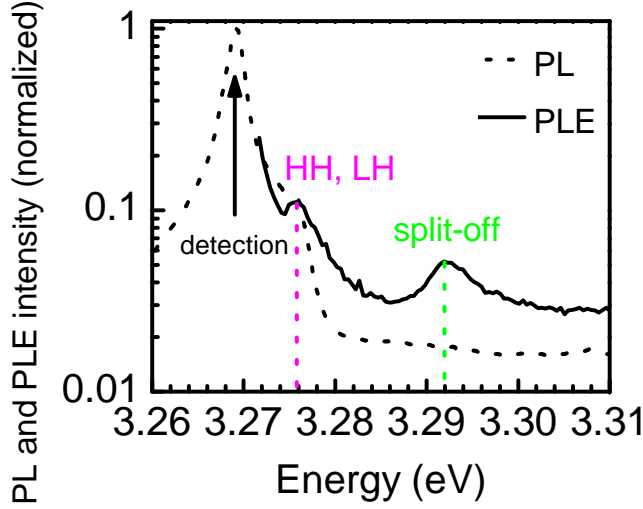


Figure 2.20 – Photoluminescence excitation spectrum at 4 K of sample N1130

Photoluminescence excitation at low temperature was also performed on this sample¹⁴. By detecting at the energy of the donor-bound exciton, we clearly resolve the free-exciton with heavy or light holes, at 3.2756 eV and the free-exciton with holes coming from the *split-off* valence band at 3.2925 eV. This gives a *spin-orbit splitting* of 16.8 meV, consistent with the value of 17 meV reported in [RF94].

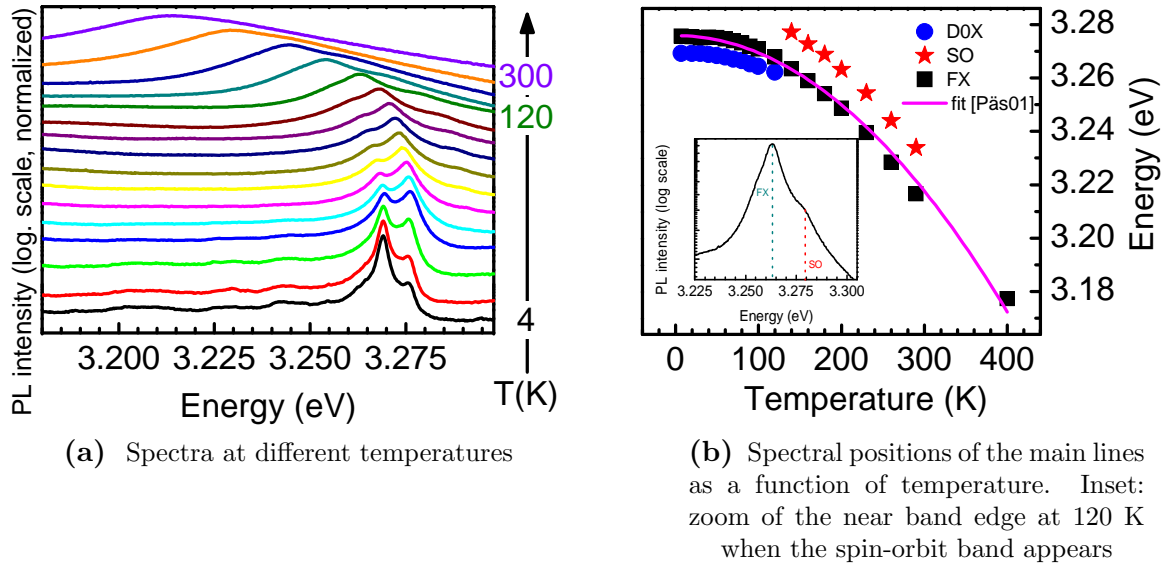


Figure 2.21 – Temperature-dependent macro-photoluminescence on sample N1130 between 4 and 400 K - D0X stands for the donor-bound excitons, SO, for the split-off band excitons, and FX for the free excitons.

The identification of the donor-bound exciton, the free-exciton from the heavy hole band, as well as the exciton from the split-off band is confirmed by temperature-

¹⁴For a setup description, please refer to page 202

dependent measurements, depicted on figure 2.21. The lower energy line (donor-bound exciton emission, blue circles in figure 2.21b) quenches above 120 K, while the upper one (free-exciton, black squares in figure 2.21b) increases with temperature. Another line appears at even higher energy with increasing temperature from 120 K and is ascribed to the split-off band. The inset of figure 2.21b shows the split-off exciton at 120 K. A good agreement was obtained when fitting the data with this formula [Päs01] (giving more accurate results for nitride materials than Varshni's law):

$$E_{FX}(T) = E_{FX}(0) - \frac{\alpha\Theta}{2} \left[\left[1 + \frac{\pi^2}{6} \left(\frac{2T}{\Theta} \right)^2 + \left(\frac{2T}{\Theta} \right)^4 \right]^{1/4} - 1 \right] \quad (2.1)$$

with parameters $E_{FX}(0)=3.2757$ eV, $\alpha=0.55$ meV K⁻¹, and $\Theta=650$ K.

2.5.3 Luminescence enhancement with laser exposure

In some experiments we conducted at a usual low power (around 1 W/cm²), the excitonic lines originating from the cubic phase were hardly measurable. In other measurements, on the contrary, the intensity of the cubic lines were comparable to that of the wurtzite phase. This strong intensity variation was understood when we discovered that *a strong enhancement of the emission from the cubic excitons has actually been observed under either low-power prolonged exposure or high-power fast exposure to the 244 nm laser excitation*. The result of a systematic dose-depending study, varying either exposure time or power density on the same spot of the sample, is shown in figure 2.22.

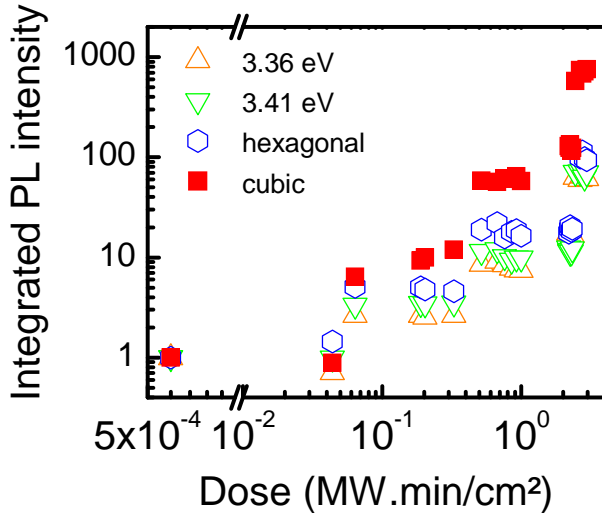


Figure 2.22 – Microphotoluminescence integrated intensities normalized to the first value of donor-bound excitons from both the cubic and the hexagonal phases, excitons bound to stacking faults and emission at 3.36 eV at 4 K, versus laser dose, normalized to their values at lowest dose. The unit W.min/cm² was used in order to be comparable to an instantaneous surface excitation power - sample N1130

The micro-photoluminescence experiment was performed as follows: first, alignment was performed on a first sample spot. Then, another unexposed spot was chosen and exposed at very low power. Luminescence spectra were recorded periodically. As no saturation was found after a few hours, power was increased further several times in this manner. We stopped the experiments when saturation was observed. It seems that this

process is reversible after temperature is increased to room temperature and decreased again.

We compare in figure 2.22 the luminescence enhancement of all the contributions presented in figure 2.19. They are all sensitive to intense UV exposure dose, but the emission from the cubic phase increases by a factor of 1000 whereas the hexagonal part, as well as the excitons bound to stacking faults and the emission at 3.36 eV only increase by a factor of 100.

Schlager *et al.* were the first to report the luminescence enhancement of wurtzite GaN nanocolumns under UV exposure [Sch06]. The enhancement was more pronounced for free excitons than bound excitons. An intense exposure finally led to a decrease of the intensity of the whole spectrum. However, in the same way than what we observe, this phenomenon was reversible with temperature.

The luminescence enhancement of GaN nanowires with UV exposure was the main topic of a recent paper [Pfü10]. The authors reported on an increase by a factor of 5 of the intensity of the donor-bound exciton and 2.5 in that of the 3.45 eV line after a 90 minute long exposure to a low-power He-Cd laser. The phenomenon happens whatever the temperature, as long as the sample is kept under vacuum. This led them to ascribe this enhancement to oxygen desorption. We performed this experiment only at helium temperature: therefore, we cannot check that the observed phenomenon also originates from oxygen desorption.

It has to be mentioned that the results presented on zinc-blende nanowires were preliminary. Due to the sample degradation with time and the non-reproducibility of the growth of such a sample, it was impossible to perform them again. Yet it was originally and qualitatively observed on the whole sample. Note that some nanorod samples made of hexagonal GaN also exhibited this intensity enhancement with exposure as reported in [Pfü10], while the majority of them did not. It thus seems that, depending on the growth conditions or the ambient where a sample is stored in the laboratory, some nanorods are more sensitive than others. This observation should be correlated to different surface states, which do not evolve in the same way with time. The main time-sensitive process one can think about is oxidation. More detailed studies have to be performed regarding this issue.

Conclusion

We made use of GaN nanowires as nano-substrates to grow zinc-blende GaN nanorods. Thanks to an efficient strain relaxation allowed by the one-dimensional geometry, the best GaN cubic material ever, in terms of optical properties, has been grown. This enabled to measure accurately both the donor-bound exciton binding energy and the spin-orbit splitting. A strong enhancement of the intensity of the luminescence of the zinc-blende was observed with UV laser exposure, attributed to a modification of surface states.

The mysterious emission at 3.45 eV

IN THE PREVIOUS CHAPTER, we have shown that MBE-grown GaN nanowires exhibit excellent optical properties, with a spectral position and linewidth of the donor-bound exciton recombination showing that the material is relaxed and homogeneous. However, one of their main spectroscopic feature is still a subject of discussion by the community: the unknown nature of the emission at 3.45 eV observed on low-temperature photoluminescence spectra. After a summary of the state of the art concerning this optical line, illustrating its controversial nature, the results of polarization- and magnetic field-dependent photoluminescence experiments will be described. The cases where this recombination disappears, as well as the cases where it is enhanced (mainly by decreasing the density), will be discussed. Eventually, its recombination dynamics will be compared to the other features composing the near band edge.

Contents

3.1	State of the art: the controversy	70
3.2	Polarization of this line	72
3.3	Magnetophotoluminescence experiments	73
3.3.1	Magneto-optical measurement of the line at 3.45 eV	76
3.3.2	Magneto-optical properties of bound excitons	77
3.4	Mechanisms responsible for a quenching of the 3.45 eV transition	80
3.4.1	Variable emission from wire to wire	80
3.4.2	Consequences of p-doping	81
3.4.3	Orientation of the silicon substrate	82
3.4.4	Influence of the growth techniques	82
3.5	Influence of the nanocolumn density on the intensity of the emission at 3.45 eV	83

3.5.1	Growth conditions and optical results	84
3.5.2	Discussion	88
3.6	Influence of the nanocolumn density on the decay dynamics of the near band edge	92
3.6.1	Preamble on decay time measurements	93
3.6.2	Decay dynamics of dense GaN nanowires	93
3.6.3	Variation of the spontaneous emission rate	95
3.6.4	Results	96
3.6.5	Discussion and perspectives	97

3.1 State of the art: the controversy

In bulk GaN, the line at 3.45 eV has been attributed to a *two-electron satellite of the donor-bound exciton* [Fio97]. A two-electron satellite has the same initial state as the donor-bound exciton (depicted on figure 3.1a) but it leaves one electron in an excited state of the donor orbitals (see figure 3.1b).

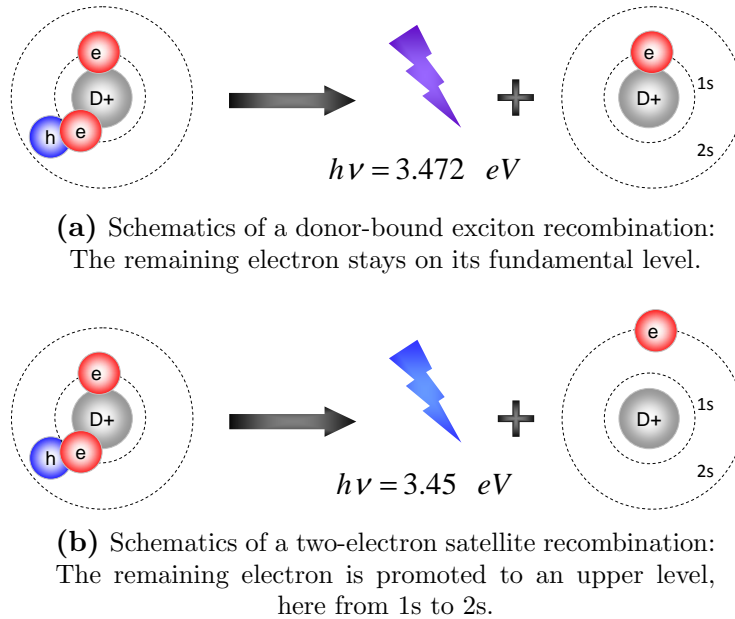


Figure 3.1 – Schematics of donor-bound exciton and two-electron satellite recombinations

In the spectra of GaN nanowires, the first mention of the peak at 3.45 eV in the literature was achieved by Calleja and coworkers [Cal00]. They observed that the emission is centered at 3.45 eV but is actually a doublet of two lines, one at 3.452 eV and another at 3.458 eV, which gives the same splitting as between the A and B valence bands. Furthermore, they also report that the relative intensity of the

3.45 eV transition compared to that of the donor-bound exciton increases either when the nanocolumn density or the diameter is decreased [Cal00]. According to Calleja *et al.*, this peak appears when GaN nanowires are grown on Si (111) as well as on sapphire [Cal00]. Finally, the authors observed that the two components shift neither with power nor with temperature, so that the energy difference of the doublet remains constant [Cal00]. Their intensity drops around 50 K, the temperature at which the donor-bound exciton also quenches: they concluded that the emission at 3.45 eV is an excitonic feature coming from both the A and B bands [Cal00].

In nanowires, the first study solely dedicated to this line in the literature was performed by Corfdir *et al.* [Cor09], and consisted in time-resolved photoluminescence measurements fitted to a model taking into account core (or “bulk”, inner part of the column) and surface donor-bound excitons with different recombination times. Assuming that the line at 3.45 eV is a two-electron satellite, this model explained well the slower dynamics of the 3.45 eV recombination compared to the “bulk” donor-bound exciton and the intensity ratio of both peaks. *Corfdir and coworkers ascribed the 3.45 eV emission from nanowires to a two-electron satellite, with an intensity enhancement due to surface effects.* One year later, the same team proposed that the 3.45 eV transition is intrinsic to the nanocolumn surface [Lef11]. Lefebvre *et al.* indeed reported that its relative intensity increases relatively to that of the donor-bound exciton when the growth conditions lead to fewer coalescence and more isolated wires [Lef11].

However, this assignment has already been questioned. Brandt *et al.* [Bra10] only stated the hypothesis that the 3.45 eV emission is due to excitons bound to “an abundant surface defect”. They stressed that, when increasing the excitation power, the intensity of this line increases linearly whereas the intensity of the donor-bound exciton emission shows a quicker saturation, following the initial linear power-dependence.

Moreover, similarly to what was observed on zinc-blende nanowires in 2.5.3, Pfüller *et al.* [Pfü10] noticed that UV exposure under high vacuum conditions leads to an intensity increase of both the donor-bound exciton line and the 3.45 eV emission, attributed to oxygen desorption. They confirmed by time-resolved photoluminescence measurements that oxygen desorption enhanced by UV exposure gives rise to positive charges at the surface of the nanowires, which decrease the electric field¹ along the nanocolumn diameter. As a consequence, the increased overlap between electrons and holes allows a decrease of the decay time of both transitions and thus an enhancement of the integrated intensity. The less pronounced increase of the intensity of the 3.45 eV emission compared to that of the donor-bound exciton shows that the 3.45 eV line is less sensitive to an increase of electric field than the donor-bound exciton one. This observation rules out the possibility of a surface donor localization of the 3.45 eV transition. Indeed, if the 3.45 eV line originated from the surface, one should expect it to be more sensitive to the

¹described in 1.4.2

reduction of the band bending than the donor-bound exciton, because the band bending is maximum at the vicinity of the surface. Let us note that this result rules out the identification of this line as originating from a defect located close to the *surface* only, and not the two-electron satellite hypothesis itself. But this result is in contradiction with the first hypothesis, suggested by the same team, the same year (2010), of an “abundant *surface* defect” [Bra10].

In this context, we have sought to evaluate the values of the physical features of this line and to compare them with the well-known values of the GaN bulk two-electron satellite line. We first studied the polarization of the 3.45 eV emission, and then its magneto-optical properties.

3.2 Polarization of this line

A schematics of the geometry chosen for the polarization-dependent photoluminescence experiment is given in figure 3.2².

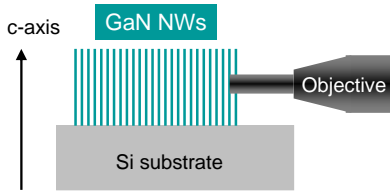


Figure 3.2 – Schematics of the polarization-dependent microphotoluminescence experiment of an array of as-grown GaN nanowires

Figure 3.3 shows the result of the polarization-dependent microphotoluminescence measurements. The *degree of polarization DOP* is defined as:

$$DOP = \frac{I(E \parallel c) - I(E \perp c)}{I(E \parallel c) + I(E \perp c)} \quad (3.1)$$

We clearly see that the donor-bound exciton emission, which appears at 3.472 eV, is polarized perpendicular to the \vec{c} axis with a *DOP* of 0.80, which is the symmetry expected for an A-band exciton³. The discrepancy compared to a polarization purely perpendicular to the \vec{c} axis (*DOP* =1) can be ascribed to photon diffusion inside the nanocolumn layer, which is rather rough. It can also be attributed to the misverticality of the nanowires: in the geometry described on figure 3.2, only the first nanorods closest to the edge of the sample are probed. Due to prior sample manipulations, the axis of the nanowires closest to the sample edge is often tilted. Note that the imperfections of the $\lambda/2$ waveplate we used, as well as any other depolarizing elements from our setup can also account for a depolarization of the order of 5%.

On the other hand, *the dipole of the 3.45 eV line is rather polarized parallel to the*

²More details on this setup are provided on page 200.

³ see table 1.6 for calculated matrix elements

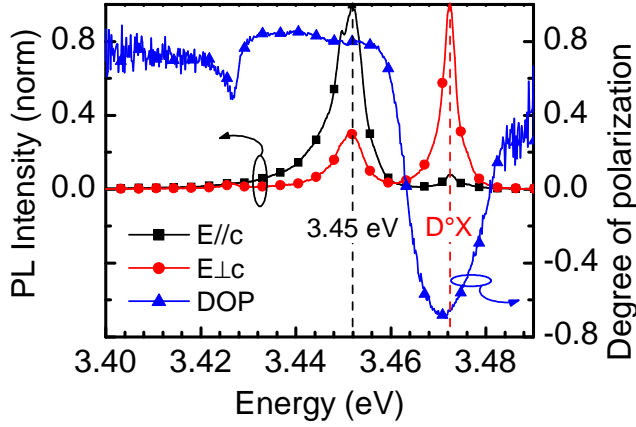


Figure 3.3 – Normalized intensity of the low-temperature microphotoluminescence emission with polarizer parallel (black line) and perpendicular to the \vec{c} axis (red lines) and resulting degree of polarization - courtesy J. Renard

\vec{c} axis, with a *DOP* of 0.67. Is this \vec{c} polarization intrinsic to this transition, or is it due to the dielectric environment, *i.e.* the nanorod geometry? We must keep in mind that the nanocolumn geometry favors the emission of an isotropic dipole in the direction of its axis, *i.e.* the \vec{c} direction [Rig10]. However, if this effect was preeminent in this experiment, one should expect the B donor-bound exciton to appear in the spectrum measured with the polarizer parallel to the \vec{c} axis. Indeed, 1/3 of its dipole³ is parallel to \vec{c} and the states of the B valence band are already populated at 4 K⁴. Experimentally, we can check that the intensity of the B donor-bound exciton is smaller in the $\vec{E} // \vec{c}$ polarization than in the $\vec{E} \perp \vec{c}$ polarization, which shows that the bulk polarization selection rules are still valid in an ensemble of nanowires.

Conclusion

A donor-bound exciton and its associated two-electron satellite have exactly the same initial state, and a final states that only differ by the state occupied by the remaining electron bound to the donor. Therefore they both follow the same selection rules, as experimentally confirmed in [Pas07]. The observation of a polarization mainly perpendicular to that of the A donor-bound exciton is a first proof that the line at 3.45 eV cannot be ascribed to a two-electron satellite originating from the A exciton.

3.3 Magnetophotoluminescence experiments

One of the peculiarities of a two-electron satellite is its high sensitivity to both magnetic fields perpendicular and parallel to the \vec{c} axis [Wys02]. A good way to compare the electronic properties of the emission at 3.45 eV with that of the bulk two-electron satellite is indeed to probe its behaviour under intense magnetic field. This section

⁴as depicted on figures 2.4b and 2.6b

reports our measurements of some intrinsic electronic features of the line at 3.45 eV in GaN nanowires, such as its gyromagnetic splitting and diamagnetic shift.

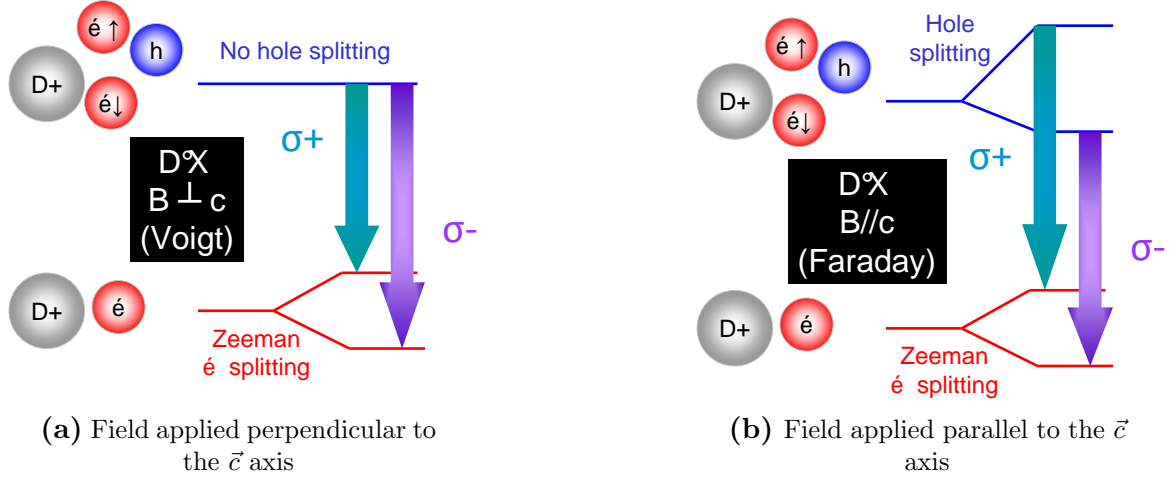


Figure 3.4 – Expected splittings for the donor-bound exciton recombination from A valence band depending on the direction of the magnetic field

We first provide some theoretical details on the experiments and on the *Zeeman splitting* of an optical excitonic line. Figure 3.4 explains the consequences of a magnetic field on a bound exciton recombination, taking that of the A donor-bound exciton as an example. The initial state contains one exciton bound to a neutral donor. Of both electrons, one is spin up and the other is spin down. Their spin state thus does not split, whatever the direction of an applied magnetic field. When the field is applied perpendicular to the \vec{c} axis (*Voigt configuration*), the energy of the hole in the A valence band does not split either due to the symmetry of the A valence band. The final state contains one remaining electron, whose energy level splits. When the field is applied parallel to the \vec{c} axis (*Faraday configuration*), the state of the hole from the initial state splits. So does the state of the electron from the final state. When the field is applied parallel to the \vec{c} axis, there are two possible initial states and two possible final states, which result in four possible lines (see figure 3.4, right panel). Yet, due to symmetry conservation, only two of them are not forbidden. In both configurations, the spectral position of both resulting lines is given by:

$$E = E_0 \pm \frac{1}{2}g\mu_B B + DB^2 \quad (3.2)$$

where g is the *gyromagnetic factor* which accounts for the splitting (first order) and D is the *diamagnetic factor* which describes the amplitude of the shift (second order) of a line when a magnetic field is applied. From the previous discussion and figure 3.4, we can conclude that in the Voigt configuration, the gyromagnetic factor of the transition will be $g_{D0X\perp} = g_{e\perp}$ where $g_{e\perp}$ is the electronic gyromagnetic factor. In the Faraday configuration, $g_{D0X//} = g_{e//} - g_{h//}$ where $g_{e//}$ and $g_{h//}$ are the electron and hole

gyromagnetic factor in Faraday configuration, respectively. A wider splitting is thus expected in the Voigt configuration.

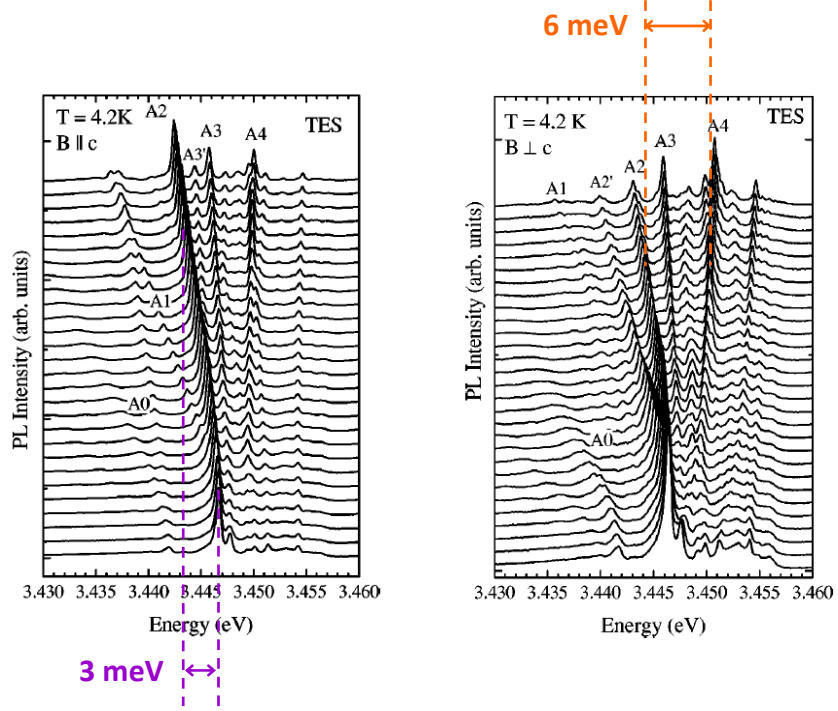


Figure 3.5 – Low-temperature two-electron satellite emission of an homoepitaxial layer for Faraday (left) and Voigt (right) configurations with field varying from 0 to 28 T (extracted from [Wys02]). The diamagnetic shift (respectively splitting) between 0 and 22 T is evaluated in the Voigt (respectively Faraday) configuration.

Let us come back to the evolution of the two-electron satellite lines when a magnetic field is applied. The results of Wysmolek *et al.* are reproduced in figure 3.5, displaying the scan of the photoluminescence around 3.45 eV for a magnetic field varied between 0 and 28 T. Between 0 and 22 T (which is the maximum magnetic field we have used during our own experiments):

- in Faraday configuration (left plot), when $\vec{B} // \vec{c}$, the two-electron satellite splits into several lines. The most intense A2 shows a redshift of 3 meV between 0 and 22 T.
- in Voigt configuration (right plot), when $\vec{B} \perp \vec{c}$, the two-electron satellite also splits into a variety of lines. The two most intense, A2 and A4, exhibit a splitting of 6 meV at 22 T.

We are thus going to probe the line at 3.45 eV observed in the spectra of MBE-grown nanowires, and see if it exhibits such clear signatures of a two-electron satellite.

3.3.1 Magneto-optical measurement of the line at 3.45 eV

First, we apply the magnetic field perpendicular to the \vec{c} axis of the crystal (Voigt configuration) and measure the magnetophotoluminescence on an ensemble of GaN nanowires grown in standard conditions⁵. Figure 3.6a displays the resulting photoluminescence and compares the spectra obtained at 0 T (blue circles) and 22 T (red stars). The donor-bound exciton line exhibits a splitting which will be analyzed in section 3.3.2. However, we evidence no splitting of the line around 3.45 eV.

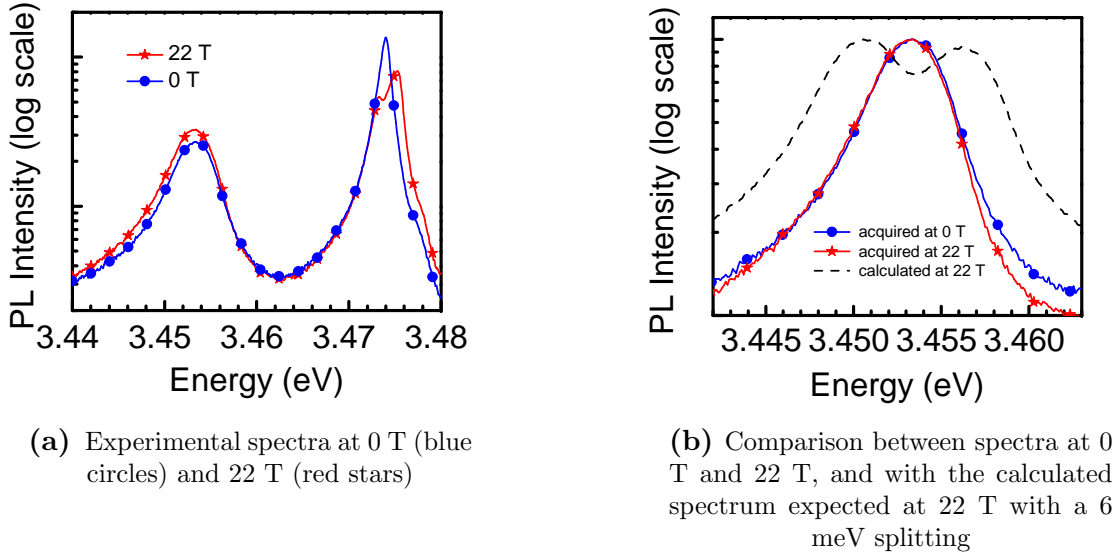


Figure 3.6 – Low-temperature macrophotoluminescence emission of an ensemble of GaN nanowires in Voigt configuration with field varying from 0 to 22 T

To better compare our results at 3.45 eV with the expected behaviour of a typical two-electron satellite, we present in figure 3.6b two experimental spectra and a simulated one. The experimental ones are the two spectra of figure 3.6a zoomed around 3.45 eV. The third spectrum (dashed line) is a calculation of the expected splitting for a two-electron satellite at 22 T in the Voigt configuration, extrapolated from (i) the photoluminescence spectrum at 0 T and (ii) the typical 6-meV splitting observed in figure 3.5 (right panel) on the two-electron satellite line. The comparison between extrapolated and experimental plots at 22 T is striking. Despite the broad 5-meV linewidth of the emission at 3.45 eV, a splitting of 6 meV would be clearly observed if it originated from a two-electron satellite. The absence of any splitting at this energy is thus a second proof against the two-electron satellite hypothesis.

We also carried out measurements with an applied magnetic field parallel to the \vec{c} axis. Figure 3.7a shows the behaviour of both the donor-bound exciton and the 3.45 eV lines in Faraday configuration. This time, we clearly see neither splitting nor shift of the donor-bound exciton and of the 3.45 eV line. However, the shift observed in the literature

⁵as described in 2.1.1

on free-standing GaN samples on the two-electron satellite line in this configuration is clear. From 0 to 22 T, a 3 meV redshift was observed (figure 3.5, left panel).

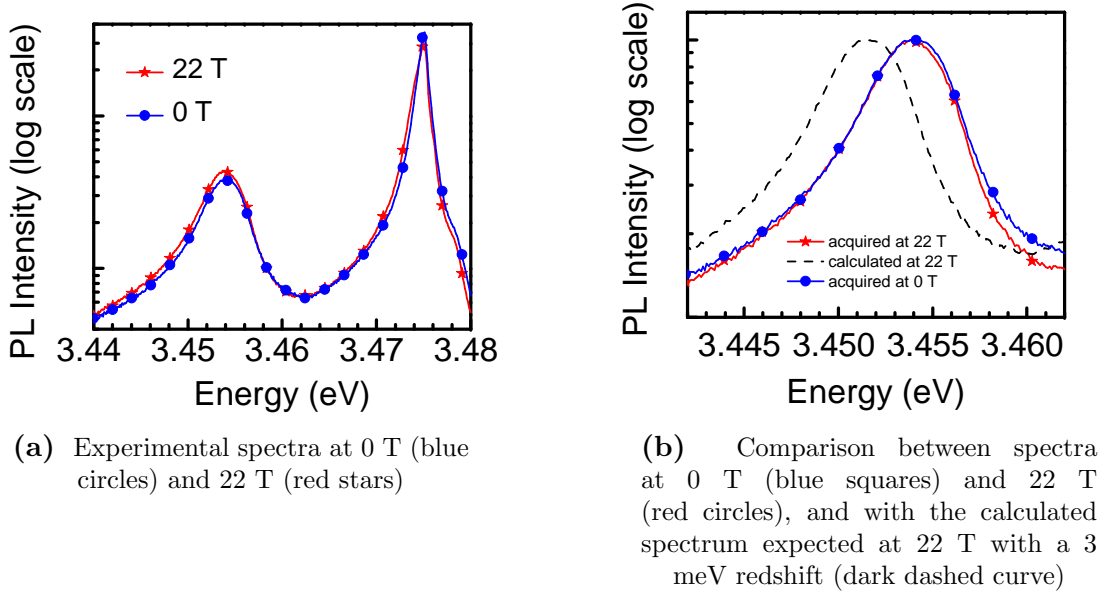


Figure 3.7 – Low-temperature macrophotoluminescence emission of an ensemble of GaN nanowires in Faraday configuration with field varying from 0 to 22 T

We used this value to simulate the shift we should observe on our samples by extrapolating the photoluminescence spectrum acquired without magnetic field. Both experimental spectra at 0 and 22 T, as well as the extrapolated one at 22 T, are plotted on figure 3.7b. One can see that, despite the broad linewidth of the two-electron satellite recombination, a 3 meV redshift would be clearly measurable if the line at 3.45 eV was a two-electron satellite. The total absence of shift in the 3.45 eV line originating from nanowires shows that, again, the 3.45 eV line cannot be a two-electron satellite.

3.3.2 Magneto-optical properties of bound excitons

We observed that the emission at 3.45 eV in nanowires does not behave like a two-electron satellite. We need to confirm that this discrepancy appears only at 3.45 eV and not on the whole spectrum, *i.e.* that donor-bound excitons and acceptor-bound excitons in nanowires behave as in homoepitaxial layers when a magnetic field is applied.

We already performed this measurement for the donor-bound exciton line. The spectrum for the magnetic field perpendicular to the \vec{c} axis was given in the last subsection: see figure 3.6a for the Voigt configuration. A clear measurable splitting can be observed. Figure 3.8a shows the resulting splitting of the donor-bound exciton extracted from figure 3.6a. From a linear fit, we could extract a value of the gyromagnetic factor of 1.75, which is consistent with the result of 1.87 obtained on homoepitaxial layers [Ste98].

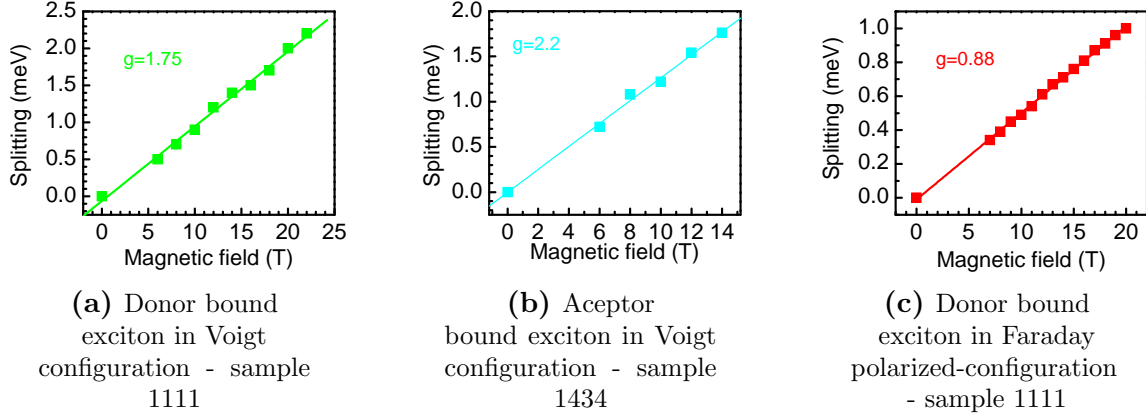


Figure 3.8 – Determination of the gyromagnetic factor of bound excitons in GaN nanowires

To get a deeper insight on the magnetophotoluminescence of bound excitons and confirm their bulk behaviour, we probed the p-doped sample already described in 2.2.2 in the Voigt geometry, for a magnetic field varying from 0 to 14 T. The spectral linewidth of this sample is at least 50% smaller than in the previous sample, therefore we were able to measure a splitting even under such a lower magnetic field. The resulting spectra are plotted in figure 3.9a. The acceptor-bound exciton exhibits a clear splitting, better observed on figure 3.9b. On figure 3.8b, we plot the acceptor-bound exciton splitting between 0 and 14 T. We report on a gyromagnetic factor for the acceptor bound exciton line of 2.2, which is again consistent with previous results on two-dimensional GaN, measuring a value of 2.1 [Ste98].

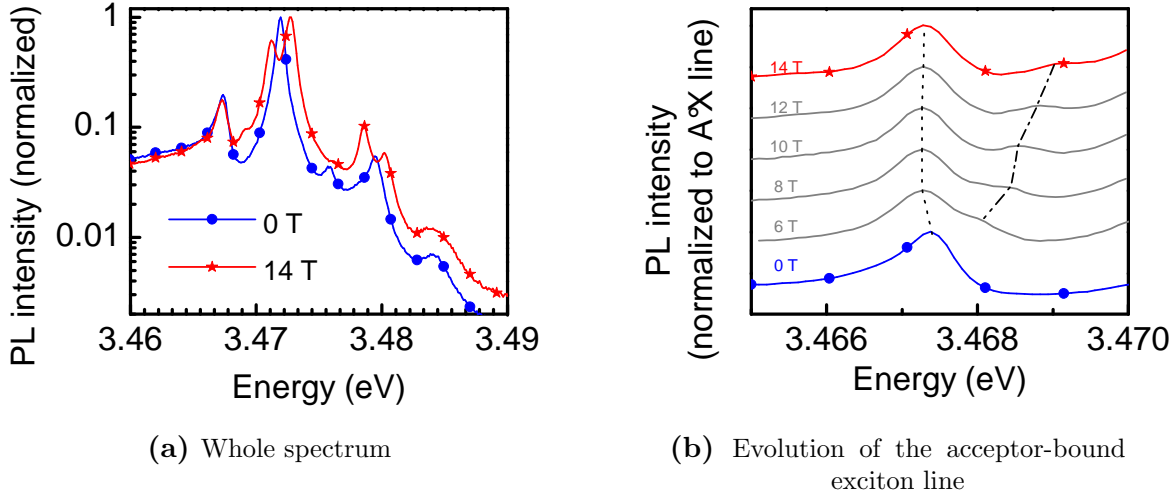


Figure 3.9 – Low-temperature macrophotoluminescence emission of an ensemble of p-doped GaN nanowires in Voigt configuration with field varying from 0 to 14 T

Yet one can argue that the results shown in the previous subsection for the magnetic field parallel to the \vec{c} axis are not convincing because no clear magnetic-field dependent signature on the donor-bound exciton either was observed (see figure 3.7a). We thus

performed additional experiments to make sure that changes could be observed in the spectra of GaN nanowires in the Faraday configuration. We used a polarizer to select either the σ^+ or the σ^- polarization of both the emission and the excitation beams. The resulting spectra are depicted on figure 3.10a: no clear change is observed between 0 T and 20 T with the polarizer in the σ^+ configuration. But, for σ^- polarization, the shape of the donor-bound exciton line changes when changing the polarization. Figure 3.8c shows the splitting extracted from figure 3.10b. The linear evolution of the splitting gives a gyromagnetic factor of 0.88, of the same order of magnitude than the value of 0.64 reported in the literature [Ste98].

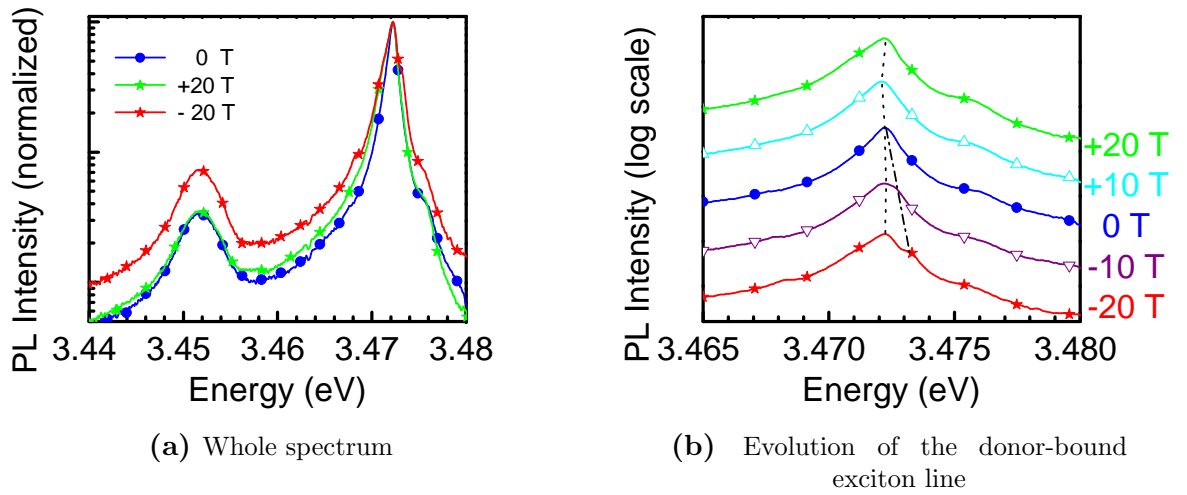


Figure 3.10 – Low-temperature macrophotoluminescence emission of an ensemble of GaN nanowires in polarized Faraday configuration with field varying from 0 to 20 T with the polarizer in the σ^+ and the σ^- configurations

The emission of bound excitons in GaN nanowires thus behave similarly to that of homoepitaxial layers when a magnetic field is applied parallel or perpendicularly to the \vec{c} axis.

Conclusion

We probed the electronic properties of the line at 3.45 eV by performing magnetophotoluminescence experiments. Again, the 3.45 eV recombination does not behave like a two-electron satellite, whatever the orientation of the magnetic field. Yet, this discrepancy is unlikely to originate from a modification of the "bulk" electronic properties of the 3.45 eV emission induced by the nanorod geometry: all bound excitons were indeed shown to behave similar to their bulk counterparts.

3.4 Mechanisms responsible for a quenching of the 3.45 eV transition

Now we can ascertain that the emission at 3.45 eV is not a two-electron satellite, it seems interesting to investigate the conditions when this line is detected and when it is not. We will investigate the occurrence of this line and compare it to that of the donor-bound exciton. The growth conditions leading either to the presence of this emission, or its total disappearance, will also be discussed.

3.4.1 Variable emission from wire to wire

We already have shown in 2.3.2 that each probed nanocolumn exhibited a unique spectrum. In this part, we will try to answer the question: is the emission at 3.45 eV present in the emission of all non-intentionally n-doped samples? Furthermore, is there a correlation between the existence of a donor-bound exciton recombination and a peak at 3.45 eV?

In figure 3.11a, we present the low-temperature micro-photoluminescence spectra of two single nanocolumns laid on a silicon dioxide substrate. The red one (open circles) shows both lines, *i.e.* the donor-bound exciton recombination and the emission at 3.45 eV. Yet on the blue one (open squares), we can only see the contribution from the donor-bound exciton. This is rather unexpected. Indeed, due to the polarization selection rules, collecting the photoluminescence perpendicularly to the axis of the nanowires is more efficient for the emission of an electric field parallel to the \vec{c} axis than for an emission with electric field perpendicular to \vec{c} . We have seen in figure 3.3 that the dipole of the 3.45 eV line was mainly parallel to the \vec{c} axis. One thus expects to better detect the 3.45 eV emission in this geometry with respect to the as-grown nanowires.

We should conclude that the transition at 3.45 eV is not intrinsic. The same conclusion has been drawn by Brandt *et al.* [Bra10]. However, one could argue that due to the high surface to volume ratio, the fact that the nanorod is lying on a substrate may affect its optical properties because of its contact with the substrate⁶.

We thus performed the same experiment on single as-grown nanowires. The measurements were performed on the sample exhibiting a density-gradient⁷, which allows to probe the luminescence of a single as-grown nanocolumn. Three different spectra corresponding to three different nanocolumns are presented on figure 3.11b. The lower (red) one is dominated by an emission at 3.42 eV, attributed to excitons bound to stacking faults [Con09], but also presents three excitonic emissions between 3.47 and 3.48 eV, attributed to three different radial donor positions as proposed by Brandt *et*

⁶see previous discussion in 2.3.2

⁷as described previously in 2.4.1

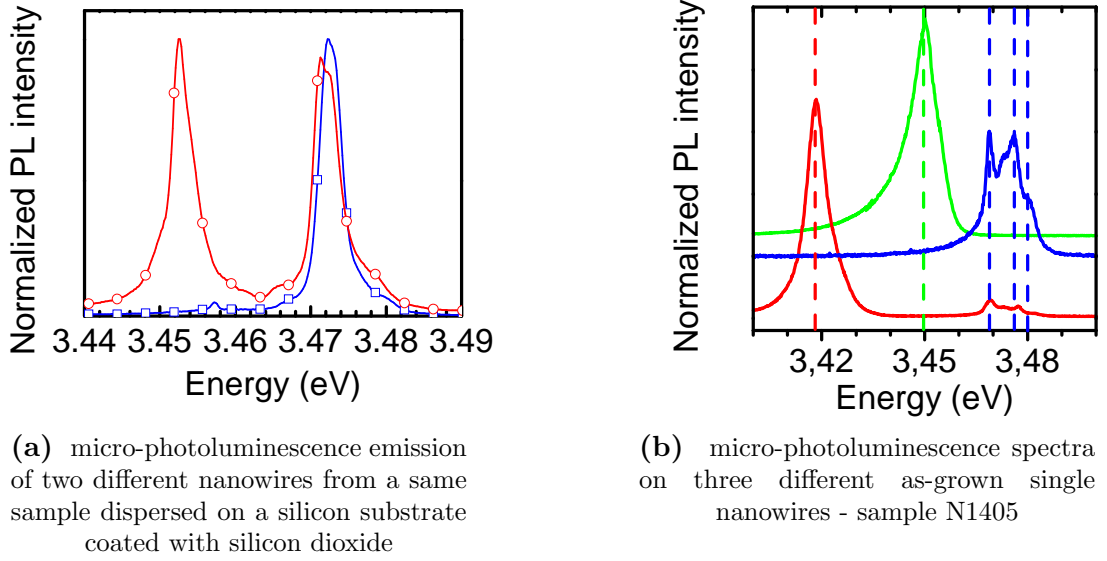


Figure 3.11 – Low-temperature micro-photoluminescence spectra of single nanowires

al. [Bra10]. The middle (blue) one shows only excitonic emissions between 3.47 and 3.48 eV. Most important, the upper (green) one only presents the 3.45 eV line.

Both experiments thus lead to the same conclusion. From the statistics we performed, some nanowires only emit at 3.45 eV without any emission from the donor-bound exciton. In other words, *we can observe the 3.45 eV emission on a wire free of any optically-active donor*. This last result rules out the two-electron satellite hypothesis again.

3.4.2 Consequences of p-doping

We have observed in 2.2.2 the total disappearance of the emission at 3.45 eV when slightly doping the nanowires with Mg, as pointed out on figure 3.12. This observation was also reported by Furtmayr *et al.* [Fur08]. On the contrary, the two-electron satellite does not seem to be affected by p-type doping: in the reference [Mon06] the authors studied a sample exhibiting an intense emission from both the two-electron satellite and the acceptor-bound exciton. Therefore both emissions from the two-electron satellite and of the acceptor-bound exciton can be observed on the same sample.

If we consider that surface states lead to the appearance of upward band bending [Cal05], optically-excited carriers should be separated: the holes will diffuse towards the surface, whereas the electrons will move towards the bulk part of the nanocolumn. Hence, donor-bound excitons will not be particularly affected by surface effects because the neutral donors will be spatially located in the bulk part only — the donors close to the surface will be ionized. The opposite is true for acceptors: in this framework, we indeed expect the acceptor-bound exciton emission to come from surface acceptors, because only these will be neutral. Hence, if the 3.45 eV emission mainly comes also from the surface, there could be a competition between both recombinations. The disappearance

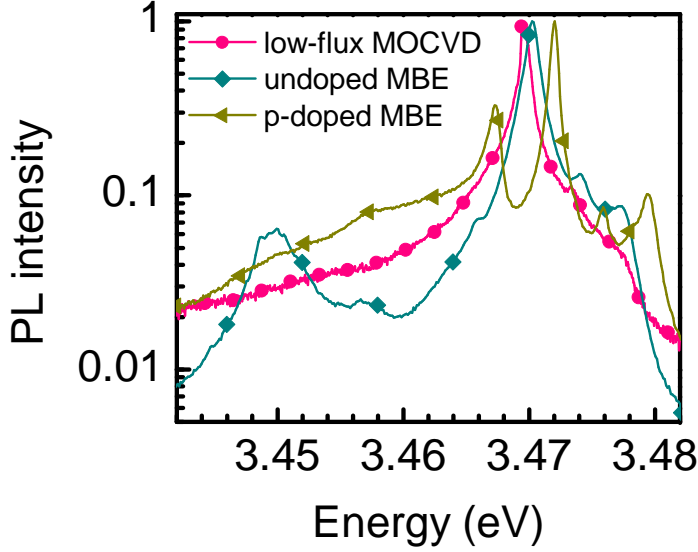


Figure 3.12 – (pink circles) Microphotoluminescence spectrum at 4 K of a single standing GaN nanowire grown by MOCVD with low-flux conditions; (blue diamonds) macrophotoluminescence spectrum at 4 K of non-intentionally doped MBE-grown nanowires; (dark yellow triangles) macrophotoluminescence spectrum at 4 K of p-doped MBE-grown nanowires

of the 3.45 eV line shows that this competition may be in favor of the acceptor-bound exciton emission.

The disappearance of the line at 3.45 eV by magnesium doping could also originate from the growth conditions. As Mg acts as a surfactant on both the [0001] and the $[1\bar{1}20]$ planes [Mon04] [Lah09], it could also behave as a surfactant on the lateral $[1\bar{1}00]$ nanocolumn facets. By changing the surface stability, the Mg incorporation could influence that of the surface defect which we assume to be at the origin of this emission at 3.45 eV.

3.4.3 Orientation of the silicon substrate

We are used to growing nanowires by MBE technics on Si(111), and to a less extent on sapphire. In both cases, the emission at 3.45 eV always appears. A statistical analysis of the spectra of about 50 as-grown nanowires [Pfü10] gives an occurrence of the 3.45 eV emission approximatively equal to one third that of the donor-bound exciton. However, several groups reported the absence or at least a decreased intensity of the recombination at 3.45 eV when the growth substrate was Si(100) compared to its intensity when the substrate was either Si(111) or sapphire [Pfü10][Gee11][Cor09][Cer06]. This observation suggests that either impurity diffusion processes or surfaces states could be varied with the epitaxial relationship between the substrate and the GaN nuclei.

3.4.4 Influence of the growth techniques

It can also be pointed out that the emission at 3.45 eV is dependent on the growth techniques. In the following, the appearance of this line will be analyzed in nanowires obtained by two methods, differing from the pure MBE we discussed up to

this point.

Another way of growing nanowires is the dual MOCVD-MBE process. GaN nanowires can be grown after nitridation of a \vec{r} -plane sapphire substrate and deposition of GaN islands, both steps performed in a MOCVD reactor prior to the MBE nanocolumn growth [Asc09]. On such samples, no emission was detected at 3.45 eV. This suggests that the first growth steps, *i.e.* the nucleation processes, must fix either the presence or the absence of the defect responsible for this transition.

As far as nanowires grown by MOCVD in low-flux conditions are concerned, we have already seen in 2.3.4 that it is possible to obtain state-of-the-art optical quality GaN nanowires. This can be achieved by decreasing the precursor fluxes, the growth being performed on a sapphire substrate. These nanowires exhibit both a diameter and a photoluminescence emission comparable to MBE-grown ones. We remind that the main difference between both emissions lies in the total absence of recombination at 3.45 eV in the spectrum of MOCVD-grown nanowires, as pointed out on figure 3.12.

In both cases — either a prior MOCVD nucleation followed by a MBE growth, or low-flux MOCVD growth — we attribute the quenching of the 3.45 eV recombination either to the MOCVD nucleation or to the higher diameter compared to MBE-grown nanorods. The diameter of the nanowires grown by Aschenbrenner *et al.* are around 400 nm [Asc09], that of the nanorods grown by low-flux MOCVD is around 200 nm. The influence of the nucleation process and the final diameter of the nanocolumns seem more relevant to explain the quenching of the luminescence at 3.45 eV than the use of a sapphire as growth substrate. Indeed, it was shown from the first publication dealing with the optical properties of GaN nanowires that MBE-growth on sapphire leads to a strong emission at 3.45 eV [Cal00].

Conclusion

Our experiments show that, depending on the nanowires we probe among a given sample and the chosen growth technique, the emission at 3.45 eV can be detected or not. It is also strongly suppressed by Mg-doping or by varying the nucleation conditions and the nanocolumn diameter. These observations suggest that it originates from a point defect

3.5 Influence of the nanocolumn density on the intensity of the emission at 3.45 eV

From the first study by Calleja *et al.*, most publications relate the 3.45 eV line to surface effects [Cal00]. Its relative intensity strongly increases when one grows samples with smaller nanocolumn density. Density is correlated to the nanocolumn diameter by the possible coalescence of dense-enough nanowires: this increases the effective

nanocolumn diameter. Yet, up to now, there has been no study analyzing all possible causes of this enhancement, which was only attributed to an increased surface to volume ratio [Lef11]. The description of two types of samples, as well as the optical measurements we performed, will first be provided. In a second part, we will analyze the results and conclude.

3.5.1 Growth conditions and optical results

In this part, the description of the growth applied in order to decrease the density of as-grown nanowires is presented, as well as the main photoluminescence results we obtained.

High-temperature growth of self-assembled nanowires

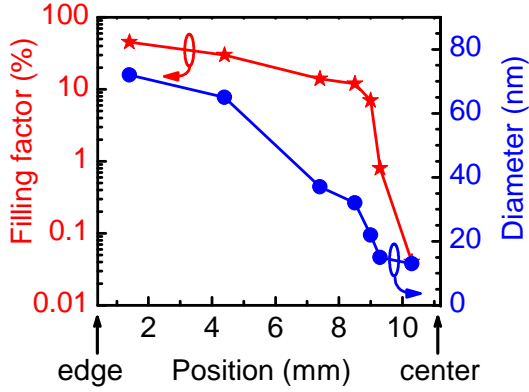


Figure 3.13 – Variation of the filling factor and the wire diameter versus the position along the wafer - sample N1405

Studying the nanowire density as a function of temperature led us to grow a sample at 850°C directly on Si(111) and with the usual N/Ga flux ratio of about 3. The growth was 13 hour long. A density gradient along the wafer radius was achieved. For more details about this sample, see 2.4. We remind that the hottest point of the wafer is located in the center due to the geometry of the sample holder during growth. As a consequence, in the center, no wire did grow at all. Close to the edges of the wafer, the nanocolumns were dense and coalesced because these are the coldest zones of the wafer. In figure 3.13 we plot the evolution of wire filling factor (defined by the area covered by GaN nanowires for a given Si surface) and diameter. At the edge of the wafer, the filling factor reaches 45% and the mean diameter is 70 nm because nanorods are coalesced. When going towards the center of the wafer, from 0 to 9 mm, both filling factor and diameter decrease smoothly. From 9 mm onwards, the decrease is sharper. No wire were observed at positions greater than 10.3 mm. Note that, when density decreases, the nanocolumn orientation is less and less perpendicular to the substrate.

We performed photoluminescence experiments at 10 K and 25 K at different positions along the radius. This sample is one of our best in terms of optical quality, as accounted

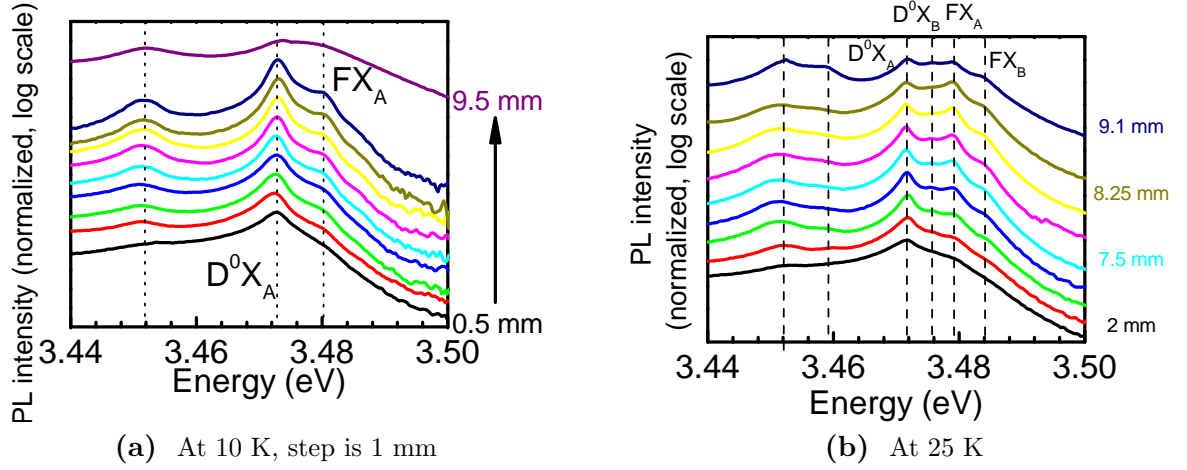


Figure 3.14 – Variation of the macrophotoluminescence emission along the wafer, *i.e.* along the temperature gradient with varying position at different temperatures - sample N1405

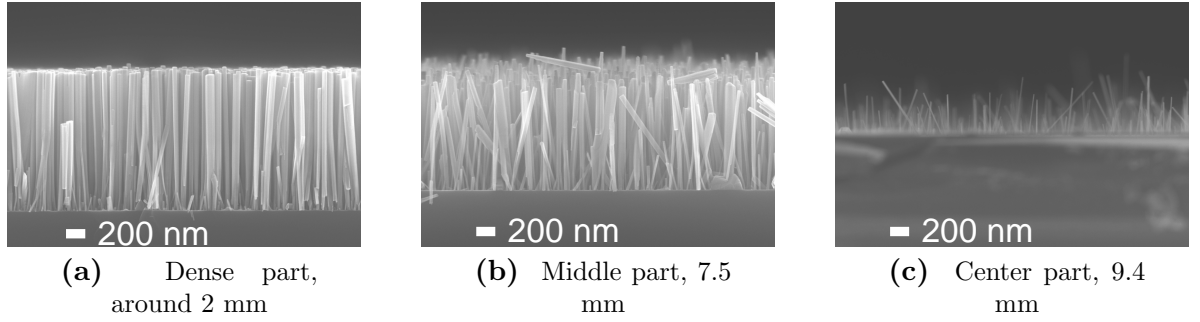


Figure 3.15 – SEM images of sample N1405 at different positions along the wafer diameter

by the linewidth of the A-donor-bound exciton, which is between 1 and 2 meV. Figures 3.14a and 3.14b show the variation of the luminescence at 10 K and 25 K, respectively, when we go from the edge (bottom spectrum) towards the center (top spectrum) of the wafer. At 10 K, the spectrum is dominated by the A donor-bound exciton, and both the A free-exciton and the 3.45 eV lines are also visible. We observe that the intensities of both the 3.45 eV line and the free exciton recombination increase compared to that of the donor-bound exciton when moving towards the center of the wafer. At 25 K, the B-donor-bound exciton, the B-free-exciton and the A-free-exciton are enhanced compared to the spectra at 10 K thanks to thermal population of these higher energy levels. The intensity enhancement of the B donor-bound exciton and of the A free exciton compared to that of the A donor-bound exciton is clearly observable on figure 3.14b. In parallel, the enhanced intensity of the recombination around 3.45 eV allows to observe two contributions split by 8 meV: a low-energy one at 3.452 eV and a high energy one at 3.46 eV which is more intense at lower density.

Selective-area plasma-assisted molecular beam epitaxy growth

Here the idea is to fix the position where nanowires must nucleate and grow by prior patterning of the substrate. The team of Pr. Kishino was the first to report selectively-grown nanowires in a PAMBE machine. In [Ish08] the authors selectively grew GaN nanowires on a Si(111) substrate with a nitridated Al hole pattern. Then, in [Sek08], the same team performed selective area growth of GaN nanocolumns on a GaN substrate with nitridated Ti mask. One year later, Seo *et al.* reported on a good selectivity with a W mask [Seo09]. However, these approaches present a major drawback: they rely on growing on GaN substrates. In this context, we aimed at developing selective-area-growth on Si. Simultaneously, the team of Pr. Calarco began the study of selective-area growth on silicon, coated by an AlN buffer layer and a SiO_x mask patterned by electron-beam lithography [Sch11]. Pr. Bertness also reported on selective-area growth of GaN nanowires through a SiN_x mask deposited on Si substrates [Ber10].

In our group, we have developed in collaboration with Siltronic and CEA-LETI a TiN / SiO_2 / Si(111) mask obtained by nano-imprint lithography, within the ANR project SINCRONE. The deposited layers were both about 20-nm thick. It consisted in ten squares exhibiting holes of different diameters, all separated by the same 500-nm distance. The mask pattern is depicted on figure 3.16 (left panel). Figure 3.16 (right panel) shows the filling factor of the column layer (a GaN homogeneous two-dimensional layer would have a filling factor of 1) as a function of hole diameter, as well as the size of the squared growth zone. The growth was performed in the standard conditions⁸ to obtain 1.5- μm long nanowires.

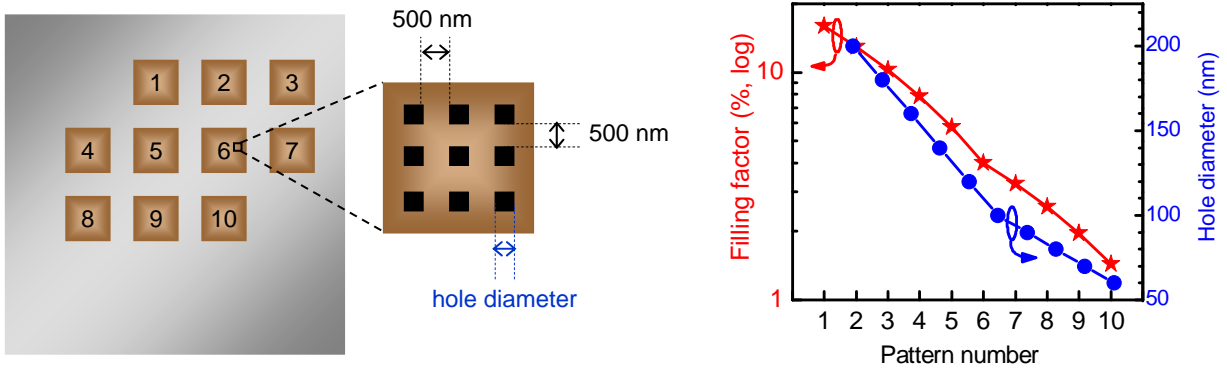


Figure 3.16 – (left) Schematics of the patterned substrate. (right) filling factor and size of the growth area on each pattern of sample N1568

Figures 3.17a, 3.17b and 3.17c display the wires grown on the various patterns. GaN nanowires with constant diameter clearly fill the entire holes, whatever their size: if the holes are much bigger than the nucleation diameter, several nanocolumns will nucleate and coalesce inside each hole. Note that, when density decreases, the nanocolumn orientation is less and less perpendicular to the substrate. During this

⁸as described in 2.1.1

growth, several parameters were not controlled precisely: the mask may significantly affect the diffusion lengths of the species. Moreover, temperature cannot be calibrated on the patterned substrate.

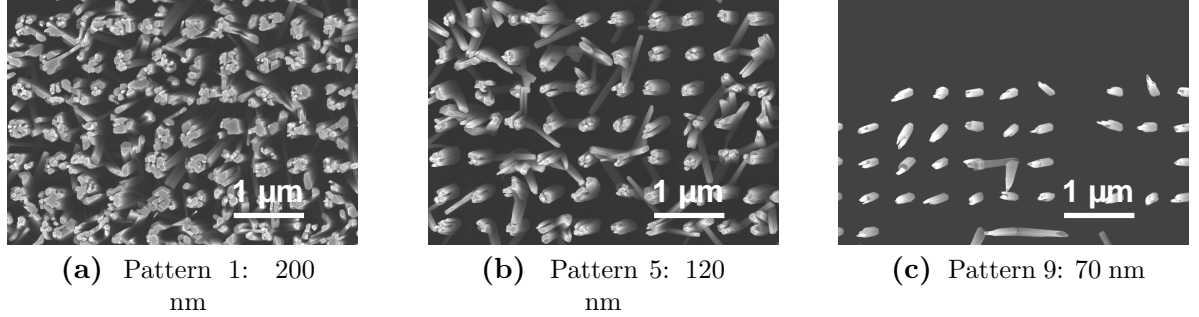


Figure 3.17 – SEM images of the selectively-area-grown sample N1568 with different hole diameter

The low-temperature macrophotoluminescence spectra recorded on each of the ten patterns are depicted in figure 3.18. Both the donor-bound exciton and the 3.45 eV emissions are observable. This sample has a state-of-the-art optical quality, with donor-bound exciton linewidth between 2 and 2.5 meV. When going from pattern 1 to pattern 10, an increase of the intensity of the 3.45 eV line compared to that of the donor-bound exciton is evidenced. A slight blueshift of 0.6 meV of the 3.45 eV line and a redshift of the same amplitude of the donor-bound exciton recombination were observed when lowering the density. This blueshift of the 3.45 eV emission has already been reported in [Fur08] but cannot be easily explained for the moment.

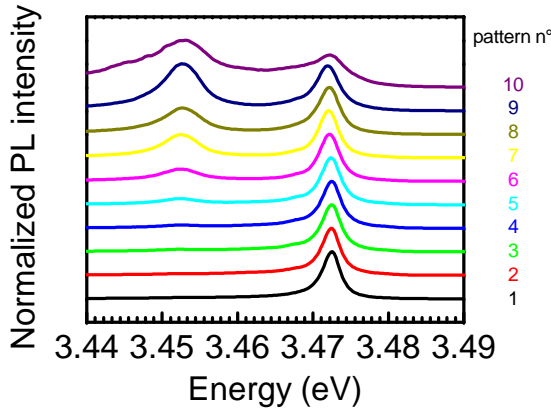


Figure 3.18 – Normalized macrophotoluminescence spectrum on the different patterns at 4 K

In figure 3.19 (a), we show the ratio of the photoluminescence intensity of the 3.45 eV recombination to that of the donor-bound exciton, for each nanorod pattern. Data are extracted from the plots of 3.18. The intensity at 3.45 eV increases by a factor of 20 compared to that of the donor-bound exciton when density decreases from pattern 1 to 10. We also plotted in figure 3.19b the integrated intensity for each line after normalization to the filling factor: the 3.45 eV emission is 500 times more intense when the filling factor decreases from 16% to less than 1.5%. It has to be noted that the

donor-bound exciton intensity also increases by a factor of almost 20 from pattern 1 to 10.

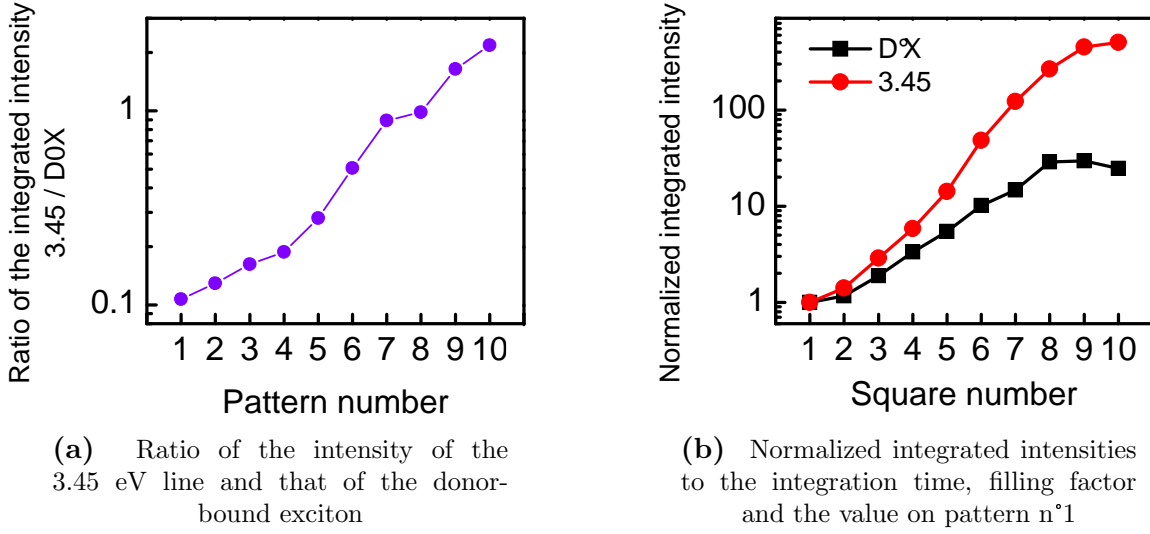


Figure 3.19 – Photoluminescence integrated intensities of donor-bound exciton and 3.45 eV line - sample N1568

This first successful try could be improved by defining smaller patterns, but this would need further efforts as far as nano-imprint lithography is concerned. The 500 nm spacing between each pattern is still very small and inconvenient for micro-photoluminescence studies of single nanowires. Besides, we see that the vertical alignment of the columns is affected by the relatively high growth temperature, but it could be improved by inserting a thin AlN layer [Son07] before fabricating the mask.

3.5.2 Discussion

On both samples, the absolute and relative intensities of the near-band-edge emission appear to vary strongly when the density was modified. In the following, we will investigate the possible phenomena inducing this evolution. Let us remind that when standard macrophotoluminescence experiments are performed on a typical sample⁹, the optical axis of the detection is parallel to the \vec{c} axis. In this case, the A donor-bound exciton always dominates the spectrum. However, when measuring the microphotoluminescence of a single dispersed nanocolumn¹⁰, the optical axis of the detection is perpendicular to the \vec{c} axis and the nanocolumn is in contact with the host substrate. In these measurements, the relative intensity of the line at 3.45 eV and that of the donor-bound exciton varies strongly from wire to wire. These observations suggest that the differences on the intensities of both lines can originate either from the *geometry of the nanorods* on the sample, *e.g.* their surface to volume ratio, their

⁹with the setup described on page 199

¹⁰with the setup described on page 200

dielectric environment, and their diameter. These variations can also be ascribed to the *geometry of the setup*, *e.g.* the orientation of the optical axis of the detector relative to the \vec{c} axis. In the following, the processes which can originate from a decrease of the density are addressed, as well as their consequences.

Better overall extraction efficiency On both samples, we observed an *enhancement of the intensities of both the 3.45 eV line and the donor-bound exciton recombination when we probe a smaller amount of matter*. The data is not shown for the high-temperature sample¹¹. For the selective-area-growth sample, the data are plotted on figure 3.19. This can be explained by a better extraction efficiency. In [Hen11], the authors calculated the extraction efficiency at 450 nm of 1.3- μm high GaN nanowires grown on a silicon substrate and containing an axial InGaN quantum well 700 nm above the GaN / Si interface. Without superstrate (in the air), it monotonously increases when density decreases, in other words, when the average index of this layer decreases with the density.

A further enhancement of the 3.45 eV line is clearly observed compared to the intensity increase of the donor-bound exciton, as evidenced qualitatively in both figures 3.18 and 3.14a, and quantitatively in figure 3.19a. Several effects can explain the huge intensity increase of the 3.45 eV line when the density is lowered. We will first analyze the geometry of the system, *i.e.* the coupling efficiency of the dipoles with the electric field. Then, other arguments such as the increase of surface to volume ratio will be addressed.

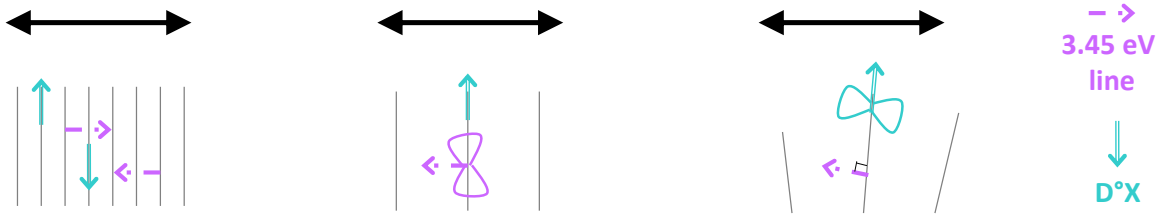


Figure 3.20 – Schematics of the coupling efficiency of both donor-bound exciton and 3.45 eV lines for dense and vertical nanowires (left), decreased density (middle), and tilted nanowires (right). Decreasing both the nanocolumn density and orientation leads to an increase of the donor-bound exciton to 3.45 eV line ratio. The arrows represent the wave-vectors. The radiative patterns are also depicted.

Enhanced detection efficiency of the 3.45 eV line A dipole inside a nanowire does not emit as in a homogeneous material (*i.e.* rather isotropically) because its spontaneous emission is either inhibited or enhanced depending on the geometry and the size of the system relative to the emission wavelength. We saw in 3.2 that the emission at 3.45 eV is polarized mainly parallel to the \vec{c} axis, while the donor-bound

¹¹described on page 84

exciton is polarized perpendicular to the \vec{c} axis. We remind that, in both samples, the nanorods were less and less perpendicular to the substrate when density was lowered. Figure 3.20 illustrates that, compared to reference nanowires (dense and purely vertical nanowires, left panel), the less perpendicular orientation of the nanorods with respect to the normal of the substrate enhances the detection of light emitted by dipoles parallel to the optical axis, hence with wavevectors perpendicular to the \vec{c} axis (right panel). The projection of the detectable electric field indeed increases from a theoretically null value with increasing nanocolumn tilting. On the contrary, this deviation from perfectly vertical nanowires is expected to decrease the donor-bound exciton intensity (right panel). Furthermore, lowering the density is expected to decrease the photon-recycling process by a neighbouring wire, which is more likely to happen for the 3.45 eV emission than for the A exciton emission, because of the orientation of their respective polarization (middle panel).

In the following discussion, dipole directions are given in the usual cylindrical coordinates $(\vec{\rho}, \vec{\varphi}, \vec{z})$ and the emitting directions, in the spherical coordinates $(\vec{\rho}, \vec{\theta}, \vec{\varphi})$. In the article [Mas06], the authors show that, for an *isolated, infinitely-long* nanocolumn of radius R varying from 170 to 190 nm at 3.472 eV, the directionality of the near-band-edge emission originating from a GaN nanocolumn is strongly modified (see figure 3.21). The emission is mainly θ polarized and mainly originates from z -polarized emitters for $\omega R/c=1.5$ (85 nm radius for emission at 3.472 eV, top plot), while it is mainly φ -polarized, originating from both ρ - and φ -polarized emitters for $\omega R/c=1.65$ (equivalent radius of 95 nm, bottom plot).

The spectral variation from 3.472 to 3.45 eV in the value of $\omega R/c$ should have negligible consequences on the pattern of the free space profile. However the variation of the diameter from 200 to 50 nm in the selective-area-grown sample and from 70 to 15 nm in the temperature-gradient sample is expected to strongly modify the far-field pattern. The fact that the donor-bound exciton and the 3.45 eV line have rather perpendicular dipoles can lead to very different consequences on the far-field pattern when diameter decreases — from enhancement to quasi-total inhibition — and hence the coupling with the detection setup should also be very different. The diameter decrease could explain why the emission at 3.45 eV is enhanced when going towards lower density regions.

Let us remark that in these computations, the authors considered a single, infinite nanocolumn: the problem is indeed even more complex when dealing with an ensemble of short-length nanowires, and the phenomena happening close to the tip of the nanorods are unknown too.

Preeminence of surface recombinations Other phenomena can account for the enhancement of the intensity of the 3.45 eV line: it has been reported to originate close to the nanocolumn surface in [Cal00][Kou08] and more recently in [Lef11]. However in those cases, the intensity of this line was compared from sample to sample. The intensity

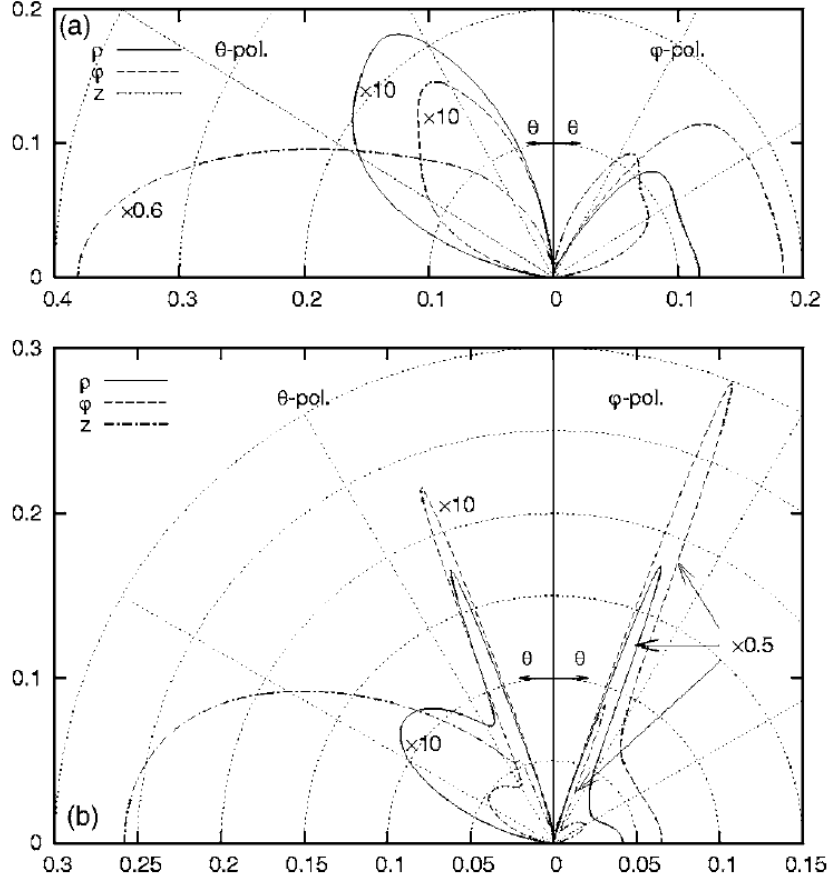


Figure 3.21 – Calculated pattern of free-space radiation for (a) $\omega R/c=1.5$ and (b) $\omega R/c=1.65$. In each case, the left and right panels show the power of the θ - and φ -polarized far fields, respectively - extracted from [Mas06]

of this recombination appeared to increase when decreasing nanocolumn density. Note that when the density decreases, coalescence is less likely to occur and thus the average diameter also decreases: lowering the density thus leads to a subsequent increase of the surface to volume ratio. In the above publications, as well as in the temperature-gradient sample we studied, the density was modified by varying the growth conditions such as temperature or flux ratio. This could possibly lead to non-equivalent nanowires, displaying differences from one to another because they were not grown with exactly the same conditions. One possible example could be the impurity incorporation. On the contrary, in the selective-area growth sample, nanowires are identical and grown on the same one cm-size silicon wafer, ensuring a good homogeneity. There, the decrease of the 3.45 eV emission with higher nanocolumn density can be attributed to increasing coalescence, and thus to a decreased surface to volume ratio.

Enhancement of the free-exciton line and "self-purification" In the sample displaying a temperature-gradient, we also have noticed (see figure 3.14a) an increase of the intensity ratio of the free-excitons compared to that of the donor-bound excitons. Towards the center, where the temperature is higher, we suggest that the impurity

incorporation is less probable than in the cold region at the edge of the wafer. We can assume that, during the growth of nanowires, the impurities diffuse towards the free surfaces in order to decrease their formation energy: this is the so-called "self-purification" [Bra10]. The authors pointed out this process to explain the absence of luminescence of the donor-bound exciton by several nanowires. As a consequence, the number of donors where an exciton can bind to is lower when the growth temperature is higher and therefore the intensity of the donor-bound exciton line decreases relatively to that of the free-exciton.

This process should happen for donors as well as for point defects, therefore we would expect that point defect density should be lowered when going to regions where the growth temperature was higher. The observation of a huge increase of the intensity at 3.45 eV when increasing growth temperature weakens the Ga vacancy hypothesis proposed in [Fur08]. This is unless self-purification does not annihilate the point defects but only change their spatial distribution, possibly leading to a lower concentration in the bulk part of the nanowires and an enhanced impurity density close to the surface.

Notice that the 3.45 eV line is sometimes composed of a doublet separated by 8 meV. The increase of the high-energy contribution compared to the low-energy one seems to follow the same trend when density is lowered as either the A free-exciton compared to the A donor-bound exciton, or their B counterparts. Yet, this splitting is not typical of all the samples we have studied.

Conclusion

Up to this point, we have seen two methods which allow to probe the luminescence of nanowires with decreasing density. In both samples, the whole emission increases when lowering nanorod density because of a more efficient light extraction. A larger enhancement of the luminescence at 3.45 eV is observed when decreasing the nanocolumn density. Yet, it is difficult to know whether this further increase is due to surface effects (the surface to volume ratio increases with decreasing density) or rather to a more efficient collection (because of its polarization selection rule). These experiments do not allow us to conclude.

3.6 Influence of the nanocolumn density on the decay dynamics of the near band edge

In this part, we investigate the possible influence of the nanorod density on the spontaneous emission rate of the donor-bound exciton, the 3.45 eV line and the free exciton. As the oscillator strength is expected to vary strongly with the dipole geometry, we can assume different behaviours when lowering density and diameter.

3.6.1 Preamble on decay time measurements

One of the main features of an exciton recombination consists in its decay time. It is proportional to the reciprocal of the oscillator strength. In bulk and two-dimensional GaN, the literature reports very different values concerning the whole spectral range of the near band edge. A free-exciton decay time smaller than 100 ps is generally reported [Mon06]. Concerning the donor-bound exciton recombination, values of the decay times are in the range of 100 - 500 ps [Mon06]. On both lines, one can observe a biexponential decay, with a 2-ns long decay time [Mon08]. Longitudinal optical phonon replica and two-electron satellites show monoexponential decay times between 1 and 2 ns [Mon08]. The authors thus attribute the shorter decay times observed on bound and free exciton to non-radiative recombinations induced by the surface [Mon08]. The authors proposed that the intrinsic decay time is that of longitudinal optical phonon replica and two-electron satellites. According to the authors, the different measured decay times suggest that phonon-replica and two-electron satellite luminescence originate from a different donor population than the donors giving rise to the donor-bound exciton luminescence. Otherwise, the fast decay observed for both the donor-bound exciton and the free-exciton recombinations would also be observable on the two-electron satellites and the phonon-replica. Moreover, the decay times of the donor-bound exciton and the free-exciton decrease with the doping level, suggesting that these values are still short because of high non-intentional doping level: a better sample quality could give even longer recombination times [Mon10].

To conclude, in bulk GaN, the decay times one measures on the zero-phonon lines vary strongly from sample to sample, from a few 100 ps to 2 ns. The dynamics of the dominant physical phenomena, such as non-radiative recombinations or carrier transfer [Mon10] are not fully understood yet. In nanowires, we expect an even greater role of surface states, which may strongly affect the excitonic decay times.

3.6.2 Decay dynamics of dense GaN nanowires

Coming back to a dense array of nanowires, the free and bound exciton decay times can give important clues on the exciton environment. Figure 3.22a shows the transients¹² obtained on a standard sample¹³ for the four main contributions. The decay times are extracted by integrating from t_0 , beginning of decay, to infinity. Indeed, if intensity is normalized to 1 and purely monoexponential, then $\int_{t_0}^{\infty} I(t)dt = [-\tau \exp^{-t/\tau}]_{t_0}^{\infty} = \tau$. It can be seen that the free-exciton decay time is about 80 ps, while that of the donor-bound exciton is slightly slower, around 100 ps. Two contributions at 3.45 eV are differentiated, with longer decay times than the excitonic lines. The donor-bound exciton and free-exciton decay times for nanocolumn samples are thus comparable to those reported on

¹²More details on the time-resolved photoluminescence setup can be found in page 200.

¹³The standard growth conditions are described in 2.1.1

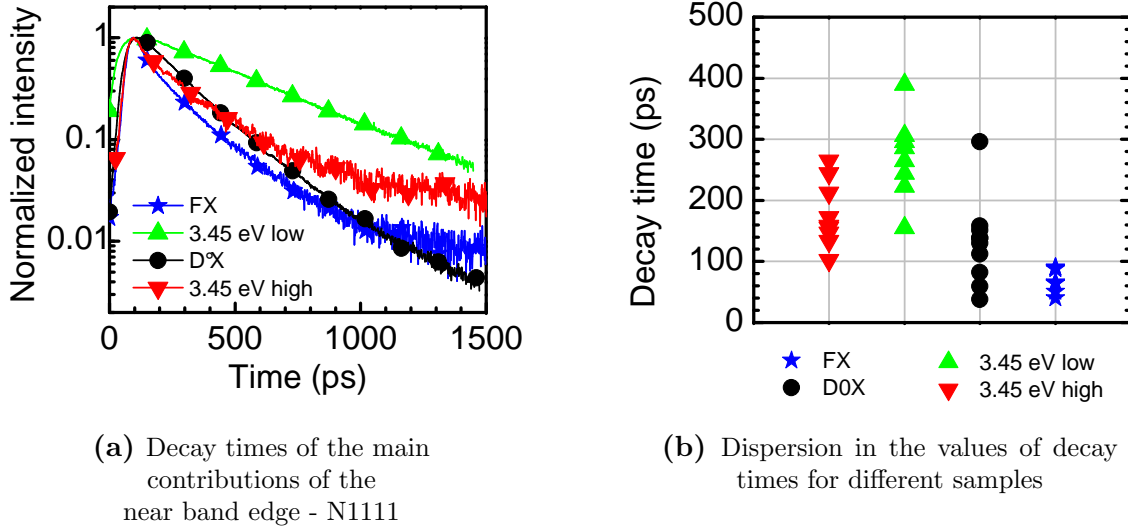


Figure 3.22 – Decay times at 4 K

heteroepitaxial as well as homoepitaxial GaN [Poz99][Mon08].

However, the decay times prove to be very sample-dependent, as well as the reported values in the literature on bulk GaN. Figure 3.22b shows the dispersion of the measured values for the four contributions, on five different as-grown samples and various positions on each wafer. Contrary to the full width at half maximum of the donor-bound exciton, which remains quasi constant along a 2" wafer, the decay times are much more sensitive to slight changes of the growth conditions. The decay time of the donor-bound exciton varies between 30 and 150 ps. That of the 3.45 eV ranges between 180 and 400 ps for the low-energy contribution, and 100 - 290 ps for the high-energy one. The free-exciton decay time lies in between 50 and 100 ps.

Surfaces may induce one of the dominant recombination mechanisms governing decay times and may vary with precise growth conditions. We remind that GaN nanowires with diameter smaller than 80–100 nm are expected to be completely depleted, due to Fermi level pinning at their surfaces at 0.5–0.6 eV below the conduction band [Cal05], inducing carrier separation. However, these small nanowires also present a decreased surface potential barrier and, therefore, surface recombinations are possible and may even be preeminent. In photoluminescence experiments, an increased oscillator strength has been evidenced on the donor-bound exciton emission [Pfü10] and the excitonic zinc-blende emission¹⁴ after intense UV exposure. This effect is further observed in unpassivated GaAs nanowires, which exhibit luminescence only if their diameter is greater than 100 nm. [Dem10]. We have assumed in 2.4.1 that GaN nanowires smaller than 20 nm do not show luminescence either.

¹⁴see 2.5.3

3.6.3 Variation of the spontaneous emission rate

We have seen that the coupling between a dipole and the electromagnetic field can lead to an increase of the emission intensity when the nanowire density decreases. We also expect that a change in the dielectric environment of the wires could affect their recombination time. When the average index seen by a dipole decreases, we expect a reduction of the light-matter coupling, leading to longer recombination times.

In the following we present some experimental examples taken from the literature. Beveratos *et al.* have compared the recombination time of nitrogen-vacancy centers in bulk diamond and diamond nanocrystals [Bev01]. They report a decay time 2.2 times longer for nanocrystals than for bulk. More recently, in [Ble10], the authors reported either an inhibition or an enhancement of the spontaneous emission of an InAs quantum dot embedded in a GaAs photonic wire of diameter d . Below $d/\lambda = 0.16$, they evidenced a clear inhibition of 16 compare to the emission in free space.

In [Mas06], the authors studied the power emitted into guided modes along the nanocolumn and radiative (leaky) modes by various dipole distributions in an isolated, infinitely long, self-standing nanowire. Figure 3.23 shows the calculated total power emitted by a semiconductor nanocolumn, normalized to the power emitted by a dense layer of the same semiconductor, and various dipole orientations given in the usual cylindrical coordinates $(\vec{\rho}, \vec{\varphi}, \vec{z})$. Oscillations are due to the apparition of higher order guided and free-space modes. We observe that a radial or azimuthal dipole emission in a nanowire is always quenched compared to its emission rate in bulk. However, a dipole parallel to the wire axis can have its emission rate either enhanced or quenched, depending on the diameter of the nanocolumn.

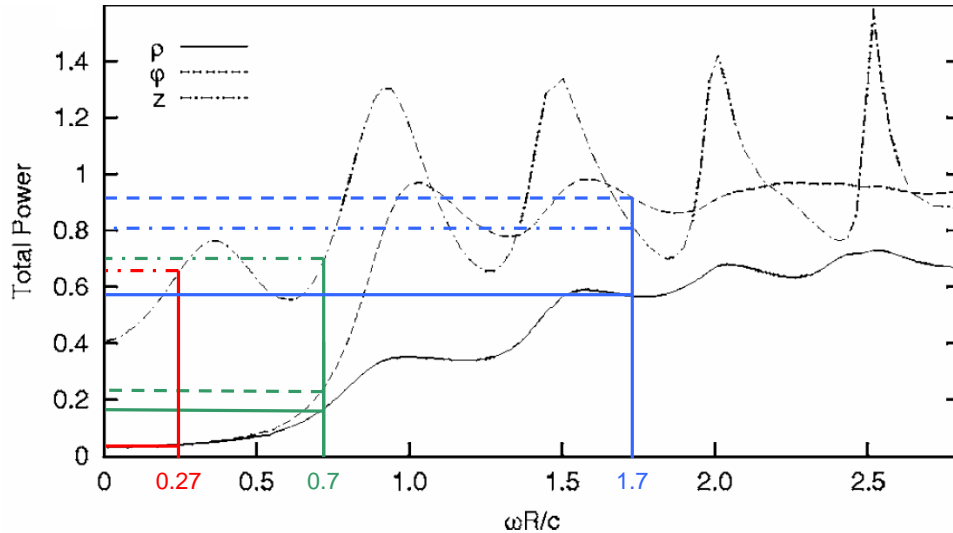


Figure 3.23 – Expected power emitted by a set of dipoles uniformly distributed inside the wire, with varying their orientation, with $\omega R/c$, *i.e.* either the emission wavelength and / or the nanocolumn radius. The standard cylindrical space coordinates (ρ, φ, z) are used - extracted from [Mas06]

In this work, we studied the decay time along the radius of the sample exhibiting a temperature-gradient described in 3.5.1 and 2.4. Our sample shows several differences compared to the isolated, infinitely long, self-standing nanowire studied in [Mas06]. First, the nanocolumns are not isolated, especially in the high density region where coalescence takes place. They are not infinitely long. On the contrary, due to temperature-enhanced desorption, in the lowest density zone the nanocolumns become much shorter (100 nm long instead of more than 1 μm in the high density zone). We also have to take into account the influence of the higher absorption coefficient of the silicon substrate, because its absorption becomes preminent when the length and the density are both reduced. Besides, in the calculations, a homogeneous density of emitting dipoles is assumed inside the wire. Other simulations [Mas06] predict a variation of the emission rate with dipole position along the nanocolumn diameter. During nanocolumn growth, self purification may occur, leading to an accumulation of impurities close to the sidewalls compared to the core, as suggested by Brandt *et al.* [Bra10] and discussed in 3.5.2.

Line	Dipole orientation	$R(\text{nm})$		
		100	40	15
		$\omega R/c$		
		1.7	0.7	0.27
3.45 eV	z	0.8	0.7	0.63
D ⁰ X and FX	$\rho ; \varphi$	0.58 ; 0.92	0.17 ; 0.02	0.02

Table 3.1 – Expected power emitted in both radiative and free space, for various ranges of diameter [Mas06]

The common point with the simulated system is the knowledge of the polarization of the emission lines. We have seen in 3.2 that the recombination of the A exciton is polarized perpendicular to the \vec{c} axis, as expected, while the emission at 3.45 eV has its dipole mainly parallel to the \vec{c} axis. From this observation, we can summarize the expected spontaneous emission rate for various diameters and dipole orientations in table 3.1, extracted from figure 3.23. We should therefore observe a progressive inhibition of both the donor-bound exciton and the free-exciton lines when the diameter is reduced, whereas the spontaneous rate of the recombination at 3.45 eV is not expected to change dramatically.

3.6.4 Results

Figure 3.24 shows the measured decay time¹⁵ along the wafer radius of sample N1405. We can observe two regimes.

Between 0 and 9 mm, the recombination times of the three contributions increase

¹⁵extracted from the integration method described in 3.6.2

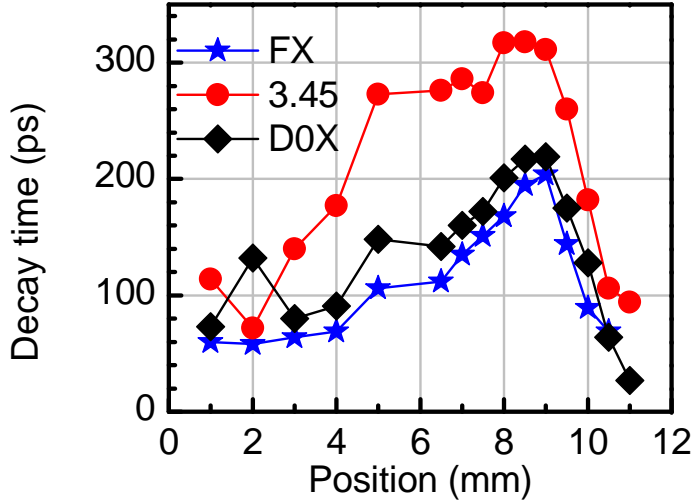


Figure 3.24 – Evolution of photoluminescence decay times for the three main contributions as a function of the position along the wafer radius - sample N1405

by a factor of almost 4. The inhibition of the spontaneous emission rate increases when density and diameter are reduced, as reported in [Bev01] and [Ble10]. Indeed, for a small enough isolated standing nanowire, the dipoles couple mainly to free-space modes. The unexpected result lies in the fact that the emission rate of the three contributions are modified in the same way, whereas theory expects a much greater inhibition of the excitonic lines compared to the 3.45 eV transition (see table 3.1).

From 9 mm onwards, the measured decay times decrease very rapidly and reach a value close to their initial ones in the highest density region. This observation could be explained by an enhancement of non-radiative channels, compatible with the hypothesis that smaller nanowires do not show any luminescence¹⁶.

3.6.5 Discussion and perspectives

It has to be pointed out that there is no simulation taking into account several nanowires randomly distributed in space. It is however of paramount importance to take into account photon recycling in the whole density range of the sample. This process could lead to an increase of the effective (and measured!) decay time, especially in high density regions. In order to model the system, one should also consider the increasing role of the high index silicon substrate as the nanocolumn density decreases. Indeed, when tilting the nanowires and simultaneously decrease their density, thus increasing the surface of uncovered silicon, an increasing part of the luminescence is trapped and absorbed by the silicon substrate.

Besides, we must keep in mind the dependency of the decay times on the sample and on the position on a sample observed in 3.6.2. This suggests that the measured decay times should be considered carefully because they should be very sensitive to

¹⁶as discussed in 2.4.1

surface states: the decay times of the various contributions can only be compared at a given point of a given sample, because surface states may vary strongly along the wafer diameter. In GaAs, Demichel *et al.* have shown that the optical recombination properties of as-grown GaAs nanowires (from 70 to 14 nm in diameter) were governed by the pinning of the Fermi level, whereas nanorods passivated by a 4-nm thick AlGaAs shell, the time-resolved photoluminescence was dominated by surface recombinations.

Moreover, we have to mention here that no clear influence of the nanocolumn density was observed on the decay time of any of the three contributions in the case of the selective-area-grown sample described in 3.5.1. It gives us a clue that the parameters governing spontaneous emission in the samples discussed in this section (temperature-gradient and selective-area growth) are not only density and diameter. In any case, the mechanisms active here will only be understandable when samples varying *either* the density *or* the diameter (with no extra parameter variation such as coalescence and tilting) are available.

Conclusion

In these experiments, we expected the radiative decay time of the excitonic lines to become longer when the diameter decreases, while no strong variation was foreseen on the emission at 3.45 eV, both originating from the one-dimensional geometry. What we observe is a shortening of the spontaneous emission rate of the same order of magnitude for the three contributions (donor-bound exciton, free-exciton and 3.45 eV line) when lowering the nanocolumn density, which we ascribe to purely isotropic dielectric effects. Yet, in the region of strong variation in the nanocolumn diameter, the decay times of the three contributions sharply decrease. This could originate from the enhancement of some additional non-radiative recombinations, as discussed in the previous chapter¹⁷.

¹⁷see 2.4.1

Spectroscopy of GaN / AlN microdisk resonators

*I*N THIS CHAPTER, we will focus on the optical characterization of AlN microdisks with embedded GaN quantum dots.

Our fundamental studies on GaN/AlN cavities have two main objectives: evidencing the Purcell effect in nitride cavities and lasing in such μm -size structures in the UV range. Both will be discussed in more details in chapter 6. The Purcell factor is given by the following relation:

$$F_P = \frac{3Q(\lambda_{\text{cav}}/n)^3}{4\pi^2 V_{\text{eff}}} \quad (4.1)$$

where V_{eff} is the modal effective volume, λ_{cav} is the wavelength of the cavity mode, n the refractive index of the material, and Q is the cavity quality factor.

We see from equation 4.1 that, at a given wavelength, we can maximize F_P by maximizing the quality factor and / or minimizing the modal volume. In this context, microdisks are good candidates for low threshold lasing due to their low mode volume and high achievable quality factors.

This chapter therefore aims at introducing these cavities, before analyzing their potentialities as far as the Purcell effect and lasing are concerned in chapter 6. They are also easier to process than photonic crystals: it is therefore the first system we studied, in terms of active layer and photonic properties. The knowledge acquired on these cavities was then used to fabricate photonic crystal cavities, which are much more challenging — the etching patterns are far smaller and the underetching needs to be complete. This will be developed in chapter 5.

Contents

4.1	Whispering gallery modes	100
4.1.1	The slab waveguide	101
4.1.2	Whispering gallery mode approximation	104
4.1.3	Intensity profile of a given mode (ℓ, m, n)	105
4.2	Fabrication	106
4.2.1	The active layer	106
4.2.2	Design of the microdisk geometry	108
4.2.3	Studied samples	109
4.3	Free spectral range and diameter	110
4.3.1	Comparison with calculations in the whispering gallery mode approximation	110
4.3.2	Comparison with FDTD simulations	112
4.4	Measurements of record quality factors	113
4.4.1	Measurements of the quality factor	113
4.4.2	Origins of losses in the microdisk resonator	114
4.5	Directionality and polarization of the emission	120
4.5.1	Directionality of the emission	120
4.5.2	Polarization of the emission	122
4.6	Whispering gallery modes — towards a Purcell-enhanced microdisk laser	123

4.1 Whispering gallery modes

The *whispering gallery modes* were reported for the first time by lord Rayleigh for acoustic waves. A practical illustration of the existence of these modes lies in the possibility for two persons to converse by whispering, whatever the distance between each other, as long as they stay close enough to the periphery of the dome of Saint Paul's cathedral in London.

In first approximation, a microdisk can be considered as a planar waveguide with specific boundary conditions due to its radial geometry. To analyze this optical system, we will decouple the light confinement. *Perpendicularly to the waveguide* (figure 4.1, left panel), we will consider an infinite slab waveguide of refractive index $n_{\text{AlN}} \approx 2.2$ and thickness h surrounded by air ($n = 1$): the silicon post on which the disk is mounted is thus not considered in this first analysis. The origin of the z axis is taken in the

middle of the slab. Due to the small enough thickness of the slab, photons confined in this structure still “feel” the surrounding air of index 1. As a consequence, we will associate an *effective index* to the waveguide: $n_{eff} \leq n_{AIN}$. This will be treated in section 4.1.1. *In the plane* (figure 4.1, right panel), photons whose incident angle are above the critical value $\arcsin(1/n_{AIN})$ are confined along the periphery of the disk by total internal reflection. This will be treated in section 4.1.2

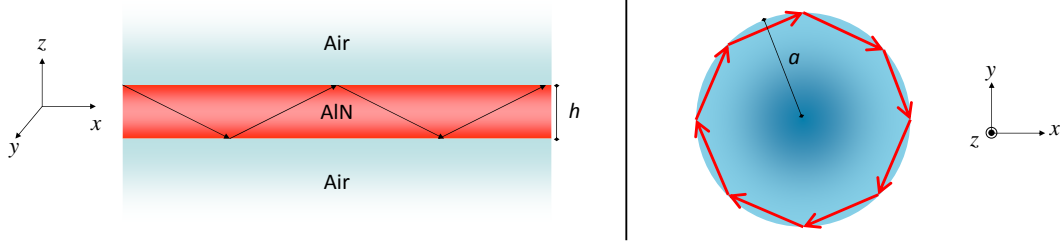


Figure 4.1 – Schematics of (left) out-of-plane and (right) in-plane treatments of a microdisk

In the geometrical approach, the light beam stays in phase with the incident light after one turn if:

$$2\pi a = \frac{m\lambda_0}{n_{eff}} \quad (4.2)$$

where a is the radius of the microdisk, λ_0 is the vacuum wavelength and m an integer. The spectral frequency spacing between two modes, called the *free spectral range*, thus writes:

$$\Delta\nu_0 = \frac{c}{2\pi a n_{eff}} \quad (4.3)$$

4.1.1 The slab waveguide

In this subsection, we omit the circular shape of the microdisk to calculate the modes that can propagate into the slab waveguide, which will be considered as infinite in the (x, y) plane. The calculation of the effective index of this mode will be explained. We will see that our structure has been chosen to allow the propagation of only one mode. Let β be the wavevector of the guided mode and the fields have these expressions:

$$\vec{E}(\vec{r}, t) = \vec{E}(x, y, z, t) = \vec{E}_0(x, y, z)e^{i(\omega t - \beta x)} \quad (4.4)$$

$$\vec{H}(\vec{r}, t) = \vec{H}(x, y, z, t) = \vec{H}_0(x, y, z)e^{i(\omega t - \beta x)} \quad (4.5)$$

In the infinite waveguide, Maxwell’s equations reduce to:

$$\frac{d^2 \vec{E}_0}{dz^2} + (k_0^2 - \beta^2) \vec{E}_0 = 0 \quad \text{in air} \quad (4.6)$$

$$\frac{d^2 \vec{E}_0}{dz^2} + (k_0^2 n_{AlN}^2 - \beta^2) \vec{E}_0 = 0 \quad \text{in the AlN waveguide} \quad (4.7)$$

where $k_0 = \omega_0 \sqrt{\mu_0 \epsilon_0}$ is the propagative constant in air. Equivalent equations can be written for the magnetic field.

Maxwell's equations lead us to consider two types of modes:

- Modes with only one non-zero component of the electric field (along the y -axis in our geometry) and two non-zero components of the magnetic field (along the x and z -axis) are called TE modes, for *transverse electric*. The TE modes are numbered by an integer number ℓ by increasing effective index, *i.e.* by order of appearance when the slab thickness h is increased.
- Modes with only one non-zero component of the magnetic field (along the y -axis in our geometry) and two non-zero components of the electric field (along the x and z -axis) are called TM modes, for *transverse magnetic*.

However, we can already note that, for a thickness small enough, the slab waveguide will be monomode: only the TE $\ell=0$ mode will be efficiently guided. In the following, we will thus consider neither the contributions from TE modes with higher effective indexes (characterized by higher values of ℓ) nor that from TM modes. The whole analysis can be found in [Yar97]. The field can be written as:

$$\begin{aligned} E_y \left(|z| \geq \frac{h}{2} \right) &\propto \exp \left[-p \left(|z| - \frac{h}{2} \right) \right] && \text{in the air} \\ E_y \left(|z| \leq \frac{h}{2} \right) &\propto \cos(qz) && \text{in the slab} \end{aligned} \quad (4.8)$$

where:

$$p = \sqrt{\beta^2 - k_0^2} \quad (4.9)$$

$$q = \sqrt{n_{AlN}^2 k_0^2 - \beta^2} \quad (4.10)$$

From the continuity of the tangential component of E_y , we obtain a transcendental equation which allows a graphical determination of the values of (p, q) . We find the propagating mode by stating that:

$$p \frac{h}{2} = q \frac{h}{2} = \sqrt{(n_{AlN}^2 - 1) k_0^2} \frac{h}{2} \quad (4.11)$$

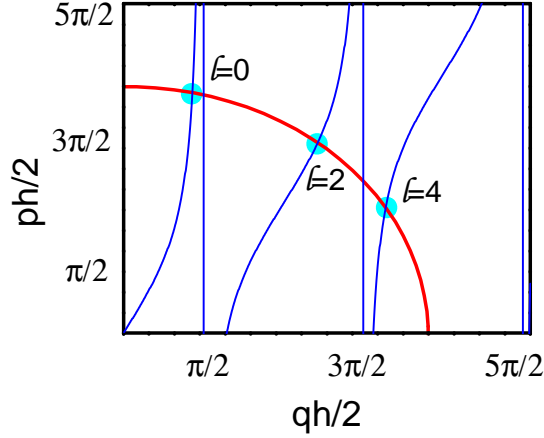


Figure 4.2 – Example of graphical resolution of the transcendental equation 4.11 for even values of ℓ

Figure 4.2 shows the values of $ph/2$ and $qh/2$, and the intersection with the circle of radius $\sqrt{(n_{AlN}^2 - 1)k_0^2 h^2}$. We can notice that the higher the discontinuity between the refractive index of air (1) and that of the slab thickness (n_{AlN}), the higher the number of possible propagating modes. This plot gives us access to the effective index of the slab waveguide, reminding the expressions of p and q from equations 4.9 and 4.10:

$$n_{eff} = \frac{\beta}{k_0} = \frac{\sqrt{k_0^2 n_{AlN}^2 - q^2}}{k_0} = \frac{\sqrt{k_0^2 + p^2}}{k_0} \quad (4.12)$$

Figure 4.3 shows the effective index of a 70-nm thick AlN layer — 1.6 at 3 eV — and a 110 nm-thick one — 1.75 at 3 eV. The AlN refractive index is shown for comparison: it is around 2.1 at 3 eV.

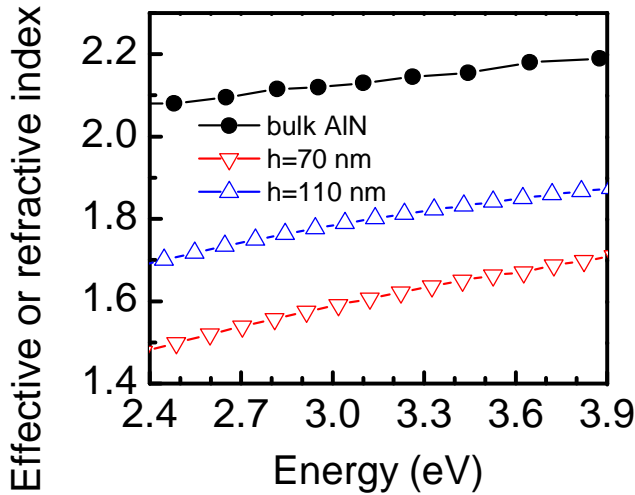


Figure 4.3 – Comparison of the effective index of 110 nm and 70 nm AlN slab waveguides with refractive index of bulk AlN from reference [AV03]

Coming back to the propagation of a given mode in the waveguide, one can write that the mode indexed by ℓ ($\ell=0,1,2,\dots$) will be able to propagate only if $qh \geq \ell\pi$. Keeping in mind the definition of q (equation 4.10), we deduce that the condition for

the ℓ^{th} mode to propagate into the waveguide writes:

$$h/\lambda_0 \geq \frac{\ell}{2\sqrt{n_{AlN}^2 - 1}} \quad (4.13)$$

where λ_0 is the wavelength in vacuum. For an AlN slab of thickness h , about $4h/\lambda_0$ modes can propagate. *Therefore, to keep the waveguide monomode for an emission at 380 nm, we need to keep the thickness below 95 nm.* This requirement will have serious consequences on the quality of the active layer, as will be discussed in 4.2.1.

4.1.2 Whispering gallery mode approximation

Now the infinite slab waveguide has been analyzed and the effective index has been determined, we have to take into account the circular shape of the microdisk and the boundary conditions which apply at the circumference. The propagation equation writes:

$$\Delta \vec{F} + n_{eff}^2 \frac{\omega^2}{c^2} \vec{F} = \vec{0} \quad (4.14)$$

where \vec{F} may be either the electric or the magnetic field.

Then we can make the following approximations. In TE polarization, we *choose* to consider only H_z , E_r and E_θ . In addition, in cylindrical coordinates, we choose to decouple the treatment perpendicular to the waveguide and in the plane (this is an approximation): $H_z(r, \theta, z) = \Psi(r, \theta)Z(z)$. Equation 4.14 becomes:

$$\Delta H_z + n_{eff}^2 \frac{\omega^2}{c^2} H_z = 0 \quad (4.15)$$

Invariance with any rotation of θ allows us to write:

$$\Psi(r, \theta) = R(r) \exp(im\theta), \quad m \in \mathbb{N} \quad (4.16)$$

where m is called the *azimuthal number*. The propagation equation along z has been solved in the previous part. The last step is thus to elucidate the radial dependence of the field. The solution of:

$$\frac{d^2 R}{dr^2} + \frac{1}{r} \frac{dR}{dr} + \left(\frac{\omega^2 n_{eff}^2}{c^2} - \frac{m^2}{r^2} \right) R = 0 \quad (4.17)$$

is the m^{th} Bessel function for $r \leq a$:

$$R(r) \propto J_m \left(\frac{n_{eff} \omega r}{c} \right) \quad (4.18)$$

At the periphery of the microdisk, for $r \geq a$:

- either we consider the analytical solution of equation 4.17: a Hankel function, which can be approximated by an exponential decay:

$$R(r) \approx J_m \left(\frac{n_{eff}\omega r}{c} \right) \exp[-\kappa(r - a)] \quad (4.19)$$

where $\kappa = k_0 \sqrt{n_{eff}^2 - 1}$

- or we suppose that the field is null around the periphery of the disk:

$$R(r) = 0 \quad (4.20)$$

This is the *whispering gallery mode approximation*. This approximation does not take into account the coupling between the modes and free space but leads to satisfying results when calculating the properties of a given mode, such as its modal volume.

4.1.3 Intensity profile of a given mode (ℓ, m, n)

The *in-plane index* ℓ gives the number of the waveguide TE mode. The fundamental mode is a cosine inside the waveguide, whose wavevector is determined graphically from a plot similar to that of figure 4.2. The decay out of the waveguide is exponential and also obtained graphically. The *azimuthal index* m is the order of the Bessel function. There are $2m$ zeros around the periphery of the disk. The intensity varies like $\cos(\theta m)$. The *radial index* n indexes each zero of the Bessel function ($n = 1$ is the first zero, *etc...*). The radial profile of the field corresponding to n will thus show $n - 1$ nodes. Both vertical and radial dependences of the electric field intensity are depicted on figure 4.4.

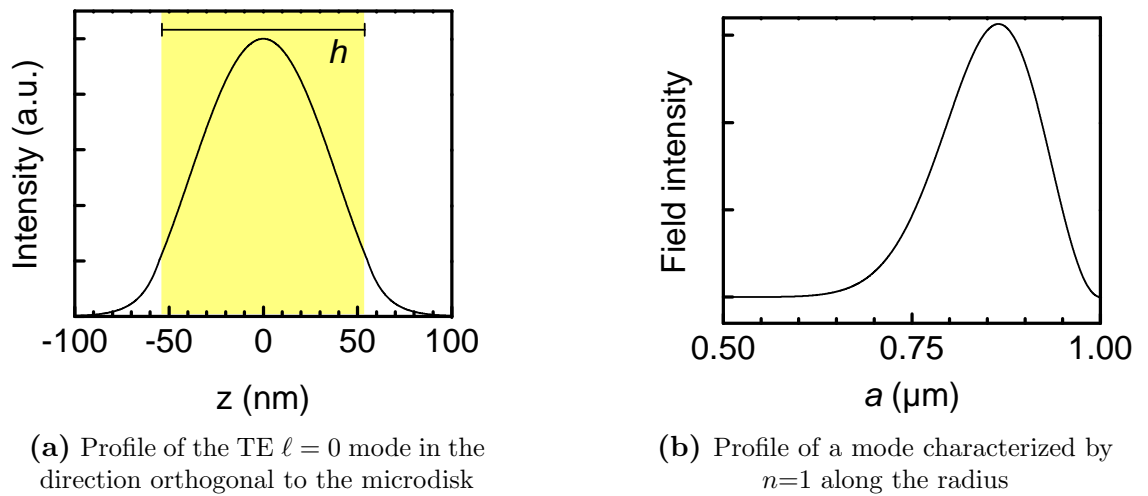


Figure 4.4 – Intensity profile of a whispering gallery mode of a microdisk 110-nm thick, 2- μm of diameter

We have already defined whispering gallery modes as describing photons confined due to total internal reflection, providing a wide enough incident angle at the disk / air interface. Qualitatively, this condition requires a high enough value of m , a rather small value of n and leads to light confinement close to the sidewalls of the disk. On the contrary, radial modes (small values of m) have a too small incidence angle to be confined to the periphery of the disk. They rather remind us of the waves created by a pebble thrown into a steady surface of water. For more details please refer to [Mai98]. Whispering gallery modes display a higher quality factor than radiative ones and these are the modes we can observe on a microphotoluminescence spectrum.

Conclusion

In this section, we have seen that the whispering gallery mode approximation states that the electric field is null at the periphery of the disk. It gives satisfactory results in terms of resonance spectral range and modal volume. In the vertical direction, we will consider only the first TE mode because the total thickness of our sample is always smaller than half of the wavelength in the material, *i.e.* $h < \lambda_0/2n_{\text{AlN}}$.

4.2 Fabrication

4.2.1 The active layer

The properties of the active layer is of tremendous importance. Indeed, in our case, GaN/AlN quantum dots will feed the cavity modes with photons. They must therefore satisfy several conditions in order to couple efficiently to the cavity. This coupling is the key for both the Purcell effect and lasing, as we will discuss in chapter 6. For the samples investigated in this work, the active layer is grown by ammonia-MBE in CRHEA (CNRS Valbonne). We will begin by a brief overview of the specificities of GaN / AlN quantum dots grown by ammonia-MBE. We require the the planar waveguide to be monomode: this will raise several which will then be discussed.

Historically, GaN/AlN quantum dots were first grown in MBE reactors using nitrogen plasma [Dau97]. The two-dimensional to three-dimensional growth transition is typical of a Stranski-Krastanow process and the relaxation is purely elastic. However, in ammonia-MBE, NH_3 acts like a surfactant and inhibits the three-dimensional growth: no three-dimensional growth transition occurs and the two-dimensional layer relaxes plastically. In order to grow quantum dots, it is necessary to stop the fluxes after depositing GaN on a relaxed AlN layer [Dam99]. The total relaxation of the underneath AlN layer is necessary to maximize the lattice mismatch with GaN (2.5% for an elastic relaxation of GaN on relaxed AlN). Using this technique, it is even possible to observe a three-dimensional transition of the growth with smaller lattice mismatch: the successful

growth of GaN / Al_{0.5}Ga_{0.5}N quantum dots was demonstrated (with a maximal lattice mismatch of 1.2%) [Ser09b]. Typical GaN / AlN quantum dots grown with this methods are 2 nm high, with a diameter of 10–15 nm and a density in between 10¹⁰ and 10¹¹ cm⁻² [Ser09b] [Ser11].

To maximize emitter-light coupling, we want to limit the thickness of the guiding slab to $\lambda/4$ as already discussed in 4.1.1. This way the membrane is kept monomode, and the photons emitted by the quantum dots will all couple to only one slab mode, TE($\ell = 0$). This ensures a maximal coupling factor. As we target an emission around 380 nm, the total thickness should be thinner than 95 nm. However, we have seen in introduction¹ that the heteroepitaxy of nitrides on silicon led to highly-dislocated and strained materials. This is the reason why GaN quantum dots are usually grown on a 1- μ m thick AlN buffer layer. Yet this is not compatible with the monomode requirement. Therefore the optical quality of GaN quantum dots grown close to the silicon substrate must be investigated.²

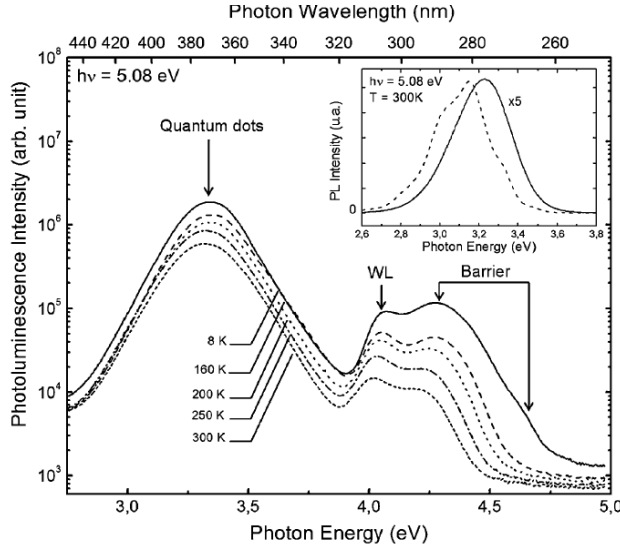


Figure 4.5 – Influence of temperature on the photoluminescence of 9 monolayer-GaN/Al₅₀Ga₅₀N quantum dots. Inset: comparison between the photoluminescence intensity of quantum dots grown with a 35-nm (line) and 1- μ m (dashes) AlN buffer layer - extracted from [Ser09b]

The inset of figure 4.5, extracted from [Ser09b], compares the intensity of one layer of GaN/Al_{0.5}Ga_{0.5}N quantum dots grown on an Al_{0.5}Ga_{0.5}N barrier as thin as 35 nm (dislocation density estimated to $2 \cdot 10^{11}$ cm⁻²), and the same quantum dots grown on a 1 μ m thick buffer layer (dislocation density around $3 \cdot 10^{10}$ cm⁻²). The emission of the quantum dots grown on the thicker Al_{0.5}Ga_{0.5}N layer is 5 times more intense than the emission on the thinner barrier. This quenching is attributed to an enhancement of non-radiative recombinations by the greater number of dislocations in thinner Al_{0.5}Ga_{0.5}N layers compared to that in thicker Al_{0.5}Ga_{0.5}N layers. Indeed, by exciting GaN / Al_{0.5}Ga_{0.5}N at 5.1 eV, the carriers are first generated into the barriers and then relax to the quantum dots. Increasing the dislocation density by a factor of 10 thus mainly decreases the excitation efficiency.

¹see 1.1.2

²This work was done by Sylvain Sergent during his PhD [Ser09a].

However, if we look at the temperature-dependence of the photoluminescence intensity depicted on figure 4.5, we see that 1/3 of the luminescence measured at 8 K remains at room temperature. This is consistent with the internal quantum efficiencies reported for usual GaN / Al_{0.5}Ga_{0.5}N quantum dots. In GaN / AlN quantum dots grown on a thick AlN layer, the ratio between low- and room-temperature intensities is $\frac{I_{300\text{ K}}}{I_{4\text{ K}}} = 0.65$ (for an excitation at 244 nm) [Ren09b]. In the GaN / Al_{0.5}Ga_{0.5}N systems, this ratio is expected to be lower because of the weaker confinement induced by smaller band offsets. The internal quantum efficiency $\frac{I_{300\text{ K}}}{I_{4\text{ K}}}$ measured on GaN / Al_{0.5}Ga_{0.5}N quantum dots grown on a 35-nm thick barrier demonstrates that three-dimensional confinement is still efficient compared to thick Al_{0.5}Ga_{0.5}N layers. This is despite the one order of magnitude larger dislocation density — in the order of $4 \cdot 10^{11} \text{ cm}^{-2}$: notice that in our samples, the dislocation density is comparable to that of the quantum dots! The weaker intensity on samples grown with a thinner buffer layer can also be explained by the proximity of the emitters to the silicon substrate, which has a high absorption coefficient $\alpha_{Si,3.2\text{ eV}} = 3 \cdot 10^4 \text{ cm}^{-1}$ [Jel82]. Even if the intensity at 4 K is less intense than that of thicker layers, the $\frac{I_{300\text{ K}}}{I_{4\text{ K}}}$ ratio remains unchanged when measuring the photoluminescence with increasing temperature. The temperature-dependent behavior of the photoluminescence of the quantum dots grown on thin barriers is thus close that of thicker samples.

4.2.2 Design of the microdisk geometry

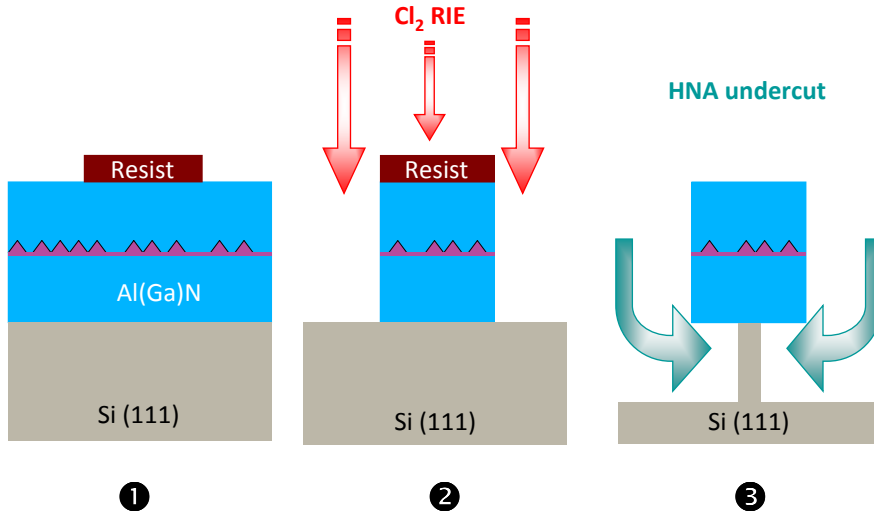


Figure 4.6 – Main steps of the top-down approach. RIE stands for reactive ion etching, and HNA for HF : HNO₃ : CH₃COOH

In this part, the fabrication of microdisk resonators is described. The processing steps are summarized on figure 4.6. After depositing a negative resist, either optical or e-beam lithography is performed on the as-grown layers (step ❶). The whole structure (AlN and silicon) is then etched using a Cl₂ / CH₄ / Ar plasma during 3 to 4 minutes (step ❷).

Finally, the Silicon is under-etched to fabricate the post and release the microdisk in $\text{HF} : \text{HNO}_3 : \text{CH}_3\text{COOH}$ (step ③). These processing steps are performed by our colleagues from either CRHEA or Institut d'Electronique Fondamentale (Université d'Orsay).

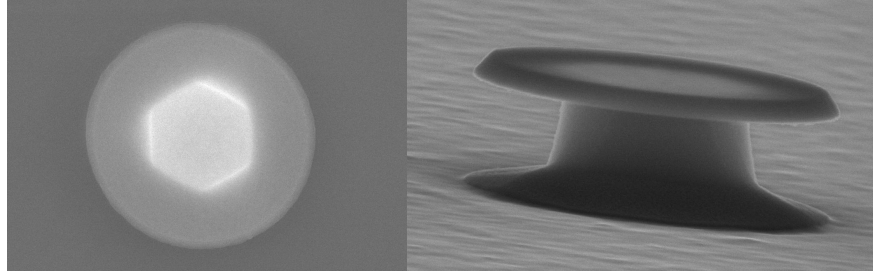


Figure 4.7 – SEM pictures of a $2\ \mu\text{m}$ disk - sample A1497-5

An example of structures designed by e-beam lithography is depicted on figure 4.7. A high quality etching is evidenced by the low roughness of the sidewalls. The silicon post underneath the microdisk is also observable. We will see in 4.4.2 that, depending on its diameter, the post can be a major source of cavity losses for some of the whispering gallery modes observable in a microdisk.

4.2.3 Studied samples

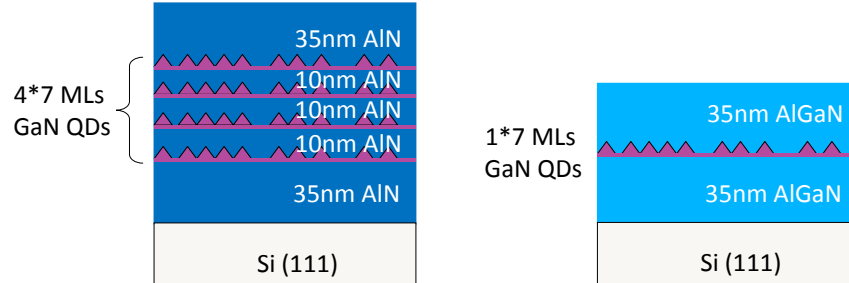


Figure 4.8 – Composition of the epitaxial layers: (left) samples A1496 and A1497. (right) sample A1282

In this work, we studied two types of samples. The first is formed by the stacking of four GaN/AlN quantum dot layers, grown on top of a 35-nm AlN layer, and capped by the same AlN thickness to ensure symmetry, and for a total slab thickness of 110 nm (figure 4.8, left panel). The fabrication used e-beam lithography. This is referred by the sample numbers A1496 or A1497. The second type is formed by the stacking of one GaN / $\text{Al}_{0.5}\text{Ga}_{0.5}\text{N}$ quantum dot layer, grown on top of a 35-nm $\text{Al}_{0.5}\text{Ga}_{0.5}\text{N}$ layer, and capped by the same $\text{Al}_{0.5}\text{Ga}_{0.5}\text{N}$ thickness, and for a total slab thickness of 70 nm (figure 4.8, right panel). The fabrication used photo-lithography. In the following, we will refer to this sample as A1282.

Figure 4.9 depicts the room-temperature microphotoluminescence spectra of two microdisks fabricated by e-beam lithography, one of $5\ \mu\text{m}$ in diameter (a) and the second

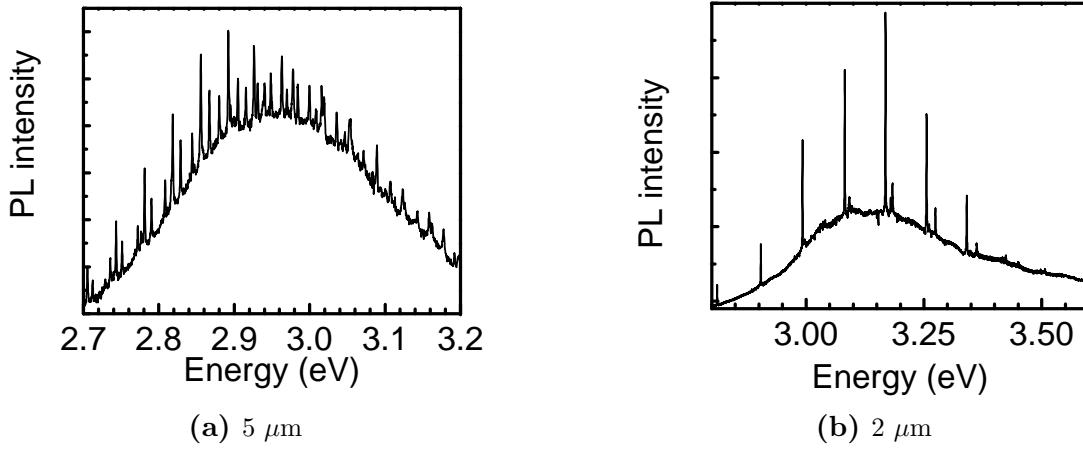


Figure 4.9 – Room-temperature micro-photoluminescence spectra of microdisks of two different diameters, top-detection (CEA): the broad emission of the GaN/AlN quantum dots are spectrally filtered by the whispering gallery modes - sample A1497

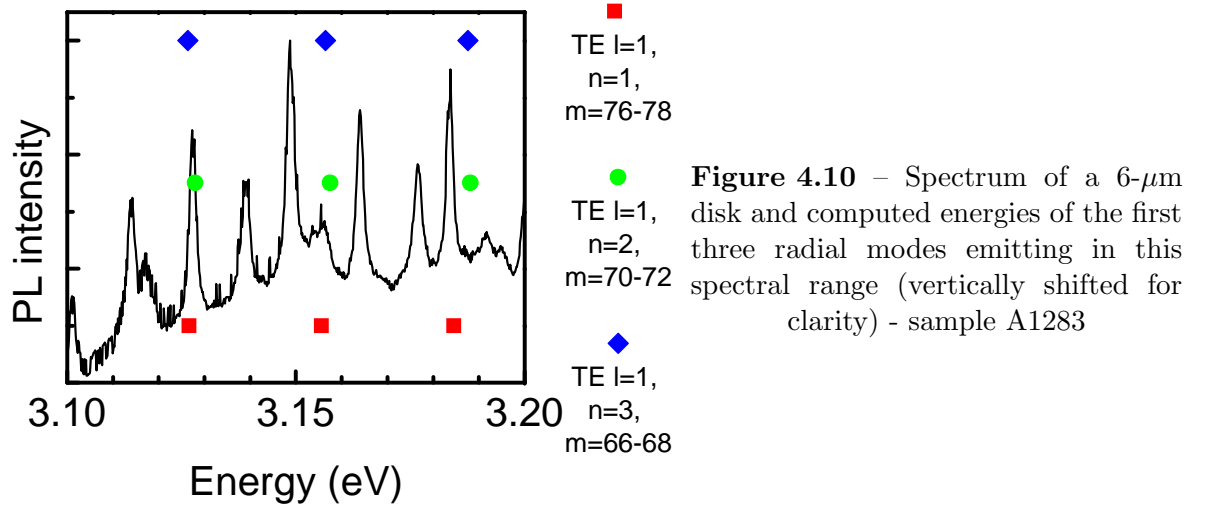
of 2 μm (b). The emission from 2.7 to 3.5 eV originates from the inhomogeneously-broadened emission of the quantum dots to the cavity electric field (full width at half maximum between 300 and 600 meV). On given precise spectral positions, however, each sharp peak originates from the emission of quantum dots coupled to a given whispering gallery mode.

4.3 Free spectral range and diameter

Now that the peculiarities of a microdisk resonator have been theoretically analyzed, the next step is to gain more knowledge on the whispering gallery modes appearing on a spectrum. They should have different properties because of different spatial or spectral localization. In this section, we will see that modal indexation is far from obvious, except when the mode number is small enough.

4.3.1 Comparison with calculations in the whispering gallery mode approximation

A zoom on the spectrum of a 6- μm disk is displayed in 4.10. We count on average 10 modes in a 100 meV spectral range. These structures have a rather wide diameter and the silicon post has a small radius, around 0.5 μm . By comparing with calculations made in the whispering gallery mode approximation, it thus appears that we must consider the modes of radial index $n = 1, 2, 3$ and values of the azimuthal index around $m = 70$. Let us remind that in the case presented on figure 4.10, the comparison between calculation and experiment is only about the *number of modes in a given spectral range, and not about the precise spectral position of a whispering gallery mode*. We must remember



that the spectral position of the modes obtained by calculations cannot be compared to the experimental ones because they are very sensitive to the effective index (and thus the exact slab thickness) and the exact diameter of the disk. However, the *free spectral range*, defined as the splitting between two modes issued from the same guided mode (TE $l=0$, TE $l=1, \dots$), same radial index n and successive azimuthal index $m \rightarrow m + 1$, better characterizes a given mode family.

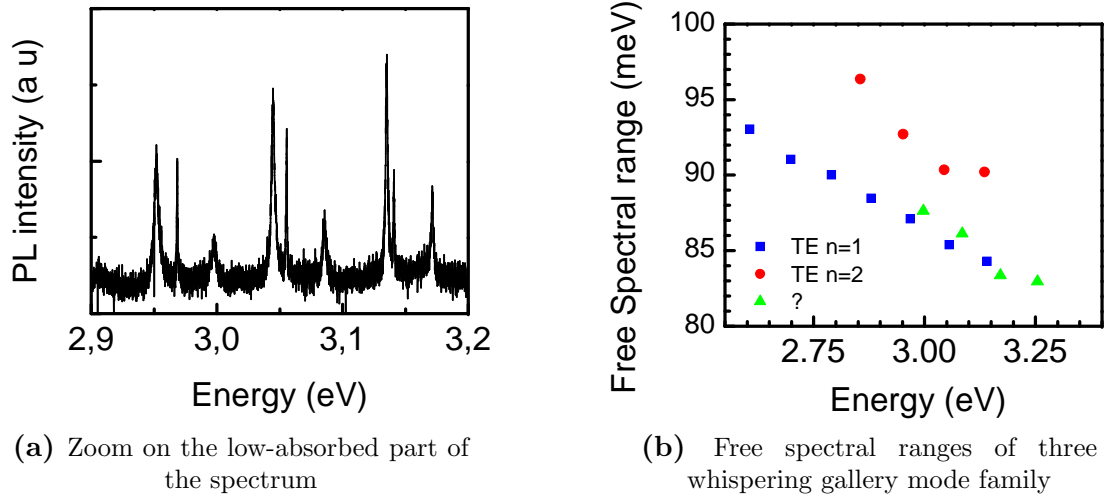


Figure 4.11 – Low-energy part of the spectrum of a 2 μm disk and corresponding free spectral range - courtesy M. Mexis

Figure 4.11a shows a zoom of the spectrum of a 2-μm disk. On figure 4.11b, three families of modes are observable. In this case we are able to recognize the modes belonging to the same families more easily than in figure 4.10 because the disk is three times smaller; the post is proportionally three times larger and thus makes the high-radial order cavity modes disappear³; the quality factors of the sample fabricated by e-beam lithography is several times larger than that of the disks designed by optical lithography. We

³by absorption by the silicon post, as discussed in 4.4.2

plotted the spectral range of the spectrum in the low energy part of the quantum dot emission. This is indeed the spectral region where the degradation of the quality factor due to cavity absorption is the lowest³ and thus the region where the modes are best resolved. For a 2- μm disk, this spacing lies in between 85 and 100 meV (figure 4.11b), whereas it seems to be in the range of only 30 meV in the case of a 6- μm diameter (figure 4.10). Calculations in the whispering gallery mode approximation were performed on a 2.06- μm disk and gave the free spectral range of two families of modes. The first family (first radial mode and azimuthal numbers m in the range 18–29) is found to have a free spectral range of 83 meV, whereas for the second family ($n=2$ and $m=14-24$), the free spectral range is 93 meV. Both were calculated around 3 eV. Thus we can ascribe the blue square modes to the $n = 1$ family and the modes depicted by red circles, to the mode family defined by $n = 2$.

The third mode family (green triangles on figure 4.11b) possesses the same free spectral range as the former $n=1$ group. We can thus tentatively suppose that the "blue square" modes and the "red triangle" modes stem from the same whispering gallery mode, split in two modes by a structural defect which couples the clock-wise and counter-clock-wise modes [Bor05].

4.3.2 Comparison with FDTD simulations

To confirm the previous attributions, more sophisticated simulations were conducted. These modes are depicted in figure 4.12, obtained by FDTD simulations⁴.

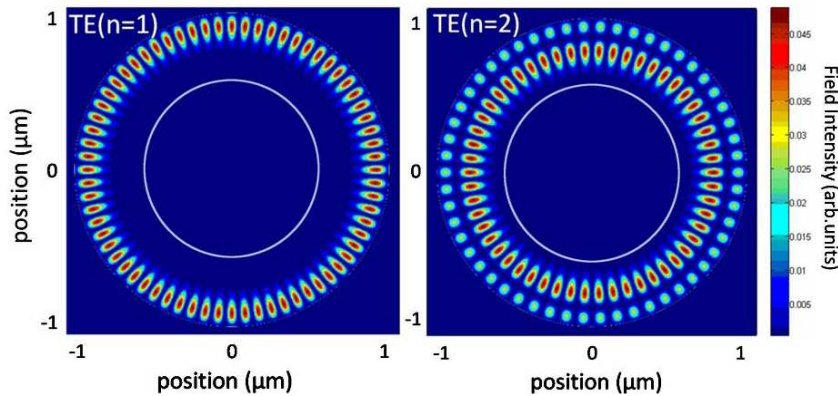


Figure 4.12 – FDTD first (left) and second (right) radial order modes for a 2.06 μm -diameter disk showing the TE field distribution within the disk plane (the light gray circle represents the post periphery) - extracted from [Mex11]

⁴see 5.2.2 for a reminder of the key principle

4.4 Measurements of record quality factors

We have seen that the modes can be indexed. It allows to gain more information about their spatial localization on the microdisk (by the values of n and m) and their spatial confinement (by the calculation of V_{eff}). Another feature which must be characterized for each mode is the quality factor. The quality factor of a cavity describes the time a photon stays confined into a cavity mode. Indeed, the field inside the cavity is damped:

$$E(t) = E_0 \exp\left(-\frac{\omega t}{Q}\right) \quad (4.21)$$

In practical terms, the longer the photons stay into the cavity mode, the smaller the cavity linewidth becomes in the emission spectrum. The quality factor is determined by this expression:

$$Q = \frac{\lambda_{cav}}{\Delta\lambda} \quad (4.22)$$

where $\Delta\lambda$ is the linewidth and λ_{cav} is the wavelength of the cavity mode, respectively. Without coupling to any electromagnetic mode from outside the cavity, a cavity mode does not show any broadening: it is purely monochromatic. When coupling to the continuum of free-space modes, it acquires a Lorentzian shape and therefore a finite full width at half maximum. The goal of this section is to understand which processes are responsible for photon losses.

4.4.1 Measurements of the quality factor

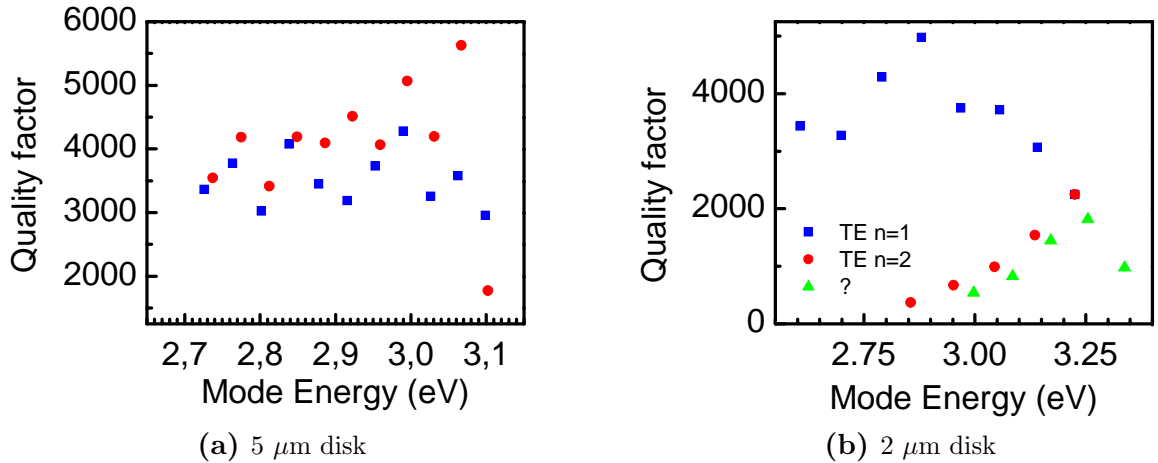


Figure 4.13 – Mode quality factors as a function of their spectral position - courtesy M. Mexis

Figure 4.13 shows the quality factors measured on microdisks fabricated by e-beam lithography. Values span between $Q=2000$ and 6000 for a microdisk of $5\text{-}\mu\text{m}$ diameter (figure 4.13a), and between 500 and 5000 for a $2\text{-}\mu\text{m}$ diameter (figure 4.13b). The

largest recorded value (not shown here) is $Q=7300$ at 3 eV on a 5 μm disk [Mex11] on a comparable cavity: this is the highest quality factor ever reported in AlN cavities.

A careful observation of the variation of Q leads to the following first comments. One can observe that the quality factor increases with the microdisk diameter. Furthermore, the families of the modes depicted in figure 4.13b have been determined (see labeling inside the plot). The evolution with energy depends on the mode family (same waveguide mode and same radial index). This is better evidenced in figure 4.13b, where the $n=1$ modes display an increased quality factor from 2.6 to 2.9 eV, and then a decrease until 3.3 eV. On the contrary, $n=2$ modes depict a quality factor increasing with energy. To understand these observations, we will discuss the possible origin of photon losses inside a microdisk.

4.4.2 Origins of losses in the microdisk resonator

The measured quality factor can be written as:

$$\frac{1}{Q} = \frac{1}{Q_{int}} + \frac{1}{Q_{abs}} + \frac{1}{Q_{scatt}} + \frac{1}{Q_{Si}} \quad (4.23)$$

where Q_{int} is the intrinsic contribution to losses, Q_{abs} is the absorption quality factor, Q_{scatt} stands for losses induced by scattering on the surfaces and Q_{Si} represents the coupling of light to the silicon post. The value that we actually probe is in general comparable to the smallest of the four above contributions. Let us detail their origins and discuss which are the dominant loss processes.

Intrinsic losses McCall *et al.* [McC92] have calculated the intrinsic quality factor of a microdisk, *i.e.* the losses attributed to the tunneling of the decaying light in the vicinity of the cavity periphery (between a and $n_{eff}a$):

$$Q_{int} = \exp(2mJ) \quad (4.24)$$

where m is the azimuthal index and:

$$J = \tanh \sqrt{1 - \frac{1}{n_{eff}^2}} - \sqrt{1 - \frac{1}{n_{eff}^2}} \quad (4.25)$$

with n_{eff} , the effective index of the slab waveguide. For an effective index of 1.75⁵, this results in an intrinsic quality factor $Q_{int} = 10^6$ for an azimuthal index $m = 20$ (typical of a 2- μm disk). For $m = 40$, the value of the intrinsic quality factor is $Q_{int} = 10^{12}$ (for a disk of diameter around 4 μm). These values are several orders of magnitude greater than the measured ones: *losses are thus extrinsic.*

⁵1.75 is the effective index of a 110 nm AlN layer for an emission at 3 eV

Cavity and quantum dot absorption Another possible origin of cavity photon losses is the absorption by the cavity. The quality factor associated to absorption is given by [Slu93]:

$$Q_{abs} = \frac{2\pi n_{eff}}{\alpha \lambda} \quad (4.26)$$

where α is the absorption coefficient of the layer. There are two main mechanisms contributing to absorption by the cavity.

First, we need to consider the *absorption by the quantum dots*. The quantum dot emission displays an approximately Gaussian inhomogeneous broadening, varying between 400 and 600 meV and centered around 3 eV (see figure 4.14). As a consequence, high-energy photons (around 3.7 eV), generated by smallest quantum dots, are likely to be reabsorbed by the excited states of larger quantum dots. Let us imagine that the microdisk is made of bulk GaN. Then equation 4.26 gives a value $Q_{abs,GaN} = 12000$ in the low-energy tail of the quantum dot emission, if we take for the value of the GaN absorption coefficient $\alpha_{GaN}(2.7 \text{ eV}) = 20 \text{ cm}^{-1}$ [Bru97]. In the high-energy tail of the quantum dot emission, however, as the GaN absorption coefficient is $\alpha_{GaN}(3.7 \text{ eV}) = 5.10^3 \text{ cm}^{-1}$ [Bru97], we deduce $Q_{abs,GaN} = 65$. In both calculations, the effective index was taken equal to 1.75.

This simple calculation shows the high sensitivity of the quality factor to absorption and explains why whispering gallery modes are not as well resolved in the high-energy tail of the quantum dot emission as in the low-energy tail: the quality factors of these modes become too small to observe them. Indeed, the best quality factors are recorded in the low-energy part of the quantum dot spectrum, as shown on figures 4.13b and 4.14. We can then ascribe the decrease of the quality factor from 2.85 to 3.25 eV to an increased absorption by GaN quantum dots.

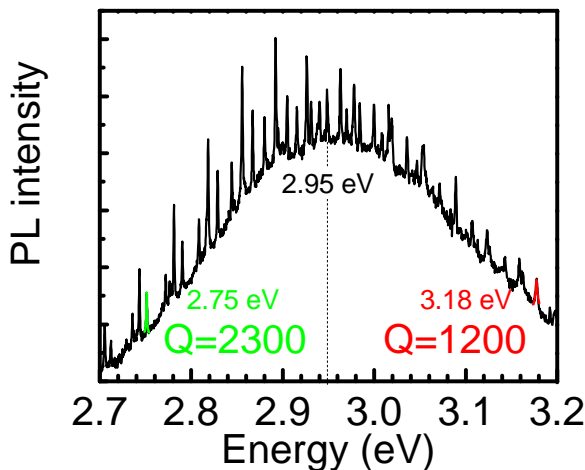


Figure 4.14 – Comparison of the quality factors in the low and high energy part of the quantum dot emission - sample A1497

However this strong dependence on the emission wavelength is partly smoothened by the low amount of active material in the total cavity thickness. We are working with quantum dots, which provide a small density of states, and thus a much weaker

absorption than bulk GaN. An evidence that absorption by the quantum dots is weak even at higher energy is the observation of whispering gallery modes all over the spectral range covered by the emitters, and contrary to what has been reported on microdisks using InGaN / GaN quantum wells as active layer [Sim07]. Yet the degradation of the quality factor from the low to the high energy tail of the quantum dot emission is observed in all our spectra: an example is given in figure 4.14, showing a factor of 2 between both values of the quality factor.

Note that a way to determine whether absorption by the active layer is the preeminent cause of losses is to study the mode linewidth with power. At transparency conditions (when half of the quantum dots are in the excited states), absorption and emission compensate each other: a clear narrowing is expected since Q_{abs} increases. This process has been reported *e.g.* by Peter *et al.* in [Pet05a]. We did not succeed in observing this transparency regime: with increasing the excitation power, the modes shift and sometimes vanish. These phenomena will be discussed in chapter 6.

As far as absorption is considered, this low density of states is an advantage. However, absorption and oscillator strength are related: when lasing is considered, the equality required between both absorption and stimulated emission rate will decrease the gain of a quantum dot laser compared to a quantum well laser. Lasing will therefore be less favorable with quantum dots as emitters. This aspect will be further discussed in chapter 6, section 6.4.

The other possible loss channel is the *absorption by the slab waveguide*. Most of the cavity volume is composed of AlN. It is thus relevant to consider in which amount its absorption — characterized by its absorption coefficient α_{AlN} — is responsible for a decrease of the quality factor. In our spectral range, the AlN absorption coefficient is $\alpha_{AlN}(390\text{ nm})=10^2\text{ cm}^{-1}$ [Dem86]. It leads to a quality factor of $Q_{abs,AlN} = 2800$ if $n_{eff} = 1.75$. As AlN absorption varies smoothly along the whole spectral range of quantum dot emission (which remains very far below the band gap), the losses originating from the cavity $Q_{abs,AlN}$ are expected to vary by around 30%.

From this value of $Q_{abs,AlN}$, we conclude that the absorption by AlN barriers could be one of the major processes inducing photon losses. Yet, again, this discussion is only qualitative since α_{AlN} is not precisely known and it strongly depends on the quality of the layer. Indeed, the presence of deep defects absorbing close to the wavelength range under consideration can increase the absorption coefficient [Nat03].

The comparison between GaN/AlN and GaN / Al_{0.5}Ga_{0.5}N quantum dot microdisks of 2- μm diameter fabricated with the same process have shown notable differences: the maximum quality factor of the former is around 5000 as reported on figure 4.13, whereas the latter is only 1450 [Mex11]. This observation shows that AlGaIn absorption is the preeminent source of losses. This loss enhancement when increasing the Ga content is due to an increasing defect density in the bandgap of the AlGaIn layer, which results in an enhancement of the absorption coefficient below the bandgap (in a spectral region

where it should not be absorbing). One must keep in mind the final goal of our studies, *i.e.* the fabrication of an electrically-pumped microlaser. Up to now, AlN microcavities display higher quality factors, but contacting these structures will be difficult as efficient doping of AlN layers is not achievable for now. On the contrary, AlGaIn layers would be easier to contact, but the quality factors of AlGaIn microcavities are lower. In order to increase the quality factors of AlGaIn cavities, further studies are therefore necessary to grow AlGaIn layers with a reduced sub-bandgap absorption.

Surface scattering The “bulk” source of losses has been analyzed in what precedes. One can wonder what is the surface contribution to the quality factor, more precisely the role of surface scattering in the determination of the quality factor. We have seen that whispering gallery modes lead to a strong confinement of the photons close to the sidewalls of the microdisk. Yet, as can be seen on figure 4.4b and 4.4a, the electric field leakage from the microdisk is expected to occur along the radius and along the vertical axis. Therefore the lateral surfaces ($r = a$), as well as the up and down surfaces close to the microdisk periphery (in $r \lesssim a$ and $z = \pm h/2$) are the places where intrinsic losses could occur. The quality of these sidewalls is thus of tremendous importance to measure a quality factor as close as possible to the intrinsic one.

It can be shown that the quality factor of a TE-built whispering gallery mode associated with a roughness defined by its correlation length L and amplitude standard variation σ can be written as [Bor05]:

$$Q_{scatt} = \frac{3\lambda_0^3(n_{eff}^2 - n_{air}^2)n_{AlN}}{4\pi^{7/2}n_{air}(n_{AlN}^2 - n_{air}^2)n_{eff}} \frac{\pi a}{Lh\sigma} \quad (4.27)$$

From this equation, we can already notice that Q_{scatt} decreases when the emission energy increases, because defects induced by roughness become of the same order of magnitude than wavelength. However, in the spectral range under consideration (2.8 – 3.2 eV), λ_0^3 decreases by a factor of 1.5 only. Besides, Q_{scatt} increases linearly with the radius a : we have seen that the smaller the diameter, the closer to the periphery the modes are. This observation explains why they become more and more sensitive to defects on the sidewalls.

Sylvain Sergent [Ser10] deduced the roughness correlation length and amplitude standard variation from an analytic treatment of high-resolution SEM images of microdisks fabricated by electronic-beam lithography. He found $L=50$ nm and $\sigma=2\pm 1$ nm. He then used equation 4.27 and obtained that, for a 2 μ m disk of 100-nm thickness, sidewall scattering leads to a quality factor of $3 \cdot 10^4$ in the spectral range of 2.8 – 3.2 eV. For a 5 μ m disk, sidewall scattering leads to a quality factor of 10^5 around 3 eV.

These values are one or two order(s) of magnitude greater than our experimental ones. Scattering by sidewall roughness therefore seems to be a negligible process as far as quality factors are concerned and confirms the qualitative statement based on the

observation of SEM images of the sidewalls. Yet, we have to keep in mind that the uncertainty under the evaluation of σ is 50%, therefore this evaluation of Q_{scatt} is valid with an accuracy of a factor of 3. However, in the case of UV lithography, the roughness of the sample is estimated to be $\sigma=10$ nm and $L=70$ nm. Therefore the quality factors due to scattering processes are around one order of magnitude below the values estimated for e-beam samples and may become the major source of losses.

Coupling with the silicon post At this point, it can be argued that the silicon post supporting the microdisk has not been taken into account in the previous calculations. One can also wonder if the silicon post underneath the cavity may result in detrimental additional losses due to the strong absorption coefficient of silicon. The coupling with the silicon post thus needs to be addressed. We can treat its physical consequences as a perturbation of the symmetrical system air / AlN / air (studied up to now) by using the following “trick”: the presence of the high index post will only affect the absorption beneath the microdisk ($\alpha_{Si,3.2\text{ eV}} = 3 \cdot 10^4 \text{ cm}^{-1}$ [Jel82], the field profile being the one calculated for the air / AlN / air geometry. We use the same absorption-induced quality factor as in equation 4.26:

$$Q_{Si} = \frac{2\pi n_{eff}}{\alpha_{Si}\lambda} \quad (4.28)$$

We thus take into account an effective absorption coefficient ascribed to the photon loss underneath the disk ($z < -h/2$, $r < b$):

$$\alpha_{eff} = \eta \alpha_{Si} \quad (4.29)$$

where b is the radius of the post and:

$$\eta = \frac{\iiint_{air+Si} |E|^2 d^3r}{\int_{space} |E|^2 d^3r} = \frac{2\pi \int_{r=0}^{r=b} \int_{-\infty}^{-h/2} (E_r^2 + E_\theta^2) r dr dz}{2\pi \int_{r=0}^{r=a} \int_{-\infty}^{+\infty} (E_r^2 + E_\theta^2) r dr dz} \quad (4.30)$$

is the fraction of electric field intensity which is likely to be absorbed by the silicon post. This calculation leads to figure 4.15, showing the proportion of intensity leakage versus the position along the radius of the microdisk, for the first five radial modes.

In a typical $2 \mu\text{m}$ disk, the post has a radius of $0.65 \mu\text{m}$ ⁶. As a consequence, absorption leaves the first radial modes unaffected: η is equal to $5 \cdot 10^{-4}$, thus the associated quality factor Q_{Si} is $2 \cdot 10^4$ if we consider an effective index of 1.75 and an emission at 3.2 eV. The absorption by the silicon post lowers the intensity of the second radial mode, but in a moderate way so it is still visible: η is equal to 10^{-2} , thus the quality factor Q_{Si} is 1000. However, it couples so well to the modes of higher radial indexes that we cannot observe them at all: for $n=3$, the ratio η reaches $4 \cdot 10^{-2}$: in this

⁶as measured in the typical SEM picture of figure 4.7

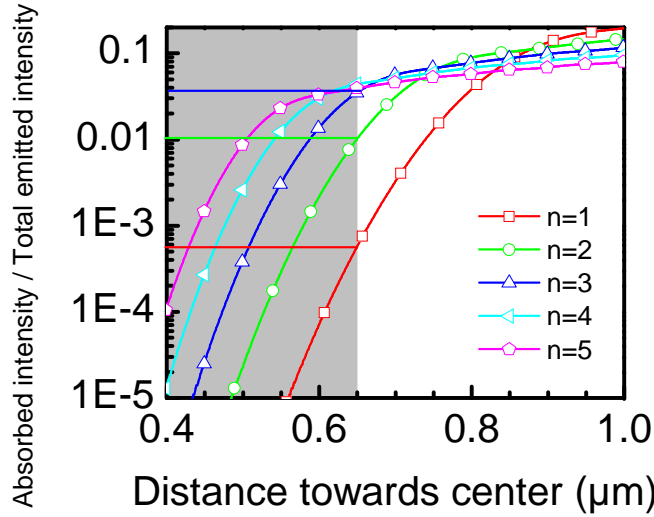


Figure 4.15 – Proportion of lost intensity normalized to the total intensity emitted by a $2 \mu\text{m}$ microdisk of thickness 70 nm. The first five radial modes are considered and the azimuthal number is taken equal to 20.

case, the losses induced by the silicon post Q_{Si} are as low as 200.

This process explains well the lower quality factor measured for the mode family defined by $n=2$ compared to that of the modes characterized by $n=1$ in figure 4.13b: the modes defined by $n = 1$ are localized much closer to the periphery than the $n = 2$ modes. Moreover, the third family of modes (green triangles on figure 4.13b) shows quality factors close to the values measured for $n = 2$. Furthermore, they seem to follow the same trend: increasing quality factor with increasing energy. From the values of their quality factors, they may belong to the $n = 2$ counter-clockwise family, and not to the $n = 1$ counter-clockwise family, as suggested in 4.3.1 from the values of their free-spectral range.

Conclusion

Table 4.1 summarizes our discussion and shows that the nature of the preminent source of losses is very sample-dependent.

Type of loss	Quality factor	Comments
intrinsic	$\geq 10^8$	irrelevant when compared to experimental values
active layer	$\geq 10^2 - 10^4$	unknown because α_{GaN} QD unknown
cavity	$1 \cdot 10^3 - 3 \cdot 10^3$	for $\text{Al}_{0.5}\text{Ga}_{0.5}\text{N}$ - AlN
scattering	$10^3 - 3 \cdot 10^4$	for UV – for e-beam lithography
silicon post	$10^2 - 10^4$	for $n=2$ – for $n=4$ and a radius post b : $b/a \approx 0.6$

Table 4.1 – Comparison of the quality factors induced by the major sources of photon loss in microdisks

In GaN/AlN quantum dot microdisks, photon losses mainly originate from AlN residual absorption. The coupling to silicon post is also a main channel for second order modes ($n > 1$). The absorption by the quantum dots is difficult to assess but is expected to be

non-negligible. Making use of e-beam lithography compared to optical lithography allows to reduce scattering losses by one order of magnitude.

4.5 Directionality and polarization of the emission

4.5.1 Directionality of the emission

Let us remind what is the origin of the observation of *positive peaks standing for whispering gallery modes in the photoluminescence spectra*. This stems from the fact that whispering gallery mode photons are emitted in preferential directions in the collection solid angle. Note that this is by no means a proof of the Purcell effect [Gay08].

As whispering gallery mode photons are confined in the slab waveguide, the emission is expected to be mainly in the microdisk plane. With our setup, we can collect the luminescence from the top of a microdisk (figure 4.16, left schematics). In order to collect more photons from the microdisk sidewalls, it is also possible to glue the sample on a tilted sample holder (figure 4.16, middle schematics). Our collaborators from Laboratoire Charles Coulomb (Université de Montpellier)⁷ can detect both in the top and in the side geometry (figure 4.16, right schematics).

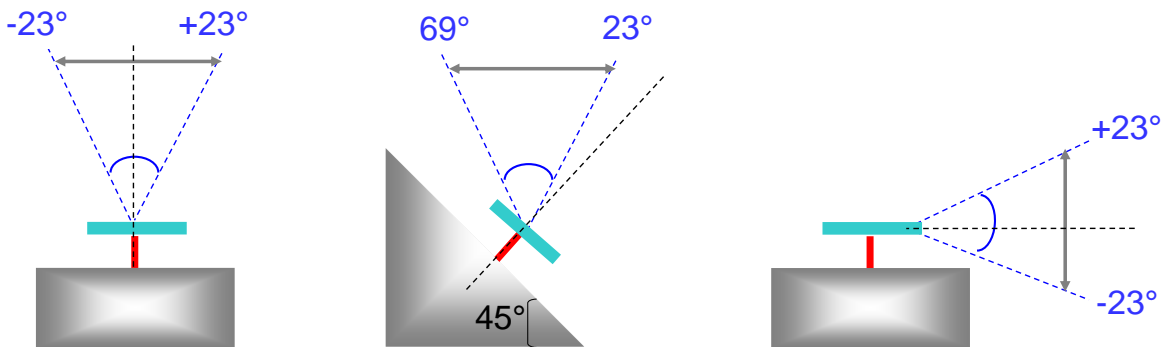


Figure 4.16 – Different collection geometry used for the results of this chapter: (left) top detection; (middle) top detection, with a tilted sample support; (right) side detection. The angles give the aperture of the light cone (numerical aperture is 0.4).

Figure 4.17 compares the spectrum of the same 3- μm microdisk, with varying detection geometry by the top or by the edge, respectively, as illustrated by figure 4.16, on the right or the left panel, respectively. We clearly see an enhancement of the signal originating from whispering gallery modes: the mode contrast is increased by a factor of 4 from top to side collection. Hence figure 4.17 shows that photons coupled to whispering gallery modes go out of the cavity with an approximatively in-plane wavevector.

From sample to sample, we found a variation of the mode intensity compared to

⁷Setup of Meletis Mexis, Christelle Brimont and Thierry Guillet

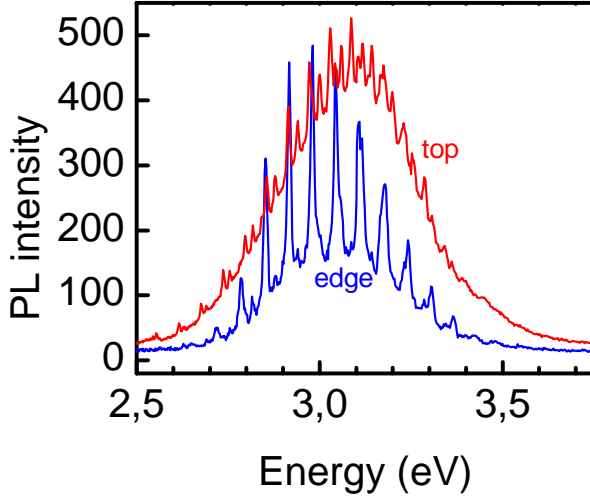


Figure 4.17 – Comparison between the spectra of the same 3 μm microdisk, detected either by the top or by the edge (L2C) - sample A1496 - disk A6

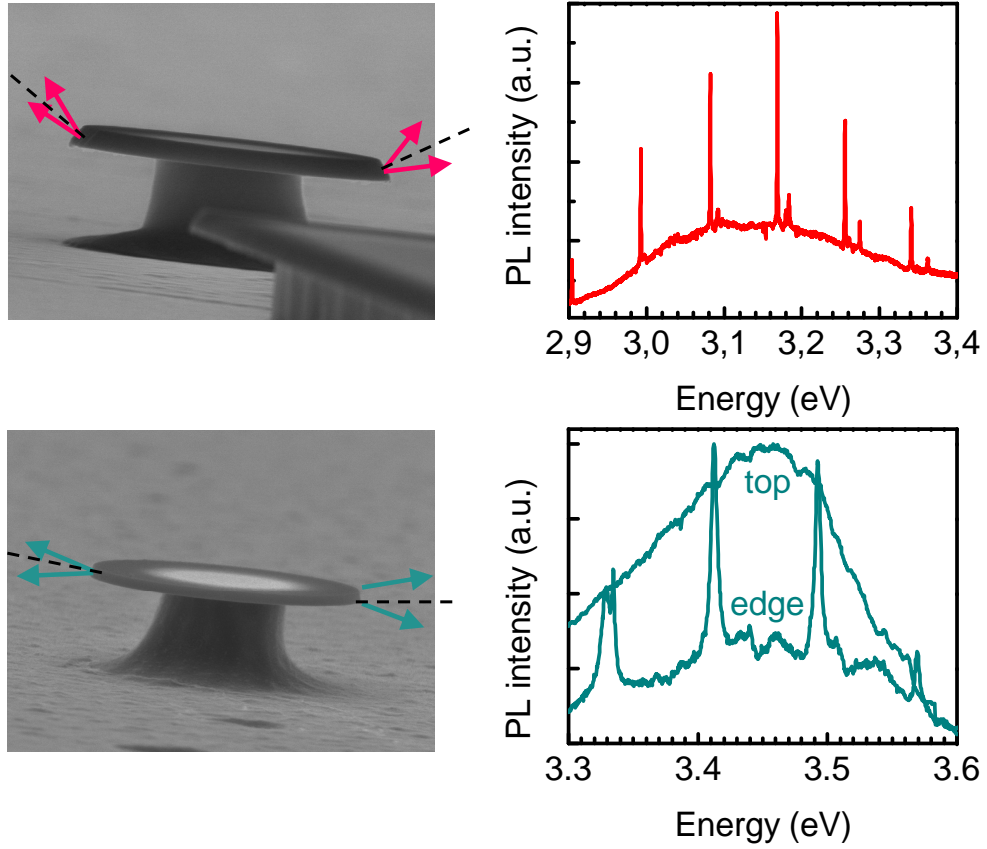


Figure 4.18 – Influence of mode contrast with etching profile: (top) detection by the front of the microdisk (INAC) - samples A1497-5; (bottom) detection by the top (INAC) and the side (L2C) - sample A1282-7

that of the uncoupled quantum dots (mode contrast). We will see that it is correlated to the *etching profile of the sidewalls*. In the far-field pattern of a microdisk, the directionality of the emission results from the directionality given to the cavity photons by the main directional loss mechanism, *i.e.* the directional process which displays the lowest quality factor. For a perfect structure, the directionality is fixed by intrinsic losses, thus we expect no whispering gallery mode emission when detecting by the front

of the microdisk. Peter *et al.* have conducted precise measurements of the emission angle in GaAs/AlGaAs microdisks [Pet07] and they obtained an emission centered around 7° , with a full width at half maximum as low as 6° . This angle broadening was attributed to constructive interferences with mode photons reflected by the substrate. On the contrary, a residual emission from the modes is observed in figure 4.17, suggesting that the direction propagation of the cavity photon was fixed by an extrinsic process.

Figure 4.18 depicts the spectra of two microdisks from two different samples, acquired in the top geometry, as well as their associated SEM pictures, depicted on the left hand side of the spectra. No whispering gallery mode are observable on the bottom spectrum of figure 4.18 when the detection was made by the top. In our own laboratory, we can only collect the luminescence by the top, and if necessary tilt the sample by 45° (see 4.16, middle sketch). Note that tilting this sample was not sufficient to detect emission from the whispering gallery modes. On the contrary, whispering gallery modes are observable in the side-detection geometry, as depicted on the top spectrum of figure 4.18. In order to explain this difference, we can point out different etching profiles: the top picture depicts very tilted sidewalls, around $30\text{--}40^\circ$, whereas the bottom picture displays an angle of around 5° . This difference could account for the difference in emission directionality. Consider the variation of thickness in the case of tilted sidewalls. In the bottom part of the periphery of the disk, the effective index is decreased, and so is the out of plane confinement: intensity leakages through the air cannot be ignored. This could account for a non-negligible redistribution of the allowed wave-vectors when coupling to free space is considered.

4.5.2 Polarization of the emission

From the beginning of this chapter, we have assumed that our slab is thin enough so as to ensure a perfect TE monomode waveguide, and that no TM mode could propagate into the waveguide. Let us check whether this assumption holds experimentally.

Figure 4.19a shows the spectra of the same $3\text{ }\mu\text{m}$ microdisk, with a polarizer detecting either the TE or the TM polarization. As expected, the emission is much more intense in the TE polarization: we observe an enhancement by a factor of 4 of the mode contrast when the signal is detected in the TE compared to the TM polarization. Quantum dots out of resonance with any whispering gallery mode couple much more efficiently with the TE polarization, and the ones which are in resonance with a cavity mode also emit much more photons in the TE mode than the TM mode, as evidenced by the better mode contrast in TE polarization. Yet the coupling to the TM mode cannot be completely ruled out: figure 4.19b shows that, even if most whispering gallery modes are built on a pure TE or essentially TE polarization (TE>TM), a very small proportion of them are essentially TM (TM>TE) or even 100% TM. However, this extra-coupling will not decrease the value of the coupling efficiency to the TE modes. Indeed, both TE and TM

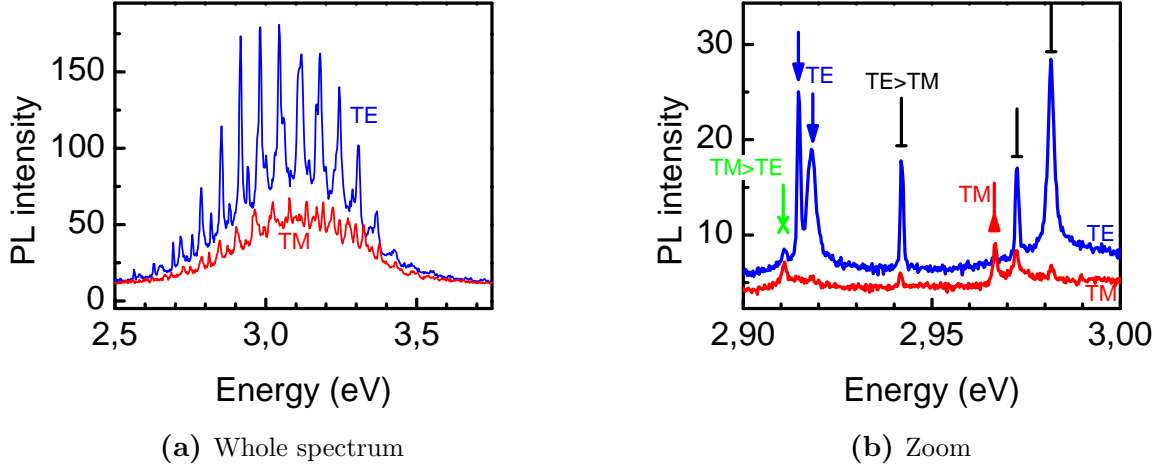


Figure 4.19 – Polarization of the modes (L2C) of a 3 μm disk. The emission of uncoupled quantum dots and from the whispering gallery modes is mainly TE. Some modes are hybrid TE-TM, with a larger contribution from the TE polarization (TE>TM) or TM (TM>TE). Very few modes are purely TM - sample A1496-2 - disk A5

modes are not emitted at the same energy, and thus a quantum dot in resonance with a TM mode usually could not have coupled to a TE mode. The observation of some pure TM modes suggest that the dipole of the quantum dots has a small component perpendicular to the microdisk (parallel to the \vec{c} axis), contrary to the polarization of a pure strain-free A excitonic emission, which is entirely perpendicular to \vec{c} .

Conclusion

To conclude, the emission from a microdisk is intrinsically directional, but extrinsic factors such as the angle between the waveguide and the etching direction can weaken this directionality. As far as the polarization is concerned, a TM emission is observed, but it remains weak compared to the TE one. The hypothesis of considering only the first TE mode, stated in 4.1.1, is therefore justified *a posteriori*.

4.6 Whispering gallery modes — towards a Purcell-enhanced microdisk laser

We expect the emission of a microdisk to lie in the slab plane. Yet, depending on the etching profile and the roughness of the sidewalls, a good mode contrast can be achieved by collecting from the top. For wide diameters (greater than 3 μm) and small enough post diameters it is rather difficult to index each mode of a microdisk spectrum. For smaller diameters or greater post diameters, the comparison of both calculated and measured free spectral range allows to index each mode.

With a modal volume of $6(\lambda/n)^3$ and a quality factor of 4000, the maximal Purcell factor we would be able to measure is around $F_{P, max} = 60$. The spectral and spatial mismatch between quantum dot dipole and cavity electric field leads to a smaller measurable value, of the order of 1/3 of the maximal enhancement, leading to an expected Purcell effect of $F_P=20$: it should be high enough to be detected.

On small enough microdisks (around 2 μm in diameter) we can isolate a few families of high-quality factor modes separated by a free spectral range around 90 meV. This makes the comparison of the lifetimes of both resonant and non-resonant quantum dots comfortable for a tentative measurement of the Purcell effect by time-resolved photoluminescence.

The mode coupling factor β measures the ratio of photons emitted in a cavity mode over the total number of photons emitted by a quantum dot and can be written as:

$$\beta = \frac{F_P}{F_P + 1} \quad (4.31)$$

if the emitter is coupled to one mode only. In our case, with the average value of $F_{P, average}=20$, $\beta=0.95$. These structures may behave like micro- thresholdless-lasers.

Both points will be discussed in chapter 6.

Optical study of GaN/AlN nanocavities in photonic crystal waveguides

COMPARED TO MICRODISKS, photonic crystal cavities offer much more possibilities in terms of design: much more parameters can be tuned. It is indeed possible to vary the photonic band gap, by changing the periodicity and / or the hole radius. This way, we are able to change both the spectral and wavevector ranges which are forbidden for any photon inside the photonic crystal. The cavity, which consists in creating an allowed discrete state inside this band gap, can also be tuned by e.g. its shape or its dimensions.

However, the price to pay to obtain an optimized structure is the much more difficult fabrication process compared to that of microdisks, especially in the UV range since the hole radius must be in the 40-50 nm range in order to obtain a band gap around 380 nm. Both lithography and etching processes need to be controlled in the range of single nanometers, which is all the more challenging knowing the inertness of nitride materials towards etching processes.

We first studied structures exhibiting a modal volume as low as $0.8(\lambda/n)^3$, i.e. modified L3 cavities. An L3 cavity consists of the omission of three holes from the same “line” of the photonic crystal (see SEM picture on figure 5.1(e)). It was modified because holes adjacent to the cavity were shifted (see discussion in part 5.1.3 of this chapter). Our colleagues from L2C measured a maximal quality factor of 1800 at 425 nm [Née11], while the intrinsic quality factor was calculated by FDTD simulations and estimated to be 4800. Measuring an experimental quality factor equal to 40% the predicted value is quite satisfactory, knowing that these photonic crystals were fabricated in a challenging bottom-up approach depicted in figure 5.1 (a) - (d). However, these structures turned out to be very sensitive to fabrication-induced defects, resulting in a poor reproducibility.

This chapter therefore aims at studying more complex structures which were designed to be more robust as far as processing defects are concerned.

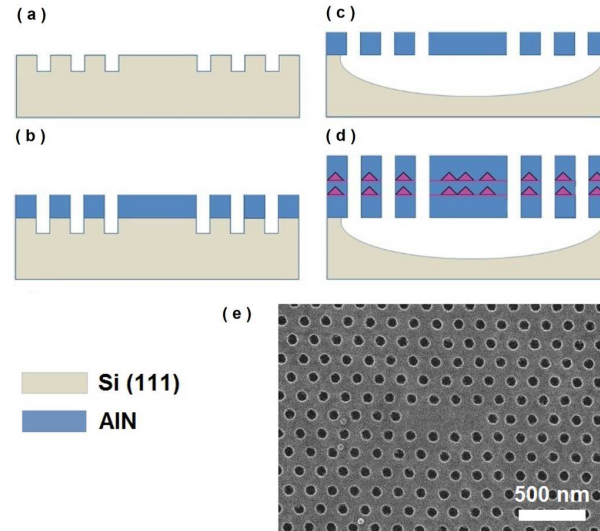


Figure 5.1 – (a) - (d) Main steps of the bottom-up fabrication process. (e) SEM picture of the L3 cavity. Extracted from [Née11]

Contents

5.1	Introduction	127
5.1.1	Opening of a photonic bandgap around 3.2 eV	127
5.1.2	Fabrication process	127
5.1.3	Design	128
5.2	First experimental results and simulations	130
5.2.1	Mode spectral positions	130
5.2.2	FDTD simulations	131
5.3	Identification of the modes	133
5.3.1	By their spectral positions	133
5.3.2	By comparison with calculated mode splittings	134
5.3.3	By micro-photoluminescence scan along the waveguide axis	136
5.4	Quality factors	140
5.4.1	Origin of extrinsic losses	141
5.4.2	Record value of the quality factor	142
5.5	Highest energy series: towards UV nanoresonators	144
5.5.1	Mode spectral positions and splittings	144
5.5.2	Quality factor at 3.46 eV	145
5.6	Chapter conclusion : towards the Purcell effect	146

5.1 Introduction

5.1.1 Opening of a photonic bandgap around 3.2 eV

Our goal is to confine light on defects whose energy lies inside a photonic band gap. We target an emission around 3.2 eV: this is the central spectral position of our quantum dot emission. The first step was to determine which photonic crystal could achieve the largest band gap possible centered at 3.2 eV. All the photonic computations presented here were performed at Institut d'Electronique Fondamentale (Université Paris Sud)¹. Such calculations use a two-dimensional plane-wave expansion of the electromagnetic field, followed by a Fourier transform. The supercell method is used to apply periodic boundary conditions in the two-dimensional photonic crystal plane, while the thickness of the slab layer is taken into account by using an effective index. The value of the permittivity is thus entered in the software at any point of the photonic crystal. Afterwards, the dispersion profile is plotted for each particular mode.

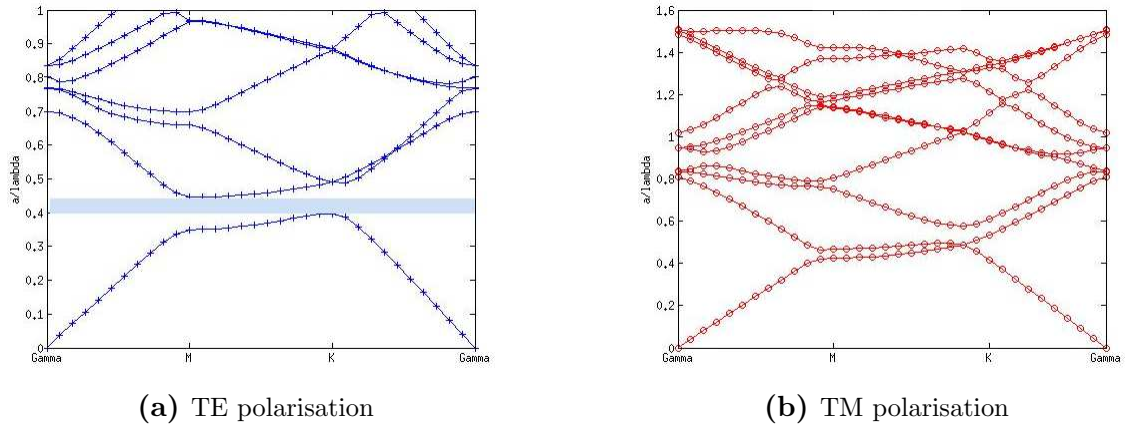


Figure 5.2 – Photonic band gap structures for a 100-nm thick AlN membrane , $a=170$ nm and $r/a=0.324$

The optimal structure was found to have a periodicity $a=170$ nm, and a hole radius to periodicity ratio r/a of 0.324. In these conditions, a forbidden energy gap opens in TE polarisation for normalized photon wavelengths between $a/\lambda=0.4$ and 0.44 , *i.e.* λ between 386 and 425 nm. Figure 5.2a illustrates the presence of this gap in TE polarization, while figure 5.2b shows the absence of any gap in TM polarization.

5.1.2 Fabrication process

The fabrication process is described on figure 5.3.

First, a 35 nm AlN layer was deposited by ammonia-source MBE on a Si(111) wafer, on top of which a GaN quantum dot layer was grown. Capping by 35 nm of AlN was

¹by Delphine Néel and Xavier Checoury

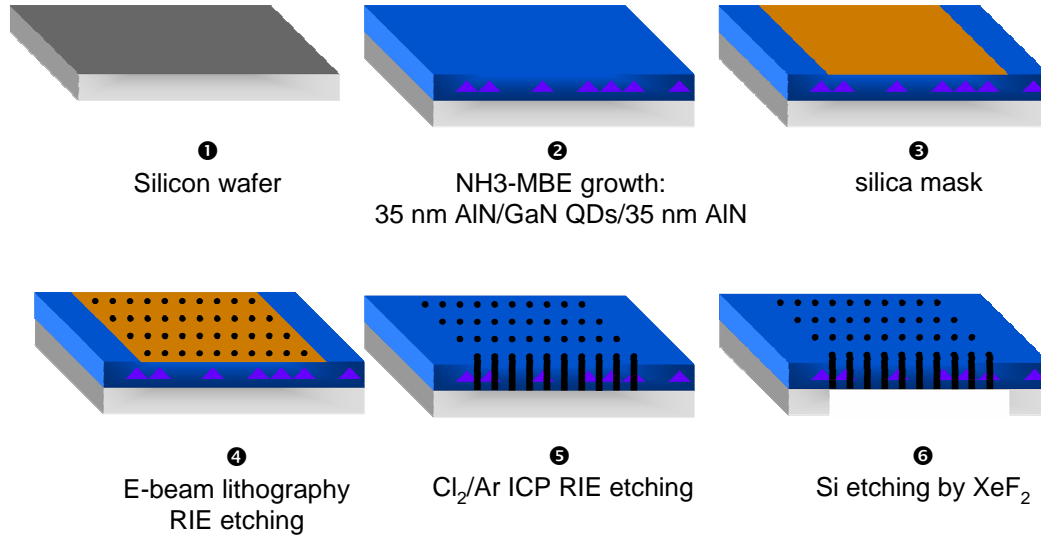


Figure 5.3 – Main steps of the fabrication process

then performed to ensure the symmetry of the slab structure. It has to be mentioned here that the high optical quality of GaN/AlN quantum dots on a very thin buffer layer and highly mismatched Si substrate is still challenging². After growth, a 70 nm slab guide containing a layer of quantum dots designed to emit around 380 nm is obtained. This epitaxy deposition was performed in CRHEA (CNRS, Valbonne).

Second, a 100-nm thick silica layer is then deposited in order to be used as a hard mask for AlN etching. The silica layer is patterned by a 80 keV e-beam lithography followed by reactive ion etching. After cleaning of the resist residues, the pattern is transferred to AlN by chlorine-based inductively coupled plasma etching with Cl₂/Ar (20 sccm/5 sccm) gas. Finally, the membrane is released by selective etching of the first 200 μm thick Si substrate using XeF₂ gas. These processing steps were performed in Institut d'Electronique Fondamentale (Université Paris Sud).

5.1.3 Design

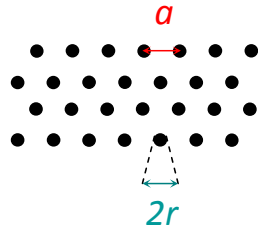


Figure 5.4
– Schematics of the photonic crystal pattern

We will begin by describing the structure of the photonic crystal. A schematics is given on figure 5.4. As the fabrication process is not precise within the nm, the

²as discussed in chapter 4

periodicity, the hole radius and the lithography dose were varied in order to seek for the optimal set of parameters. The periodicity a of the photonic crystal was varied from 150 to 210 nm, while the hole radius r ranged from $r/a=0.25$ to 0.33 so as to achieve a band gap at around 380 nm. The lithography dose was also varied. It is defined as the ratio of the electron intensity used during the process to the intensity needed to design the same pattern, if it was completely isolated. This parameter affects mainly the hole dimension and was chosen to span from $D=0.35$ to 0.50. Modes were clearly resolved for $r/a=0.25$ to 0.29, and a dose ranging from 0.35 to 0.45. Above these values, we obtained too large a photonic band gap, and the modes were centered at too high an energy to be probed by our quantum dots, whose emission was centered at 3.2 eV with 400 meV as full width at half maximum. The filling factor is:

$$f = \frac{S_{1 \text{ hole}}}{S_{\text{lattice}}} \approx 30\% \quad (5.1)$$

where $S_{1 \text{ hole}}$ (respectively S_{lattice}) is the surface occupied by one hole (respectively one unit cell) for the structures investigated in what follows.

Then, compared to a purely symmetrical 2D array, the central hole line was omitted, forming a *one-dimensional W1 photonic crystal waveguide*. A photonic waveguide confines light in the direction of its axis by photonic bandgap guiding: light is diffused by each air hole of the surrounding cladding and interferes constructively (see figure 5.5). This way, light propagation along the waveguide is possible.

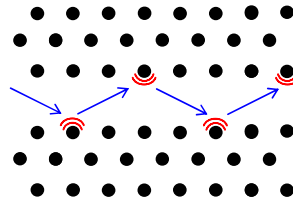


Figure 5.5
– Schematics of photonic
band gap guiding

The spacing between both adjacent hole lines was equal to $\sqrt{3}a$. The schematics of the photonic band structure of a W1 waveguide is shown in figure 5.6. Inside the bandgap, discrete modes are visible: they account for the quantization of the wavevectors originating from the criterion of constructive interferences. Each mode has its own cut-off frequency. At these points, the photonic density of states diverges because these regions correspond to low group velocities. For more information on photonic crystal waveguides, please refer to [Lou08] and [Oli02].

Then, the *cavity* was designed. At the center of the cavity structure, thirty holes were slightly shifted in the direction perpendicular and opposite to the waveguide to create a photonic cavity. On each side, two holes belonging to the line adjacent to one-dimensional waveguide (a) were shifted by d , varying from $d=0$ nm (no cavity) to $d=12$ nm. The four holes adjacent to these two holes (b) were shifted by $2d/3$. Finally, the eight holes adjacent to these five were shifted by $d/3$ (c). This way, we can avoid

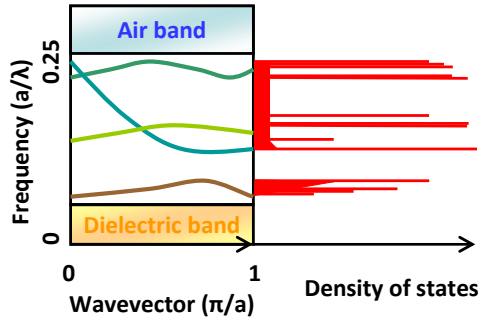


Figure 5.6 – Schematics of the photonic bandgap structure of a W1 waveguide inside a triangular lattice of air holes inside a dielectric slab layer and associated density of states

abruptness in the cavity design. It was indeed reported that the Q/V ratio is maximum when the confinement is “gentle” [Aka03]. Experimentally, this means that a slight shift of the adjacent holes in a photonic crystal cavity smooths the Bragg reflection conditions, and therefore decreases the losses for smaller wavevectors.

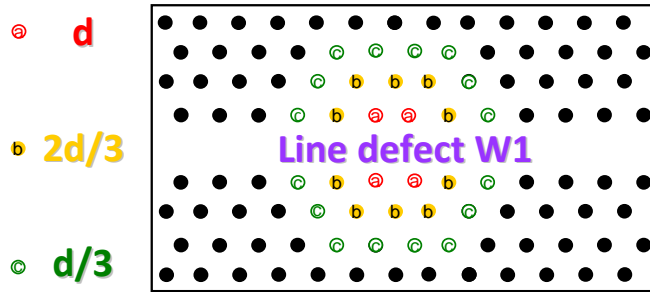


Figure 5.7 – Design inspired by [Kur06]

Figure 5.7 shows a schematics of the targeted design (design A1 of reference [Kur06]). Figure 5.8 displays a SEM picture of the structure. We clearly see the waveguide, but the cavity is too small to be evidenced with this magnification.

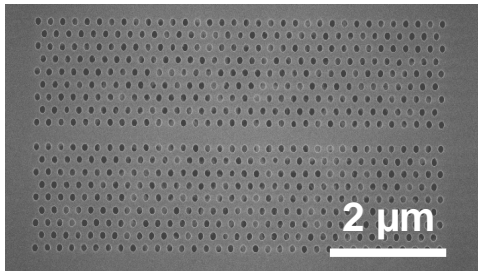


Figure 5.8 – SEM view of a photonic crystal

5.2 First experimental results and simulations

5.2.1 Mode spectral positions

Figure 5.9 depicts the micro-photoluminescence of a series of photonic crystal waveguide cavity with increasing the hole shift d at room temperature and ambient pressure. The top spectrum is the luminescence of the bare waveguide, with no additional displacement. In the lower graphs we plotted the luminescence of the cavities with increasing hole shift.

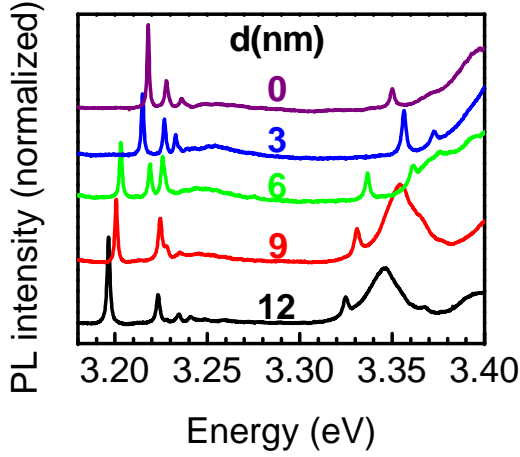


Figure 5.9 – Room-temperature micro-photoluminescence of photonic crystal structures of various cavity size - sample A1507: $D=0.40$; $r/a=0.27$; $a=170$ nm

Several modes are detected. We can observe a low energy group between 3.22 and 3.24 eV. The fact that modes are clearly visible even at $d=0$ nm indicates that they are related to the waveguides: they should be *guided modes* displaying Fabry-Pérot interferences. Besides, a lower energy peak appears between 3.19 and 3.21 eV, and blueshifts by 30 meV from $d=12$ to either 3 or 6 nm, while being absent in the spectrum of the pure waveguide. This result suggests a different light confinement for $d=12$ than for 3 nm. We therefore tentatively ascribe these low-energy modes to the *cavity*. At higher energy, between 3.325 and 3.335 eV, another mode blueshifts with decreasing hole shift. It should also be ascribed to the cavity emission: it may be an excited state of the cavities.

We will see in 5.4 that these structures exhibit high quality factors, in the 2000–3000 range.

5.2.2 FDTD simulations

The near- and far-field emission from these structures have been predicted by calculations performed in Institut d'Electronique Fondamentale. In figure 5.10a, we have plotted the near-field expected for a cavity embedded in a waveguide. This plot gives access to the spectral position and quality factor of the mode resonances of the structure. It is computed by a three-dimensional finite decomposition of the field in the base of evanescent sinusoidal functions. A large broadband excitation without any particular symmetry leads to the spectral positions of the resonances. Then, a quasi-monochromatic excitation, with fixed symmetry, gives access to the modal volume. The cavities under study were found to have a modal volume of $V_{eff} = 2.2(\lambda/n)^3$. On figure 5.10b, the far-field deduced from 5.10a is depicted. It is obtained by performing the Fourier transform of the near-field, which is the mathematical equivalent to light propagation in free-space. One thus obtains locally spherical waves, with non-zero intensities in some given directions only, corresponding to propagating directions. The

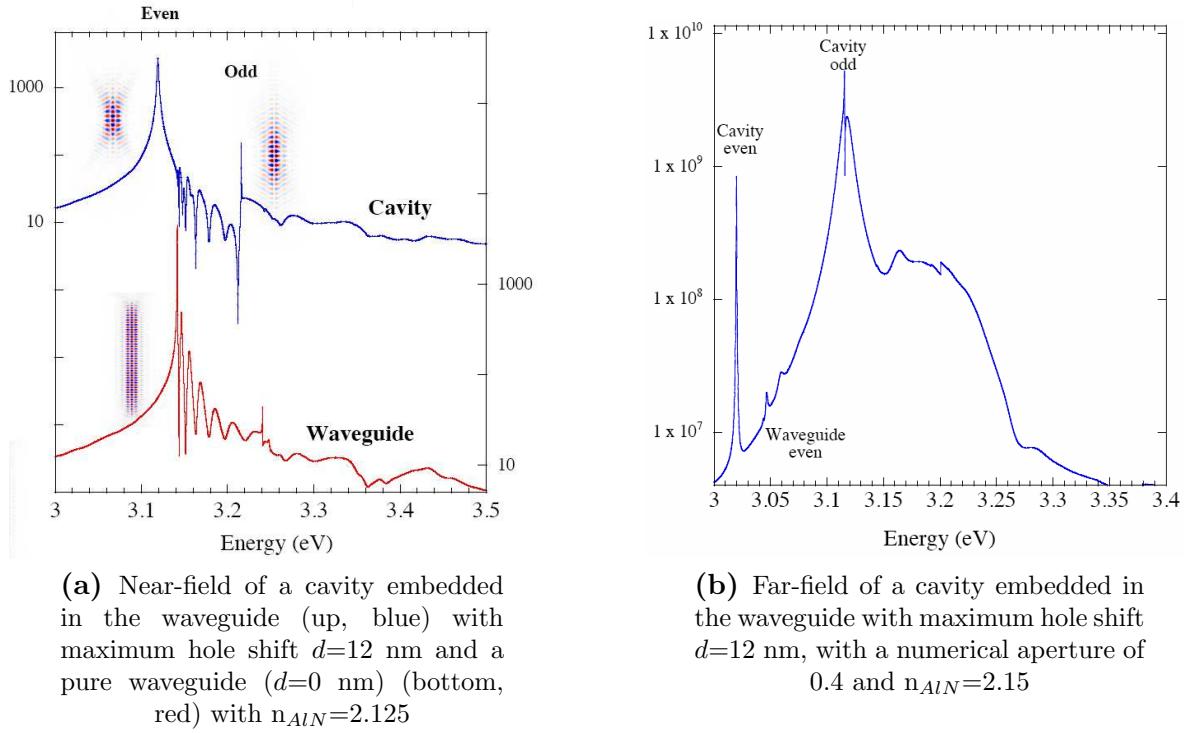


Figure 5.10 – Calculated spectra of the structure considering a membrane 65 nm thick, $a=170$ nm, $r/a=0.25$

values of the used set of parameters are given in the caption and were adjusted around their nominal value in order to fit the experimental spectra studied in this section. Note that the slight blueshift between the near- and the far-field profiles is due to a different slab index taken for the calculations.

Conclusion

In this first section, we have seen that the top-down processing of nitride layers can lead to high optical quality photonic crystal cavities. This is a more comfortable approach than bottom-up design, which consists in conformal overgrowth on an etched silicon layer. Moreover, extended defects such as photonic crystal waveguides can efficiently confine light, in spite of the lower index of AlN layers compared to that of the materials usually used to design such structures (GaAs or silicon). Finally, both micro-photoluminescence and calculated spectra seem to display similarities. We need to confirm the attribution of the modes in the experimental results by further discussions and measurements.

5.3 Identification of the modes

5.3.1 By their spectral positions

From both figures 5.10a and 5.10b, we can identify several families of modes. The microphotoluminescence spectra of figure 5.9 are plotted again on figure 5.11, so the modes are indexed by a comparison to the near- and far-field profiles from figures 5.10a and 5.10b. Two main resonances separated by 100 meV are attributed to the cavity. The lower (respectively higher) peak has an even (respectively an odd) parity. Their profiles are plotted on figure 5.12: the fundamental mode (up-left) has an even parity compared to the waveguide axis and radiates in the (\vec{x}, \vec{y}) slab plane, towards the corners of the photonic crystal. On the other hand, the first excited cavity mode (up-right) has an odd parity and radiates more efficiently perpendicularly to the plane waveguide, in the \vec{z} direction.

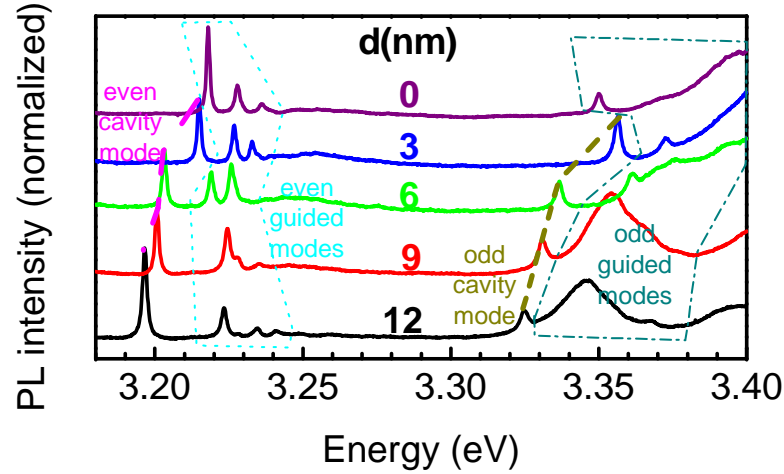


Figure 5.11 – Room-temperature microphotoluminescence of photonic crystal structures of various cavity size - sample A1507: $D=0.40$; $r/a=0.27$; $a=170$ nm

Several resonances are observed 20 meV above both cavity modes. From their field cartography, they can be ascribed to Fabry-Pérot guided modes, the lower (respectively higher) energy group between 3.15 and 3.20 eV (respectively above 3.35 eV) being even (respectively odd) modes. Multiple oscillations are obtained in the near-field profile. However, on the far-field computation, a smaller number of guided modes are observed, due to a limiting collection geometry. The field profile of the fundamental guided mode is depicted on figure 5.12 (bottom): as expected, this mode extends on the whole waveguide.

Such a high variety of cavity and waveguide modes were detected in our experiment because we probe all the polarizations by exciting the photoluminescence of embedded quantum dots, similar to the studies performed by Stumpf *et al.* [Stu07]. Usually these structures are probed by transmission measurements with a symmetrical laser beam (see

e.g. [Kur06]), therefore only the fundamental modes can be observed.

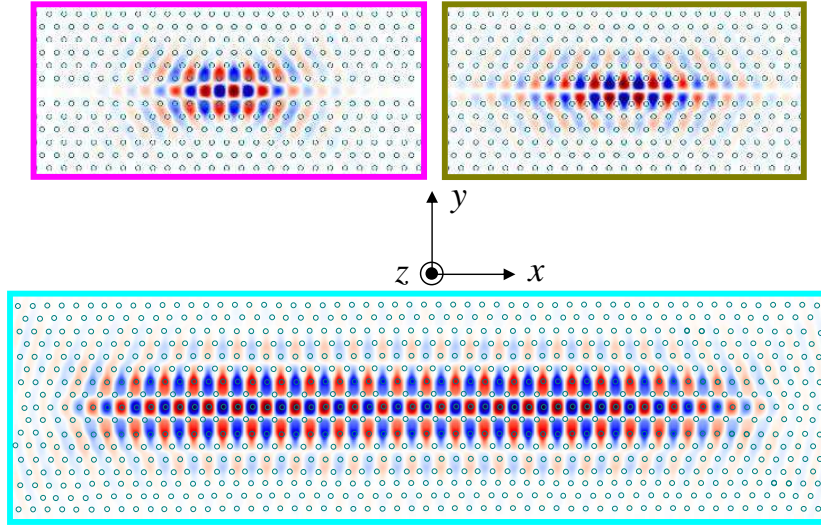


Figure 5.12 – Cartography of the field H_z or E_y for both even (up, left) and odd (up, right) cavity modes and the fundamental waveguide mode (bottom). The three profiles are plotted at the same scale

Figure 5.13 shows the spectral positions of both cavity and guide modes, from both experimental spectra and FDTD computations. In the series investigated, the agreement is satisfactory, except for the odd guided modes.

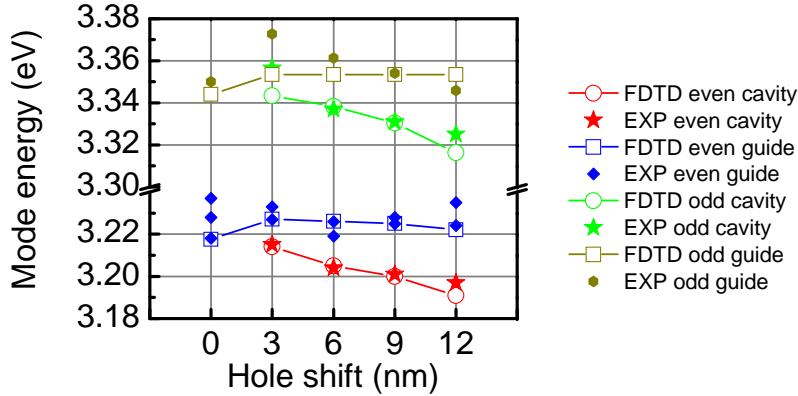


Figure 5.13 – Evolution of the spectral positions of odd and even cavity and guided modes with increasing hole shift - sample A1507: $D=0.40$; $r/a=0.27$; $a=170$ nm

5.3.2 By comparison with calculated mode splittings

The series of cavities presented in figures 5.9 and 5.13 follows a rather monotonic trend in terms of mode spectral positions when varying the cavity size. Yet this was not the case for all the series we studied, and we therefore chose to assign the mode nature by studying the splittings between the modes rather than their absolute positions.

Imperfections inside a photonic crystal such as non-intentional shift of the position of one hole and sub- or sur-insolation during the lithography process have to be considered. If such defects are randomly located inside the crystal, we expect the guided modes to be more affected than the cavity mode, as the first are deconfined along the whole waveguide and therefore have a mode volume much greater than the volume of the cavity mode.

Moreover, from one photonic crystal to another, inhomogeneities appearing during lithography have also to be taken into account. When we consider a series of photonic crystals with increasing hole shift, other parameters which are meant to be fixed could be slightly different at the scale of the whole photonic crystal, such as hole position or hole diameter. By considering the splittings instead of the absolute positions, spectral shifts should compensate each other, at least between modes of equivalent modal volumes, because both will be affected by the same defects, hence their emission will be equally shifted.

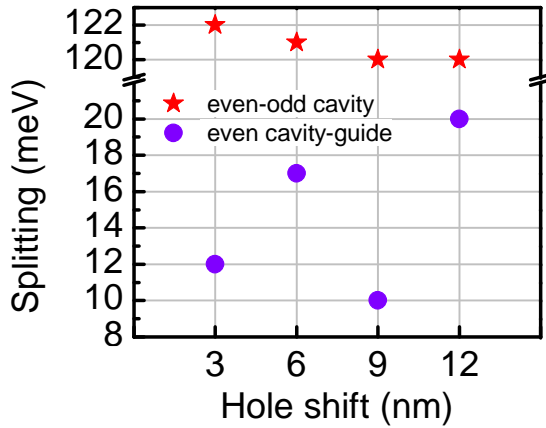


Figure 5.14 – Experimental splittings between even cavity and first even guided mode and odd and even cavity modes - sample A1507: $D=0.40$; $r/a=0.25$; $a=170$ nm

To illustrate this point, we plotted in figure 5.14 the splitting between both even cavity and guided modes and even-odd cavity modes splittings, for another series with parameters close to the one studied up to this point. We can see that the splitting between even cavity and guided modes is erratic, because the inhomogeneities of the photonic crystal parameters strongly affect the waveguide mode. On the contrary, the spectral difference between even and odd cavity modes, probing smaller volumes, keeps the smooth and expected behavior.

In the following, we will thus compare both simulated and experimental splittings. For the series under study, the results are plotted in figure 5.15. The agreement is satisfactory, unless for the splitting between even and odd cavity mode for $d = 3$ nm. Further studies will be presented in 5.3.3 on this structure in order to understand the discrepancy between the simulated and the experimental values of the splitting.

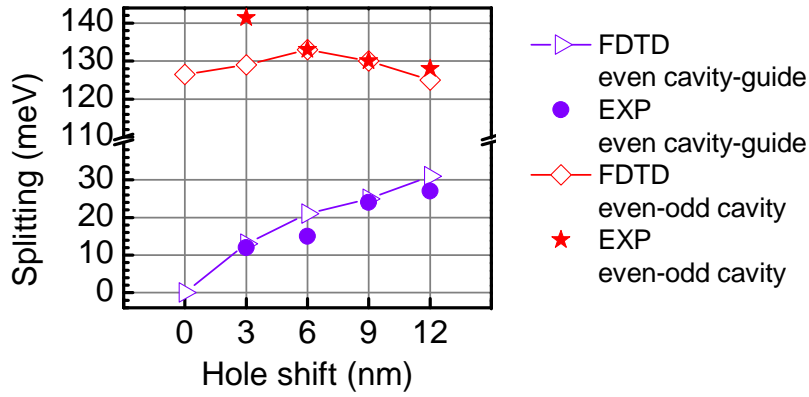


Figure 5.15 – Experimental and calculated splittings between even cavity and first even guided mode, and odd and even cavity modes - sample A1507: $D=0.40$; $r/a=0.27$; $a=170$ nm

5.3.3 By micro-photoluminescence scan along the waveguide axis

The previous subsections allowed us to index each mode present in our experimental spectra. It is also possible to validate this assignment with further experimental measurements. Indeed, as we can see from figure 5.12, the extension of the cavity mode is much smaller than that of the guided modes. Comparing the intensity of the peaks as a function of the probing position along the waveguide axis should indeed confirm their different spatial extension. The laser spot is approximatively $1 \mu\text{m}$ in diameter. Using the piezoelectric base of our microscope objective³, we can probe the emission of the center of the photonic crystal and then move the excitation spot with iterative steps of 500 nm, as illustrated on figure 5.16. All the experiments are performed at room temperature, in air.

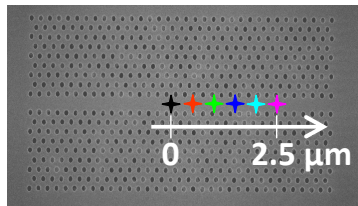


Figure 5.16 – Illustration of the scan positions and associated color code

It has to be mentioned that the redshift observed between the first experiments conducted on these membranes, depicted on figure 5.9, and the following ones, is due to long laser exposition. This shift will be discussed in chapter 6.

Pure waveguide

Let us begin by analyzing the micro-photoluminescence along the pure waveguide ($d=0$ nm). Figure 5.17 shows the spectra as directly measured (no normalization), the scanning excitation step being 500 nm. We can observe on figure 5.18 that most of

³Details of our setup can be found in page 200

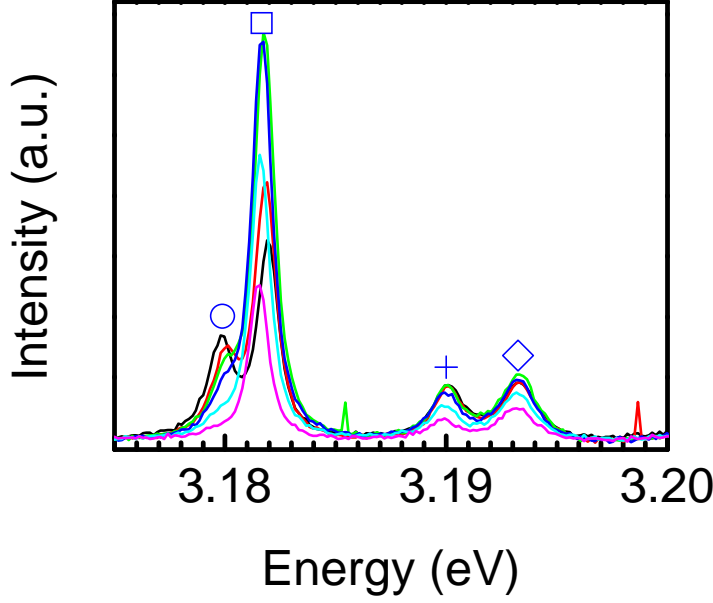


Figure 5.17 – Evolution of micro-photoluminescence when scanning along the waveguide of the photonic crystal without cavity ($d=0$ nm) - sample A1507: $D=0.40$; $r/a=0.27$; $a=170$ nm

the modes only begin to loose intensity after going $2 \mu\text{m}$ away from the center of the W1, with an exception for the first mode, which appears more like a shoulder of the second one and looses 60% of its intensity after a $1.5 \mu\text{m}$ shift. This is still a much less pronounced quenching than the decrease of the cavity mode intensity which will be discussed in the next paragraph. This therefore leads us to attribute these four modes to the waveguide.

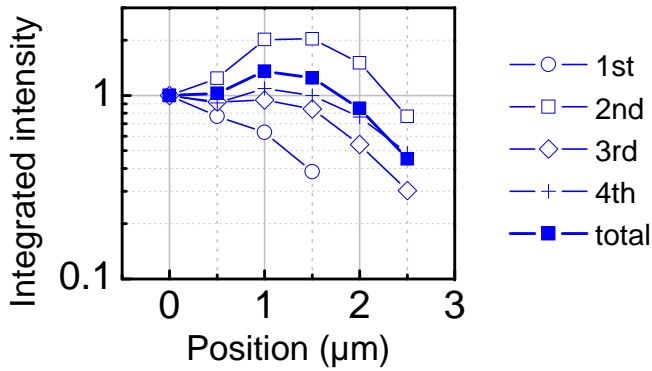


Figure 5.18 – Integrated intensities of the guided modes and of the ensemble of guided modes

d=12 nm cavity

Figure 5.19 depicts the spectra acquired from a scan similar to that performed on the pure waveguide and described on figure 5.16. The data is normalized to the intensity of the lower-energy mode, whose origin needs to be confirmed as the cavity mode by the current experiment. We can see that if we keep its intensity constant along the scan, the emission from the higher energy modes —attributed to the waveguide— increases. To be more quantitative, we plot on figure 5.20 the integrated intensity of the lower energy mode, the two following modes at higher energy, and the ensemble of higher energy

modes, attributed in the last subsection to even guided modes. The data are normalized to their value at the center of the photonic crystal.

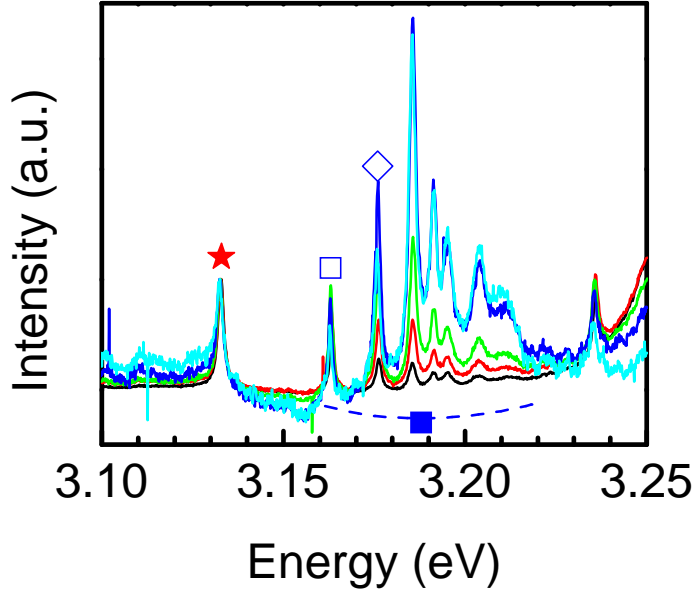


Figure 5.19 – Evolution of micro-photoluminescence spectrum normalized to the low-energy (cavity) mode intensity, when scanning along the waveguide for a cavity defined by $d=12$ nm - sample A1507: $D=0.40$; $r/a=0.27$; $a=170$ nm

From figure 5.20, we can point out that the lowest energy mode is the only peak to be quenched after a 500 nm shift of the excitation beam. On the contrary, the intensity of the other lines tend to slightly increase. This is also the only emission to be attenuated by 90% when moving the spot away from the center of the photonic crystal by $2.5 \mu\text{m}$. Both higher energy modes are quenched by only 33% and the mean attenuation for the ensemble of guided modes is 40%. The monotonic decrease of the lowest-energy peak is caused by an effective light confinement, whereas the fluctuations of the intensity of the higher energy contributions show that these emissions probe a greater part of the photonic crystal, and are therefore more sensitive to inhomogeneities. To conclude, this experiment leads to the same mode attribution as did FDTD calculations.

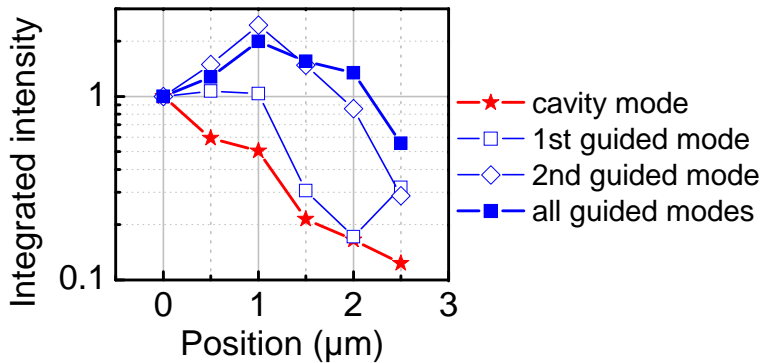


Figure 5.20 – Integrated intensities of the three first modes — cavity and two low-energetic guided modes and of the ensemble of guided modes

$d=3$ nm cavity

We have seen in figure 5.11 that the nature of the lowest energy mode at 3.216 eV for $d=3$ nm is still uncertain: its spectral position is intermediate between that of fundamental

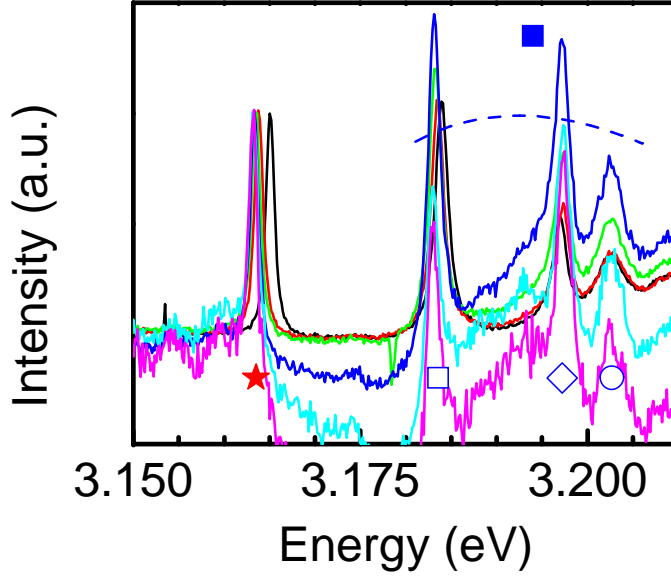


Figure 5.21 – Evolution of micro-photoluminescence spectrum normalized to the low-energy (cavity) mode intensity, when scanning along the waveguide for a cavity defined by $d=3$ nm - sample A1507: $D=0.40$; $r/a=0.27$; $a=170$ nm

cavity and guided modes. Besides, we have validated that a scan along the waveguide allowed to discriminate cavity from guide modes on the $d=12$ nm cavity. Let us try the same experiment to dispel doubts on the nature lowest energy mode of the spectrum of the $d=3$ nm structure: is it really a cavity mode? On figure 5.21, we have plotted the spectra when scanning along the axis of the waveguide after normalizing each spectrum to the intensity of the cavity mode. We can already observe that the enhancement of the luminescence from guided modes at a fixed cavity intensity is much weaker than in the previous case when $d=12$ nm.

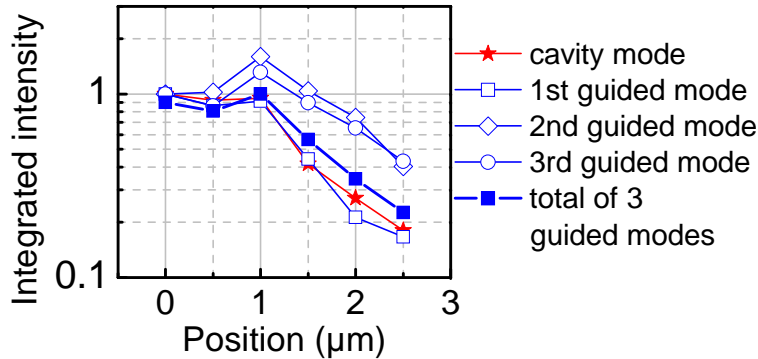


Figure 5.22 – Integrated intensities of the three first modes — cavity and two low-energetic guided modes and of the ensemble of guided modes

Quantitative data are displayed in figure 5.22: both the lowest-energy fundamental guided modes and the “cavity” mode display very similar decay: a quasi-constant intensity on the first $1 \mu\text{m}$ of the scan, followed by an abrupt loss of 80% of their initial intensity between 1 and $2.5 \mu\text{m}$. This trend is very similar to the decay of the first guided mode of the $d=12$ nm structure. In this case, the conclusion seems to be that some modes are mixed between pure cavity and pure Fabry-Pérot modes. It is not surprising that we observe this hybridization on the structure designed for the smallest hole shift. Indeed, this shift may be too small to induce an optimal confinement of the electric field, and leakage is expected to be stronger than in the case of the wider cavity

formed by a hole shift of $d=12$ nm.

Conclusion on mode attribution

To conclude, the comparison between experimental and simulated spectral positions is good enough to allow us to index our spectra. The low-energy mode of the photonic crystal which displays a cavity is attributed to the fundamental state of this cavity, with even symmetry compared to the waveguide axis, while the first excited state, of odd parity, is detectable 100 meV above. Their positions shifts almost linearly when the dimension of the cavity increases. Several resonances from the waveguides are evidenced a few 10 meV above the fundamental cavity modes, with an even parity. Their odd counterparts are distinguishable 230 meV above.

The different cavity / waveguide mode nature is further pointed out by probing the evolution of their respective intensity when scanning the structure along the waveguide axis, the emission originating from the cavity being much more localized than that of the guide when the hole shift is rather wide. For the smallest value of d , however, the lowest energy mode seems hybrid in-between a cavity and a guided mode.

5.4 Quality factors

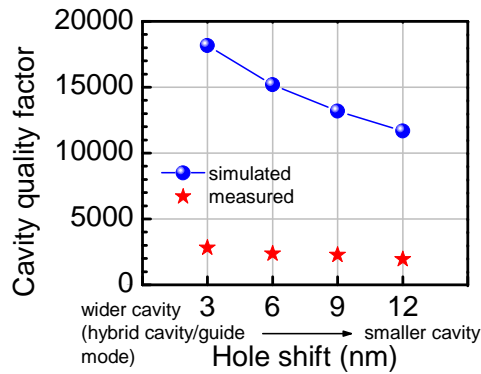


Figure 5.23 – Comparison between measured and calculated values for various cavity size - sample A1507
 $D=0.40$; $r/a=0.27$; $a=170$ nm

On the cavities studied in this section, quality factors span between 1900 and 2800, whereas the intrinsic, theoretical quality factor expected for the series of cavities studied up to now are between 10000 and 20000, increasing with increasing cavity size, in agreement with the simulations performed by Kuramochi *et al.* The intrinsic quality factor is the value obtained by simulations, which only take into account the losses induced by the reflections at the interfaces between the inner and the outer parts of the cavity. These theoretical values, as well as the measured ones, are plotted on figure 5.23. The huge discrepancy between experimental and calculated values suggests that the quality factor is determined by imperfections of the structure, because the measurable quality factor is given by:

$$\frac{1}{Q_{measured}} = \frac{1}{Q_{intrinsic}} + \frac{1}{Q_{extrinsic}} \quad (5.2)$$

We see that if the loss of photons by the cavity is dominated by a process much quicker than the intrinsic way, i.e. $Q_{intrinsic} \gg Q_{extrinsic}$, the measured value will be close to the quality factor induced by the extrinsic loss process.

Note that the combination of cavity embedded in a waveguide has shown better robustness towards process-induced defects compared to L3 cavities which were designed on the same sample. From the statistical study we performed on both types of structure, quality factors were higher by a factor of two.

5.4.1 Origin of extrinsic losses

A whole review of the influence of defects on the quality factor can be found in [Asa06]. The most relevant are listed below.

Residual absorption is a potential source of cavity photon losses. L3 cavities processed in the same conditions on the same sample exhibit lower quality factors (in the 1000-2000 range). Yet the considered nanocavities embedded in waveguides show greater spatial extension of the confined light inside the structure than L3 cavities: the modal volumes are 3 times wider in the structures investigated in this chapter. Residual absorption would thus have an even larger effect in waveguide cavities than in L3 cavities if it was the preeminent loss process. The observed trend seems to indicate that residual absorption is not the dominant factor. It rather confirms the hypothesis that the waveguide cavities show more robustness with respect to processing defects than L3 cavities.

Losses induced by a *misverticality of the hole sidewalls* cannot be ignored. They induce a coupling between TE and TM modes [Tan03] and thus decrease the coupling factor to the cavity mode. Further experiments, such as polarization-dependent microphotoluminescence measurements⁴, are needed to evaluate the magnitude of this losses.

Scattering on process-induced defects must also be considered. A 2-nm roughness of the hole sidewalls (which represents 0.5% of the pattern periodicity $a=420$ nm of [Asa06]) induces a quality factor of 8.10^6 [Asa06]. But in our case, $a=170$ nm, so in order to keep the same process quality we need to keep roughness well under 1 nm. However, the roughness on the sidewalls of AlN microdisks was determined to be around 2 nm^5 . This corresponds to 1% of the hole periodicity and 5% of the hole radius. These figures illustrate the issues one encounters when the typical roughness on the etched surfaces is not negligible anymore compared to the structure typical dimensions. In our structures, scattering is therefore expected to be one of the dominant phenomenon lowering the

⁴such as the ones performed on microdisks in 4.5.2

⁵see 4.4.2

quality factor.

One should also consider the *deviations from the nominal design*. Our fabrication methods guarantees hole positioning with an accuracy better than 1 nm. As the electronic beam is only a few nm size, the radius is expected to be reproducible among a single photonic crystal.

Finally, the *absorption by surface states* may also induce photon losses. It is relevant to consider that the free AlN surface is oxidized and has a non-negligible density of trapped charges. Note that the ratio of the total etched surface of a photonic crystal (periphery of all the holes) over the total surface developed by this structure (hole etched surfaces and slab waveguide surface) is around 20%, whereas that of a microdisk (disk periphery) is around 5%. The states of these etched surfaces may therefore influence more strongly the quality factor of photonic crystal cavities than that of microdisks. Moreover, these states appeared to change upon long laser exposure as will be discussed in the next chapter. They could be one of the major sources of photon losses.

5.4.2 Record value of the quality factor

For a slightly different set of parameters, our partners from Laboratoire Charles Coulomb (Université de Montpellier) measured a maximal value of 4400 around 3.14 eV, for $d=6$ nm, as illustrated by figure 5.24. It thus seems relevant to consider that the quality factors of these cavities are limited by extrinsic losses to this value: $Q_{extrinsic}=4400$. Therefore the value of the quality factor on the whole sample should be lower than or equal to $Q_{extrinsic}$.

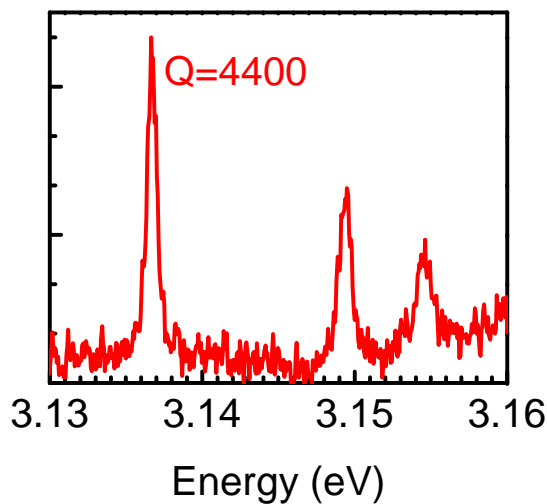


Figure 5.24 – Quality factor for $d=12$ nm - sample A1507 - $D=0.40$; $r/a=0.25$; $a=170$ nm

On figure 5.25, we plotted the calculated value (black circles), as well as the theoretical quality factor obtained for $Q_{extrinsic}=4400$ (cyan circles). The resulting values are still higher than the experimental ones (red stars), suggesting that the extrinsic

quality factor is lower than 4400. Fitting with $Q_{\text{extrinsic}}=3000$ (purple diamonds) leads to a qualitative agreement with the experimental values. It is interesting to note that when fixing a value for $Q_{\text{extrinsic}} \ll Q_{\text{intrinsic}}$ — be it 4400 or 3000, the variation of $Q_{\text{intrinsic}}$ still affects the resulting quality factor $(1/Q_{\text{extrinsic}} + 1/Q_{\text{intrinsic}})^{-1}$. It can be observed when varying the cavity size: the trends of both simulated values of the quality factor with either $Q_{\text{extrinsic}}=4400$ (cyan circles) or $Q_{\text{extrinsic}}=3000$ (purple diamonds) are indeed comparable to that of the intrinsic quality factor (blue circles). To be more quantitative, we resolved equation 5.2 where $Q_{\text{extrinsic}}$ is the unknown variable. The results are plotted in figure 5.25 (centered black squares). We see that $Q_{\text{extrinsic}}$ varies with the cavity size: in the series investigated here, it increases when the cavity gets wider. This trend is however not typical of all the series we analyzed. All the cavities investigated exhibited a quality factor around or above 1000. Yet it seems that the quality factor is more sensitive to process-induced defects than any other parameter, such as a small variation of d .

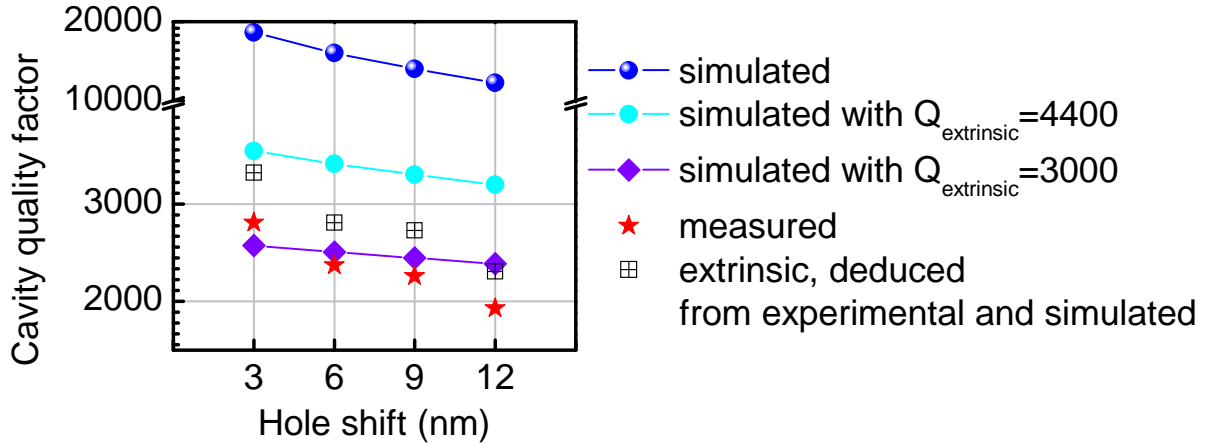


Figure 5.25 – Comparison between measured, calculated and extrinsic values of the quality factor - sample A1507 $D=0.40$; $r/a=0.25$; $a=170$ nm

Conclusion

Intrinsic quality factors range between 10^4 and $2 \cdot 10^4$ when the cavity size increases. We have experimentally measured a value up to 4400, but typical values span between 2000 and 3000, with an extrinsic quality factor calculated as ranging from 2300 to 3300. The main sources of losses are process-induced defects such as hole roughness. The associated quality factor varies more strongly than the intrinsic one. Therefore, a monotonic increase of the measured quality factor with cavity size is not typical of all the structures we investigated.

5.5 Highest energy series: towards UV nanoresonators

In the last section, we demonstrated a good control of the experimental modal emission, close to the values theoretically calculated, but at a spectral position still lower than the targeted UV wavelengths. In this section, we will see that the above discussion at 3.2 eV is still valid for photonic crystal designed for an emission deeper in the UV.

5.5.1 Mode spectral positions and splittings

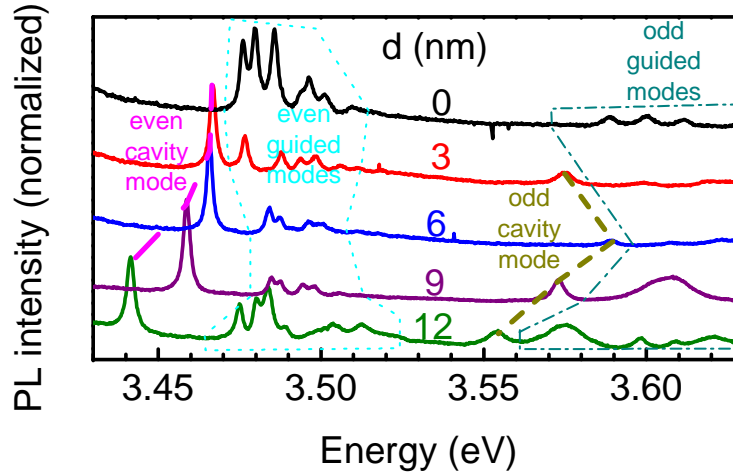


Figure 5.26 – Room-temperature microphotoluminescence spectra of photonic crystal structures with varying the size of the cavity - sample A1507: $D=0.45$; $r/a=0.25$; $a=150$ nm

Figure 5.26 shows the dependence on cavity size of the microphotoluminescence spectra. This time, the even group of modes emits in the 3.45 – 3.50 eV range. The lowest-energy mode in-between 3.44 and 3.47 eV when varying the cavity size, is attributed to the fundamental cavity mode. From 3.47 to 3.51 eV, the fundamental guided modes are observable. The mode located in-between 3.55 and 3.59 eV is attributed to the odd cavity mode. Further higher-energy modes are the odd modes of the waveguide. Spectral positions of even and odd modes are plotted on figure 5.27a.

From the comparison of both figures 5.27a and 5.27b, we observe that the absolute positions of even guided modes seem erratic, but the splitting between even cavity and guided mode increases linearly with hole shift. However, the splittings between even and odd modes do not seem to vary smoothly. It could be attributed to the fact that compared to the previous series, the relevant dimension of the photonic crystal are around 10 % smaller: periodicity is reduced from 170 to 150 nm, while hole radius decreases from 46 to 38 nm. In this range, the slightest fluctuation of hole size or position, on the same order of magnitude for all the series, becomes of the same order of magnitude as the hole periodicity a and the hole radius r : these fluctuations become more damaging here than in the structures studied previously and emitting at lower

energy. It is therefore easy to understand why the spectral positions of the waveguide are not as precisely controlled as they were for greater periodicities and hole radii: the present structures are more affected by disorder.

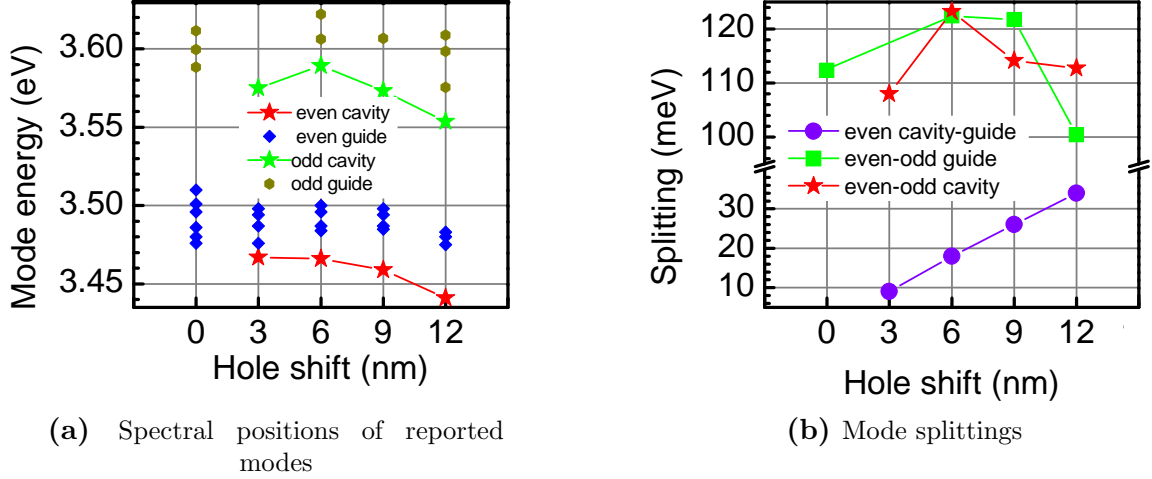


Figure 5.27 – Extracted data from the micro-photoluminescence with varying cavity size - sample A1507 - $D=0.45$; $r/a=0.25$; $a=150$ nm

5.5.2 Quality factor at 3.46 eV

In this spectral range, we expect lower quality factor values than on the samples described in the last section (5.4) and emitting around 3.2 eV. Indeed, going to higher energy needs smaller dimensions — periodicity a and hole radius r — for designing the photonic crystal. Yet process-induced defects remain the same and therefore, relatively to the typical hole periodicity a and hole radius r , their contributions increases. As wavelength is reduced we are also more sensitive to any scattering defects. However, we always measured quality factors in the range 1000-2300 for an emission between 3.4 and 3.5 eV, which is a proof of the robustness of these structures.

The record value on this sample was 2300 at 3.46 eV, as we can see on figure 5.28. This is a state-of-the-art value, when compared to the literature on GaN/AlN quantum dot photonic crystal cavities. The group of Pr. Arakawa has reported record quality factors. In 2007, this group reported a value of 2400 at 3.24 eV on a L7 cavity — seven missing holes displayed linearly — embedded in a triangular pattern of air holes [Ari07]. In 2012, they measured $Q=5000$ at 3.26 eV and $Q=1000$ at 3.88 eV in a cavity formed by the slight shift of holes inside a one-dimensional array of air holes etched in a GaN / AlN quantum dot membrane [Ser12]. Around 3.46 eV, the quality factors they reported also span between 1000 and 3000.

This huge improvement opens the way to the strong coupling regime between such a cavity and GaN excitons, as discussed in the prospects of this thesis.

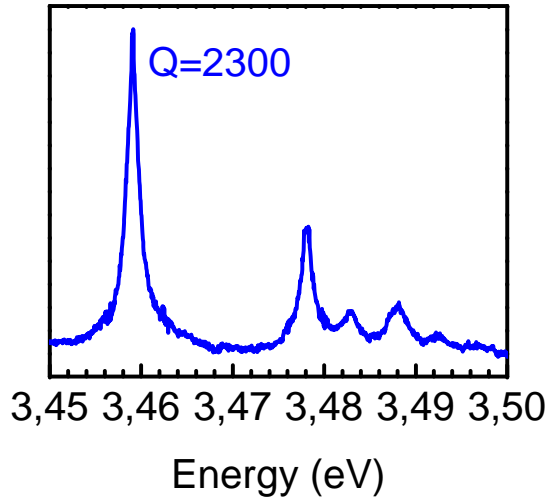


Figure 5.28 – Quality factor for $d=6$ nm- sample A1507 - $D=0.45$; $r/a=0.25$; $a=150$ nm

5.6 Chapter conclusion : towards the Purcell effect

In these structures, the mode volume calculated by FDTD simulations is $2.2(\lambda/n)^3$. With our best value of the quality factor, this gives a maximum Purcell factor of 150, meaning an measurable enhancement of the spontaneous emission rate by a factor of 50. More details will be provided in the next chapter.

Towards the Purcell effect and lasing with GaN/AlN cavities

WE HAVE SEEN in both previous chapters, that despite some technological limitations such as poor etching efficiency and selectivity, and stronger sensitivity of UV light to processing defects, we can achieve light confinement with high quality factors in the UV-visible range (360 – 420 nm).

However, cavity quantum electrodynamics signatures, such as Purcell effect and lasing, reported for the first time around 2000 in InAs/GaAs microcavities, are still to be evidenced with GaN/AlN microcavities. Only strong coupling has been observed in one-dimensional nitride cavities [Mal02][Chr07][Chr08]. In this context, the goal of this chapter is to discuss the potentialities of our systems for our ultimate goal: a UV Purcell-enhanced microlaser grown on a silicon substrate.

Contents

6.1	Towards the Purcell effect with nitrides	148
6.1.1	Experimental demonstrations of the Purcell effect in arsenide compounds	148
6.1.2	The expected Purcell effect in GaN/AlN cavities — dependence on the homogeneous linewidth of the emitters . .	150
6.1.3	Measurements on GaN/AlN microdisks	154
6.1.4	Measurements on GaN/AlN nanocavities embedded in photonic crystal waveguide	155
6.2	Modal instability with exposure time	157
6.2.1	Instability of a whispering gallery mode under pulsed excitation	158
6.2.2	Whispering gallery mode shifting under continuous-wave excitation	160
6.2.3	Photonic crystal cavity mode: stable or instable?	163
6.2.4	Possible explanations for cavity mode shift	166

6.3	Instability of quantum dot emission under long exposure . . .	170
6.3.1	Checking the stability of non-etched quantum dots	170
6.3.2	Instability of etched quantum dots	171
6.3.3	Possible processes resulting in the blueshift and a quenching of the emission of etched samples	173
6.4	Towards UV microlasers	175
6.4.1	Theory	175
6.4.2	Lasing experiments	179
6.4.3	Comparison between our system and experimental demonstrations of lasing microcavities	179
6.4.4	Prospects to achieve lasing with GaN/AlN microcavities . . .	182

6.1 Towards the Purcell effect with nitrides

6.1.1 Experimental demonstrations of the Purcell effect in arsenide compounds

We have seen that the two parameters we can tune to maximize the Purcell effect are the quality factor Q and the volume of the cavity mode V_{eff} , which can be controlled independently in three-dimensional microcavities. The maximum enhancement of the spontaneous emission rate for an emitter coupled to the cavity mode is:

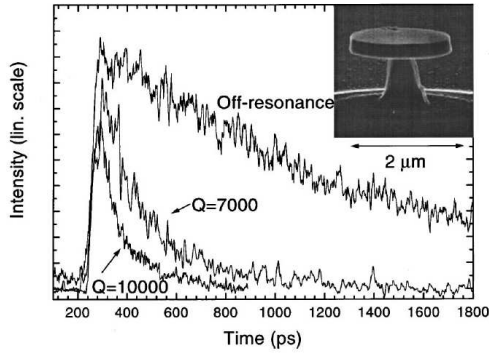
$$F_P = \frac{3Q(\lambda/n)^3}{4\pi^2 V_{eff}} \quad (6.1)$$

Small V_{eff} and high Q are indeed desirable to increase the coupling of the emitter to the cavity electric field. This factor determines the ability of a cavity to enhance the spontaneous emission rate of a given emitter.

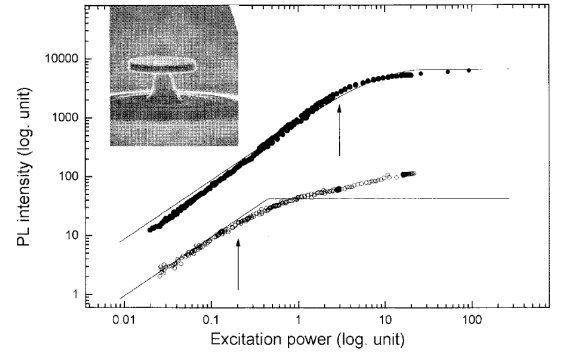
In solid-state physics, the first demonstration of the Purcell effect was performed in 1998 on GaAs micropillars with InAs quantum dots as emitters. By time-resolved photoluminescence experiments, the authors measured up to a five-fold enhancement of the emission rate of quantum dots in resonance with the cavity mode, compared to out-of resonance ones [G'98]. For this 1- μ m-micropillar exhibiting a quality factor of 2250, the Purcell factor (*i.e.* the maximum enhancement) was 32. A monotonic increase of the experimental Purcell factor $\frac{\tau_{on}}{\tau_{off}}$ versus the calculated one F_P from equation 6.1 was reported, where τ_{on} and τ_{off} are the decay times of the emitter in resonance and out of resonance with the cavity mode, respectively. Yet $\frac{\tau_{on}}{\tau_{off}}$ is always five times lower than F_P . Indeed, for any circular-shaped microcavity, the authors fit their experimental decay time in resonance with the cavity mode with the relation:

$$\frac{\tau_{off}}{\tau_{on}} = \frac{2F_p}{3} \cdot \frac{|\vec{d} \cdot \vec{E}(\vec{r}_e)|^2}{|d|^2} \cdot \frac{\Delta\omega_{cav}^2}{4(\omega_{em} - \omega_{cav})^2 + \Delta\omega_{cav}^2} + 0.8 \quad (6.2)$$

where \vec{d} is the emitter dipole, $\vec{E}(\vec{r}_e)$ is the electric field at the position of the emitter \vec{r}_e , $\Delta\omega_{cav}$ is the linewidth of the cavity mode and ω_{em} , that of the emitter. In equation 6.2, the factor of 2 in the numerator originates from the two possible circular modes (circular and contracircular), the factor of 3 in the denominator comes from the random orientation of the emitter dipole, and the additional 0.8 value accounts for the cavity leakage outside the considered mode.



(a) Time-resolved microphotoluminescence signal of InAs quantum dots on and off-resonance with the $TE_{13,1}$ whispering gallery mode of a 2- μ m microdisk [Gay01]



(b) Photoluminescence intensity versus excitation power for a 1.8- μ m diameter microdisk [Gér99]

Figure 6.1 – Experimental evidences of Purcell effect in InAs/GaAs microdisk

Three years later, the Purcell effect was observed in InAs/GaAs microdisks. Time-resolved photoluminescence measurements showed a 12-fold shortening of the decay time of the quantum dots coupled to the cavity, compared to the uncoupled ones (see figure 6.1a). Besides, the saturation power of the same emitters was found to be 15 times higher when they were on resonance with the mode (figure 6.1b).

Note that a major issue when trying to go to even lower V_{eff} values, *i.e.* lower diameter microcavities, is the increasing efficiency of scattering by surface roughness. The direct consequence is that Q is decreased, as depicted on figure 6.2. However, if the etching process is optimized, the decrease of Q due to enhanced sensitivity of the modes to surface roughness can be counterbalanced by a decrease of the mode volume, as plotted on figure 6.2.

One of the main target of this work was to perform time-resolved photoluminescence experiments on GaN/AlN quantum dot microcavities to observe the Purcell effects in nitride optical resonators for the first time.

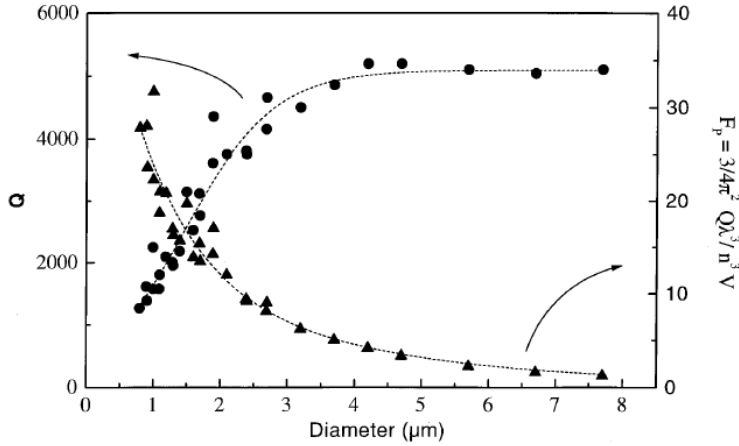


Figure 6.2 – Evolution of quality factor (circles) and Purcell factor (triangles) with decreasing pillar diameter - illustration of the increasing part of scattering losses due to surface roughness [G98]

6.1.2 The expected Purcell effect in GaN/AlN cavities — dependence on the homogeneous linewidth of the emitters

Let us remember what were the hypothesis needed to obtain the Purcell factor as a function of Q and V_{eff} :

1. the emitter should be placed at the maximum of the electric field intensity, in order to maximize their interaction
2. the emitter should be in spectral resonance with the cavity mode
3. the emitter dipole should be parallel to the electric field direction, their interaction being proportional to $\vec{d} \cdot \vec{E}$
4. *the emitter spectral linewidth should be smaller than the linewidth of the cavity mode.*

If these assumptions are not fully respected, the spontaneous emission enhancement $\frac{\tau_{on}}{\tau_{off}}$ will be smaller than the Purcell factor calculated in equation 6.1. Both first assumptions are not fully respected but lead to a reduction of the measurable Purcell effect by a factor around 3¹. The third one should in general be satisfied with GaN/AlN quantum dots at low power because their fundamental state is mainly built on the A bulk exciton which lies perpendicular to \vec{c} . As the planar waveguides we work on are designed to be monomode and they therefore mainly guide the fundamental TE mode, the coupling is expected to be efficient.

However, we cannot ascertain the fourth hypothesis, because the homogeneous linewidth of GaN/AlN quantum dots is unknown. In the following, the value of the *spectral linewidth of GaN/AlN quantum dots* is discussed. The first spectroscopic study of a single GaN/AlN dot was achieved in 2006: linewidths around 6 meV at 4 K were reported [Kak06]. Since then, the community succeeded in growing layers of improved

¹as already discussed with equation 6.2 [G98]

quality: Simeonov *et al.* measured a 1-meV broad emission [Sim08]. This is still two to three orders of magnitude broader than the best InGaAs quantum dots [Bay02] and InAs quantum dots [Ber06], be they excited either in resonance or out of resonance. What are the possible explanations for this broadening?

Preamble on the main broadening mechanisms The full width at half maximum of a single quantum dot is determined by both its *homogeneous* and *inhomogeneous* broadening. The *homogeneous* linewidth is given Heisenberg's inequality:

$$\Gamma = \frac{2\hbar}{T_2} = \hbar \left(\frac{1}{T_1} + \frac{2}{T_2^*} \right) \quad (6.3)$$

where T_2^* takes into account the pure dephasing processes. T_1 is the transition lifetime and takes into account both radiative time τ_R and non radiative time τ_{NR} :

$$\frac{1}{T_1} = \frac{1}{\tau_R} + \frac{1}{\tau_{NR}} \quad (6.4)$$

The decay time of our dots emitting at 3.2 eV is around 100 – 250 ns. If exciton coherence was to be determined by radiative lifetime only, the linewidth would be in the order of 1 neV, which is far from the narrowest values reported. Indeed, in much more understood and mastered systems such as InAs quantum dots, the best full width at half maximum are in the order of a few μeV at liquid He temperature [Bay02][Ber06]. The *pure dephasing processes by elastic scattering*, *e.g.* by interactions with phonons or with other carriers [Ber06] (in T_2^*) must also be considered. In the above criterion about the linewidth of the emitter used to calculate the Purcell factor, the homogeneous linewidth must be considered. However, its value is difficult to measure because other processes hides the homogeneous broadening.

The *inhomogeneous* linewidth originates from a variation of the environment of the quantum dot, at a temporal scale longer than its decay time. It could originate from fluctuations of the electric field, enhanced by a variation of the amount of charges around the quantum dot: this mechanism is called *spectral diffusion*. Several studies on arsenide quantum dots have found experimental conditions which allow to reduce the inhomogeneous broadening. First, one has to excite the sample resonantly. If not, charge fluctuations in the wetting layer and the barrier (if absorbing) are enhanced before thermalisation can occur in the quantum dot states [Bay02]. Moreover, working at both low temperature and low power allows charge trapping processes to occur, while detrapping processes are strongly quenched [Ber06]. Finally, one should rather probe the absorption rather than the photoluminescence: by tuning the excitation energy of a tunable laser around the resonance, a linewidth as low as 1.47 μeV was measured on a single InAs/GaAs quantum dot [Vam07].

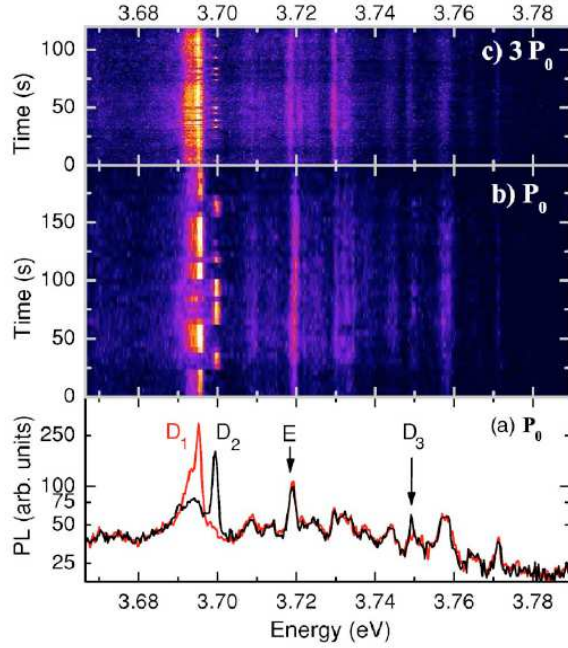


Figure 6.3 – Evidence of spectral diffusion: (a) time-averaged spectra of both possible configurations, semi-logarithmic scale; Time evolution of the spectrum at (b) $P_0=230$ W.cm^{-2} and (c) $3P_0$, acquisition time of (b) 5 s and (c) 1 s [Bar06]

Is it possible to measure the homogeneous linewidth of GaN/AlN quantum dots?

Now that the inhomogeneous broadening processes have been reminded, one can wonder whether the homogeneous linewidth of a GaN/AlN quantum dot is measurable. At low temperature, the phonon population is expected to be scarce, but the reported linewidths are still in the range of one to several meV [Kak06][Sim08]. This broadening is attributed to an inhomogeneous linewidth. Bardoux *et al.* [Bar06] have observed a dynamic evolution of the spectral position of one excitonic line: in the time range of 1 s, it “beats” between two energies, with a splitting of 4 meV in the example depicted on figure 6.3. This range of splitting is consistent with an electric field of 60 kV/cm [Bar07], which can be accounted by the successive trapping and detrapping of a single charge on a single defect positioned in the vicinity (at around 5 nm) of the dot. It follows that, depending on the value of the integration time compared to the typical time needed to “jump”, we will distinguish both lines or detect one single, broader line. Hence, only the spectral diffusion phenomena occurring with a typical time greater than the detection time can be observed, but the same kind of processes are likely to occur also at a much quicker speed, and therefore account for the broadening observed even at 4 K. One could get rid of the inhomogeneous broadening by performing single dot absorption experiments. However, in the UV range, there is no tunable laser source which allows to spectrally scan a dot around its resonance.

The time acquisition is of the order of the second in order to detect enough photons from the photoluminescence of a single quantum dot. It results that the measurement of the homogeneous linewidth is made impossible by the occurrence of fast spectral diffusion processes. The spectral diffusion is a photo-induced process (as pointed out by figure 6.3), therefore measurements at low power should lead to values closest to the homogeneous broadening. However, these measurements require to increase the

acquisition time, and thus long-time spectral diffusion processes are more visible.

Increasing temperature We will see in the next section of this chapter that the attempts to measure the Purcell factor had to be performed at room temperature. It would thus be necessary to know the homogeneous linewidth of a GaN/AlN quantum dot *at room temperature* to make sure that our system is still in the framework of Fermi's golden rule. With increasing temperature, phonon coupling becomes more efficient. Kako *et al.*, in their pioneer report of a GaN single photon source until 200 K [Kak06], have demonstrated the existence of the 1 LO phonon replica 90 meV below the excitonic main line. Furthermore, Fabian Rol has shown during his PhD [Rol07a] that, in non polar quantum dots, the broadening of excitonic emission from 1 to 3 meV between 5 and 180 K originates from the contribution of phonons [Rol06] (see figure 6.4).

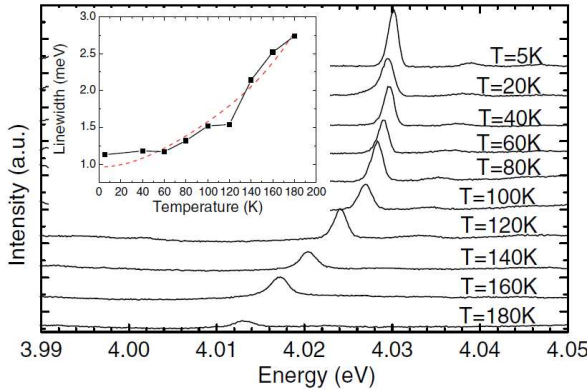


Figure 6.4 – Evidence of exciton-phonon coupling: evolution of the microphotoluminescence spectra of a single quantum dot with temperature; inset: full width at half maximum - extracted from [Rol06]

At this point, let us notice that *a single GaN/AlN quantum dot was never successfully followed from 4 to 300 K*. The best studies all stop around 200 K, whatever their polarity, as reported in [Rol06] and [Kak06]. This stands in contrast with the large exciton binding energy and high band offsets. Table 6.1 compares the band offsets of a GaN/AlN heterostructure to the thermal energy at 4 K and 300 K. The two order of magnitude lower value of the thermal energy at room-temperature suggests that quantum confinement is still very efficient at this temperature. Both the high GaN excitonic binding energy and the high band offsets indeed result in a good thermal robustness of the photoluminescence intensity and decay time of an *assembly* of quantum dots [Ren09b]. The mechanisms of spectral diffusion, phonon coupling, intermixing with excited states are expected to be enhanced when temperature increases, and measurements on a single quantum dot are still lacking above 150 – 200 K. This could be explained by a carrier redistribution due to a strong change in the mechanisms governing the localization of the exciton. This hypothesis was assumed in [Rol07a] to explain the quenching of the luminescence of non polar quantum dots observed above 140 K, as depicted in figure 6.4.

To conclude, photoluminescence experiments in non-resonant conditions are expected to induce inhomogeneous broadening, and thus the homogeneous broadening of a single GaN/AlN quantum dot is unknown, even at 4 K. In arsenide quantum dots, linewidths

Parameter	Value (eV)
Difference between gaps	-2.71
Valence band offset	-0.7
Conduction band offset	2.04
Thermal energy at 4 K	3.10^{-4}
Thermal energy at 300 K	0.025

Table 6.1 – Band offsets in a GaN/AlN heterostructure and comparison to thermal energy - extracted from [Wu09]

as small as a few μV have been measured [Ber06]. We will see in the following² that the experiments we carried out had to be performed at 300 K: in these conditions, the measurement of the homogeneous linewidth is even more tricky because of an efficient coupling to phonons. At room temperature, the homogeneous broadening of a GaN/AlN quantum dot is unknown: in arsenide quantum dots, it should be between 3 and 15 meV [Mat00][Bor99]. The value for GaN quantum dots may be comparable.

6.1.3 Measurements on GaN/AlN microdisks

As we seen in chapter 4, microdisk resonators are good candidates to observe the Purcell effect. With a 2- μm disk exhibiting a quality factor around 4000, a mode volume of $6(\lambda/n)^3$, the maximum Purcell factor will be around 60. We thus performed time-resolved photoluminescence measurements, hoping to evidence a shortening of the decay time of quantum dots in resonance with a whispering gallery mode.

The excitation was provided by a frequency-tripled Ti-sapphire laser at 270 nm. The 76 MHz-repetition rate was lowered by using a cavity dumper, so the periodicity was 500 ns. We use our microphotoluminescence setup³ to obtain a laser spot of the order of 5 μm and a power around 10 μW on the sample (after the microscope objective). The detection was performed either by a CCD camera or the streak camera, which were positioned on two different spectrometers⁴.

We proceeded as follows. First, the sample and the fine position of the microscope objective were aligned using a CCD camera as detector, using a piezoelectric stage to maximize the emission from the whispering gallery modes. The process is much easier than when using the streak camera and we can obtain a better contrast between the whispering gallery modes and uncoupled quantum dots. Then, we switched the detection towards the streak camera. After the alignment of the detection path in the time-integrated mode, we performed acquisitions in time-resolved mode.

²Details will be provided in 6.2.2 and 6.2.3.

³further described on page 200

⁴Details about the time-resolved photoluminescence setup can be found on page 200

This experiment requires long acquisition times. We had enough power to observe the whispering gallery modes in time-integrated mode, but *a time-resolved acquisitions needed around 90 minutes*. This can be due to several reasons. First, the excitation power is limited to the efficiency of the Ti-sapphire tripling process and the low pump power providing enough stability of the cavity dumper. Further, the strong quantum-confined Stark effect present in our quantum dots leads to decay times in the order of 100 ns. This induces a decrease of the emitted intensity per time unit compared to field-free quantum dots. Therefore they do not provide many photons per time unit (10^7 photons per second for a recombination time of 100 ns). Then, the density of our quantum dots lies between 10^9 and 10^{10} cm $^{-2}$ and cannot be easily increased⁵. One must not forget either that the signal is collected by the front surface of the microdisk, and not by the edge. Yet the emission from the whispering gallery modes is expected to radiate more in the slab plane rather than perpendicularly to this plane⁶. Finally, we had to work at room temperature in order not to damage the cavity after a few minutes of exposure (see next section), so 2/3 of the quantum dot emission was lost in non-radiative recombinations⁵.

These are explanations for the low-level signal, but providing that the system is stable enough, we should have been able to perform acquisitions during several hours to obtain the required dynamics. Yet, when performing long acquisitions, whispering gallery modes were not observed in the streak camera. They should have appeared as more intense spectral zones, but only the broad emission of uncoupled quantum dots was observable. It seems that we detected only the emission from quantum dots. We finally understood that a long-time excitation was modifying the cavity properties, as will be discussed in 6.2.2.

6.1.4 Measurements on GaN/AlN nanocavities embedded in photonic crystal waveguide

We also studied cavities embedded in photonic crystal waveguides, exhibiting similar quality factors, but with smaller modal volume $V_{eff} = 2.2(\lambda/n)^3$. The maximum Purcell factor in these resonators is thus as high as 150. We therefore performed time-resolved photoluminescence measurements on this sample, with the method described previously for microdisks. Experiments were also conducted at room temperature, as prior experiments had shown a quenching of the luminescence at low temperature possibly due to a degradation of the membrane under laser exposure and in vacuum. This quenching will be discussed further in 6.2.3.

Figure 6.5a shows the image detected by the streak camera: we clearly distinguish several modes from the background luminescence, even after a 90 minute acquisition.

⁵ as explained in 4.2.1

⁶as seen in 4.5.1

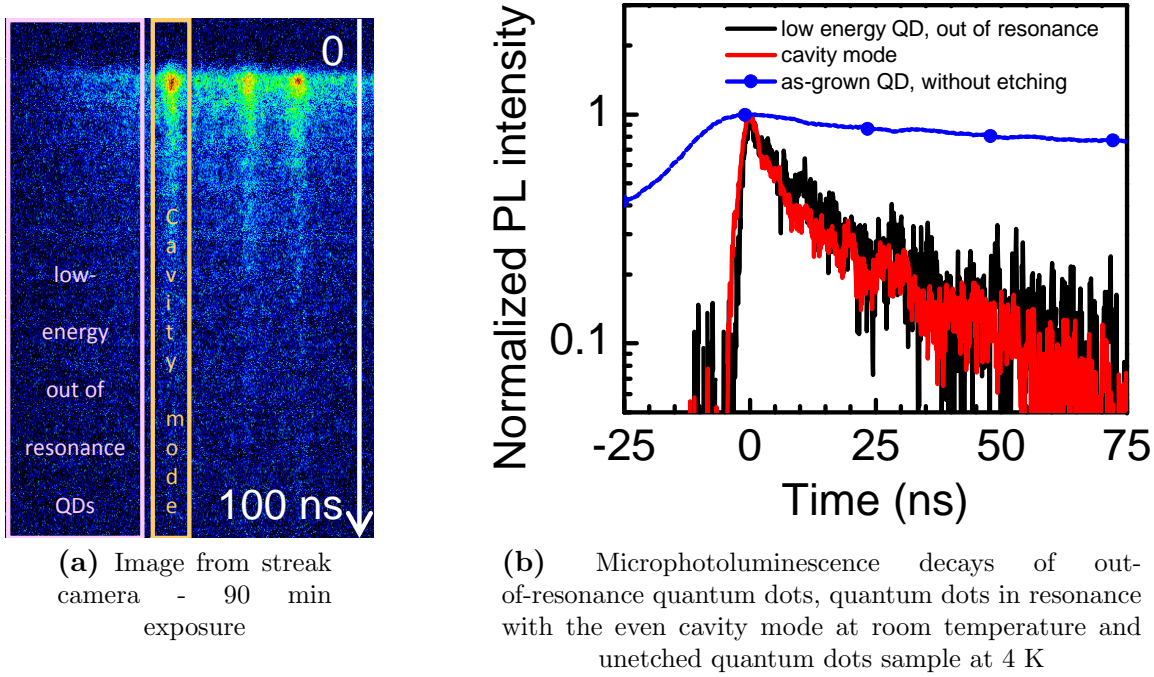


Figure 6.5 – Time-resolved microphotoluminescence measurements on sample A 1507
 - $D=0.35$, $r=0.25a$, $a=170$ nm

This is a proof of satisfactory stability of the system under long exposure. Yet when plotting both the decay time of the cavity mode and the decay of lower-energy quantum dots (figure 6.5b), we find no difference between them. Table 6.2 gives the decay times extracted from figure 6.5b.

Emission	Decay time (ns)
Cavity mode (300 K)	16
Out-of-resonance quantum dots (300 K)	20
As-grown quantum dots (4 K)	250

Table 6.2 – Comparison of the decay time of quantum dots in and out of resonance with the cavity mode at 300 K and the decay time of unprocessed quantum dots at 4 K

This data shows a slight enhancement around 0.8 of the spontaneous emission rate of quantum dots in resonance with the cavity mode compared to out-of resonance ones (on figure 6.5b and more precisely on figure 6.6). However, an unprocessed sample of quantum dots studied at 4 K as a reference gives a decay time of 250 ns. The comparison with our system is straight-forward: on photonic crystal structures, be they either in or out of resonance emitters, the decay times are 10 times lower. This suggests that in our etched system, the dominant recombination mechanism is non-radiative. However, temperature-dependent time-resolved photoluminescence measurements performed by our colleagues in Laboratoire Charles Coulomb (Université de Montpellier) have shown

that the decay time of quantum dots grown by nitrogen-MBE on a thin AlN buffer layer was not affected by raising the temperature between 4 and 300 K. Their behaviour is comparable to that grown by PA-MBE in thick AlN buffer layer [Ren09b]. We therefore attribute the main non-radiative recombination channel to the unpassivated surface etched surfaces. Yet, in order to weaken these non-radiative channels, we could try to work at lower temperature. Therefore, we have investigated the robustness of these structures to laser exposure while they are kept under vacuum and at low temperature in 6.2.3 .

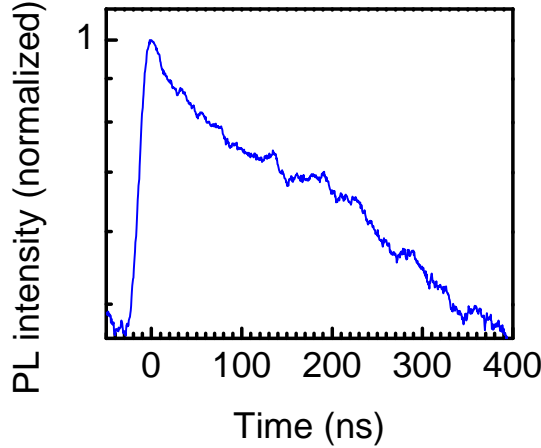


Figure 6.6 – Time-resolved microphotoluminescence decay curve at 4 K of an ensemble of polar GaN/AlN quantum dots emitting around 3.2 eV - sample A1676

Conclusion

We have performed time-resolved photoluminescence experiments at room-temperature in order to observe the shortening of the decay time of quantum dots coupled to a cavity mode without damaging the cavities. The measurement proved to be impossible in the case of microdisks. We managed to measure the decay time of a photonic crystal cavity embedded into a waveguide. However, the transients of both cavity-coupled and uncoupled quantum dots are several times shorter than that measured on unprocessed samples. Therefore the main recombination channel that we measured is non-radiative. We ascribe it to the roughness of the etched surfaces of the photonic holes.

6.2 Modal instability with exposure time

We have seen that rather long (typically 90 minutes) acquisitions were needed to get enough photons in time-resolved experiments in order to observe the Purcell effect in our nanocavities. However, when performing long acquisitions, the signal originating from the whispering gallery modes was lost in the background of the uncoupled quantum dots. Furthermore, from previous studies that we will present in this section, it appeared mandatory to work at room temperature. While doing so on the photonic crystal nanocavity sample, the decay time of both in resonance and out of resonance

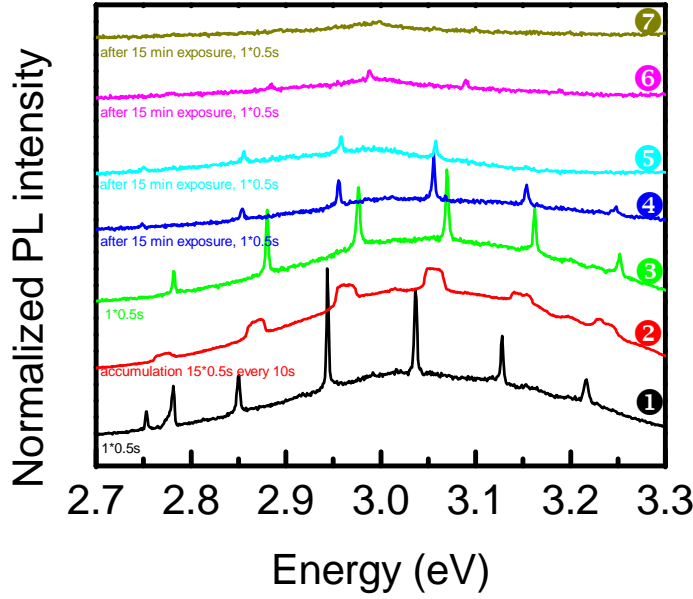


Figure 6.7 – Temporal evolution of micro-photoluminescence spectrum with 270 nm tripled pulsed Ti-sapphire exposure at room temperature and ambient atmosphere

quantum dots was fixed by non-radiative channels, attributed to the large amount of etched surfaces. In this section, we aim at understanding the processes which prevented us from measuring the Purcell factor of our structures, and evidencing in which conditions long acquisitions times are possible without sample degradation.

6.2.1 Instability of a whispering gallery mode under pulsed excitation

During time-resolved photoluminescence measurements, we performed acquisitions as a function of exposure time. The power of the frequently-tripled Ti-sapphire was kept low (of the order of 100 W/cm^2) and the sample was kept in air and at room temperature during the whole experiment. Figure 6.7 shows the resulting data. Spectrum ❶ corresponds to the first acquisition, once the mode contrast was maximized with the piezoelectric stage. Spectrum ❷ shows the addition of 15 acquisitions, performed every 10 seconds: we can see a clear broadening of the cavity modes, and an associated decrease of the mode contrast. From the comparison of spectra ❶ and ❷, it seems that the modes have blueshifted, which explains the broadening when long acquisitions are performed. The following five spectra are taken every 15 minutes. We observe a decrease in the intensity of both uncoupled quantum dot and whispering gallery mode luminescence. However, as the luminescence of the emitters feed the cavity modes, the quenching of the mode signal seems due to the quenching of the quantum dot luminescence, which provide fewer photons to the cavity modes.

In the following, we will use quantitative data extracted from the above results to answer the following question: is there a quenching of both whispering gallery mode and quantum dot emission? From figure 6.7, we extracted the energy and linewidth of the

quantum dot emission, plotted on figure 6.8a, as well as the integrated intensity of the dots in figure 6.8b.

Figures 6.9a and 6.9b focus on one mode, emitting at 2.945 eV during the first acquisitions; it may not be the same in all the spectra, because it is difficult to follow them as they shift by several times their linewidths between two successive acquisitions. In figure 6.9a, we have plotted the normalized data, after dividing by the intensity of the dots $I_{dot\ max} - I_{background}$ and then normalization. Indeed, without this data treatment, the mode contrast is hidden by the decreased dynamics of the quantum dot emission. The mode contrast is displayed in figure 6.9b and is defined as:

$$C = \frac{I_{mode\ max} - I_{mode\ min}}{I_{dot\ max} - I_{background}} \quad (6.5)$$

where $I_{mode\ max}$ is the intensity at the maximum of the mode, $I_{mode\ min} = I_{dot\ max}$ is the intensity at the minimum of the mode or the intensity of uncoupled quantum dots spectrally closer to the cavity mode, and $I_{background}$ is the detection noise (constant during the whole experiment).

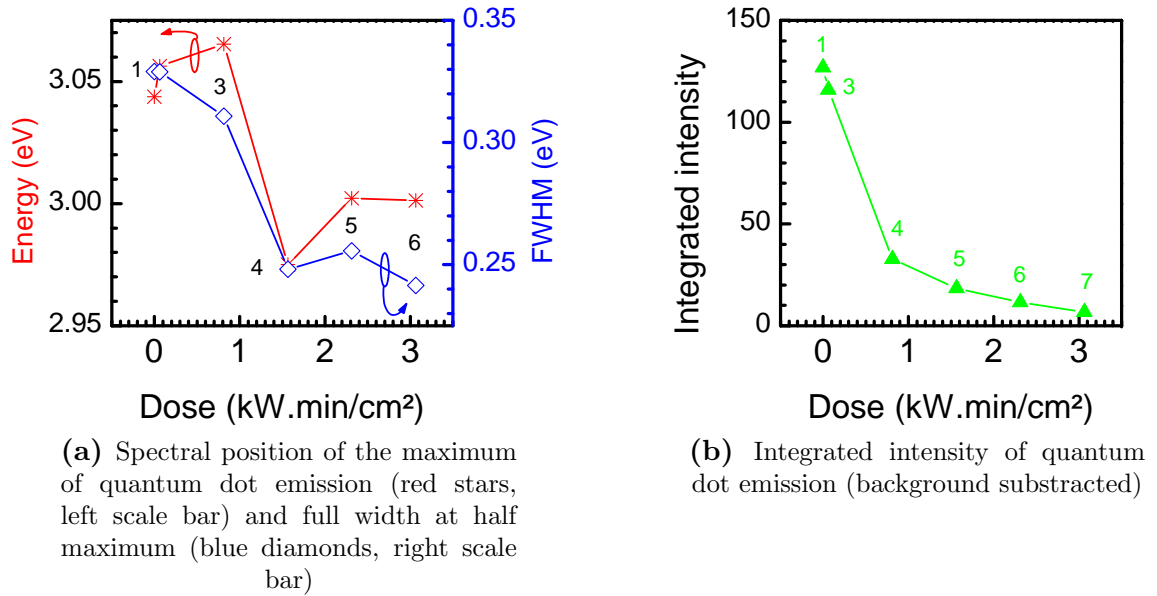


Figure 6.8 – Temporal evolution of quantum dot emission: extracted data from figure 6.7

The hypothesis of a quenching of the quantum dot emission providing fewer and fewer photons to whispering gallery modes is confirmed by the reasonably good mode contrast during the whole experiment. The luminescence intensity from the quantum dots loses a factor of 16 during this experiment (see figure 6.8b), while the mode contrast is only decreased by a factor of 4 (see figure 6.9b).

We thus conclude that during this one hour-long exposure to pulsed Ti-sapphire laser, the *whispering gallery modes have blueshifted*, which makes a one-hour long acquisition

in time-resolved conditions pointless as the spectral positions of the cavity modes evolve during the measurements. Moreover, after a few minute exposure, *the luminescence from the quantum dots begin to quench, and completely disappears after one hour.*

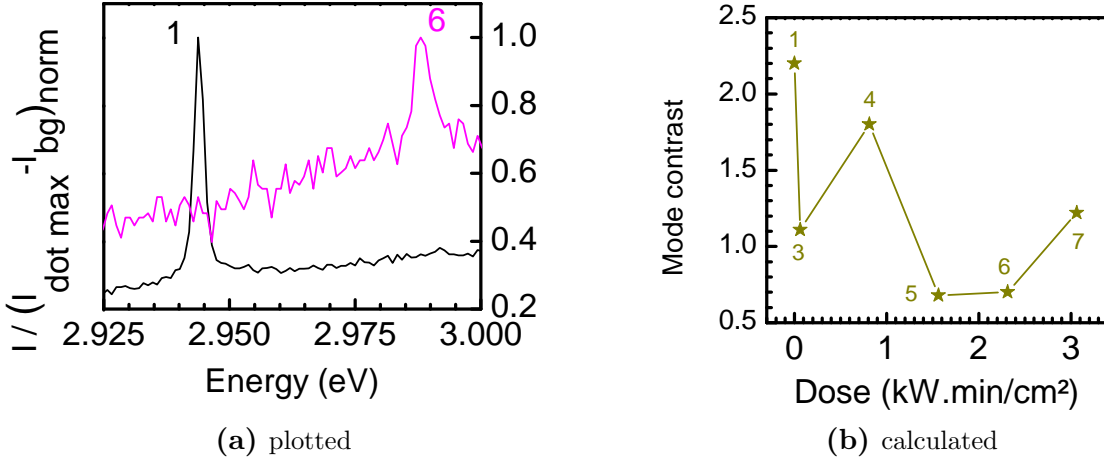


Figure 6.9 – Mode contrast extracted from figure 6.7

Both effects are expected to originate from different mechanisms. A variation of the *electronic* properties of the quantum dots can explain the quenching of their luminescence, by *e.g.* a modification of the position of the Fermi level due to a different density of charges trapped on the surface states. Indeed, GaN/AlN quantum dots can be used as sensitive probes of their environment: Weidemann *et al.* [Wei09] reported a 10% variation of the luminescence intensity when exposed to H₂ while under negative bias. Thus, they could be used as “optical transducers for field effect chemical sensors” [Wei09]. The phenomenon considered in the experiment reported by these authors is however of much smaller dynamics (10%) than that occurring on the microcavities we probed, where the quantum dot luminescence intensity decreases by a factor of 16 relative to its initial value. Furthermore, the blueshift of a cavity mode must be ascribed to a change of the *photonic* properties of the cavity, by *e.g.* the effective index, or the size of the cavity.

6.2.2 Whispering gallery mode shifting under continuous-wave excitation

At this point, we can wonder whether this instability of both cavity modes and quantum dots is related to the pulsed excitation, or is intrinsic to long UV exposure. This is the reason why we performed additional experiments under continuous-wave excitation.

Low-temperature evolution Figure 6.10a compares the emission of the same microdisk (at 4 K and under 266 nm excitation at 40 μ W), right after the alignment is achieved, and after a five minute exposure. The second spectrum is clearly blueshifted: the emission

from quantum dots moved by 78 meV towards higher energy, while the whispering gallery modes also seem to be blueshifted.

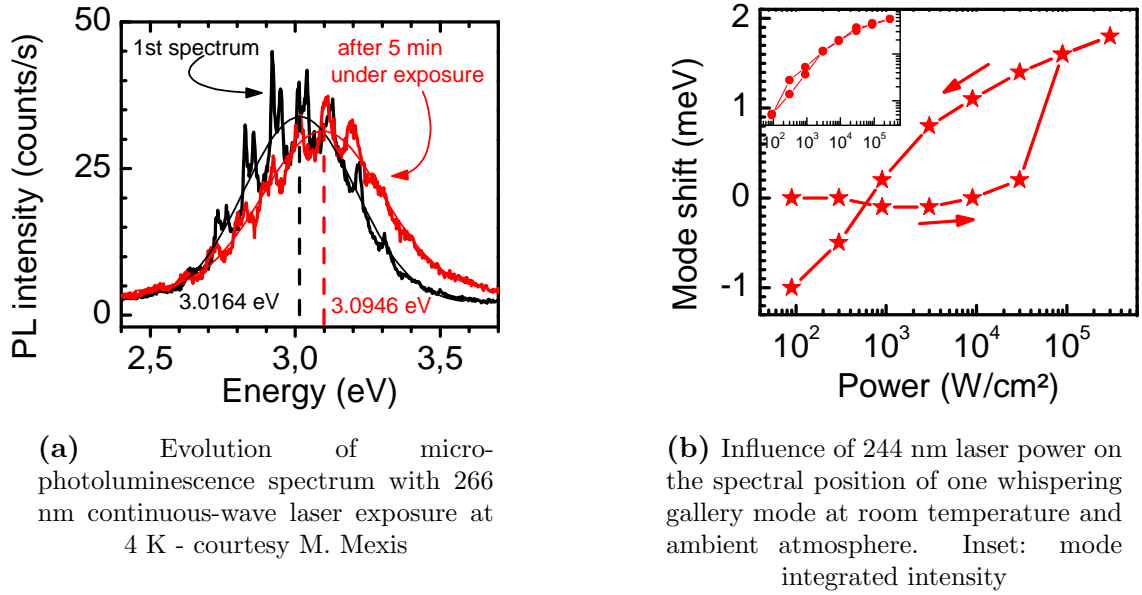


Figure 6.10 – Time- and power-dependence of the microphotoluminescence of microdisks

Power-dependent measurements Figure 6.10b shows the evolution of the spectral position of a whispering gallery mode of a microdisk in air at 300 K when power is increased. With an increase by two orders of magnitude the mode remains stable. From 30 to 100 kW/cm², however, the mode starts to blueshift by more than its linewidth (in the order of 1 meV). Decreasing the power to reach the conditions of the first acquisition leads to a progressive redshift of the emission. Yet the system does not come back to its initial position and, at the end of the whole measurement, the mode is redshifted by 1 meV compared to the first measurements. Despite the fact that a continuous-wave excitation provides smaller peak power than a pulsed excitation (with comparable mean power and photo-generated carriers), irreversible effects are also observed when using this laser source for a duration of several minutes (figure 6.10a) or at a rather high power (figure 6.10b). To get more insight on the processes responsible for shifting the cavity modes, we performed systematic scans with exposure time: the laser was kept on the sample and the software automatically and periodically acquired a spectrum.

An example of whispering gallery mode blueshift in air Applying this method to a microdisk in ambient air at room temperature led to the cartography of a given mode depicted in figure 6.11a. A linear blueshift of 350 $\mu\text{eV} / \text{min}$ is observed. To give an order of magnitude, it means that the mode shifts by its linewidth every three minutes. This process seems to be endless, as no saturation is observed after 70 minutes of exposure. Yet the mode was not damaged by the long exposure: after 70 minutes, figure 6.11b

shows that the quality factor is still 85% of its initial value, and the mode integrated intensity (after subtracting the background luminescence of uncoupled quantum dots) stays of the same order of magnitude. Let us notice that the increase of both quality factor and integrated intensity after 20-30 minutes (dose 30-50 kW.min/cm²) of exposure is still not explained.

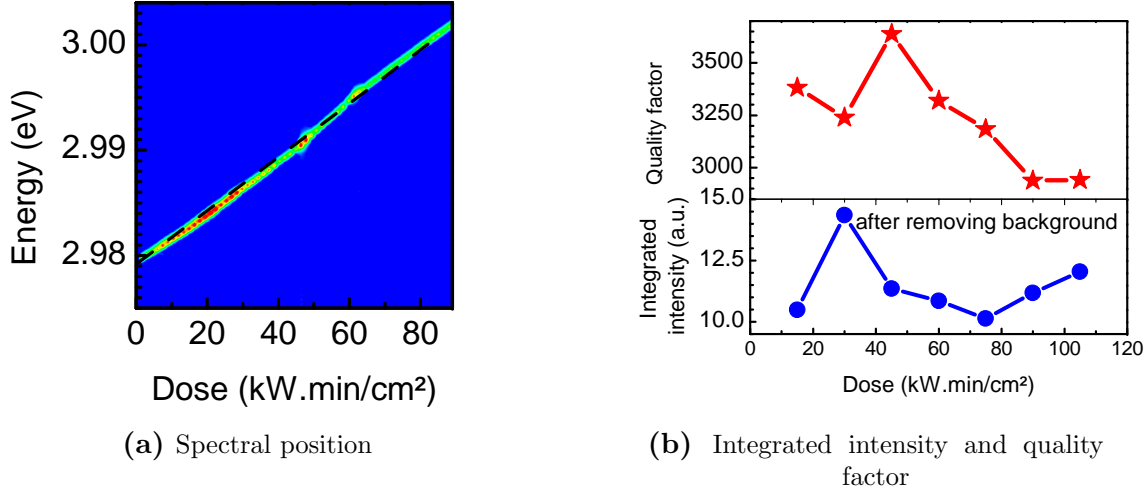


Figure 6.11 – Temporal evolution of the microphotoluminescence of one whispering gallery mode at room temperature and ambient atmosphere with exposure time with a 244 nm laser

Examples of whispering gallery mode redshift in nitrogen and vacuum environments

The trend observed on figure 6.11a is not typical for all the microdisks probed. Some displayed no shift under comparable exposure, or a redshift. Figure 6.12a shows the result from a 100 minute-long exposure to a 10- μ W laser at 244 nm while the sample is kept under vacuum and room temperature. We follow one whispering gallery mode. The sudden intensity drop around 50 kW.min/cm² is an artifact of the plot. A clear redshift of 26 meV in 90 minutes — *i.e.* 0.8% of the emission energy — is observed, as well as a saturation of the spectral position of the mode.

Figure 6.12b gives an example of the spectral evolution when the cryostat is pumped and then filled with nitrogen prior to laser exposure. The microdisk under study is kept at 300 K and shows three whispering gallery modes originating from two different families. We will focus on the two lower-energy modes, labeled ❶ and ❷. Both modes exhibit a redshift with exposure, but it is interesting to note that mode ❶ shifts more strongly than ❷: 320 against 95 μ eV/min (28 meV against 8 meV in 90 minutes). From the comparison of their free spectral range, we tentatively ascribe mode ❶ as belonging to the TE, $\ell=1$, $n=1$ mode family and mode ❷, to $n=2$.

Note that, contrary to the results obtained with a pulsed excitation (figure 6.7), no quenching of the luminescence was observed during the experiments using the continuous-wave laser.

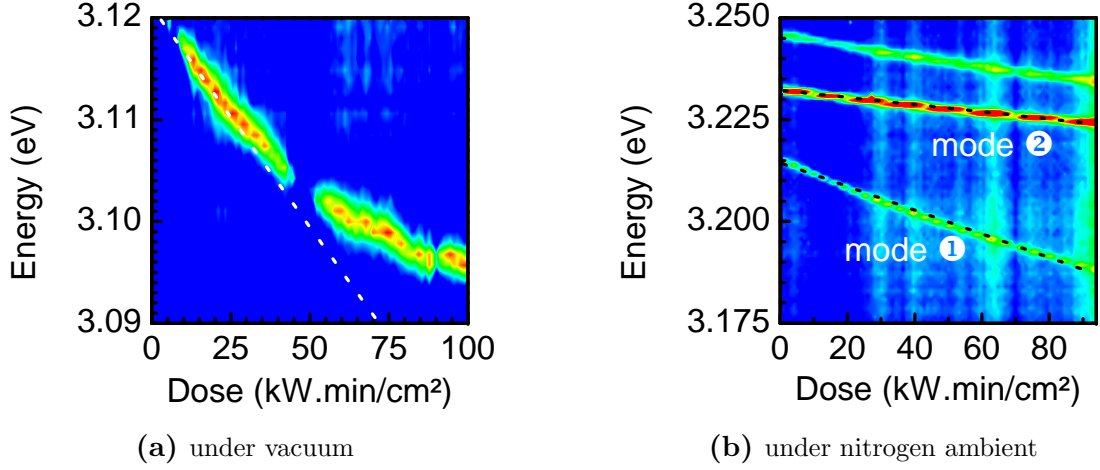


Figure 6.12 – Evolution of whispering gallery modes at room temperature and with exposure time with a 244 nm laser

6.2.3 Photonic crystal cavity mode: stable or instable?

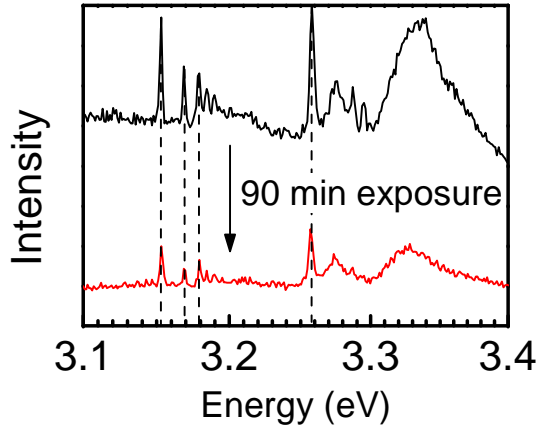


Figure 6.13 – Evolution of the modal emission from the cavity and the waveguide before and after a 90 minute exposure by a frequency-tripled Ti-Sa at 300 K in air - sample A1507 - $D=0.40$, $r=0.27a$, $a=170$ nm, $d=12$ nm.

Stability under pulsed Ti-sapphire excitation in air As far as nanocavities embedded in photonic crystal waveguides are concerned, we have seen in figure 6.5a that the spectral position of the modes were stable under long Ti-sapphire laser exposure of the order of 90 minutes at room temperature. Figure 6.13 compares the spectrum of a cavity right after the alignment and after the long exposure: 40% of the mode contrast is conserved, and no shift is observable. Yet we have proven that the Purcell effect was hidden by non-radiative processes in these structures when probed at 300 K. Therefore we investigated their robustness to simultaneous exposure to frequency-doubled Argon laser at 244 nm and temperature decrease in order to find experimental conditions suitable for a decreased efficiency of such non-radiative processes.

A quenching of the luminescence with decreasing temperature Figure 6.14 shows the peculiar evolution of both cavity and guided modes, with varying the environment

(details in table 6.3). The excitation source is a 244 nm Ar laser. We can observe that, when pumping the cryostat at room temperature, the spectrum blueshifts by 4 meV (spectra ❶ - ❷). Furthermore, while being at liquid He temperature, the laser exposure "kills" the emission before any alignment could be performed (spectrum ❸). This is not due to an instability of our setup due to vibrations, because we removed the pump (which is the major source of vibration) as soon as the sample reached 4 K. From 50 to 200 K, the modes appear again, with an increasing contrast and a blueshift of 8 meV (spectra ❹ - ❺). At 250 K, the modes disappear again (see spectrum ❽). This could be caused by the significant degradation of the vacuum between 200 K and 250 K⁷. When the temperature reaches 300 K, under vacuum, modes are still absent (not shown here). However, as soon as air fills the cryostat, the modes appear again (spectrum ❾). Between spectra ❾ and ❿, we simply waited for three days without any additional experiment in the meantime. The modes were strongly redshifted by 19 meV.

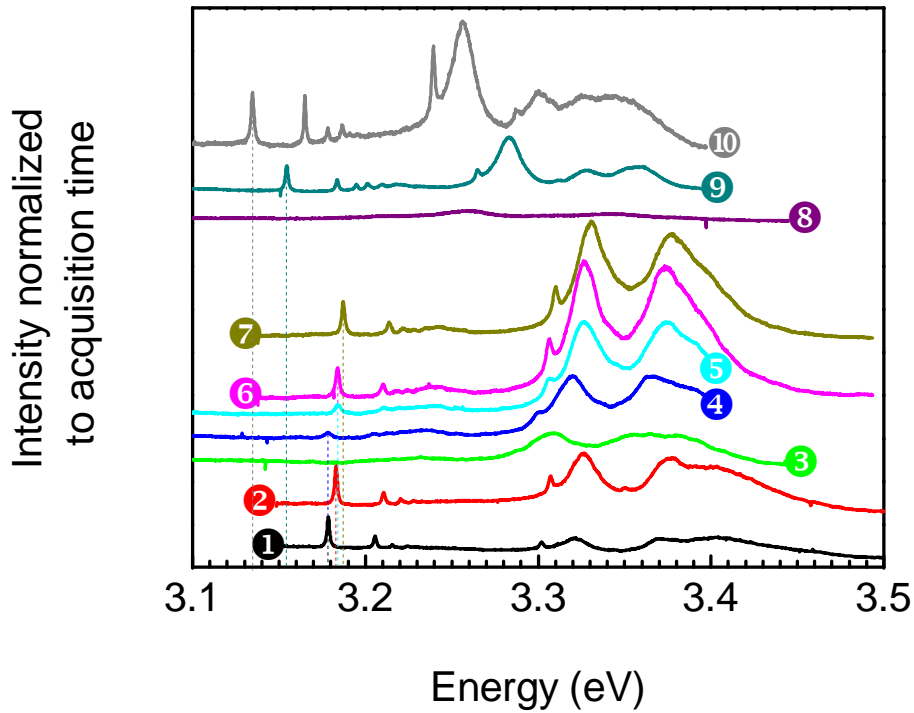


Figure 6.14 – Evolution of the emission from the cavity and the waveguide when pressure and temperature are changed, under frequency-doubled Argon exposure at 244 nm: conditions are summarized in table 6.3 - sample A1507 - $D=0.40$, $r=0.27a$, $a=170$ nm, $d=12$ nm

After this first experiment, as soon as we pumped the cryostat while still at room temperature, the modes totally disappeared. However, we were able to perform additional measurements on all the cavities of the sample, as long as the sample was kept under atmospheric pressure. Yet, even on the cavities which were not probed during low-temperature experiments, we were not able to see the modes when pumping the

⁷We could not measure the vacuum as the pump and its gauge had been removed

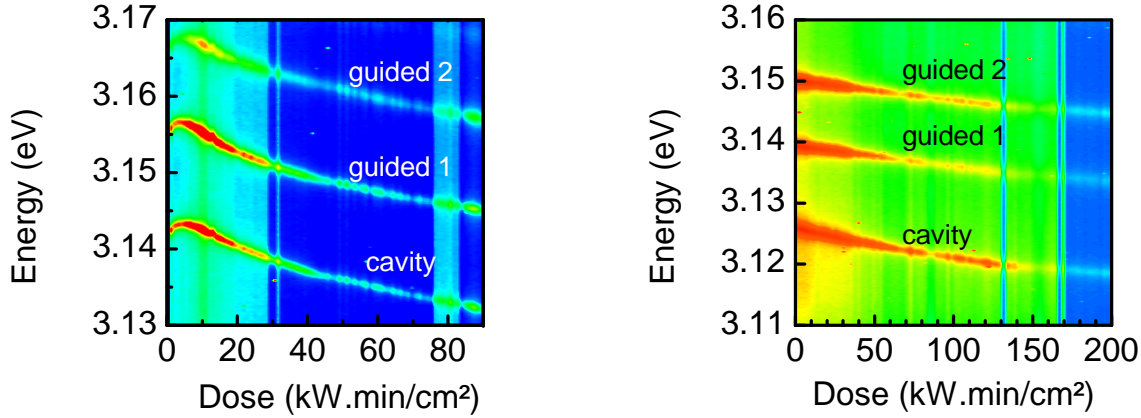
Spectrum number	Pressure (mbar)	Temperature (K)
❶	10^3	300
❷	5.10^{-4}	300
❸	5.10^{-5}	4
❹	5.10^{-5} ?	50
❺	5.10^{-5} ?	100
❻	5.10^{-5} ?	150
❼	5.10^{-5} ?	200
❽	5.10^{-5} ?	250
❾	10^3	300
❿	10^3	300

Table 6.3 – Acquisition conditions for spectra 1 - 10 of figure 6.14

cryostat again for further experiments. It thus seems that the photonic crystal structures have “kept the memory” of going to low temperature: this seems to have strongly and irreparably affected the surface states of the whole photonic crystal cavities.

Mode redshift with continuous-wave exposure in air We have previously determined that such structures are stable under long exposure times to a pulsed excitation. Yet, their luminescence is strongly quenched when probed at low-temperature with a continuous-wave excitation. In order to decouple the influence of the excitation and that of the sample temperature, experiments similar to that presented on figure 6.11a were conducted with excitation at 244 nm, at 300 K in air: the power is fixed low (1 kW/cm^2) and we perform 90 automatic and periodical acquisitions lasting 10 s each, with a repetition time of 70 s or 80 s. The influence of the dose on the microphotoluminescence is plotted on figures 6.15a and 6.15b. Between both measurements, 20 minutes of additional exposure (without acquisitions) and 16 hours without laser illumination have passed.

Such experiment allowed us to observe that these photonic crystal structures were not stable under continuous-wave exposure to a 244 nm frequency-doubled Ar laser. From these plots, we observe a parallel evolution of the three modes investigated, originating from both the cavity and the waveguide. This suggests an evolution of the properties of the whole photonic crystal, rather than a localized modification. After a slight blueshift happening during the first minutes of exposure, the modes redshift by 20 meV without showing any visible saturation. The continuity between the last spectrum of the first series and the first spectrum of the second series (16 hours have passed between them) in terms of spectral position shows that *the redshift is irreversible*. After a careful extraction of the data from figures 6.15a and 6.15b (not shown here), we have noticed that the integrated intensities of the three modes first increases during the first 10 minutes ($0 - 10 \text{ kW.min/cm}^2$), and their values are then doubled compared to their initial ones. Then they decreases during the next 50 minutes ($10 - 50 \text{ kW.min/cm}^2$), increase again



(a) First measurement: 90 acquisitions lasting 10 s each repeated every 70 s

(b) Second measurement: with an additional 20 min long exposure, 16h after last exposure, 89 acquisitions lasting 30 s each and repeated every 80 s

Figure 6.15 – Evolution of the spectral position of the cavity mode and two guided modes with exposure time at 244 nm at 300 K and in air - A1507 $D=0.40$, $r=0.25a$, $a=170$ nm, $d=9$ nm

towards their initial values (first measurement). From 100 minutes of exposure onwards, they decrease to a total quenching of the luminescence (second measurement). The initial quality factor of the cavity mode is 3300, that of the two guided modes are 2700 and 1900. During the first series, the quality factor slightly increases by 3% during the first 30 minutes of exposure. Then it monotonously decreases (during the end of the first series and the second series) towards a value in-between 1500 and 2000. The degradation of both quality factor and integrated intensities in the same amount for the three modes suggests *a degradation of the whole photonic crystal* during the second series.

6.2.4 Possible explanations for cavity mode shift

In this part, we will investigate all the possible phenomena responsible for the shift and / or the quenching we observe. The first processes one can consider are *thermo-optic*.

Heating up the cavity Rastelli *et al.* have performed experiments on an InAs/GaAs quantum dot microdisk [Ras07] in order to shift a whispering gallery mode so as to bring it in resonance with a quantum dot. Increasing the power continuously (without stopping the exposure) led to a strong redshift of the emission from both InAs wetting layer and GaAs barriers. It is due to the heating of the cavity, leading to a shortening of the band gap. Moreover, a more modest redshift of the cavity mode under study was observed. It is attributed to thermal effects, leading to a decrease of the GaAs refractive index. By fitting the evolution of the spectral position of both the wetting layer and the barrier, they access to the temperature of the microdisk: when the power is 0.1

MW/cm², the temperature at the periphery of the disk reaches 700 K!

The spectral dependence of the mode energy E with effective index is:

$$m \frac{\hbar c}{E} = n_{\text{eff}} a \quad (6.6)$$

where m is the azimuthal index, n_{eff} is the effective index and a , the radius of the microdisk. With $m=20$ and $a=1 \mu\text{m}$ ($E \approx 3 \text{ eV}$), the derivative of equation 6.6 shows that a mode redshift of 25 meV (the order of magnitude of what is observed on figures 6.12b and 6.12a) can originate from a reduction of 0.01 of the refractive index (0.5% of its value). For AlN, the change of the refractive index with temperature is $\frac{dn}{dT}=5 \cdot 10^{-4} \text{ K}^{-1}$ for a photon energy around 3 eV [Wat08]. An increase of the effective index by 0.01 corresponds to a heating by 20 K, which is absolutely possible.

To confirm that in the absence of oxygen (both in vacuum and nitrogen), the dominant mechanism responsible for the shift of the whispering gallery mode (figure 6.11a) is thermal, we would need to check the reversibility of the process. The spectral positions of the modes we studied should have come back to their initial values after a while without any laser exposure. The absence of reversibility of the redshift observed on the photonic crystal structures exposed to the 244 nm continuous-wave laser show that the process at stake does not have a thermal origin.

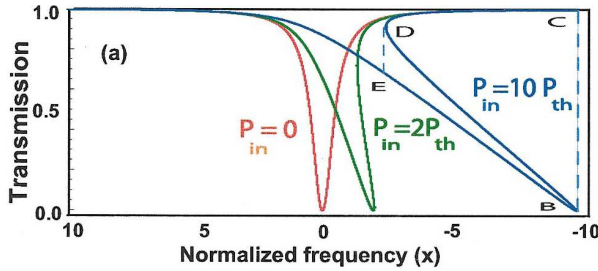


Figure 6.16 — Thermal shift of the resonance frequency of a silica microtoroid and associated distortion of the cavity mode transmission for different input power. P_{th} is the power needed to shift the resonance by its linewidth. [Rok04]

If the shifts we observe originated from thermal effects, the response time needed to reach thermal equilibrium would be very long: even when the shift we measure is sublinear (as observed on figure 6.12a), we never observed the appearance of a clear steady-state regime after several hours of exposure. Indeed, in silicon, bistability (illustrated on figure 6.16) can be used as an all-optical switch [Alm04] with time response quicker than a second. Yet contrary to bistability studies, we are not changing the power quickly but only the dose: response time may be strongly enhanced in our case. Figure 6.12b shows that $n=1$ modes shift four times quicker than $n=2$ modes. The observation of a wider redshift for the $n=1$ modes, localized closest to the sidewalls, suggests that the periphery of the disk is more strongly modified than the inner part of the disks during the exposure. This is in accordance to the thermal hypothesis. Indeed, the $n=2$ modes undergo fewer heating because of the possible thermal transfer to the silicon post. As consequence, they undergo fewer increase of the effective index compared to the $n=1$ modes.

A shift of the cavity mode spectral position can also be accounted for an *in-situ modification of the cavity size by chemical adsorption or desorption*. We consider the relation between the microdisk radius a and the spectral position of the mode E (equation 6.6).

Modification of the diameter We see that a blueshift such as displayed on figure 6.11a could be ascribed to a decrease of the microdisk diameter. Quantitatively, the derivative of equation 6.6 shows that the mode blueshifts of 25 meV could be attributed to a reduction of the radius by 6 nm (0.6% of the total radius). This is physically possible if we consider that the laser beam can ablate atoms from the surface.

Modification of the thickness A modification of the cavity size could also originate from a thinning of the cavity: for a 2 μm disk, a 25 meV blueshift requires an effective index drop by 0.01, which could be accounted to by a thickness decrease of 5 nm (5% of the total thickness), *i.e.* a slab thickness of 105 nm instead of the initial value of 110 nm.

In both cases (reduction of either diameter or thickness), it will be difficult to check the hypothesis: the sensitivity of scanning electron microscope may not be enough to measure such a small size variation of the microdisk. In the InAs / GaAs quantum dot microdisk system, it has been reported that increasing the power while stopping the exposure between each increasing step leads to a blueshift of the whispering gallery modes [Ras07]. From 0 to 0.1 MW.min/cm², the TM mode blueshifted by 5 meV, while the TE mode, by 1.5 meV. Besides, there have been some reports about either the absorption or the desorption of species adsorbed on the surfaces of cavities kept at low-temperature [Str06][Mos05] resulting in a shift of cavity modes. Rastelli *et al.* thus concluded that the blueshift was attributed to a shortening of the effective size of the microdisk by laser-induced desorption of adsorbed molecules. From the comparison of their results to calculations, they deduced that mainly the thickness of the microdisk was shortened. Then, they computed the thickness variation accounting for the blueshifts mentioned above: they obtained a shortening of the thickness of 3.6 nm (1.5% of the whole size).

"Cryo-gettering" One possible explanation of the observed redshift and quenching of the mode emission of a photonic crystal cavity (see figure 6.14) could lie in the irreversible deposition of impurities from the cryostat on the surface of the sample when it is kept at low temperature (cryopumping), because the sample is one of the coldest regions inside the cryostat. These impurities could change the surface states, and affect the optical properties in a large extent, considering the total etched surface. For future temperature-dependent experiments on new samples, we therefore suggest not to let the sample be at 4 K and always heat it to 10-15 K, so it never becomes the coldest surface

inside the cryostat.

This process has been observed on InAs / GaAs photonic crystal cavities [Str06]: adsorption was promoted by the low-temperature of the sample, kept at 4 K. Strauf *et al.* have studied the consequences of the adsorption of molecules on the surface of a photonic crystal cavity, a phenomenon they call “cryo-gettering” [Str06]. They found that *this process is totally reversible by a temperature-cycling from 4 to 410 K*. Besides it *saturates* after a few hours and was found to be more pronounced on a photonic crystal cavity rather than on a microdisk. It leads to a redshift of 6 meV in 200 minutes at 15 μ W but induces *no quenching* of the mode emission. On the contrary, the redshift we observed is irreversible, and a clear quenching is observable.

Hole filling During the experiments we performed on photonic crystal cavities with varying the dose (see figures 6.15a and 6.15b), however, the sample was kept at room temperature and in air: it is therefore unlikely to adsorb more species than the amount they already have at equilibrium, *i.e.* without exposure.

Qualitatively, a redshift could be attributed either to an increase of the hole periodicity or to a decrease of the hole radius. This is consistent with filling the holes with deposited atoms, originating from organic molecules, cracked by the laser on the surface of the photonic crystal. The hypothesis of the enhancement of hole filling with the exposure of a Ar laser seems in contradiction with the stable mode emission when the cavity is excited with a tripled Ti-sapphire laser. Maybe these molecules are not sensitive to this pulsed illumination at 270 nm, while they are much more affected by a continuous-wave frequency-doubled Argon laser exposure at 244 nm.

This is in contradiction with the laser ablation of the microdisk surfaces when it is kept in air. Yet the geometry of both systems are different, and the amount of etched surfaces in a photonic crystal is enhanced by a factor of 4 compared to microdisks.

Conclusion

We have seen that it was mandatory to work at room temperature in order to measure stable cavity modes. From the various statistics we performed, no clear tendency was found for each given probed atmospheres, but they all seem to induce an instability on the mode spectral position. One possible solution would be to find a way to first saturate the mode shift, and then perform the long-time time-resolved photoluminescence experiments to observe the Purcell effect.

6.3 Instability of quantum dot emission under long exposure

We have seen that the emission originating from quantum dots was also modified during a long laser exposure, be it either with a continuous wave experiment (see figures 6.10a) or a pulsed illumination (see figure 6.8b). We investigated the underlying processes responsible for this instability. First, we checked that these evolutions were not intrinsic to GaN/AlN quantum dots grown on a thin buffer layer, but due to the presence of etched, unpassivated surfaces.

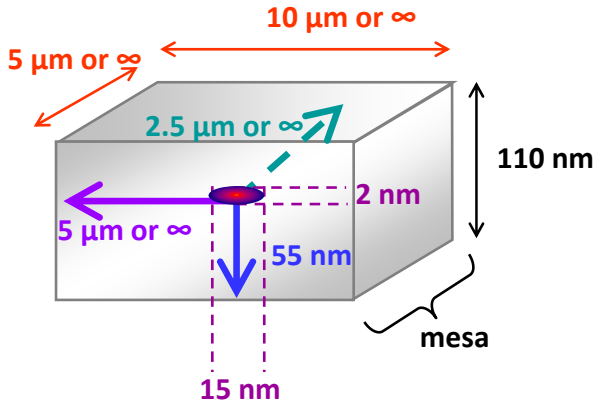


Figure 6.17 – Schematics showing the proximity to surfaces for any quantum dot in a $5 \times 10 \mu\text{m}^2$ etched mesa (proximity 2.5 μm and 5 μm to the lateral surfaces) or in an unetched layer (there is a quasi-infinite distance between the quantum dot and the lateral surfaces).

Both etched and unetched samples consist in four layers of quantum dots, separated by a 15-nm AlN barrier, coated by a topmost 35-nm AlN barrier and grown on a bottommost AlN barrier of the same thickness. The epitaxial structure is thus identical to that of the sample used to obtain the microdisks studied in chapter 4 and in 6.2.2. A schematic of the sample is depicted on figure 6.17. In the etched sample, the lateral surfaces are closer than 5 μm to any quantum dot and the horizontal surfaces are closer than 55 nm. However, in unetched samples, the quantum dots are located several mm far from lateral surfaces (suggested by the ∞ symbol in figure 6.17), while the horizontal surfaces are again 55 nm far away from the quantum dots. The main difference in the environment of a quantum dot in both samples therefore concerns the proximity of lateral surfaces.

We probed the evolution of the luminescence of quantum dots at room temperature and atmospheric pressure, at two different excitation powers, 10 and 100 μW (called afterwards series 1 and series 2). In order to show when the power was increasing by a factor of 10, we displayed a vertical broken line in the plots.

6.3.1 Checking the stability of non-etched quantum dots

In this part, we focus on the consequences of a long-exposure time on as-grown quantum dots. The emission seems completely stable in the investigated dose range. This is

confirmed by the extraction of both the emission energy and the full width at half maximum (obtained with a Gaussian fit), plotted and figure 6.18a. Furthermore, figure 6.18b shows the evolution of the integrated intensity of the emission, after background subtraction.

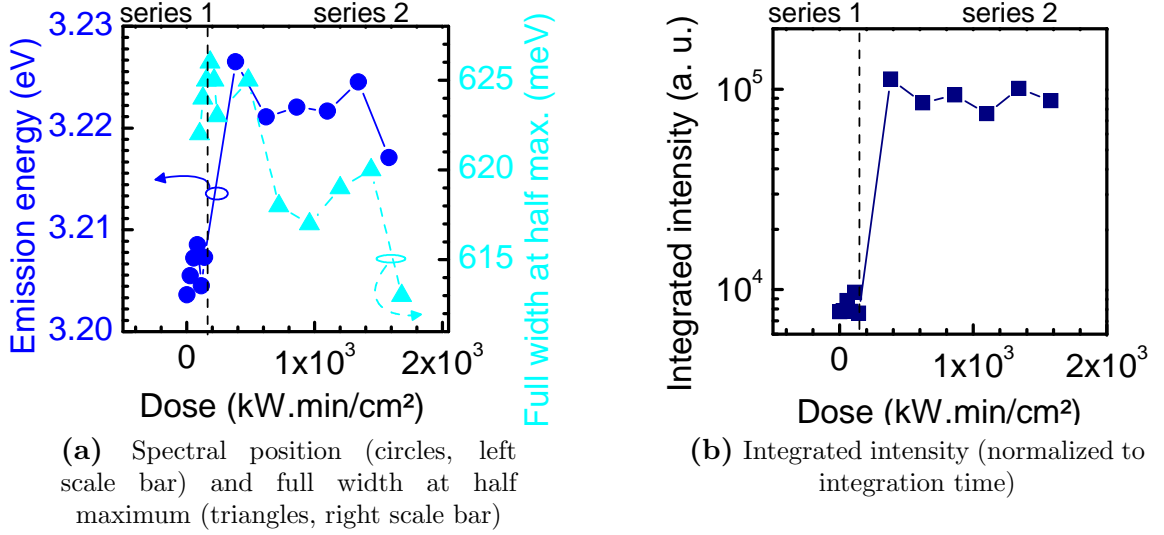


Figure 6.18 – Evolution of the emission of unetched quantum dots with exposure dose to a 244 nm frequency-doubled Ar laser at 300 K, in air. The vertical broken lines shows when the power was increased by a factor of 10 - sample A1676

These figures allow us to point out that no energy shift is observed with increasing dose at a fixed power, but a blueshift happens as soon as the power is raised by a factor of 10. As a consequence, it cannot be ascribed to a long exposure, but rather to a partial screening of the quantum-confined Stark effect due to the high carrier density generated by a higher excitation power. Besides, the sharpening of the emission is in the 2% range and thus in the order of magnitude of the errors generated by the fit. At a fixed power, the integrated intensity remains stable. To conclude on this part, we have shown that *a quenching and / or a blueshift of the luminescence with exposure dose is not intrinsic to unetched quantum dots.*

6.3.2 Instability of etched quantum dots

To get further insight on the processes responsible for an evolution of the luminescence of etched quantum dots, we performed exactly the same experiments than what was described in 6.3.1 on etched samples: a first series of automatic acquisitions at 1 kW/cm², and a second one at 10 kW/cm². We focus the laser on a rectangular pattern of about 50 μm^2 , etched during the same process than the microdisks studied in chapter 4. We thus expect to decorrelate the evolution of out-of-resonance quantum dots from that of cavity modes. Note anyway that the amount of etched surface relative to the volume of the structure is smaller by a factor of around 3 than in "real" microdisks. Therefore the

quenching or / and the shift we will analyze in this part are expected to be weaker than in quantum dots embedded in a microcavity. Figure 6.17 illustrates the system under study; note that this pattern should embed 500 quantum dots in each of the four layers of the structure.

Figures 6.19a and 6.19b display the spectral position, full width at half maximum and integrated intensities. During the first 30 minutes of series 1 ($0 - 30 \text{ kW.min/cm}^2$), the emission stays stable, as far as spectral position, linewidth and intensity are concerned. After a 30 minutes exposure (series 1), the intensity is enhanced and the whole emission is asymmetrically blueshifted. When increasing the power by a factor of 10, the asymmetrical blueshift goes on: there is no quenching of the low-energy emission but an enhancement of the high-energy part, confirmed by the increase full width at half maximum on figure 6.19a. Finally, the luminescence starts to quench after 30 minutes of illumination at 10 kW/cm^2 .

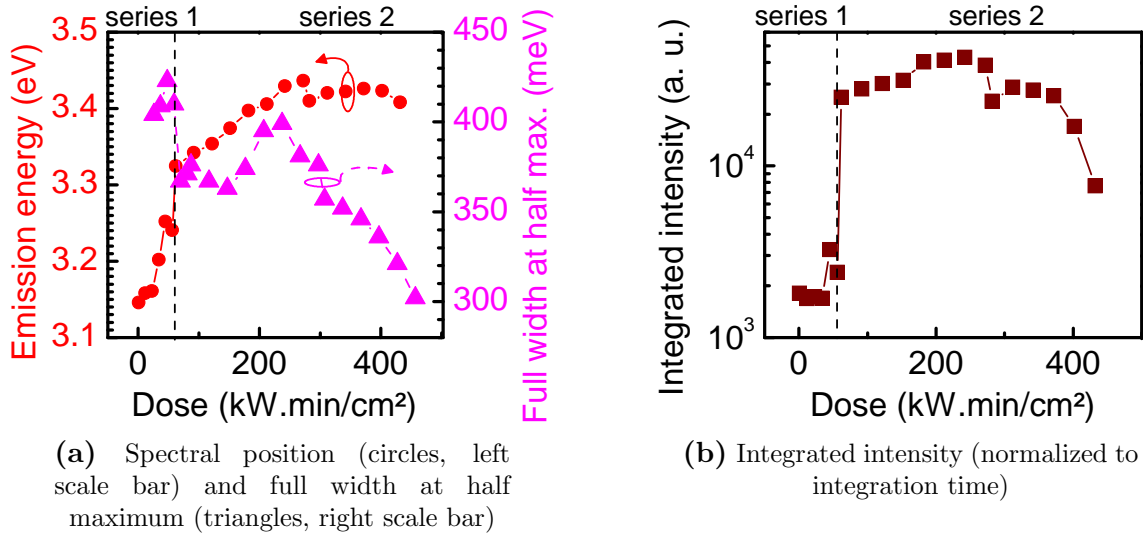


Figure 6.19 – Evolution of the emission of etched quantum dots with exposure dose to a 244 nm frequency-doubled Ar laser at 300 K, in air. The vertical broken lines show when the power was increased by a factor of 10 - sample A1497-4

We can compare these results from figures 6.18a and 6.18b which depict the measurements performed on unetched quantum dots. Many differences are visible in the evolution of emission with exposure time. As it was observed on as-grown samples, the rapid blueshift in both series is attributed to a partial screening of the quantum-confined Stark effect by band filling. However, on etched samples, the emission also shifts continuously with time and even at fixed power. During both the first and the second series, the spectral position of the maximum increases by around 100 meV. At short time scales, the full width at half maximum varies in a rather chaotic way. These short-time fluctuations are maybe due to a deviation of the emission shape from a pure Gaussian function, giving a considerable error in the determination of its value. Yet on the whole experiment, the emission is narrowed by 25%. The luminescence intensity

increases during the first series. During the second series, it first continues to increase and then starts to decrease.

6.3.3 Possible processes resulting in the blueshift and a quenching of the emission of etched samples

The modification of surface states is expected to have serious consequences on a GaN/AlN heterostructure. This has been pointed out by computing the band structure of the same heterostructure with varying only the nature of the cap layer [Kan08]. These computations show that an AlN cap layer lowers the first electronic state under the Fermi level, while a GaN cap layer depletes the heterostructures. This strong effect is due to polarization fields. Therefore, the electronic level of nearby surfaces can significantly change the charge state of the active layer.

A screening of the quantum-confined Stark effect? The association of a blueshift and an enhancement of the intensity is in favor of a long-time screening of the electric field. Brandt *et al.* excited GaN/AlN quantum dots emitting at 3.3 eV with a He-Cd laser at 3.8 eV at high power (20 kW/cm²). They observed a blueshift of the quantum dot emission by 0.2 eV, a narrowing from 320 to 200 meV and an enhancement of the intensity by a factor of 2 after ten minutes of illumination — equivalent to a dose of 200 kW.min/cm², *at a temperature around 77 K only*. These effects were reported to be too slow at low temperature, and too fast to be measured at room temperature. Afterwards, the values saturated. They observed this particular trend on all the samples of polar quantum dots investigated. However, none of the non-polar samples they probed exhibited a similar evolution. They attributed these strong changes to the transfer of charges trapped by edge-dislocations located in the vicinity of quantum dots, which are typical defects to \bar{c} -axis samples only.

The electric field in these structures is around 9 MV/cm [Bre06]. The calculation of the electric field created by a single charge trapped on a defect inside a quantum dot gives a field of about 50-100 kV/cm [Rol07a][Bar07]. If it is located 10 nm away from the center of this dot, it creates a field of less than 10 kV/cm [Rol07a]. Both the shift and the screening of the quantum dot luminescence could then be explained by charge transfer from the surfaces towards the quantum dots.

Nakaoka *et al.* have studied the influence of an electric field parallel to the growth axis of a single GaN/AlN quantum dot emitting around 3.6 eV [Nak06a]. They see a blueshift of 100 meV when a forward bias of 14 V is applied. However, the voltage drop across both AlN and the SiC substrate is unknown - and they do not mention it. This prevents us from evaluating the field they actually applied to the dots.

Axial or lateral surfaces? However, it seems more relevant to attribute the changes we observed to the modification of the lateral surface — the ones which were etched — rather than to the axial ones. The team of Pr. Arakawa also studied the influence of a lateral field on the luminescence of a single GaN/AlN quantum dot emitting at 3.4 eV without external field [Nak06b]. Whatever the direction of the applied voltage, they reported a 10 meV symmetrical blueshift for a voltage of 8 V.

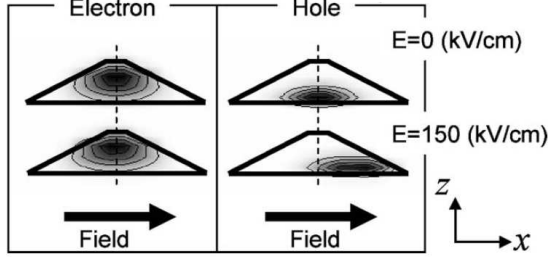


Figure 6.20 – Calculated spatial distribution of electron and hole ground state - extracted from [Nak06b]

They explain this experimental result by simulating the effect of the lateral field on both the electron and the hole. As can be observed on figure 6.20, the hole can be laterally shifted by the external voltage, while the electron remains localized at the top of the dot. They attribute this different sensitivity to the smaller electron effective mass and the stronger electronic lateral confinement. This lateral separation adds to the intrinsic axial carrier separation originating from the quantum-confined Stark effect and further decreases the oscillator strength (from 0.3 to 0.015 according to their computations). Further calculations show that the confinement does not vary significantly with increasing field. However, the exciton's increased lateral extension decreases the excitonic binding energy: this effect is expected to be at the origin of the measured blueshift.

Yet, in the explanations of Nakaoka *et al.* that the shift is due to a decrease of the excitonic binding energy, the amplitude of the blueshift is limited to the *field-free value of the binding energy in the dots, in the order of 30 meV* [Sim08]. On the contrary, the shift recorded on our sample reaches a value up to 200 meV when submitted to an exposure at fixed power. Moreover, these authors did not report on any quenching while the lateral field was applied. Therefore we cannot link our results to an alteration of the binding energy due to the appearance of a lateral electric field as Nakaoka *et al.* did.

Activation of charged defects? Another explanation of our observations could lie in the activation — by charging or migration — of defects. The influence of n-doping of GaN / AlGaIn quantum well superlattices has been studied both experimentally and theoretically by Kandaswamy *et al.* [Kan10][Kan08]. For a Si-doping level ranging around 10^{19} cm^{-3} and compared to non-intentionally doped samples, their photoluminescence *blueshift by a few 10 meV and broadens*. The authors attributed this observation to a down-shift of the fundamental electronic state, which can reach 50 meV at $5 \cdot 10^{19} \text{ cm}^{-2}$ and is attributed to band filling effects. Again, their observations do not

seem to match our results because we observe a decrease of the photoluminescence full width at half maximum.

Conclusion

As far as etched quantum dots are concerned, we can ascribe the alteration of their emission properties to a screening of the polarization electric field. We would expect these modifications to originate from lateral surfaces, because they are the most unstable one. Further experiments, such as surface passivation, are needed to be more conclusive. They are however beyond the scope of my work.

6.4 Towards UV microlasers

Quantum dot microcavities are currently under study for their potential as thresholdless lasers. We have seen that the Purcell effect can improve the proportion β of photons inside a given cavity mode. If the emitter is coupled to only one cavity mode, the *spontaneous emission factor* is given by:

$$\beta = \frac{F_P}{F_P + \gamma} \quad (6.7)$$

where γ is the coupling constant to the so-called “leaky modes”, *i.e.* all the modes except the cavity mode. β can be close to one if the Purcell factor is high enough. We define the *laser threshold* as the pumping rate needed to obtain on average one photon inside the cavity mode. With the help of the Purcell effect, one can inject almost all spontaneously emitted photons inside the cavity mode, and thus the threshold can be lowered. In the limit of $\beta=1$, the threshold becomes a fuzzy notion [Ric94]. This section thus aims at evaluating the potentialities of GaN/AlN cavities for lasing. We will begin by modeling a microlaser, and then describe our experiments. Finally, we will try to understand why our system is up-to-now not capable of lasing by the comparison to other systems, and seek for potential improvements of our structures.

6.4.1 Theory

Rate equations We consider quantum dots as three-level emitters embedded into a cavity, as depicted on figure 6.21. The analysis which follows is mainly based on reference [Lou08]. Let N_t be the total number of emitters, N be in the excited states and N_0 in the ground state, n be the number of photons inside the cavity, $1/\tau$ be the spontaneous emission rate in the cavity — taking into account both the Purcell effect and the photon

leakage:

$$\frac{1}{\tau} = \frac{F_P + \gamma}{\tau_{nat}} \quad (6.8)$$

where τ_{nat} is the natural spontaneous decay time of the emitter in free space.

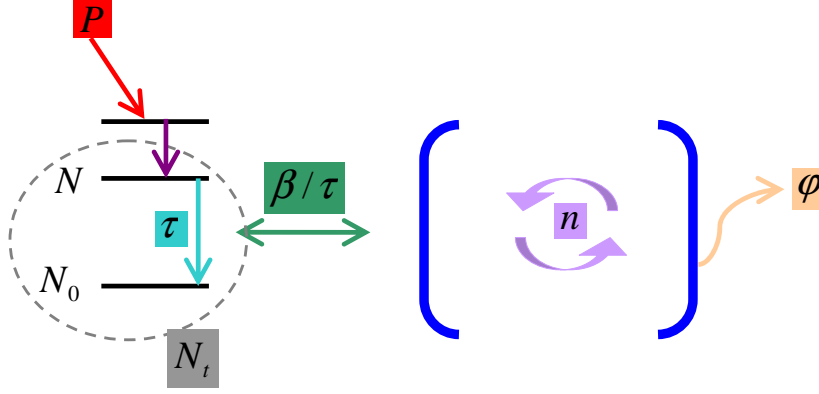


Figure 6.21 – Sketch of the microlaser system, depicting the set of useful parameters

We define P as the pump rate (in s^{-1}), and φ as the leaking rate of the cavity. The evolution of the numbers of excited emitters and photons inside the cavity are given by:

$$\frac{dN}{dt} = PN_0 - \frac{N}{\tau} - \frac{\beta}{\tau}(N - N_0)n \quad (6.9)$$

$$\frac{dn}{dt} = \beta \frac{N}{\tau} - \varphi n + \frac{\beta}{\tau}(N - N_0)n \quad (6.10)$$

where N/τ represents the number of photons generated by spontaneous emission, $\beta Nn/\tau$ counts the number of photons created by stimulated emission, $\beta N_0n/\tau$ is the absorption term and PN_0 is the pumping rate.

In the steady state regime, defined by $\frac{dn}{dt}=0$ and $\frac{dN}{dt}=0$, the *number of photons inside the cavity* can be calculated. The evolution of the number of photons in the cavity as a function of the pump rate (normalized to the cavity leaking rate) is plotted in figure 6.22a. Experimentally, its value at the "step" between both regimes well-below and well-above threshold gives the value of β . We define $M = P\beta/\varphi$ as the dimensionless pump parameter. For small enough β values (smaller than 10^{-2}), we can easily distinguish what happens far below and far above threshold:

- well below threshold, the number of photons inside the cavity first grows like βP because this regime is dominated by spontaneous emission;
- well above threshold, it is proportional to the pump rate P as practically all photons are emitted by stimulated emission inside the cavity mode.

Before going further, let us examine the *limitations of this model*. We have assumed that the variations of the numbers of photons n and the number of excited emitters

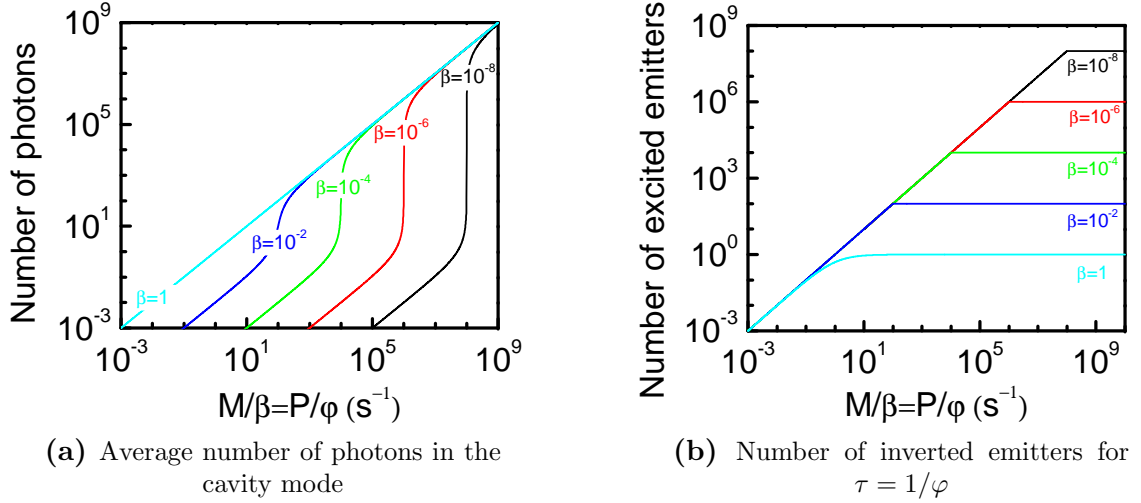


Figure 6.22 – Number of photons and excited emitters versus the ratio between pump and leaking rates for different β values

N were continuous variables. This is true for large enough systems. However, in a microcavity, the total number of emitters is small enough, therefore the excitation / desexcitation of one emitter produces a non-negligible fluctuation in the values of both N and n . Moreover, all the quantum dots are not spatially and spectrally coupled to the cavity mode. Each emitter thus has its proper recombination time and coupling factor with the mode. To account for these spectral and spatial mismatches, we will consider an average value of the Purcell effect (the maximum value being divided by a factor of 4 to account for the difference between experimental and theoretical values⁸).

The use of such a coupling coefficient β is valid for small enough values only, usually measured for classical macrolasers, as long as semiclassical theory is sufficient to explain the lasing process. However, when $\beta \geq 10^{-2}$, the two regimes described above can not be differentiated in an accurate way because the curve gets smoother, as can be seen in figure 6.22a. In that case, spontaneous emission remains preeminent even at the threshold. Still this model is capable of giving a qualitative answer to the lasing question, in agreement with the analysis of several reported microlasers (see 6.4.3).

From equations 6.9 and 6.10, we can compute the *number of inverted emitters*. Its temporal evolution with pump power is plotted in figure 6.22b for $\tau = 1/\varphi$ and different values of β .

- Well below threshold, the number of excited atoms first grows linearly with P : the power is not sufficient to invert all the emitters, so by increasing it step by step, we invert an increasing proportion of them.
- Then, well above threshold, it saturates. Indeed, when stimulated emission becomes dominant, the system reaches a balance between stimulated emission

⁸as explained with equation 6.2 in which a factor of 3 was considered [G98]

and absorption.

Lasing and transparency thresholds Let \tilde{n} and \tilde{N} be the number of photons inside the cavity and the number of inverted emitters in the steady state regime, respectively. In the steady state regime, the laser threshold P_{th} is defined by $\tilde{n} = 1$. It follows from both equations 6.9 and 6.10 that:

$$P_{th} = \frac{1 + 2\beta + 2\xi(1 - \beta)}{\tau(4\xi - 1)} \quad (6.11)$$

$$\frac{\tilde{N} - N_0}{N_t} = \frac{1}{3} \left(\frac{1}{\xi} - 1 \right) \quad (6.12)$$

We point out that the average number of photons in the cavity when half of the emitters are excited is:

$$\xi = \frac{N_t \beta}{2\tau\varphi} \quad (6.13)$$

ξ is called the *number of photons in the cavity mode at transparency threshold*, i.e. *when half of the emitters are inverted*. It measures the number of photons that the active material can create by spontaneous emission into the cavity mode ($\frac{N_t \beta}{\tau}$) before they escape the cavity (φ). It should not be mistaken for P_{th} , the *lasing threshold*, i.e. the pump rate needed to invert the system in order to obtain lasing (on average one atom into the cavity mode). ξ is actually a good figure of merit to predict the behaviour of a *microlaser* because:

- As $P_{th} \geq 0$, from equation 6.12, we deduce that *lasing is only possible if*:

$$4\xi - 1 \geq 0 \Leftrightarrow \xi > \frac{1}{4} \quad (6.14)$$

Otherwise, lasing is impossible because either (i) there is not enough active material (N_t is too small), or (ii) photons escape too quickly from the cavity to accumulate (φ is too large), or (iii) the spontaneous emission is too slow (τ is too large). In other words, there is not enough gain to achieve lasing, and/or too many photon losses.

- On the contrary, if:

$$\xi \gg 1 \Leftrightarrow N_t \gg \frac{2\tau\varphi}{\beta} \Rightarrow P_{th}(\xi \gg 1) = \frac{1 - \beta}{2\tau} \quad (6.15)$$

we deduce equation 6.15 from equation 6.11: in this case, P_{th} becomes independent of ξ . In that case, the gain is too large and the power needed to reach threshold is essentially used to reach transparency.

Both inequalities 6.14 and 6.15 are thus a practical criterion to know whether a microcavity is likely to show laser emission and if it is well-dimensioned.

6.4.2 Lasing experiments

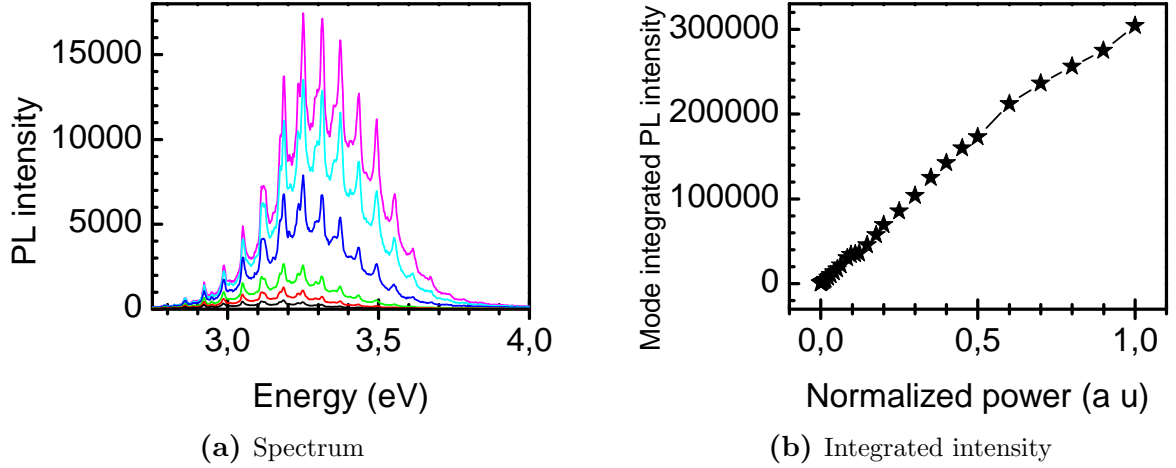


Figure 6.23 – Power-dependent measurements (L2C) performed at room temperature on a 3 μm disk. The power is normalized to the maximum, *i.e.* 5.6 mW - sample A1496 - courtesy M. Mexis

Our colleagues from Laboratoire Charles Coulomb have performed power-dependent measurements on microdisks containing four layers of GaN/AlN quantum dots⁹. A typical result is given on figure 6.23. The blueshift of the whole quantum dot emission is due to the screening of the quantum-confined Stark effect. The integrated intensity starts to increase linearly with power, and then saturates: we have inverted all the emitters but there is still on average less than one photon per cavity mode.

6.4.3 Comparison between our system and experimental demonstrations of lasing microcavities

In a previous part, we have evidenced that the main figure of merit to analyze a microlaser was the value of its transparency threshold ξ . In this part, we will compare our system, *e.g.* a typical 2- μm microdisk described in chapter 4 with two lasing nitride [Sim07] and arsenide [Pet05a] microdisks. The main parameters from these three systems are summarized in table 6.4.

1. The first parameter d is the emitter density: in the case of quantum dots, this is the density extracted from AFM measurements on an uncapped layer. As for InGaN / GaN quantum wells, it is well approximated by a dense array of quantum

⁹For a more precise description of the sample, please refer to figure 4.8, left panel

Sample	d (cm ⁻²)	$2a$ (μm)	H (μm)	Q
3*(InAs/GaAs QDs)	$4 \cdot 10^{10}$	2	250	12000
3*(InGaN/GaN QWs)	10^{12}	4	100	4000
1*(GaN/AlN QDs)	10^{11}	2	70	5000
Sample	mode	V_{eff} (μm ³)	$F_{P,max}$	β
3*(InAs/GaAs QDs)	TE(15,1)	0.075	285	1
3*(InGaN/GaN QWs)	TE(56,1)	0.053	30	0.87
1*(GaN/AlN QDs)	TE(26,1)	0.025	63	0.94
Sample	τ_{nat} (ns)	S_{eff} (μm ²)	ΔE (meV)	N_t
3*(InAs/GaAs QDs)	1	2.4	75	4
3*(InGaN/GaN QWs)	1	5.6	130	340
1*(GaN/AlN QDs)	100	1.8	400	15
Sample	E (eV)	φ (s ⁻¹)	ξ	Ref.
3*(InAs/GaAs QDs)	1.25	10^{11}	0.95	[Pet05a], [Pet06]
3*(InGaN/GaN QWs)	2.93	10^{12}	1	[Sim07]
1*(GaN/AlN QDs)	3.2	10^{12}	10^{-3}	

Table 6.4 – Comparison between two lasing microdisks reported in the literature and a typical GaN/AlN studied microdisk

dots due to the compositional fluctuations in the ternary alloy [Sch04]. From table 6.4, we see that the density of emitters in our system is in-between that of both lasing structures.

2. a is the radius of the microdisk.
3. H is the slab thickness. The requirement of the monomode feature of the waveguide¹⁰ appears clearly here as more restrictive for an emission in the UV range than in the blue or the infrared range of emission.
4. Q is the measured quality factor of the whispering gallery mode. Compared to nitride cavities, the value in arsenide systems is higher because scattering-induced defects are reduced: the fabrication process is better mastered and the near-infrared light is much less sensitive to defects of a given size than near-UV or blue light. Moreover, absorption losses are lower than in AlN microcavities¹¹.
5. Radial n and azimuthal m indexes of the mode having the maximum number of emitters in resonance with it are provided.
6. V_{eff} is the modal volume of this mode: $V_{eff} = \frac{\iiint n(r)^2 |E(r)|^2 dr d\theta dz}{n^2 |E_{max}|^2}$. It is calculated in the whispering gallery mode approximation. Going to smaller wavelengths allows

¹⁰discussed in 4.2.1

¹¹For a review of photon losses in microdisks, please refer to 4.4

- to reach smaller mode volumes. However, in the Purcell factor, this advantage is lost because F_P scales in V_{eff}/λ_{cav}^3 .
7. $F_{P,max}$ is the Purcell factor calculated from equation 6.1. In the calculation of β and thus also in ξ , this maxima is averaged by a factor of 4 to account for spectral and spatial mismatch between emitters and cavity mode¹². From table 6.4, one can see that our system displays a Purcell factor in-between both lasing structures. It is reduced by a factor of 4 compared to the arsenide system because of our lower quality factor, but enhanced by a factor of 2 compared to the InGaN / GaN system because of a smaller mode volume.
 8. β is the coupling rate of the emitters with the cavity mode and is calculated by: $\beta = \frac{F_{P,max}/4}{F_{P,max}/4+1}$. The three structures exhibit values very close to 1.
 9. τ_{nat} is the measured radiative lifetime of the uncoupled cavity, while in the calculation of $N_t\tau/\varphi$, the emitter lifetime when coupled to the cavity mode — and therefore reduced by a factor $F_{P,max}/4$ — is considered. *Here the difference between our system and both lasing structures is clear: the quantum-confined Stark effect is much more pronounced in GaN/AlN than InGaN / GaN heterostructures of the same size.*
 10. S_{eff} is the active surface: $S_{eff} = 2\pi \frac{\int_0^a n(r)^2 |E(r)|^2 dr}{n(r)^2 |E_{max}|^2}$. It is calculated in the whispering gallery mode approximation. The drawback raised by a smaller modal volume lies in the reduction of the number of emitters which can couple to the cavity mode. Yet, the mode effective surface in our sample is comparable to that of arsenide microdisks.
 11. ΔE is the homogeneous broadening of the emitters emission, taken as a Gaussian function. It appears that a large amount of photons — 3 to 5 times more than in both lasing structures — do not feed the cavity mode because they are not spectrally resonant with the whispering gallery mode. At equivalent quantum dot size fluctuations, the broadening is enhanced by the quantum-confined Stark effect in polar quantum dots compared to field-free quantum dots. This large inhomogeneous broadening is a clear drawback to achieve lasing.
 12. From S_{eff} , the density d , the mode linewidth (or the quality factor Q and the mode spectral position E) and the broadening ΔE , we deduce that N_t emitters are in resonance with the mode. N_t is comparable in both 2- μ m quantum dot microdisks (our system and the arsenide one). From the two order of magnitude higher value in the case of a 5- μ m quantum well microdisk, one can already point out the advantage of choosing a quantum well embedded in a large microdisk rather than quantum dots in a small microdisk. Yet we will see that this larger density of states is not always an advantage.

¹²see equation 6.2 where a factor of 3 was taken for this purpose [G98]

13. E is the spectral position of the mode.
14. φ is the leaking rate out of the cavity. It can be easily determined if the value of the quality factor Q is known: $\varphi = \frac{E}{\hbar Q}$.
15. $\xi = N_t \beta / 2\tau \varphi$ is the figure of merit that determines whether lasing can occur. *The value of ξ in our system is a factor of 1000 lower than in both lasing systems and originates from the two order of magnitude wider value of the emitter decay time (accounting for a factor of 100). The remaining factor of 10 originates from a 10 times smaller value of $\frac{N_t E}{Q}$ i.e. a lower emitter density or a lower quality factor compared to both lasing examples.*

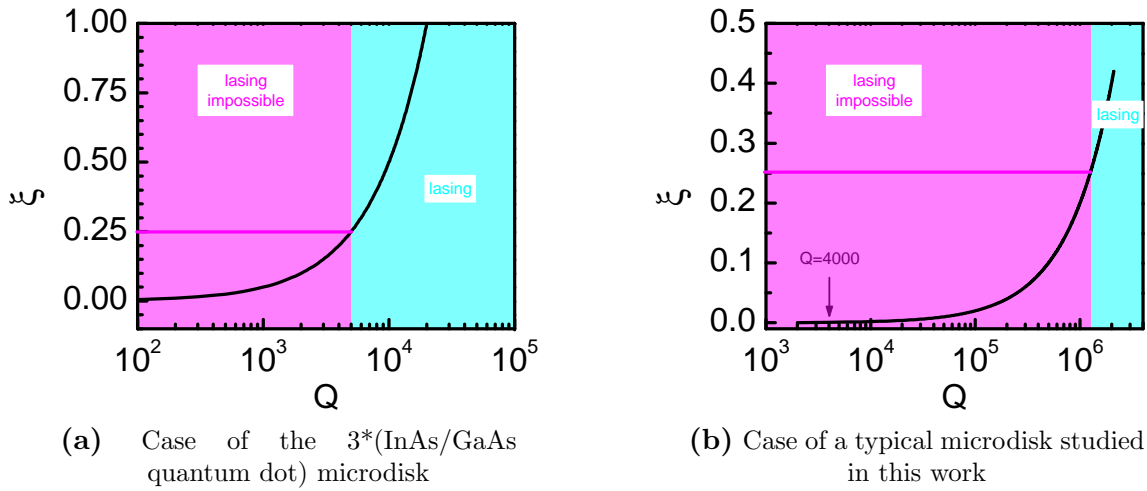


Figure 6.24 – Values of ξ versus Q and limit of achievable lasing

This calculation therefore confirms the experimental observation that our system cannot achieve lasing with the actual parameters, and that both other structures can lase. On figures 6.24a and 6.24b, $\xi(Q)$ is plotted for the arsenide system and ours, respectively. We remind that ξ scales proportionally to $1/\varphi$, thus proportionally to Q in the high Purcell factor approximation. One can observe that, with the parameters given in table 6.4, the arsenide microdisk can lase if $Q \geq 5000$. This is not the case of the GaN/AlN quantum dot microdisk. Indeed, to obtain lasing with $\xi = 1/4$ without improving the emitters (N_t/τ), figure 6.24b shows that we would need to increase Q up to 10^6 , i.e. by a factor of 400. This is very far from what is achievable with the state of the art nitride technology. The other, more realistic possibility is to improve the active layer (by increasing N_t and/or decreasing τ_{nat}) and this is the topic of the next pages.

6.4.4 Prospects to achieve lasing with GaN/AlN microcavities

In this part, and using table 6.4 as reference, we will analyze which parameters can be improved to obtain lasing. First, we will investigate how the total number of emitters

N_t can be increased. Then we will focus on weakening the quantum-confined Stark effect, and thus increasing the spontaneous emission rate of the emitters $1/\tau$.

Density and total number of emitters To increase the number of emitters coupled to the cavity mode, it is possible to increase the spatial emitter density or allow a wider number of emitters to be in-resonance with the cavity mode.

In order to increase the total density of states, quantum wells could be used instead of quantum dots. Using quantum dots, the density is already at its maximum as demonstrated in [Ser09a]. We could move from quantum dots to quantum wells and gain one or two orders of magnitude on the density. As seen in 6.2, our optical studies must be performed at room temperature. Yet the robustness in temperature of GaN/AlGaIn quantum wells, as a comparison with InGaIn/GaN quantum wells, is rather bad: as depicted in [Ren09b], the decay times and integrated intensities between 4 K and room temperature are reduced by a factor of 10^4 and 10^3 , respectively. It has to be compared to the case of GaN/AlN quantum dots, whose integrated intensity lose less than 1/3 of its value, and whose decay time remains constant, between 4 and 300 K [Ren09b]. Moreover, quantum wells are much more absorbent than quantum dots: they are expected to damage the quality factor at low power (see 4.4.2). However, reaching the transparency by increasing the excitation power enables to equally compensate absorption by stimulated emission, thus the quality factor at the lasing threshold should be greater than the value we measured at low power. Besides, the number of stacked layers cannot be increased significantly, as we are bound to a total thickness around 95 nm to keep a monomode waveguide, as already mentioned in 4.2.1.

The second possibility to increase the total number of emitters coupled to a given cavity mode is *to decrease the inhomogeneous linewidth of the GaN/AlN quantum dots*. It would ensure that more photons can be emitted in resonance with the cavity mode. Due to the quantum-confined Stark effect and the growth method, GaN/AlN quantum dots display a rather large inhomogeneous linewidth. As a consequence, very few of the total number of quantum dots in a microcavity are expected to be in spectral and spatial resonance with the cavity mode. *One way to decrease the inhomogeneous broadening is to go towards larger emission energy: in this case, the internal electric field is reduced and the spectral emission range is expected to be smaller.* We will see in the next paragraph that it is also an advantage as far as decay times are concerned.

Radiative lifetime and emission energy In GaN/AlN heterostructures thicker than 1.5 - 2 nm, the quantum-confined Stark effect dominates the interaction between electrons and holes [Bre06]. In order to decrease the built-in electric field, we can use smaller quantum dots, or use electric field-free quantum dots.

To decrease the radiative lifetime, we could grow smaller quantum dots. However, to achieve smaller dots, one needs to lower the amount of GaN deposited either by

decreasing the fluxes or increasing the temperature. In NH_3 -MBE, this leads to a subsequent decrease of the density, as demonstrated by Sylvain Sergent [Ser09a]. Table 6.5 illustrates this trend. From this point of view, it could be interesting to work with quantum dots grown by plasma-assisted MBE because this growth method allows to grow high density arrays of small quantum dots.

Nucleation time (s)	25	70	90	110
Measured maximum in the emission (eV)	2.91	3.16	3.40	3.75
Calculated mean quantum dot height (ML)	18.3	14.5	10.7	6.5
Measured quantum dot density (cm^{-2})	$5 \cdot 10^{10}$	$7 \cdot 10^{10}$	$2 \cdot 10^{10}$	$2 \cdot 10^8$

Table 6.5 – Correlation between photoluminescence emission energy and dot density of GaN/ $\text{Al}_{0.55}\text{Ga}_{0.45}\text{N}$ quantum dots. From the spectral position of the maximum, the height in monolayer (ML) is calculated with a field of 2.5 MV/cm - courtesy S. Sergent [Ser10]

An alternative could be to use *field-free emitters, either zinc-blende quantum dots or wurtzite quantum dots grown on a non-polar axis*. The quantum confinement in GaN/AlN quantum dots is well characterized by strong axial and weak lateral confinements. In this regime of weakly localized excitons in the quantum dot plane, we expect a high oscillator strength [And99] of the order of 200. In this confinement regime, oscillator strengths up to 100 have been obtained in the InAs/GaAs system (decay times around 200 ps) [Pet06]. However, in GaN/AlN quantum dots, the best reports in literature — be it on very small hexagonal quantum dots, cubic [Sim03] or non-polar quantum dots [Rol07b] — provide oscillator strengths in the range of 6 (decay time around 200 ps), as depicted in figure 6.25. *As a conclusion, experimental analysis of the decay time of non-polar GaN / AlN quantum dots show that a factor of 500 can be gained on the value of ξ by working with non-polar or zinc-blende emitters*. As we were lacking a factor of 1000 on the value of ξ in order to observe lasing, this would be a considerable improvement.

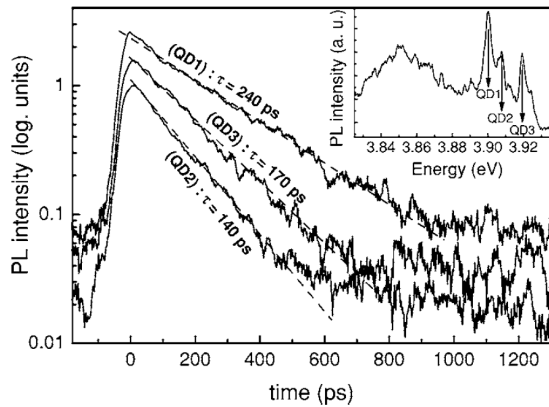


Figure 6.25 – Photoluminescence decay curves for three single non-polar GaN/AlN quantum dots - extracted from [Rol07b]

Conclusion

Quantum dot microcavities are attractive structures for low-threshold lasers because they can reach high mode coupling values. The more favourable situation for lasing is to have $\xi = \frac{N_t \beta}{2\tau \varphi}$ around 1. In order to have enough emitters which can simultaneously produce enough photons, a value of ξ greater than $1/4$ is required. Furthermore, if ξ is much greater than 1, lasing is obtained before reaching the transparency threshold and, after lasing, the additional power is still used to invert further emitters. In our case, the value of ξ is in the order of 10^{-3} , as summarized on figure 6.26. The most serious reason why we do not observe lasing originates from the long recombination time caused by the quantum-confined Stark effect. Smaller quantum dots grown by plasma-assisted MBE, as well as non-polar or cubic quantum dots could solve the problem.

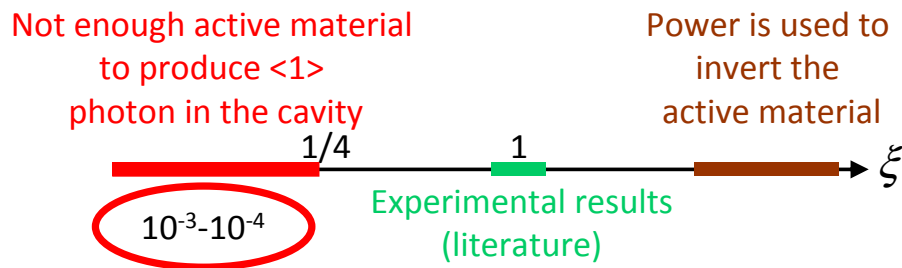


Figure 6.26 – Values of ξ and associated potential for lasing: in our structures, ξ is far too small.

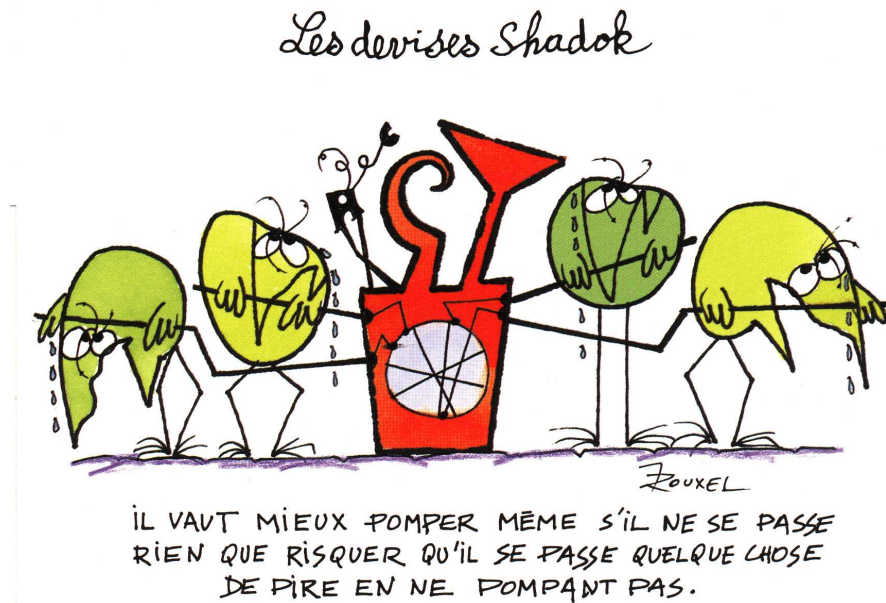


Figure 6.27 – Let us finish by citing a very philosophical motto [Rou]: *Better to pump even if nothing happens than to risk something worse happening by not pumping.*

Conclusion and prospects

7.1 Main results

This work focused on the optical characterizations of GaN nanowires and AlN microcavities containing GaN quantum dots.

In the first chapter, we presented the original properties of bulk GaN and GaN nanostructures, the latter being dominated by a strong built-in electric field. Then the specificities of the nanowire geometry were discussed. Finally, the peculiarities of nitride microcavities were addressed, in comparison with other optical resonators made in arsenide compounds which are far better well-known.

In chapter 2, we described the spectroscopy of GaN nanowires grown by MBE and MOCVD. We evidenced the exceptional properties of non-intentionally doped, MBE-grown nanocolumns in terms of exciton linewidth. The full width at half maximum indeed ranges in between 1 and 2 meV and shows a very good crystal homogeneity, obtained after growing a layer thickness as thin as a few 100 nm in columnar geometry. On the contrary, two-dimensional layers need several microns to relax. Yet these nanowires do not exhibit any excitonic confinement because their diameter is too large (around 40 nm). Their properties should however be strongly influenced by their free surfaces. Varying the diameter of the nanowires would allow to investigate the consequences of the large surface to volume ratio. It appears very difficult to decrease their diameter during growth, by tuning the growth parameters such as the temperature. However, even at such diameter, the nanorod geometry provides an efficient strain relaxation on lateral surfaces, thus allowing to study cubic GaN nanowires grown on top of hexagonal GaN nanocolumns. Their exceptional properties enabled us to accurately measure for the first time the splitting between both spin-orbit band and heavy and light hole bands in zinc blende GaN.

The third chapter was devoted to the study of the recombination at 3.45 eV observed on the luminescence spectra of GaN nanowires grown by MBE. We showed that the previous tentative attribution to a surface-enhanced two-electron satellite does not hold

by probing its intrinsic electronic properties. We expect a two-electron satellite to exhibit the same polarization than the donor bound exciton, yet we found that the 3.45 eV transition and the donor bound exciton were *quasi* contra-polarized. Moreover, the satellite is known to be very sensitive to an applied magnetic field, showing a high gyromagnetic factor (respectively diamagnetic shift) in Voigt (respectively Faraday) configuration. None of these signatures was found in the spectra of GaN nanocolumns on the line at 3.45 eV. Both polarization and magnetophotoluminescence experiments thus invalidate the origin of the 3.45 eV recombination as a two-electron satellite. Then, we studied the conditions in which this line is not present, and when it is enhanced. Clearly, decreasing the nanocolumn density leads to an increased intensity of this line. However, it is difficult to conclude whether this enhancement is due to surface effects or to a better collection efficiency.

The following chapter was dedicated to the study of AlN microdisks embedding GaN quantum dots. Record quality factors for AlN cavities have been measured around 3 eV. Yet they remain very sample-dependent. The contributions to the lowering of the quality factor compared to its intrinsic value are investigated, and we concluded that the residual absorption by GaN quantum dots and AlN barriers, as well as the losses induced by the silicon post and the scattering on sidewall defects are the main loss processes.

In chapter 5, we studied the optical properties of GaN/AlN quantum dot nanocavities embedded in photonic crystal waveguides. The agreement between theoretical predictions and experimental results show a good mastery of the fabrication processes when varying the size of the cavity. The attribution of each mode either to the waveguide or to the cavity, predicted by calculations, was confirmed by a different light localization when the excitation spot is moved along the waveguide. Excellent quality factors, up to 4400, were measured at 3.14 eV. Furthermore, around 3.45 eV, spectra with varying cavity size still show a good control of processing steps, and allowed to obtain a quality factor of 2300.

The last chapter addresses the potentialities of both systems — microdisks and photonic crystal cavities — for the Purcell effect and for microlasers. Although the expected Purcell factor is very high (around 100), we did not manage to evidence the enhancement of spontaneous emission rate of quantum dots coupled to a cavity mode. In photonic crystal cavities, non-radiative recombinations seem to dominate and prevented us from observing the Purcell effect. In microdisks, we demonstrated that both the emission from whispering gallery modes and quantum dots were unstable under long laser exposure, which prevented us from performing long enough acquisitions in time-resolved photoluminescence experiments. To get a deeper understanding of this instability with laser exposure, we performed systematic experiments as a function of the laser dose, but the lack of reproducibility did not allow us to conclude about the origin of the processes involved. This mode instability could be attributed to adsorption or desorption of chemical species on AlN surfaces. This could induce a monotonous and non-saturated evolution with time. These phenomena appear more clearly when

lowering temperature. Then, we studied the lasing potentialities of our structures. It appears that the main limiting factor to achieve lasing is the strong built-in electric field, which slows up the quantum dot spontaneous emission rate.

7.2 Prospects

7.2.1 GaN nanowires

Further studying the single nanocolumn

In order to study the influence of the surface to volume ratio, the precise knowledge of the nanorod diameter is required. Moreover, it has to be uncorrelated from the density. The selective-area-growth have been developed in order to study single nanowires of controlled diameter and previously located on the sample. The advantage of this techniques is also to ensure a better homogeneity from wire to wire, contrary to temperature-gradient samples. The prospects are thus to find the conditions which allows only one nanocolumn to nucleate in each patterned hole (contrary to the actual situation where several are present), and reach very low density to perform micro-photoluminescence experiments on a single, isolated nanocolumn. If we manage to grow thin enough wires, as the position of the nanorods would be controlled and well-known, we may be able to answer the question: do the smallest nanowires exhibit any luminescence?

We remind that, by performing micro-photoluminescence on nanowires without any previous location studies, the luminescence is only acquired on the bright zones, preliminary located by using the visualization setup. The statistics is therefore distorted because it lies only on the nanowires actually showing luminescence. Yet it can be assumed that the luminescence of some nanorods is not enough to be located by the visualization setup. On the contrary, by performing cathodoluminescence, the magnification allows to locate a nanocolumn *independent on its emission*. We therefore performed high-resolution cathodoluminescence experiments at 4 K in the University of Magdebourg (Germany), with the team of Prof. Christen, to correlate the nanocolumn diameter and the associated emission. After sonication, the wires were dispersed on a TEM carbon grid. In this case, the statistics lay on *all* the wires, as they can *all* be observed with the TEM setup. However, the high current density injected to a single wire damaged it before any measurement could be performed. The quenching of the cathodoluminescence of dispersed nanowires under intense conditions have already been reported by Robins *et al.* in [Rob07]. They attributed this observation to charge injection and trapping, as the probed volume is much smaller than when studying two-dimensional layers. These cathodoluminescence experiments were performed with nanowires dispersed on a TEM grid. Since then, additional micro-

photoluminescence experiments performed in collaboration with Aurélie Pierret have shown that the carbon film is responsible for a quenching of the luminescence of GaN nanowires, be it with electronic or photonic excitation.

In parallel, our colleague Martien den Hertog has developed new Si_3N_4 substrate membranes which are compatible with both TEM and micro-photoluminescence studies. Indeed, the emission does not seem to be quenched on these substrates; their design allows to locate the same nanocolumn both in micro-photoluminescence and in an electronic microscope; the 70-nm thickness of the membrane enables to perform high-resolution TEM studies, with the final aim to correlate structural and optical properties. It would help us to understand what makes the micro-photoluminescence emission of each nanocolumn unique and different one from another. It also opens the way to locate the nanorods and perform precise structural analysis such as measure their diameter or study their crystalline defects. By a statistical analysis, the structural properties may be correlated to a given optical signature, such as the donor-bound exciton linewidth, the detection of the emission at 3.45 eV,... One of the first uses of these membranes could indeed be the possible correlation of the presence or absence of the 3.45 eV line to a given structural defect. In order to gain more knowledge on this line, we propose to statistically correlate precise structural studies such as high-resolution TEM to the micro-photoluminescence of a given nanocolumn. Besides, the experiment in Magdebourg should be carried out again, making use of these new Si_3N_4 substrate membranes.

Other post-growth method to decrease the nanocolumn diameter

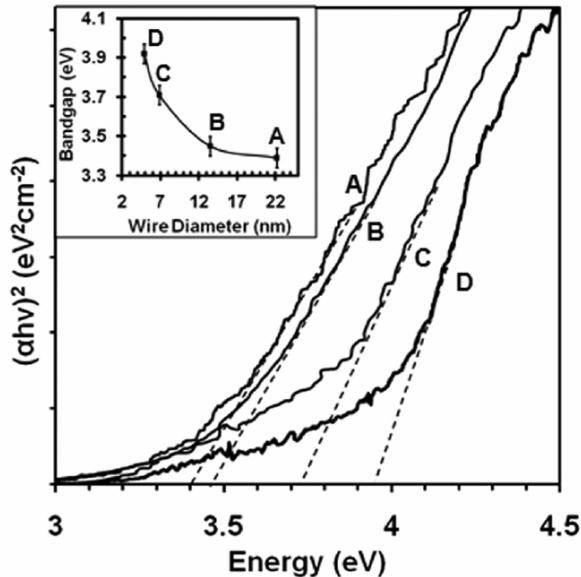


Figure 7.1 – Absorption plots with varying diameters [Bro11]

Tuning the nanocolumn diameter could provide information about the influence of the surface states on the photoluminescence of GaN nanowires. In chapter 2, we have presented one possible way to reduce the diameter of nanowires grown under the usual

MBE conditions. It makes use of GaN decomposition at 800°C and under ultra-high vacuum. Another method is to etch the nanorods with H_2 provided by a MOCVD reactor. The literature [Bro11] shows how a MOCVD reactor providing either NH_3 or H_2 can efficiently etch the wires. From a nanocolumn average diameter of 22 nm (as-grown samples) to 4.8 nm (for the longest etching process), the GaN bandgap increases from 3.4 to 3.9 eV in absorption measurements performed at room temperature, as can be seen in figure 7.1. Our goal will thus be (i) to reproduce the etching experiment and (ii) to evidence the typical one-dimensional confinement behaviour described in chapter 2 by photoluminescence and time-resolved photoluminescence experiments. We have performed similar etchings on MBE-grown GaN nanowires. We put the sample under the following conditions: 900°C, 3L/min of NH_3 , 5L/min of H_2 during five minutes. The results are depicted on figure 7.2. We clearly observed a sharpening of the diameter around the top of the nanowires (located by red lines on figure 7.2), as well as a shortening of some nanorods (located by blue ovals on figure 7.2). These were preliminary results and no optical measurements have been performed yet on this sample.

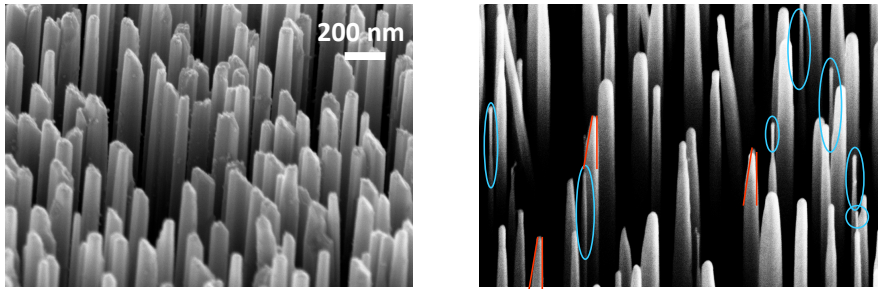


Figure 7.2 – Images of nanowires before (left) and after etching (right) - sample N1690(d)

7.2.2 GaN/AlN microcavities

Towards the strong coupling regime with GaN bulk excitons

Microdisks are high-quality microcavities which are foreseen as interesting structures in terms of exciton / photon strong coupling. Up to now, polaritons have been reported in one-dimensional nitride microcavities with quantum wells as the active layer (see [Mal02], [Chr07], and [Chr08]). Yet the splitting between lower and upper polariton branches is expected to be larger in three-dimensional cavities such as microdisks than in planar structures. For GaN, a value of 70 meV was calculated by Kaliteevski *et al.* [Kal07], taking bulk GaN excitons as emitters. Moreover, polariton scattering by phonons is expected to be much more efficient than in planar cavities [Kal07]: this geometry thus seems favorable to evidence polariton lasing. Note that the potentialities of microdisks for strong coupling have been reported experimentally for the first time in InAs / GaAs quantum dot microdisks by Peter *et al.* in 2005 [Pet05a].

In the case of nitride cavities, working with bulk GaN as active layer would enhance both the oscillator strength (no quantum-confined Stark effect) and the emitter density as a comparison to GaN quantum dots. However, the challenge is to grow thin GaN layers of good optical quality on silicon, with a full width at half maximum of the donor-bound exciton much smaller than the expected Rabi splitting of 70 meV: values around 10 meV would fit. In this case, the parameter which will be tuned to evidence the anti-crossing will not be temperature: excitonic lines broaden too quickly when temperature is raised. It would thus be necessary to vary slightly the disk diameter (by about $\pm 10\%$), and the anti-crossing will be measured indirectly by gathering the data obtained on several microdisks of various diameters.

Even more interestingly, the large number of designs allowed by photonic crystal — due to the high number of tunable parameters — would allow to vary the polariton dispersion curves. In photonic crystal cavities, strong coupling with a single quantum dot was reported in 2004 [Yos04]. However, polaritons built on a assembly of emitters (quantum well) were not reported before 2009 [Baj09]. In this paper, the authors also highlighted the potentialities of strong coupling in wide bandgap photonic crystal cavities, which will benefit from both the large tuning possibilities and the robustness of nitride excitons. The study of strong coupling between bulk GaN excitons and a cavity mode from these structures will thus be one of the next goals of our team.

Going further to UV emission with photonic crystal cavities

To achieve an emission at even higher energy, we need to modify the actual structures. Thanks to an increasing mastering of fabrication processes on nitride structures, recent years' improvements on the quality factors have shown that their values were not limited and we are confident that processes can still be optimized. We are currently working on structures defined by $a/\lambda=0.4$. Mastering a periodicity of 140 nm and a hole radius of 35 nm instead of the means current value of 170 nm and 50 nm, would allow an emission around 3.88 eV. Yet, in this case the emission from the epitaxial layer will have to be blueshifted as well. To achieve this goal without decreasing too much the density¹, alternative approaches are under-development and have been discussed in chapter 6.

Other possible ways of evidencing the Purcell effect

Until this point we have seen that quantum dots in resonance with a cavity mode produce a "positive peak" in the photoluminescence spectrum. Collection and detection efficiencies were indeed much better for cavity mode emission than for leaky mode emission. Let us imagine now that we collect and detect much more efficiently the leaky modes. For a micropillar, which is the example taken in [Gay08], this means that we need to collect better transverse photons (collection and detection efficiency B) than

¹see 6.5 or Sylvain Sergent's PhD [?] for details on this issue

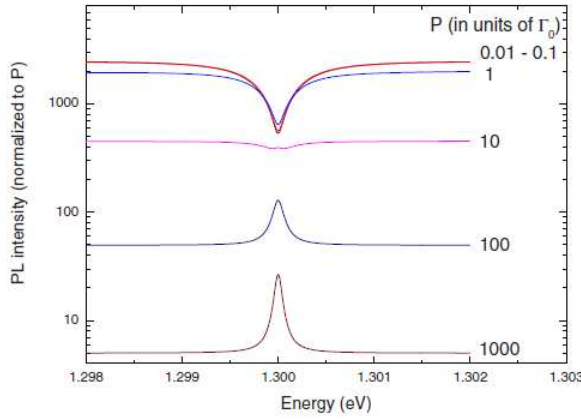


Figure 7.3 – Collected spectra for a micropillar of $1\ \mu\text{m}$ diameter and $Q = 15000$ as a function of power (normalized to the pumping rate per quantum dots) for collection of the leaky modes ten times greater than the collection of the cavity mode [Gay08].

longitudinal photons (collection and detection efficiency A). For $B = 10A$ and at low excitation power, we collect more photons from the leaky modes despite the Purcell effect because none of the quantum dots can reach saturation. The spectrum is flat with a dip at the energy of the cavity mode. However, when we increase the pumping power of the cavity, we tend to create more photons in resonance with the cavity mode because they are created faster than out-of-resonance ones — the first dots to reach saturation are the out-of-resonance ones. So the spectrum becomes flat with a bump at the energy of the cavity resonance. The results of this model are plotted in 7.3. As this analysis remains valid for any type of microcavity, for a microdisk we need to detect more efficiently photons with a wavevector perpendicular to the disk slab than photons from whispering gallery modes, whose wavevectors are all contained in a small cone around the disk plane. This means collecting perpendicularly to the microdisk slab. This experiment has not been reported yet to evidence the Purcell effect.

Another approach to be able to evidence the Purcell effect is to prevent the modal instability. Surface passivation may be the clue to prevent such an evolution. We suggest the atomic layer deposition of an alumina layer of a few nm in order to quench the possible photo-induced chemical processes such as an uncontrolled oxidation.

Résumé en français

Contexte

Les semiconducteurs nitrures, c'est-à-dire les matériaux III-V dont l'élément V est l'azote, sont généralement distingués des autres semiconducteurs III-V du fait de leurs propriétés particulières. Leur bande interdite s'étend de l'ultraviolet jusqu'à l'infrarouge: de 6.25 eV (198 nm) pour AlN, à 3.51 eV (353 nm) pour GaN et enfin, 0.7 eV (1770 nm) pour InN. L'étendue des longueurs d'onde envisageables rend les matériaux nitrures très attractifs pour des applications telles que les diodes électroluminescentes et les lasers. Le marché actuel et potentiel est vaste et couvre le stockage optique de l'information, l'éclairage public et privé, la stérilisation par destruction de l'ADN, et la lithographie optique.

Cependant, les études intensives de ces semiconducteurs ont commencé il y a une vingtaine d'années seulement, avec la première diode à base de nitrures en 1992 [Aka92]. Il est en effet difficile d'obtenir des matériaux nitrures de haute qualité et sans contrainte. L'absence de substrats nitrures disponible à bas coûts est due aux conditions drastiques nécessaires à leur fabrication [Dwi08][Por98]. Associée au manque de substrats adaptés pour l'hétéroépitaxie, la croissance de matériaux nitrures ne permet que d'obtenir des matériaux à forte densité de défauts. De plus, dans les hétérostructures nitrures, d'importants champs électriques existent. Ils proviennent de la différence de polarisations spontanée et piezoélectrique entre les différents composés de la structure. En séparant spatialement les électrons des trous, le taux d'émission spontanée en est fortement réduit.

Une efficacité totale externe de 60% dans les diodes électroluminescentes à base de puits quantiques InGaN / GaN à faible teneur en indium, bien qu'une bonne surprise, est donc plutôt inattendue. Mais ces performances exceptionnelles sont limitées à l'émission dans le bleu: en visant de plus courtes (vers l'UV) ou plus longues (vers le vert) longueurs d'onde, les rendements s'effondrent ([Kha09], [Kha08]).

En parallèle, ces trente dernières années, l'électrodynamique quantique en cavité a

été développée dans les communautés arseniures et silicium. Les régimes de couplage faible et fort ont été explorés dans des structures photoniques tridimensionnelles telles que les micropiliers, les microdisques et les cavités à cristaux photoniques. Dans les nitrures, seul le couplage fort a été mis en évidence dans des microcavités à confinement unidimensionnel. L'absence de petits lasers efficaces émettant dans le proche UV rend les cavités à boîtes quantiques GaN / AlN potentiellement très intéressantes.

Par ailleurs, ces dix dernières années, l'étude des nanofils a gagné de l'importance au sein de la communauté des semiconducteurs. Dans les composés nitrures, la géométrie filaire permet de relaxer les contraintes par les surfaces latérales, par rapport aux couches bidimensionnelles fortement contraintes. Cela permet aussi d'envisager la réalisation d'hétérostructures à important désaccord de maille quasiment sans défaut, comme des nanostructures à fort taux d'indium ou d'aluminium du type (In)GaN / (Al)GaN. Il est donc nécessaire d'étudier les propriétés optiques de ces nouveaux objets, pour pouvoir déterminer leur potentiel par rapport aux matériaux massifs.

Principaux résultats

Ce travail de thèse a porté sur la caractérisation optique de nanofils GaN et de microcavités AlN contenant des boîtes quantiques de GaN.

Dans le premier chapitre, nous avons présenté les propriétés originales des semiconducteurs massifs et des nanostructures nitrures. Ensuite, les spécificités des matériaux crûs en géométrie nanofils ont été évoquées. Enfin, nous avons analysé les particularités des microcavités nitrures, par comparaison avec les résonateurs optiques à base de matériaux arseniures qui sont bien mieux maîtrisés.

Au chapitre 2, nous décrivons la spectroscopie de nanofils de GaN crûs par épitaxie par jets moléculaires et épitaxie en phase vapeur aux organo-métalliques. En particulier, nous mettons en évidence les excellentes propriétés optiques en terme de largeur spectrale de raie des nanofils non intentionnellement dopés obtenus par épitaxie par jets moléculaires. Une largeur à mi hauteur entre 1 et 2 meV atteste d'une très bonne homogénéité du cristal, qui s'obtient pour des couches de quelques centaines de nm seulement en géométrie nanofils, à l'inverse des couches bi-dimensionnelles obtenues par hétéroépitaxie. Cependant ces nanofils ne présentent aucun confinement excitonique car leur diamètre est trop élevé (autour de 40 nm). Il apparaît difficile de diminuer le diamètre des fils suffisamment pour confiner l'exciton en changeant les conditions de croissance (plus particulièrement, la température). Par ailleurs, grâce à la géométrie filaire qui permet une relaxation des contraintes très efficace par les faces latérales, nous avons pu étudier des fils de GaN cubiques crûs sur des nanofils wurtzite. Leurs excellentes propriétés optiques ont permis de mesurer pour la première fois la différence d'énergie entre les bandes de trous lourds / légers et la bande spin orbite dans GaN.

Le troisième chapitre est consacré à l'étude de la transition à 3.45 eV observée dans les spectres de luminescence des nanofils GaN obtenus par épitaxie par jets moléculaires, et d'intensité comparable à celle de l'exciton lié au donneur neutre. Dans les couches de GaN bi-dimensionnelles, un ensemble de raies autour de 3.45 eV est attribué aux satellites à deux électrons de l'exciton lié au donneur, avec une intensité 50 fois plus faible que ce dernier. Dans les nanofils, l'origine de cette recombinaison est actuellement sujette à discussion. On l'attribue à un satellite à deux électrons comme dans le GaN massif, et son intensité décuplée est expliquée par la grande proportion de matériau sensible à la surface dans un nanofil par rapport au cas d'un semiconducteur massif. Cependant, grâce à des expériences de polarisation et de photoluminescence sous champ magnétique, nous avons pu sonder les propriétés électroniques intrinsèques de cette transition. Alors qu'on s'attend à ce que le dipole de la transition à deux électrons soit polarisé comme l'exciton lié au donneur, nous avons démontré qu'elle est polarisée majoritairement perpendiculairement. De plus, le satellite est connu pour être très sensible au champ magnétique, présentant un important facteur gyromagnétique (respectivement décalage diamagnétique) en configuration Voigt (respectivement Faraday). Or aucune de ces signatures n'est retrouvée sur les spectres des nanofils de GaN autour de 3.45 eV. Nos expériences de polarisation et de magnéto-photoluminescence infirment donc l'origine de la transition à 3.45 eV comme un satellite à deux électrons. Ensuite, nous examinons les conditions qui conduisent à l'exaltation ou à l'atténuation de son intensité. Enfin, nous confirmons les résultats de la littérature corrélant l'augmentation de son intensité avec une diminution du diamètre. Il est cependant difficile de conclure si cette augmentation provient d'effets de surfaces ou simplement d'une meilleure efficacité de détection.

Le chapitre suivant est dédié à l'étude de microdisques d'AlN contenant des boîtes quantiques de GaN. Des facteurs de qualité record pour les cavités en AlN ont été mesurés autour de 3 eV. L'ensemble des contributions participant à la dégradation du facteur de qualité est analysé, et nous en déduisons que l'absorption des boîtes quantiques et de l'AlN, de même que les pertes dues aux fuites dans le pied de silicium et la diffusion par les flancs rugueux sont à l'origine des valeurs mesurées.

Au chapitre 5, nous étudions les propriétés optiques de nanocavités AlN contenues dans des guides d'onde unidimensionnels. L'adéquation entre les prédictions théoriques et les résultats expérimentaux révèle une bonne maîtrise des étapes de fabrication quand on varie la taille de la cavité. L'attribution de chaque mode au guide d'onde ou à la cavité, prédite par des calculs préliminaires, est confirmée par une localisation différente quand on déplace l'excitation le long de l'axe du guide d'onde. D'excellents facteurs de qualité, jusqu'à 4400, ont été mesurés à 3.14 eV. Par ailleurs, autour de 3.45 eV, les spectres à taille de cavité variable montrent encore un bon contrôle des procédés de fabrication, ce qui nous permet de mesurer un facteur de qualité de 2300.

Le dernier chapitre étudie les potentialités de nos deux systèmes (microdisques et cristaux photoniques à cavité) pour l'effet Purcell et les microlasers. Si le facteur de Purcell attendu est très élevé (autour de 100), nous n'avons pas réussi à mettre en

évidence l'accélération de l'émission spontanée des boîtes en résonance avec un mode de cavité. Dans le cas des microdisques, nous avons démontré que l'émission des boîtes quantiques hors résonance et celle des modes étaient instables sous illumination laser prolongée, ce qui nous empêchait de réaliser des acquisitions longues pourtant nécessaires dans de telles expériences de photoluminescence résolue en temps. Dans les cavités à cristaux photoniques, les recombinaisons non radiatives semblent prédominer et nous empêchent d'observer l'effet Purcell. Pour comprendre l'instabilité sous faisceau, nous avons réalisé des expériences systématiques en fonction de la dose laser, mais le manque de reproductibilité ne nous permet pas de conclure quant à son origine. Il semble que les surfaces gravées soient instables et induisent une variation de la densité de charges dans les structures. L'instabilité des modes serait due à l'adsorption ou la désorption d'espèces chimiques à la surface de l'AlN, ce qui induirait une évolution monotone et impossible à saturer dans le temps. Bien entendu, ces effets paraissent encore plus clairement à plus basse température. Par ailleurs, nous étudions la possibilité d'obtenir un effet laser dans nos structures. Il apparaît que le frein à la réalisation d'un microlaser est principalement dû à l'important champ électrique interne qui ralentit l'émission spontanée des boîtes quantiques.

Experimental techniques

The following part lists all the spectroscopy techniques used to acquire the results presented in this thesis.

Continuous-wave photoluminescence experiment

In *photoluminescence* experiments, we excite the samples with a frequency-doubled Argon laser emitting at 244 nm, *i.e.* 5.1 eV. To transform the provided energy into excitons, the system first needs to *thermalise*: this process consists in emitting phonons to get rid of the excess of energy caused by the generation of carriers well above the bandgap. The optical signature of a sample may be strongly affected by the presence of impurities. In GaN, non-intentional n-doping by oxygen and silicon has to be considered. Excitons can bind to these defects because they represent local potential wells. Donors and acceptors are shallow donors because their donor binding energy is still small, thus the transition is still close in energy to the bandgap. If defects provide deeper localization centers in the bandgap, carriers can populate them by thermalization processes, and their optical signature can be detected even if the corresponding emission energy is much smaller than the bandgap and if the density of these defects is rather small.

Macrophotoluminescence experiment

Our experiment consists in pointing a frequency-doubled Argon laser emitting at 244 nm or 5.1 eV, onto a sample cooled down at 5 K by a cold finger cryostat. The excitation spot is between 50 and 100 μm in diameter. The detection is performed by a nitrogen-cooled CCD coupled to a spectrometer (focal length 46 cm). We can use two gratings, one having 600 lines/mm and the other, 1800 lines/mm. The resolution, calibrated with the 365.015 nm line of a mercury lamp, is around 400 μeV when the 1800 lines/mm grating is used.

Microphotoluminescence experiment

A sketch of our setup is depicted on figure B.1.

It displays several differences compared to the macrophotoluminescence setup. The spot is first “cleaned” by a pin-hole. It then passes a beam expander and becomes collimated with a radius of about 1 cm. After reflecting on a long-pass filter (cut-off at 266 nm), it then enters the confocal microscope objective (numerical aperture of 0.4, working distance 4 mm) and excite the luminescence of the sample inside the cryostat. The signal passes through the microscope objective and is sent to the spectrometer (focal length 55 cm) equipped with three gratings - from 600 to 3600 lines/mm. The spectral resolution is 80 μeV . The detection can be performed either by a nitrogen-cold CCD camera or by a photomultiplier. In order to visualize the sample during the study, A second optical path is used to illuminate the sample with a diode emitting around 450 nm: it enters the microscope objective and is collected by a camera.

Polarization-dependent measurements

The polarization measurements are conducted on the micro-photoluminescence setup to allow precise alignment of the excitation spot (thanks to the visualization setup), and to collect more photons (larger numerical aperture). The linear polarization is analyzed by inserting a $\lambda/2$ waveplate (Berek rotator). The polarizer angle is set so as to maximize the signal without putting the analyzer and allows to remove the contribution from the spectrometer to the polarization we detect.

Time-resolved photoluminescence

What can we learn?

When exciting a semiconductor with a pulsed laser, we can access the photoluminescence decay time. At low temperature, we can consider that non-radiative processes are quenched, and we associate the photoluminescence decay time to the radiative decay time. This parameter gives useful information such as the overlap between electrons and holes.

The setup

The excitation source is a frequency-tripled Ti-sapphire laser pumped by a frequency-doubled YAG laser and emits between 266 and 270 nm. The power is limited to 3 mW after tripling. The repetition rate is 76 MHz in the synchroscan mode, with a resolution in the ps range. The repetition rate can be lowered by inserting a cavity

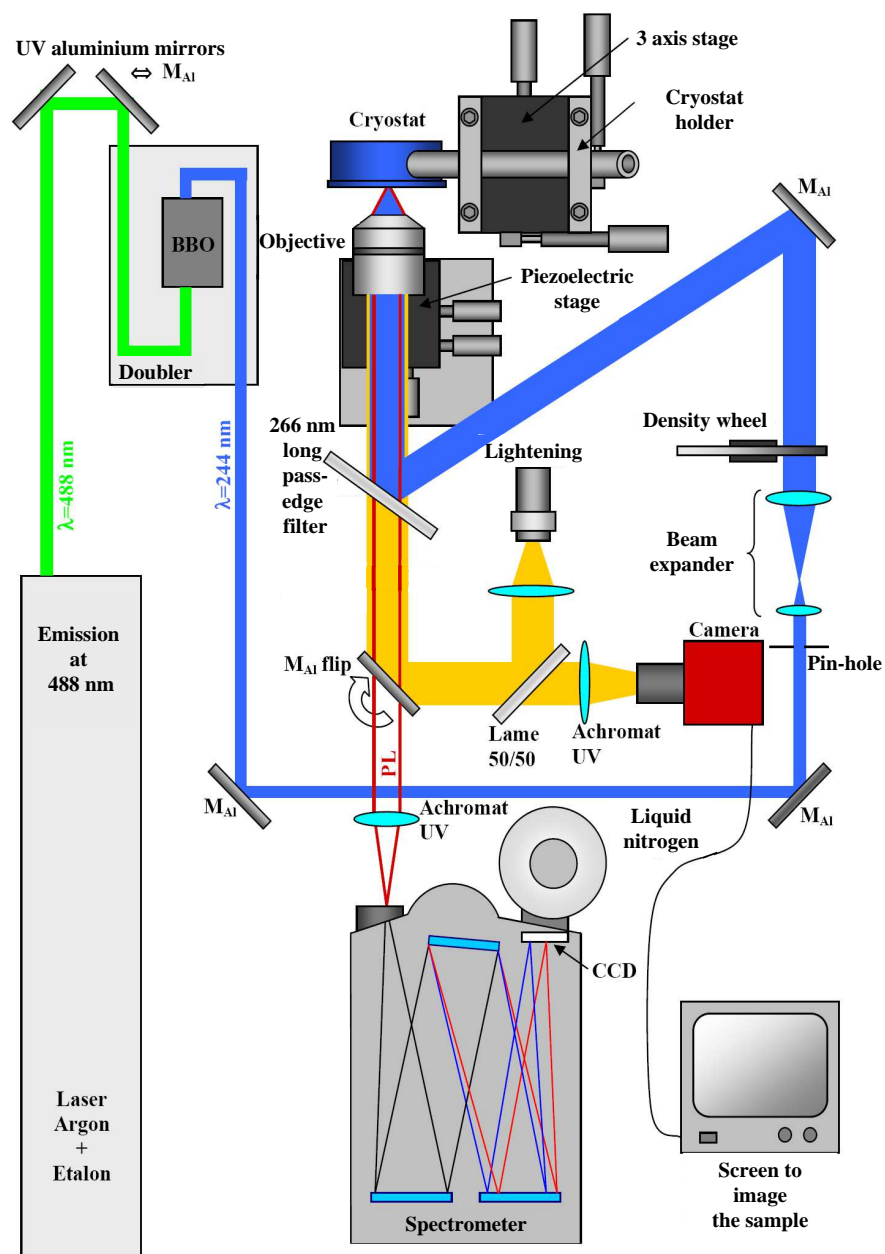


Figure B.1 – Sketch of the micro-photoluminescence setup - adapted from [Rol07a]

dumper. Depending on the experiment, either micro- or macro-photoluminescence was performed (setups described above), and the repetition rate also varied.

We have seen that photoluminescence experiments were not probing the density of states of the band structures, but rather the lowest energy levels. With photoluminescence excitation and absorption experiments one can get an insight into the density of states of a given recombination.

A photoluminescence excitation experiment consists in tuning the excitation energy while detecting at a fixed wavelength. We can therefore measure the carrier transfer: for example, if we excite around the band edge and detect at the spectral position of some defects, we can qualitatively evaluate the transfer efficiency between the near band edge and the defect band. Furthermore, when scanning the excitation energy, we will successively excite resonantly each band and suppress part of the thermalization mechanisms. The intensity one measures during photoluminescence excitation experiments depends on several factors:

202

where $I_{measured}$ is the intensity one measures, η_{abs} is the absorption efficiency of the incident photons. It is related to the density of states of each electronic level. This is thus the value one probes when performing photoluminescence excitation experiments. η_{rad} and η_{coll} are the emission and collection efficiencies, respectively. η_{relax} is the relaxation efficiency and describes the probability of an exciton to give a radiative photon. $I_{excitation}$ is the excitation intensity.

Here, we want to measure η_{abs} . However, we do not directly measure it because η_{relax} is expected to change when scanning the excitation, but it is impossible to measure. Additionally, the excitation intensity strongly varies with the wavelength: one has to normalize the detection spectrum by that of the excitation. Our setup uses a Xenon lamp filtered by a monochromator of focal length 18 cm and two gratings of 1800 lines/mm each. The emission is coupled to an optical fiber. The detection uses that of the micro-photoluminescence setup. Due to the low excitation density in the near UV-visible range, we have to open the slits of the lamp spectrometer, and therefore the resolution of the excitation is limited. Notice that reflectivity experiments could give the same information. However, analyzing reflectivity spectra on porous index materials such as layer composed by a dense arrays of nanowires is made difficult because of the large amount of scattered light.

Absorption

In this experiment, we directly measure the light transmitted through the sample by scanning either the detection or the excitation. This experiment suffers from two major drawbacks. First, the substrate must be transparent. This is one of the main motivations to master the growth of nanowires on sapphire. Moreover, the layer thickness must be adapted to the absorption efficiency at a given wavelength: if it is too thick, we will not collect enough photons to obtain a satisfactory dynamics. On the contrary, if it is too thin, the dynamics will also be too low because photons will not be absorbed enough above the bandgap.

Publications

J. Renard, G. Tourbot, D. Sam-Giao, C. Bougerol, B. Daudin, and B. Gayral, *Optical spectroscopy of cubic GaN in nanowires*. Applied Physics Letters **97**, 081910 (2010).

X. Chen, G. Perillat-Merceroz, D. Sam-Giao, C. Durand, and J. Eymery, *Homoepitaxial growth of catalyst-free GaN wires on N-polar substrates*. Applied Physics Letters **97**, 151909 (2010).

S. Sergent, J. Moreno, E. Frayssinet, Y. Laaroussi, S. Chenot, J. Renard, D. Sam-Giao, B. Gayral, D. Néel, S. David et al., *GaN quantum dots in (Al, Ga)N-based Microdisks* **210**, 012005 (2010).

G. Tourbot, C. Bougerol, A. Grenier, M. Den Hertog, D. Sam-Giao, D. Cooper, P. Gilet, B. Gayral, and B. Daudin, *Structural and optical properties of InGa_N/GaN nanowire heterostructures grown by PA-MBE*. Nanotechnology **22**, 075601 (2011).

D. Néel, S. Sergent, M. Mexis, D. Sam-Giao, T. Guillet, C. Brimont, T. Bretagnon, F. Semond, B. Gayral, S. David et al., *AlN photonic crystal nanocavities realized by epitaxial conformal growth on nanopatterned silicon substrate*. Applied Physics Letters **98**, 261106 (2011).

V. Fellmann, P. Jaffrennou, D. Sam-Giao, B. Gayral, K. Lorenz, E. Alves, and B. Daudin, *Semiconductors, dielectrics, and organic materials-031001 Ternary AlGa_N Alloys with High Al Content and Enhanced Compositional Homogeneity Grown by Plasma-Assisted Molecular Beam Epitaxy*. Japanese Journal of Applied Physics **50**(3) (2011).

X. Chen, B. Gayral, D. Sam-Giao, C. Bougerol, C. Durand, and J. Eymery, *Catalyst-free growth of high-optical quality GaN nanowires by metal-organic vapor phase epitaxy*. Applied Physics Letters **99**(25), 251910 (2011).

D. Sam-Giao, D. Néel, S. Sergent, B. Gayral, M. Rashid, F. Semond, J. Duboz, M. Mexis, T. Guillet, C. Brimont et al., *High quality factor AlN nanocavities embedded in a photonic crystal waveguide*. Applied Physics Letters **100**(19), 191104 (2012).

Publications

T. Guillet, M. Mexis, S. Sergent, D. Néel, S. Rennesson, C. Brimont, T. Bretagnon, B. Gil, D. Sam-Giao, B. Gayral et al., *High quality factor photonic resonators for nitride quantum dots*. physica status solidi (b) (2012).

D. Sam-Giao, R. Mata, J. Renard, G. Tourbot and B. Gayral, *Fine optical spectroscopy of the 3.45 eV emission line in GaN nanowires*, to be published

Index

- absorption, 20, 50, 115, 141
- acceptor-bound exciton, 18, 51
- band bending, 29
- band structure, 17
- cavity, 35
- cylindrical mode guiding, 31
- depletion, 29
- diamagnetic shift, 76
- dispersion of nanowires, 52
- donor bound exciton, 48
- donor-acceptor pair, 51
- donor-bound exciton, 18
- effective index, 101
- etching, 108, 121, 127
- exciton, 17
- excitonic binding energy, 18
- excitonic Bohr radius, 18
- excitonic confinement, 22, 26, 58
- excitonic polarization selection rules, 50
- Faraday configuration, 74
- FDTD, 112, 131
- free exciton, 18, 48
- free-space modes, 32
- GaN / AlN quantum dots, 150
- GaN / AlN band offsets, 22
- GaN decomposition under ultra-high vacuum and high temperature, 62
- GaN/AlN quantum dots, 170, 183
- gyromagnetic factor, 77
- heteroepitaxy, 12
- homoepitaxy, 12
- intensity enhancement with laser exposure, 67
- intrinsic losses, 114
- lasing threshold, 178
- lattice mismatch, 12
- lattice parameter, 11
- low-flux metal organic chemical vapour deposition, 47, 56
- metal organic chemical vapor deposition, 12, 46
- microdisks, 37
- microlasers, 175
- mode effective volume, 36
- molecular beam epitaxy, 12, 44, 106
- nanowire density, 45–47, 83
- nanowire-based light-emitting diode, 34
- p-doped nanowires, 50, 81
- photonic band gap, 37, 127
- photonic crystal cavities, 37

piezoelectric polarization, 24
polarity, 12, 46, 47
polarization, 122
polarization selection rules, 20, 72
Purcell effect, 37, 148

quality factor, 36, 113, 140, 145
quantum-confined Stark effect, 23

radiative modes, 32
refractive index, 20

scattering, 141
selective-area growth of nanowires, 86
spin-orbit splitting, 66
split-off band, 66
spontaneous emission, 36
spontaneous polarization, 13, 24
strain-relaxation in nanowires, 33
strong coupling regime, 36
surface scattering, 117

time decay, 154
transparency threshold, 178
two-electron satellite, 70

undoped nanowires, 48

Voigt configuration, 74

weak coupling regime, 36
whispering gallery mode approximation,
 105
whispering gallery modes, 37, 100
wurtzite, 10

Zeeman splitting, 76
zinc-blende, 10, 63

Bibliography

- [Aga06] R. Agarwal and C. Lieber, *Semiconductor nanowires: optics and optoelectronics*. Applied Physics A: Materials Science & Processing **85**(3), 209 (2006).
- [Aka92] I. Akasaki, H. Amano, K. Itoh, N. Koide, and K. Manabe, *GaN-based ultraviolet/blue light emitting devices*. Inst. Phys. Conf. Ser **129**, 851 (1992).
- [Aka03] Y. Akahane, T. Asano, B.-S. Song, S. Noda *et al.*, *High-Q photonic nanocavity in a two-dimensional photonic crystal*. Nature **425**(6961), 944 (2003).
- [Aki94] H. Akiyama, S. Koshihara, T. Someya, K. Wada, H. Noge, Y. Nakamura, T. Inoshita, A. Shimizu, and H. Sakaki, *Thermalization effect on radiative decay of excitons in quantum wires*. Physical review letters **72**(6), 924 (1994).
- [Alm04] V.-R. Almeida and M. Lipson, *Optical bistability on a silicon chip*. Optics letters **29**(20), 2387 (2004).
- [And99] L.-C. Andreani, G. Panzarini, and J.-M. Gérard, *Strong-coupling regime for quantum boxes in pillar microcavities: Theory*. Physical Review B **60**(19), 13276 (1999).
- [Ari07] M. Arita, S. Ishida, S. Kako, S. Iwamoto, and Y. Arakawa, *AlN air-bridge photonic crystal nanocavities demonstrating high quality factor*. Applied Physics Letters **91**(5), 051106 (2007).
- [Asa06] T. Asano, B.-S. Song, and S. Noda, *Analysis of the experimental Q factors (~ 1 million) of photonic crystal nanocavities*. Optics Express **14**(5), 1996 (2006).
- [Asc09] T. Aschenbrenner, C. Kruse, G. Kunert, S. Figge, K. Sebal, J. Kalden, T. Voss, J. Gutowski, and D. Hommel, *Highly ordered catalyst-free and mask-free GaN nanorods on r-plane sapphire*. Nanotechnology **20**, 075604 (2009).
- [AV03] N. Antoine-Vincent, F. Natali, M. Mihailovic, A. Vasson, J. Leymarie, P. Disseix, D. Byrne, F. Semond, and J. Massies, *Determination of the refractive indices of AlN, GaN, and AlGaIn grown on (111) Si substrates*. Journal of applied physics **93**, 5222 (2003).
- [Baj09] D. Bajoni, D. Gerace, M. Galli, J. Bloch, R. Braive, I. Sagnes, A. Miard, A. Lemaître, M. Patrini, and L.-C. Andreani, *Exciton polaritons in two-dimensional photonic crystals*. Physical Review B **80**(20), 201308 (2009).

Bibliography

- [Bar06] R. Bardoux, T. Guillet, P. Lefebvre, T. Taliercio, T. Bretagnon, S. Rousset, B. Gil, and F. Semond, *Photoluminescence of single GaN/ AlN hexagonal quantum dots on Si (111): Spectral diffusion effects*. Physical Review B **74**(19), 195319 (2006).
- [Bar07] R. Bardoux, *Spectroscopie de boîtes quantiques individuelles GaN/AlN en phase hexagonale*. Ph.D. thesis (2007).
- [Bay02] M. Bayer and A. Forchel, *Temperature dependence of the exciton homogeneous linewidth in $\text{In}_{0.60}\text{Ga}_{0.40}\text{As}/\text{GaAs}$ self-assembled quantum dots*. Physical Review B **65**(4), 041308 (2002).
- [Ber97] F. Bernardini, V. Fiorentini, and A. Bosin, *Spontaneous polarization and piezoelectric constants of III-V nitrides*. Appl. Phys. Lett. **70**, 2990 (1997).
- [Ber06] A. Berthelot, I. Favero, G. Cassabois, C. Voisin, C. Delalande, P. Roussignol, R. Ferreira, and J.-M. Gérard, *Unconventional motional narrowing in the optical spectrum of a semiconductor quantum dot*. Nature Physics **2**(11), 759 (2006).
- [Ber10] K.-A. Bertness, A.-W. Sanders, D.-M. Rourke, T.-E. Harvey, A. Roshko, J.-B. Schlager, and N.-A. Sanford, *Controlled nucleation of GaN nanowires grown with molecular beam epitaxy*. Advanced functional materials **20**(17), 2911 (2010).
- [Bev01] A. Beveratos, R. Brouri, T. Gacoin, J.-P. Poizat, and P. Grangier, *Nonclassical radiation from diamond nanocrystals*. Physical Review A **64**(6), 061802 (2001).
- [Ble10] J. Bleuse, M. Creasey, N.-S. Malik, M. Bazin, J. Claudon, J.-M. Gérard, I. Maksymov, C. Sauvan, J.-P. Hugonin, P. Lalanne *et al.*, *Strong inhibition of quantum dot spontaneous emission in photonic wires* (2010).
- [Bor99] P. Borri, W. Langbein, J. Mørk, J. M. Hvam, F. Heinrichsdorff, M.-H. Mao, and D. Bimberg, *Dephasing in InAs/GaAs quantum dots*. Phys. Rev. B **60**, 7784 (1999).
- [Bor05] M. Borselli, T.-J. Johnson, and O. Painter, *Beyond the Rayleigh scattering limit in high-Q silicon microdisks: theory and experiment*. Optics Express **13**(5), 1515 (2005).
- [Bra10] O. Brandt, C. Pfüller, C. Chèze, L. Geelhaar, and H. Riechert, *Sub-meV linewidth of excitonic luminescence in single GaN nanowires: Direct evidence for surface excitons*. Physical Review B **81**(4), 045302 (2010).
- [Bre03] T. Bretagnon, S. Kalliakos, P. Lefebvre, P. Valvin, B. Gil, N. Grandjean, A. Dussaigne, B. Damilano, and J. Massies, *Time dependence of the photoluminescence of GaN/AlN quantum dots under high photoexcitation*. Physical Review B **68**(20), 205301 (2003).
- [Bre06] T. Bretagnon, P. Lefebvre, P. Valvin, R. Bardoux, T. Guillet, T. Taliercio, B. Gil, N. Grandjean, F. Semond, B. Damilano *et al.*, *Radiative lifetime of a single electron-hole pair in GaN/ AlN quantum dots*. Physical Review B **73**(11), 113304 (2006).
- [Bro11] L.-R. Brockway, C. Pendyala, J. Jasinski, M.-K. Sunkara, and S. Vaddiraju, *A post-synthesis decomposition strategy for Group III-nitride quantum wires*. Crystal Growth & Design (2011).

-
- [Bru97] D. Brunner, H. Angerer, E. Bustarret, F. Freudenberg, R. Höpler, R. Dimitrov, O. Ambacher, and M. Stutzmann, *Optical constants of epitaxial AlGaIn films and their temperature dependence*. Journal of applied physics **82**, 5090 (1997).
 - [Cal97] F. Calle, F.-J. Sanchez, J. Tijero, M.-A. Sanchez-Garcia, E. Calleja, and R. Beresford, *Exciton and donor-acceptor recombination in undoped GaN on Si (111)*. Semiconductor science and technology **12**, 1396 (1997).
 - [Cal00] E. Calleja, M.-A. Sanchez-Garcia, F.-J. Sanchez, F. Calle, F.-B. Naranjo, E. Munoz, U. Jahn, and K. Ploog, *Luminescence properties and defects in GaN nanocolumns grown by molecular beam epitaxy*. Physical Review B **62**(24), 16826 (2000).
 - [Cal05] R. Calarco, M. Marso, T. Richter, A. Aykanat, R. Meijers, A. vd Hart, T. Stoica, and H. Lüth, *Size-dependent photoconductivity in MBE-grown GaN-nanowires*. Nano letters **5**(5), 981 (2005).
 - [Cer06] L. Cerutti, J. Ristic, S. Fernández-Garrido, E. Calleja, A. Trampert, K. Ploog, S. Lazic, and J. Calleja, *Wurtzite GaN nanocolumns grown on Si (001) by molecular beam epitaxy*. Applied physics letters **88**(21), 213114 (2006).
 - [Cha99] S. Chang, N.-B. Rex, R.-K. Chang, G. Chong, and L.-J. Guido, *Stimulated emission and lasing in whispering-gallery modes of GaN microdisk cavities*. Applied physics letters **75**, 166 (1999).
 - [Che10] X.-J. Chen, G. Perillat-Merceroz, D. Sam-Giao, C. Durand, and J. Eymery, *Homoepitaxial growth of catalyst-free GaN wires on N-polar substrates*. Applied Physics Letters **97**, 151909 (2010).
 - [Che11] X.-J. Chen, B. Gayral, D. Sam-Giao, C. Bougerol, C. Durand, and J. Eymery, *Catalyst-free growth of high-optical quality GaN nanowires by metal-organic vapor phase epitaxy*. Applied Physics Letters **99**(25), 251910 (2011).
 - [Chr07] S. Christopoulos, G. Von Högersthal, A. Grundy, P. Lagoudakis, A. Kavokin, J. Baumberg, G. Christmann, R. Butté, E. Feltin, J. Carlin *et al.*, *Room-temperature polariton lasing in semiconductor microcavities*. Physical review letters **98**(12), 126405 (2007).
 - [Chr08] G. Christmann, R. Butté, E. Feltin, J. Carlin, and N. Grandjean, *Room temperature polariton lasing in a GaN/ AlGaIn multiple quantum well microcavity*. Applied Physics Letters **93**, 051102 (2008).
 - [Chu96] S.-L. Chuang and C.-S. Chang, *k.p method for strained wurtzite semiconductors*. Phys. Rev. B **54**, 2491 (1996).
 - [Cla10] J. Claudon, J. Bleuse, N.-S. Malik, M. Bazin, P. Jaffrennou, N. Gregersen, C. Sauvan, P. Lalanne, and J.-M. Gérard, *A highly efficient single-photon source based on a quantum dot in a photonic nanowire*. Nature Photonics **4**(3), 174 (2010).
 - [CM10] D. Camacho Mojica and Y.-M. Niquet, *Stark effect in GaN/AlN nanowire heterostructures: Influence of strain relaxation and surface states*. Phys. Rev. B **81**, 195313 (2010).
 - [Con09] V. Consonni, M. Knelangen, U. Jahn, A. Trampert, L. Geelhaar, and H. Riechert, *Effects of nanowire coalescence on their structural and optical properties on a local scale*. Applied Physics Letters **95**(24), 241910 (2009).

Bibliography

- [Cor09] P. Corfdir, P. Lefebvre, J. Ristic, P. Valvin, E. Calleja, A. Trampert, J.-D. Ganière, and B. Deveaud-Plédran, *Time-resolved spectroscopy on GaN nanocolumns grown by plasma assisted molecular beam epitaxy on Si substrates*. Journal of Applied Physics **105**(1), 013113 (2009).
- [Dam99] B. Damilano, N. Grandjean, F. Semond, J. Massies, and M. Leroux, *From visible to white light emission by GaN quantum dots on Si (111) substrate*. Applied physics letters **75**, 962 (1999).
- [Dau97] B. Daudin, F. Widmann, G. Feuillet, Y. Samson, M. Arlery, and J.-L. Rouviere, *Stranski-Krastanov growth mode during the molecular beam epitaxy of highly strained GaN*. Physical Review B **56**(12), 7069 (1997).
- [Dau98] B. Daudin, G. Feuillet, J. Hübner, Y. Samson, F. Widmann, A. Philippe, C. Bru-Chevallier, G. Guillot, E. Bustarret, G. Bentoumi *et al.*, *How to grow cubic GaN with low hexagonal phase content on (001) SiC by molecular beam epitaxy*. Journal of Applied Physics **84**, 2295 (1998).
- [Dem86] H. Demiryont, L.-R. Thompson, and G.-J. Collins, *Optical properties of aluminum oxynitrides deposited by laser-assisted CVD*. Applied optics **25**(8), 1311 (1986).
- [Dem10] O. Demichel, M. Heiss, J. Bleuse, H. Mariette, and A. Fontcuberta i Morral, *Impact of surfaces on the optical properties of GaAs nanowires*. Applied Physics Letters **97**(20), 201907 (2010).
- [Din71] R. Dingle, D.-D. Sell, S.-E. Stokowski, and M. Ilegems, *Absorption, reflectance, and luminescence of GaN epitaxial layers*. Physical Review B **4**(4), 1211 (1971).
- [Dwi08] R. Dwiliński, R. Doradziński, J. Garczyński, L. Sierzputowski, A. Puchalski, Y. Kanbara, K. Yagi, H. Minakuchi, and H. Hayashi, *Excellent crystallinity of truly bulk ammonothermal GaN*. Journal of Crystal Growth **310**(17), 3911 (2008).
- [FG09] S. Fernández-Garrido, J. Grandal, E. Calleja, M.-A. Sánchez-García, and D. López-Romero, *A growth diagram for plasma-assisted molecular beam epitaxy of GaN nanocolumns on Si (111)*. Journal of Applied Physics **106**(12), 126102 (2009).
- [Fio97] A. Fiorek, J. Baranowski, A. Wysmołek, K. Pakula, M. Wojdak, I. Grzegory, and S. Porowski, *Two-Electron Transition in Homoepitaxial GaN Layers*. Acta Physica Polonica-Series A General Physics **92**(4), 742 (1997).
- [Fon04] V.-A. Fonoberov and A.-A. Balandin, *Radiative lifetime of excitons in ZnO nanocrystals: The dead-layer effect*. Physical Review B **70**(19), 195410 (2004).
- [Fri09] I. Friedler, C. Sauvan, J.-P. Hugonin, P. Lalanne, J. Claudon, and J.-M. Gérard, *Solid-state single photon sources: the nanowire antenna*. Optics express **17**(4), 2095 (2009).
- [Fu99] H. Fu, L.-W. Wang, and A. Zunger, *Excitonic exchange splitting in bulk semiconductors*. Physical Review B **59**(8), 5568 (1999).
- [Fur08] F. Furtmayr, M. Vilemeyer, M. Stutzmann, A. Laufer, B.-K. Meyer, and M. Eickhoff, *Optical properties of Si- and Mg-doped gallium nitride nanowires grown by plasma-assisted molecular beam epitaxy*. Journal of Applied Physics **104**(7), 074309 (2008).

- [G98] J.-M. Gérard, B. Sermage, B. Gayral, B. Legrand, E. Costard, and V. Thierry-Mieg, *Enhanced Spontaneous Emission by Quantum Boxes in a Monolithic Optical Microcavity*. Phys. Rev. Lett. **81**, 1110 (1998).
- [Gay99] B. Gayral, J.-M. Gérard, A. Lemaitre, C. Dupuis, L. Manin, and J.-L. Pelouard, *High-Q wet-etched GaAs microdisks containing InAs quantum boxes*. Applied physics letters **75**, 1908 (1999).
- [Gay01] B. Gayral, J.-M. Gérard, B. Sermage, A. Lemaitre, and C. Dupuis, *Time-resolved probing of the Purcell effect for InAs quantum boxes in GaAs microdisks*. Applied Physics Letters **78**, 2828 (2001).
- [Gay08] B. Gayral and J.-M. Gerard, *Photoluminescence experiment on quantum dots embedded in a large Purcell-factor microcavity*. Physical Review B Condensed Matter And Materials Physics **78**(23), 235306 (2008).
- [Gee11] L. Geelhaar, C. Chèze, B. Jenichen, O. Brandt, C. Pfüller, S. Munch, R. Rothmund, S. Reitzenstein, A. Forchel, T. Kehagias *et al.*, *Properties of GaN nanowires grown by molecular beam epitaxy*. Selected Topics in Quantum Electronics, IEEE Journal of (99), 1 (2011).
- [Gér99] J.-M. Gérard and B. Gayral, *Strong Purcell effect for InAs quantum boxes in three-dimensional solid-state microcavities*. Lightwave Technology, Journal of **17**(11), 2089 (1999).
- [Gil97] B. Gil and O. Briot, *Internal structure and oscillator strengths of excitons in strained α -GaN*. Physical Review B **55**(4), 2530 (1997).
- [Gla06] F. Glas, *Critical dimensions for the plastic relaxation of strained axial heterostructures in free-standing nanowires*. Physical Review B **74**(12), 121302 (2006).
- [Gla07] F. Glas, J.-C. Harmand, and G. Patriarche, *Why does wurtzite form in nanowires of III-V zinc blende semiconductors?* Physical review letters **99**(14), 146101 (2007).
- [Hab04] E.-D. Haberer, R. Sharma, C. Meier, A.-R. Stonas, S. Nakamura, S.-P. DenBaars, and E.-L. Hu, *Free-standing, optically pumped, GaN/ InGaN microdisk lasers fabricated by photoelectrochemical etching*. Applied physics letters **85**, 5179 (2004).
- [Hen11] A.-L. Henneghien, G. Tourbot, B. Daudin, O. Lartigue, Y. Désières, and J.-M. Gérard, *Optical anisotropy and light extraction efficiency of MBE grown GaN nanowires epilayers*. Optics Express **19**(2), 527 (2011).
- [Hes11] K. Hestroffer, C. Leclere, C. Bougerol, H. Renevier, and B. Daudin, *Polarity of GaN nanowires grown by plasma-assisted molecular beam epitaxy on Si (111)*. Physical Review B **84**(24), 245302 (2011).
- [Hes12] K. Hestroffer, C. Leclere, V. Cantelli, C. Bougerol, H. Renevier, and B. Daudin, *In situ study of self-assembled GaN nanowires nucleation on Si (111) by plasma-assisted molecular beam epitaxy*. Applied Physics Letters **100**(21), 212107 (2012).
- [Ish08] S. Ishizawa, K. Kishino, and A. Kikuchi, *Selective-Area Growth of GaN Nanocolumns on Si (111) Substrates Using Nitrided Al Nanopatterns by RF-Plasma-Assisted Molecular-Beam Epitaxy*. Applied physics express **1**(1) (2008).

Bibliography

- [Jac11] G. Jacopin, L. Rigutti, L. Largeau, F. Fortuna, F. Furtmayr, F.-H. Julien, M. Eickhoff, and M. Tchernycheva, *Optical properties of wurtzite/zinc-blende heterostructures in GaN nanowires*. Journal of Applied Physics **110**, 064313 (2011).
- [Jel82] G. Jellison and F. Modine, *Optical absorption of silicon between 1.6 and 4.7 eV at elevated temperatures*. Applied Physics Letters **41**(2), 180 (1982).
- [Joh87] S. John, *Strong localization of photons in certain disordered dielectric superlattices*. Phys. Rev. Lett. **58**, 2486 (1987).
- [Kak06] S. Kako, C. Santori, K. Hoshino, S. Götzinger, Y. Yamamoto, and Y. Arakawa, *A gallium nitride single-photon source operating at 200 K*. Nature materials **5**(11), 887 (2006).
- [Kal07] M.-A. Kaliteevski, S. Brand, R.-A. Abram, A. Kavokin *et al.*, *Whispering gallery polaritons in cylindrical cavities*. Physical Review B **75**(23), 233309 (2007).
- [Kan08] P.-K. Kandaswamy, F. Guillot, E. Bellet-Amalric, E. Monroy, L. Nevou, M. Tchernycheva, A. Michon, F.-H. Julien, E. Baumann, F.-R. Giorgetta *et al.*, *GaN/AlN short-period superlattices for intersubband optoelectronics: A systematic study of their epitaxial growth, design, and performance*. Journal of Applied Physics **104**(9), 093501 (2008).
- [Kan10] P.-K. Kandaswamy, H. Machhadani, Y. Kotsar, S. Sakr, A. Das, M. Tchernycheva, L. Rapenne, E. Sarigiannidou, F.-H. Julien, and E. Monroy, *Effect of doping on the mid-infrared intersubband absorption in GaN/AlGaIn superlattices grown on Si (111) templates*. Applied Physics Letters **96**, 141903 (2010).
- [Kas06] J. Kasprzak, M. Richard, S. Kundermann, A. Baas, P. Jeambrun, J.-M.-J. Keeling, M.-H. FM Marchetti *et al.*, *Bose–Einstein condensation of exciton polaritons*. Nature **443**(7110), 409 (2006).
- [Kha08] A. Khan, K. Balakrishnan, and T. Katona, *Ultraviolet light-emitting diodes based on group three nitrides*. Nature photonics **2**(2), 77 (2008).
- [Kha09] A. Khan, *Semiconductor photonics: Laser diodes go green*. Nature Photonics **3**(8), 432 (2009).
- [Koe10] R. Koester, J.-S. Hwang, C. Durand, D. Le Si Dang, and J. Eymery, *Self-assembled growth of catalyst-free GaN wires by metal–organic vapour phase epitaxy*. Nanotechnology **21**, 015602 (2010).
- [Kor99] K. Kornitzer, T. Ebner, K. Thonke, R. Sauer, C. Kirchner, V. Schwegler, M. Kamp, M. Leszczynski, I. Grzegory, and S. Porowski, *Photoluminescence and reflectance spectroscopy of excitonic transitions in high-quality homoepitaxial GaN films*. Physical Review B **60**(3), 1471 (1999).
- [Kou08] K. Kouyama, M. Inoue, Y. Inose, N. Suzuki, H. Sekiguchi, H. Kunugita, K. Ema, A. Kikuchi, and K. Kishino, *Photoluminescence of exciton and biexciton in GaN nanocolumns*. Journal of Luminescence **128**(5-6), 969 (2008).
- [Kur06] E. Kuramochi, M. Notomi, S. Mitsugi, A. Shinya, T. Tanabe, and T. Watanabe, *Ultrahigh-Q photonic crystal nanocavities realized by the local width modulation of a line defect*. Applied physics letters **88**, 041112 (2006).

-
- [Lah09] L. Lahourcade, J. Pernet, A. Wirthmüller, M.-P. Chauvat, P. Ruterana, A. Laufer, M. Eickhoff, and E. Monroy, *Mg doping and its effect on the semipolar GaN (11 $\overline{2}$ 2) growth kinetics*. Applied Physics Letters **95**, 171908 (2009).
 - [Lan08] O. Landré, R. Songmuang, J. Renard, E. Bellet-Amalric, H. Renevier, and B. Daudin, *Plasma-assisted molecular beam epitaxy growth of GaN nanowires using indium-enhanced diffusion*. Applied Physics Letters **93**, 183109 (2008).
 - [Lan09] O. Landré, C. Bougerol, H. Renevier, and B. Daudin, *Nucleation mechanism of GaN nanowires grown on (111) Si by molecular beam epitaxy*. Nanotechnology **20**, 415602 (2009).
 - [Lar08] L. Largeau, D.-L. Dheeraj, M. Tchernycheva, G.-E. Cirlin, and J.-C. Harmand, *Facet and in-plane crystallographic orientations of GaN nanowires grown on Si (111)*. Nanotechnology **19**, 155704 (2008).
 - [Lef11] P. Lefebvre, S. Fernández-Garrido, J. Grandal, J. Ristic, M.-A. Sánchez-García, and E. Calleja, *Radiative defects in GaN nanocolumns: Correlation with growth conditions and sample morphology*. Applied Physics Letters **98**(8), 083104 (2011).
 - [Ler97] M. Leroux, B. Beaumont, N. Grandjean, P. Lorenzini, S. Haffouz, P. Vennegues, J. Massies, and P. Gibart, *Luminescence and reflectivity studies of undoped, n-and p-doped GaN on (0001) sapphire*. Materials Science and Engineering: B **50**(1), 97 (1997).
 - [Lou08] J.-M. Lourtioz, H. Benisty, D. Pagnoux, V. Berger, J.-M. Gérard, and D. Maystre, *Photonic crystals: towards nanoscale photonic devices* (Springer Verlag, 2008).
 - [Mai98] R.-A. Mair, K.-C. Zeng, J.-Y. Lin, H.-X. Jiang, B. Zhang, L. Dai, A. Botchkarev, W. Kim, H. Morkoc, and M.-A. Khan, *Optical modes within III-nitride multiple quantum well microdisk cavities*. Applied physics letters **72**, 1530 (1998).
 - [Mal02] G. Malpuech, A. Di Carlo, A. Kavokin, J.-J. Baumberg, M. Zamfirescu, and P. Lugli, *Room-temperature polariton lasers based on GaN microcavities*. Applied physics letters **81**, 412 (2002).
 - [Mas06] A.-V. Maslov, M.-I. Bakunov, and C.-Z. Ning, *Distribution of optical emission between guided modes and free space in a semiconductor nanowire*. Journal of applied physics **99**(2), 024314 (2006).
 - [Mat00] K. Matsuda, T. Saiki, H. Saito, and K. Nishi, *Room-temperature photoluminescence spectroscopy of self-assembled InGaAs single quantum dots by using highly sensitive near-field scanning optical microscope*. Applied Physics Letters **76**, 73 (2000).
 - [Mat08] H. Matsubara, S. Yoshimoto, H. Saito, Y. Jianglin, Y. Tanaka, and S. Noda, *GaN photonic-crystal surface-emitting laser at blue-violet wavelengths*. Science **319**(5862), 445 (2008).
 - [Mat11] R. Mata, *Optical, structural, and electrical characterizations of GaN / AlN nanostructures: quantum wells, quantum dots and nanowires*. Ph.D. thesis (2011).

Bibliography

- [McC92] S.-L. McCall, A.-F.-J. Levi, R.-E. Slusher, S.-J. Pearton, and R.-A. Logan, *Whispering-gallery mode microdisk lasers*. Applied physics letters **60**(3), 289 (1992).
- [Mex11] M. Mexis, S. Sargent, T. Guillet, C. Brimont, T. Bretagnon, B. Gil, F. Semond, M. Leroux, D. Néel, S. David *et al.*, *High quality factor nitride-based optical cavities: microdisks with embedded GaN/Al (Ga) N quantum dots*. Optics letters **36**(12), 2203 (2011).
- [Mon04] E. Monroy, T. Andreev, P. Holliger, E. Bellet-Amalric, T. Shibata, M. Tanaka, and B. Daudin, *Modification of GaN (0001) growth kinetics by Mg doping*. Applied physics letters **84**, 2554 (2004).
- [Mon06] B. Monemar, P.-P. Paskov, J.-P. Bergman, T. Paskova, C. Hemmingsson, T. Malinauskas, K. Jarasiunas, P. Gibart, and B. Beaumont, *Time-resolved spectroscopy of excitons bound at shallow neutral donors in HVPE GaN*. Physica B: Condensed Matter **376**, 482 (2006).
- [Mon08] B. Monemar, P.-P. Paskov, J.-P. Bergman, A.-A. Toropov, T.-V. Shubina, T. Malinauskas, and A. Usui, *Recombination of free and bound excitons in GaN*. physica status solidi (b) **245**(9), 1723 (2008).
- [Mon10] B. Monemar, P. Paskov, J. Bergman, G. Pozina, A. Toropov, T. Shubina, T. Malinauskas, and A. Usui, *Transient photoluminescence of shallow donor bound excitons in GaN*. Physical Review B **82**(23), 235202 (2010).
- [Mos05] S. Mosor, J. Hendrickson, B.-C. Richards, J. Sweet, G. Khitrova, H.-M. Gibbs, T. Yoshie, A. Scherer, O.-B. Shchekin, and D.-G. Deppe, *Scanning a photonic crystal slab nanocavity by condensation of xenon*. Applied Physics Letters **87**, 141105 (2005).
- [Nak91] S. Nakamura, T. Mukai, and M. Senoh, *High-Power GaN P-N Junction Blue-Light-Emitting Diodes*. Japanese Journal of Applied Physics **30**(Part 2, No. 12A), L1998 (1991).
- [Nak06a] T. Nakaoka, S. Kako, and Y. Arakawa, *Quantum confined Stark effect in single self-assembled GaN/AlN quantum dots*. Physica E: Low-dimensional Systems and Nanostructures **32**(1), 148 (2006).
- [Nak06b] T. Nakaoka, S. Kako, and Y. Arakawa, *Unconventional quantum-confined Stark effect in a single GaN quantum dot*. Physical Review B **73**(12), 121305 (2006).
- [Nat03] F. Natali, F. Semond, J. Massies, D. Byrne, S. Laügt, O. Tottereau, P. Vennegues, E. Dogheche, and E. Dumont, *Correlation between threading dislocation density and the refractive index of AlN grown by molecular-beam epitaxy on Si (111)*. Applied physics letters **82**, 1386 (2003).
- [Née11] D. Néel, S. Sargent, M. Mexis, D. Sam-Giao, T. Guillet, C. Brimont, T. Bretagnon, F. Semond, B. Gayral, S. David *et al.*, *AlN photonic crystal nanocavities realized by epitaxial conformal growth on nanopatterned silicon substrate*. Applied Physics Letters **98**, 261106 (2011).
- [Neu94] J. Neugebauer, C.-G. Van de Walle *et al.*, *Atomic geometry and electronic structure of native defects in GaN*. Physical Review B **50**(11), 8067 (1994).
- [Oli02] S. Olivier, H. Benisty, C.-J.-M. Smith, M. Rattier, C. Weisbuch, and T.-F. Krauss, *Transmission properties of two-dimensional photonic crystal channel waveguides*. Optical and quantum electronics **34**(1), 171 (2002).

- [Onu02] T. Onuma, S.-F. Chichibu, T. Sota, K. Asai, S. Sumiya, T. Shibata, and M. Tanaka, *Exciton spectra of an AlN epitaxial film on (0001) sapphire substrate grown by low-pressure metalorganic vapor phase epitaxy*. Applied Physics Letters **81**, 652 (2002).
- [Par04] H.-G. Park, S.-H. Kim, S.-H. Kwon, Y.-G. Ju, J.-K. Yang, J.-H. Baek, S.-B. Kim, and Y.-H. Lee, *Electrically driven single-cell photonic crystal laser*. Science **305**(5689), 1444 (2004).
- [Päs01] R. Pässler, *Dispersion-related assessments of temperature dependences for the fundamental band gap of hexagonal GaN*. Journal of Applied Physics **90**, 3956 (2001).
- [Pas07] P.-P. Paskov, B. Monemar, A. Toropov, J.-P. Bergman, and A. Usui, *Two-electron transition spectroscopy of shallow donors in bulk GaN*. physica status solidi (c) **4**(7), 2601 (2007).
- [Pel92] N.-T. Pelekanos, J. Ding, M. Hagerott, A.-V. Nurmikko, H. Luo, N. Samarth, and J.-K. Furdyna, *Quasi-two-dimensional excitons in (Zn, Cd) Se/ZnSe quantum wells: Reduced exciton-LO-phonon coupling due to confinement effects*. Physical Review B **45**, 6037 (1992).
- [Pet05a] E. Peter, I. Sagnes, G. Guirleo, S. Varoutsis, J. Bloch, A. Lemaître, and P. Senellart, *High-Q whispering-gallery modes in GaAs/ AlOx microdisks*. Applied Physics Letters **86**, 021103 (2005).
- [Pet05b] E. Peter, P. Senellart, D. Martrou, A. Lemaître, J. Hours, J. Gérard, and J. Bloch, *Exciton-photon strong-coupling regime for a single quantum dot embedded in a microcavity*. Physical Review Letters **95**(6), 67401 (2005).
- [Pet06] E. Peter, *Couplage fort exciton-photon pour une bote quantique de GaAs en microdisque*. Ph.D. thesis (2006).
- [Pet07] E. Peter, A. Dousse, P. Voisin, A. Lemaître, D. Martrou, A. Cavanna, J. Bloch, and P. Senellart, *Highly directional radiation pattern of microdisk cavities*. Applied Physics Letters **91**, 151103 (2007).
- [Pfü10] C. Pfüller, O. Brandt, F. Grosse, T. Flissikowski, C. Chèze, V. Consonni, L. Geelhaar, H.-T. Grahn, and H. Riechert, *Unpinning the Fermi level of GaN nanowires by ultraviolet radiation*. Physical Review B **82**(4), 045320 (2010).
- [Pol07] L. Polenta, A. Castaldini, and A. Cavallini, *Defect characterization in GaN: Possible influence of dislocations in the yellow-band features*. Journal of Applied Physics **102**(6), 063702 (2007).
- [Por98] S. Porowski, *Bulk and homoepitaxial GaN-growth and characterisation*. Journal of crystal growth **189**, 153 (1998).
- [Poz99] G. Pozina, J.-P. Bergman, T. Paskova, and B. Monemar, *Dynamics of the Bound Excitons in GaN Epilayers Grown by Hydride Vapor Phase Epitaxy*. physica status solidi (b) **216**(1), 45 (1999).
- [Pur46] E.-M. Purcell, *Spontaneous emission probabilities at radio frequencies*. Physical Review **69**, 681 (1946).
- [Ram00] P. Ramvall, P. Riblet, S. Nomura, Y. Aoyagi, and S. Tanaka, *Optical properties of GaN quantum dots*. Journal of Applied Physics **87**, 3883 (2000).

Bibliography

- [Ras07] A. Rastelli, A. Ulhaq, S. Kiravittaya, L. Wang, A. Zrenner, and O.-G. Schmidt, *In situ laser microprocessing of single self-assembled quantum dots and optical microcavities*. Applied physics letters **90**, 073120 (2007).
- [Ray06] S. Raychaudhuri and E.-T. Yu, *Calculation of critical dimensions for wurtzite and cubic zinc blende coaxial nanowire heterostructures*. Journal of Vacuum Science & Technology B: Microelectronics and Nanometer Structures **24**, 2053 (2006).
- [Rei04] J.-P. Reithmaier, G. S  k, A. L  ffler, C. Hofmann, S. Kuhn, S. Reitzenstein, L. Keldysh, V. Kulakovskii, T.-L. Reinecke, and A. Forchel, *Strong coupling in a quantum dot micropillar cavity system*. Nature **432**, 197 (2004).
- [Rei08] J.-P. Reithmaier, *Strong exciton–photon coupling in semiconductor quantum dot systems*. Semiconductor Science and Technology **23**, 123001 (2008).
- [Ren09a] J. Renard, *Optical properties of GaN quantum dots and nanowires*. Ph.D. thesis (2009).
- [Ren09b] J. Renard, P.-K. Kandaswamy, E. Monroy, and B. Gayral, *Suppression of nonradiative processes in long-lived polar GaN/AlN quantum dots*. Applied Physics Letters **95**, 131903 (2009).
- [Res05] M.-A. Reshchikov and H. Morko  , *Luminescence properties of defects in GaN*. Journal of applied physics **97**, 061301 (2005).
- [RF94] G. Ramirez-Flores, H. Navarro-Contreras, A. Lastras-Martinez, R.-C. Powell, and J.-E. Greene, *Temperature-dependent optical band gap of the metastable zinc-blende structure β -GaN*. Physical Review B **50**(12), 8433 (1994).
- [Ric94] P. Rice, H. Carmichael *et al.*, *Photon statistics of a cavity-QED laser: A comment on the laser-phase-transition analogy*. Physical Review A **50**(5), 4318 (1994).
- [Rig10] L. Rigutti, M. Tchernycheva, A.-D.-L. Bugallo, G. Jacopin, F.-H. Julien, F. Furtmayr, M. Stutzmann, M. Eickhoff, R. Songmuang, and F. Fortuna, *Photoluminescence polarization properties of single GaN nanowires containing Al_xGa_{1-x}N/GaN quantum discs*. Physical Review B **81**(4), 045411 (2010).
- [Rin08] P. Rinke, M. Winkelnkemper, A. Qteish, D. Bimberg, J. Neugebauer, and M. Scheffler, *Consistent set of band parameters for the group-III nitrides AlN, GaN, and InN*. Physical Review B **77**(7), 075202 (2008).
- [Rob07] L.-H. Robins, K.-A. Bertness, J.-M. Barker, N.-A. Sanford, and J.-B. Schlager, *Optical and structural study of GaN nanowires grown by catalyst-free molecular beam epitaxy. II. Sub-band-gap luminescence and electron irradiation effects*. Journal of applied physics **101**(11), 113506 (2007).
- [Rod01] A.-V. Rodina, M. Dietrich, A. G  ldner, L. Eckey, A. Hoffmann, A.-L. Efros, M. Rosen, and B.-K. Meyer, *Free excitons in wurtzite GaN*. Physical Review B **64**(11), 115204 (2001).
- [Rok04] H. Rokhsari, S.-M. Spillane, and K.-J. Vahala, *Loss characterization in microcavities using the thermal bistability effect*. Applied physics letters **85**, 3029 (2004).

- [Rol06] F. Rol, B. Gayral, S. Founta, B. Daudin, J. Eymery, J.-M. Gérard, H. Mariette, L.-S. Dang, and D. Peyrade, *Optical properties of single non-polar GaN quantum dots*. physica status solidi (b) **243**(7), 1652 (2006).
- [Rol07a] F. Rol, *Etude optique de botes quantiques uniques non polaires de GaN/AlN*. Ph.D. thesis (2007).
- [Rol07b] F. Rol, S. Founta, H. Mariette, B. Daudin, J. Bleuse, D. Peyrade, J.-M. Gérard, B. Gayral *et al.*, *Probing exciton localization in non-polar GaN/ AlN quantum dots by single-dot optical spectroscopy*. Physical Review B **75**(12), 125306 (2007).
- [Rou] J. Rouxel .
- [Sch04] H. Schömig, S. Halm, A. Forchel, G. Bacher, J. Off, and F. Scholz, *Probing individual localization centers in an InGaN/GaN quantum well*. Physical review letters **92**(10), 106802 (2004).
- [Sch06] J.-B. Schlager, N.-A. Sanford, K.-A. Bertness, J.-M. Barker, A. Roshko, and P.-T. Blanchard, *Polarization-resolved photoluminescence study of individual GaN nanowires grown by catalyst-free molecular beam epitaxy*. Applied physics letters **88**, 213106 (2006).
- [Sch08] J.-B. Schlager, K.-A. Bertness, P.-T. Blanchard, L.-H. Robins, A. Roshko, and N.-A. Sanford, *Steady-state and time-resolved photoluminescence from relaxed and strained GaN nanowires grown by catalyst-free molecular-beam epitaxy*. Journal of applied physics **103**(12), 124309 (2008).
- [Sch11] T. Schumann, T. Gotschke, F. Limbach, T. Stoica, and R. Calarco, *Selective-area catalyst-free MBE growth of GaN nanowires using a patterned oxide layer*. Nanotechnology **22**, 095603 (2011).
- [Sek08] H. Sekiguchi, K. Kishino, and A. Kikuchi, *Ti-mask selective-area growth of GaN by RF-plasma-assisted molecular-beam epitaxy for fabricating regularly arranged InGaN/GaN nanocolumns*. Applied physics express **1**(12) (2008).
- [Sek10] H. Sekiguchi, K. Kishino, and A. Kikuchi, *Emission color control from blue to red with nanocolumn diameter of InGaN/GaN nanocolumn arrays grown on same substrate*. Applied Physics Letters **96**, 231104 (2010).
- [Seo09] J.-U. Seo, S. Hasegawa, and H. Asahi, *Selective area growth of GaN nanorods on patterned W/SiO₂/Si substrates by RF-MBE*. Journal of Crystal Growth **311**(19), 4437 (2009).
- [Ser09a] S. Sergent, *Fabrication and study of nitride-based photonic nanocavities containing GaN quantum dots for UV emitters integrated on silicon*. Ph.D. thesis (2009).
- [Ser09b] S. Sergent, J.-C. Moreno, E. Frayssinet, S. Chenot, M. Leroux, and F. Semond, *GaN Quantum Dots Grown on Silicon for Free-Standing Membrane Photonic Structures*. Applied Physics Express **2**(5), 1003 (2009).
- [Ser10] S. Sergent, J.-C. Moreno, E. Frayssinet, Y. Laaroussi, S. Chenot, J. Renard, D. Sam-Giao, B. Gayral, D. Néel, S. David *et al.*, *GaN quantum dots in (Al, Ga) N-based Microdisks* **210**, 012005 (2010).

Bibliography

- [Ser11] S. Sergent, B. Damilano, T. Huault, J. Brault, M. Korytov, O. Tottereau, P. Vennéguès, M. Leroux, F. Semond, and J. Massies, *Study of the growth mechanisms of GaN/(Al, Ga) N quantum dots: Correlation between structural and optical properties*. Journal of Applied Physics **109**, 053514 (2011).
- [Ser12] S. Sergent, M. Arita, S. Kako, S. Iwamoto, and Y. Arakawa, *High-Q (> 5000) AlN nanobeam photonic crystal cavity embedding GaN quantum dots*. Applied Physics Letters **100**(12), 121103 (2012).
- [SG98] M.-A. Sanchez-Garcia, E. Calleja, E. Monroy, F.-J. Sanchez, F. Calle, E. Munoz, and R. Beresford, *The effect of the III/V ratio and substrate temperature on the morphology and properties of GaN-and AlN-layers grown by molecular beam epitaxy on Si (111)*. Journal of crystal growth **183**(1), 23 (1998).
- [Sim00] J. Simon, R. Langer, A. Barski, and N.-T. Pelekanos, *Spontaneous polarization effects in GaN/Al_xGa_{1-x}N quantum wells*. Physical Review B **61**(11), 7211 (2000).
- [Sim01] J. Simon, *Etude des propriétés optiques de nanostructures quantiques à base de nitrures d'éléments III*. Ph.D. thesis (2001).
- [Sim03] J. Simon, N.-T. Pelekanos, C. Adelmann, E. Martinez-Guerrero, R. André, B. Daudin, H. Mariette *et al.*, *Direct comparison of recombination dynamics in cubic and hexagonal GaN/AlN quantum dots*. Physical Review B **68**(3), 035312 (2003).
- [Sim07] D. Simeonov, E. Feltin, H.-J. Buhlmann, T. Zhu, A. Castiglia, M. Mosca, J.-F. Carlin, R. Butté, and N. Grandjean, *Blue lasing at room temperature in high quality factor GaN/AlInN microdisks with InGaN quantum wells*. Applied physics letters **90**(6), 061106 (2007).
- [Sim08] D. Simeonov, A. Dussaigne, R. Butté, and N. Grandjean, *Complex behavior of biexcitons in GaN quantum dots due to a giant built-in polarization field*. Physical Review B **77**(7), 075306 (2008).
- [Slu93] R.-E. Slusher, A.-F.-J. Levi, U. Mohideen, S.-L. McCall, S.-J. Pearton, and R.-A. Logan, *Threshold characteristics of semiconductor microdisk lasers*. Applied Physics Letters **63**(10), 1310 (1993).
- [Son07] R. Songmuang, O. Landré, and B. Daudin, *From nucleation to growth of catalyst-free GaN nanowires on thin AlN buffer layer*. Applied Physics Letters **91**, 251902 (2007).
- [Sri07] K. Srinivasan and O. Painter, *Linear and nonlinear optical spectroscopy of a strongly coupled microdisk-quantum dot system*. Nature **450**(7171), 862 (2007).
- [Sta99] C. Stampfl and C.-G. Van de Walle, *Density-functional calculations for III-V nitrides using the local-density approximation and the generalized gradient approximation*. Physical Review B **59**(8), 5521 (1999).
- [Ste98] R. Stepniewski, A. Wyszomolek, M. Potemski, J. Lusakowski, K. Korona, K. Pakula, J.-M. Baranowski, G. Martinez, P. Wyder, I. Grzegory *et al.*, *Impurity-Related Luminescence of Homoepitaxial GaN Studied with High Magnetic Fields*. physica status solidi (b) **210**(2), 373 (1998).

- [Str06] S. Strauf, K. Hennessy, M.-T. Rakher, Y.-S. Choi, A. Badolato, L.-C. Andreani, E.-L. Hu, P.-M. Petroff, and D. Bouwmeester, *Self-tuned quantum dot gain in photonic crystal lasers*. Physical review letters **96**(12), 127404 (2006).
- [Stu07] W.-C. Stumpf, M. Fujita, M. Yamaguchi, T. Asano, and S. Noda, *Light-emission properties of quantum dots embedded in a photonic double-heterostructure nanocavity*. Applied physics letters **90**, 231101 (2007).
- [Tan03] Y. Tanaka, T. Asano, Y. Akahane, B.-S. Song, and S. Noda, *Theoretical investigation of a two-dimensional photonic crystal slab with truncated cone air holes*. Applied physics letters **82**, 1661 (2003).
- [Tou12] G. Tourbot, *Croissance par épitaxie par jets moléculaires et détermination des propriétés structurales et optiques de nanofils InGaN / GaN*. Ph.D. thesis (2012).
- [Vam07] A.-N. Vamivakas, M. Atatüre, J. Dreiser, S.-T. Yilmaz, A. Badolato, A.-K. Swan, B.-B. Goldberg, A. Imamoglu, and M.-S. Ünlü, *Strong extinction of a far-field laser beam by a single quantum dot*. Nano letters **7**(9), 2892 (2007).
- [Var67] Y.-P. Varshni, *Temperature dependence of the energy gap in semiconductors*. Physica **34**(1), 149 (1967).
- [VN06] J.-E. Van Nostrand, K.-L. Averett, R. Cortez, J. Boeckl, C.-E. Stutz, N.-A. Sanford, A.-V. Davydov, and J.-D. Albrecht, *Molecular beam epitaxial growth of high-quality GaN nanocolumns*. Journal of crystal growth **287**(2), 500 (2006).
- [Vos10] T. Voss, J.-P. Richters, and A. Dev, *Surface effects and nonlinear optical properties of ZnO nanowires*. physica status solidi (b) **247**(10), 2476 (2010).
- [Vur01] I. Vurgaftman, J.-R. Meyer, and L.-R. Ram-Mohan, *Band parameters for III-V compound semiconductors and their alloys*. J. Appl. Phys. **89**(11), 5816 (2001).
- [Vur03] I. Vurgaftman and J.-R. Meyer, *Band parameters for nitrogen-containing semiconductors*. J. Appl. Phys. **94**, 3675 (2003).
- [Waa11] A. Waag, X. Wang, S. Fündling, J. Ledig, M. Erenburg, R. Neumann, M. Al Suleiman, S. Merzsch, J. Wei, S. Li *et al.*, *The nanorod approach: GaN NanoLEDs for solid state lighting*. physica status solidi (c) (2011).
- [Wat08] N. Watanabe, T. Kimoto, and J. Suda, *The temperature dependence of the refractive indices of GaN and AlN from room temperature up to 515 C*. Journal of Applied Physics **104**(10), 106101 (2008).
- [Wei92] C. Weisbuch, M. Nishioka, A. Ishikawa, and Y. Arakawa, *Observation of the coupled exciton-photon mode splitting in a semiconductor quantum microcavity*. Physical Review Letters **69**(23), 3314 (1992).
- [Wei09] O. Weidemann, P.-K. Kandaswamy, E. Monroy, G. Jegert, M. Stutzmann, and M. Eickhoff, *GaN quantum dots as optical transducers for chemical sensors*. Applied Physics Letters **94**, 113108 (2009).
- [Wis06] L. Wischmeier, T. Voss, I. Rückmann, J. Gutowski, A.-C. Mofor, A. Bakin, and A. Waag, *Dynamics of surface-excitonic emission in ZnO nanowires*. Physical Review B **74**(19), 195333 (2006).

Bibliography

- [Wu09] J. Wu, *When group-III nitrides go infrared: New properties and perspectives*. Journal of Applied Physics **106**(1), 011101 (2009).
- [Wys02] A. Wysmolek, K.-P. Korona, R. Stepniewski, J.-M. Baranowski, J. Błoniarczyk, M. Potemski, R.-L. Jones, D.-C. Look, J. Kuhl, S.-S. Park *et al.*, *Recombination of excitons bound to oxygen and silicon donors in freestanding GaN*. Physical Review B **66**(24), 245317 (2002).
- [Yab87] E. Yablonovitch, *Inhibited spontaneous emission in solid-state physics and electronics*. Physical review letters **58**(20), 2059 (1987).
- [Yag98] H. Yaguchi, J. Wu, B. Zhang, Y. Segawa, H. Nagasawa, K. Onabe, and Y. Shiraki, *Micro Raman and micro photoluminescence study of cubic GaN grown on 3C-SiC (001) substrates by metalorganic vapor phase epitaxy*. Journal of crystal growth **195**(1), 323 (1998).
- [Yar97] A. Yariv, *Optical electronics in modern communication* (Oxford University press, 1997).
- [Yeh92] C.-Y. Yeh, Z.-W. Lu, S. Froyen, and A. Zunger, *Zinc-blende-wurtzite polytypism in semiconductors*. Phys. Rev. B **46**(16), 10086 (1992).
- [Yos97] M. Yoshizawa, A. Kikuchi, M. Mori, N. Fujita, and K. KISHINO, *Growth of Self-Organized GaN Nanostructures on Al₂O₃ (0001) by RF-Radical Source Molecular Beam Epitaxy*. Jpn. J. Appl. Phys. Vol **36**, L459 (1997).
- [Yos04] T. Yoshie, A. Scherer, J. Hendrickson, G. Khitrova, H. Gibbs, G. Rupper, C. Ell, O. Shchekin, and D. Deppe, *Vacuum Rabi splitting with a single quantum dot in a photonic crystal nanocavity*. Nature **432**(7014), 200 (2004).
- [Zho03] Z. Zhong, F. Qian, D. Wang, and C. M. Lieber, *Synthesis of p-Type Gallium Nitride Nanowires for Electronic and Photonic Nanodevices*. Nano Letters **3**(3), 343 (2003).
- [Zyw98] T. Zywiec, J. Neugebauer, and M. Scheffler, *Adatom diffusion at GaN (0001) and (0001) surfaces*. Applied physics letters **73**, 487 (1998).

Abstract

This work focuses on the optical study of GaN nanowires and AlN microcavities containing GaN quantum dots. The 1-meV linewidth of the neutral donor-bound exciton line in the photoluminescence spectrum of MBE-grown GaN nanowires evidences that the strain is homogeneous in the material. These nanowires do not exhibit any excitonic confinement, but the efficient strain relaxation allows to grow strain-free zinc-blende GaN nanowires and then to conduct fine spectroscopy on cubic GaN near band edge. Beside, we show that the tentative attribution of the recombination line at 3.45 eV in the spectrum of wurtzite GaN nanowires to a surface-enhanced two-electron satellite does not hold. Indeed, its dipole polarization selection rules and its evolution with intense applied magnetic field do not match that of a two-electron satellite.

We also performed the spectroscopy of GaN/AlN quantum dot microdisks. Record quality factors for AlN cavities were measured around 3 eV. GaN/AlN quantum dot nanocavities embedded in photonic crystal waveguides were also investigated. The attribution of each mode either to the waveguide or to the cavity, predicted by calculations, is experimentally confirmed by a different light localization. These structures allow excellent quality factors to be reached, from 2300 at 3.45 eV, up to 4400 at 3.14 eV. Although the expected Purcell factor is very high (around 100), we did not manage to observe the Purcell effect. This originates either from an enhancement of non-radiative recombination channels or from an instability of both the cavity modes and the quantum dot emission under intense exposure. Finally, it appears that the main limiting factor to achieve lasing in these structures is the strong built-in electric field, which slows up the spontaneous emission rate of the quantum dots.

Résumé

Ce travail de thèse porte sur l'étude optique de nanofils de GaN et de microcavités d'AlN contenant des boîtes quantiques de GaN. La largeur de raie de l'exciton lié au donneur neutre dans le spectre de photoluminescence des nanofils de GaN crûs par épitaxie par jets moléculaires met en évidence l'homogénéité des contraintes dans le matériau. S'ils ne présentent aucun confinement excitonique, la géométrie filaire permet une relaxation efficace des contraintes et permet d'étudier précisément le bord de bande du GaN relaxé en phase cubique. Par ailleurs, nous infirmons l'attribution de la transition à 3.45 eV observée dans le spectre des nanofils de GaN wurtzite à un satellite à deux électrons. En effet, les règles de sélection de son dipole, ainsi que son évolution sous champ magnétique intense, montrent que cette transition n'a pas les propriétés d'un satellite à deux électrons.

Nous avons également étudié la spectroscopie de microdisques d'AlN contenant des boîtes quantiques de GaN. Des facteurs de qualité record pour les cavités en AlN ont été mesurés autour de 3 eV. Des nanocavités d'AlN contenues dans des guides d'onde unidimensionnels ont également été étudiées. L'attribution de chaque mode au guide d'onde ou à la cavité, prédite par des calculs préliminaires, est confirmée expérimentalement par une localisation différente. Ces structures donnent lieu à d'excellents facteurs de qualité, de 2300 à 3.45 eV, jusqu'à 4400 à 3.14 eV. Si le facteur de Purcell attendu est très élevé (autour de 100), nous n'avons pas réussi à observer l'effet Purcell. Ceci s'explique soit par l'instabilité des modes de cavité et de l'émission des boîtes quantiques sous exposition prolongée, soit par l'importance des recombinaisons non radiatives. Enfin, il apparaît que le frein principal à l'obtention de l'effet laser dans ces structures est l'important champ électrique interne, qui ralentit l'émission spontanée des boîtes quantiques.

